University of Alaska

Coastal Marine Institute

Mapping and Characterization of Recurring Spring Leads and Landfast Ice in the Beaufort and Chukchi Seas

Principal Investigators:
Andrew R. Mahoney, Geophysical Institute, University of Alaska Fairbanks
Hajo Eicken, Geophysical Institute, University of Alaska Fairbanks

Co-Investigators:
Lewis H. Shapiro, Geophysical Institute, University of Alaska Fairbanks
Rudi Gens, Geophysical Institute, University of Alaska Fairbanks
Tom Heinrichs, Geophysical Institute, University of Alaska Fairbanks
Franz J. Meyer, Geophysical Institute, University of Alaska Fairbanks
Allison Graves Gaylord, Nuna Technologies, Homer, AK

Final Report
November 2012
OCS Study BOEM 2012-067

BOEM
Bureau of Ocean Energy Management

UAF
University of Alaska Fairbanks

Contact Information:
email: CMI@alaska.edu
phone: 907.474.6782
fax: 907.474.7204

Coastal Marine Institute
School of Fisheries and Ocean Sciences
University of Alaska Fairbanks
P. O. Box 757220
Fairbanks, AK 99775-7220

This study was funded in part by the U.S. Department of the Interior, Bureau of Ocean Energy Management (BOEM) through Cooperative Agreement No. M09AC15191 between BOEM, Alaska Outer Continental Shelf Region, and the University of Alaska Fairbanks. This report, OCS Study BOEM 2012-067, is available through the Coastal Marine Institute and select federal depository libraries. Copies can also be accessed electronically from:
http://www.boem.gov/Environmental-Stewardship/Environmental-Studies/Alaska-Region/Index.aspx.

TABLE OF CONTENTS

LIST OF FIGURES

LIST OF TABLES

ABSTRACT

This project is the continuation and extension of an earlier project with the same title (MMS OCS Study 2005-068, active from 2004-2006), supported by the Minerals Management Service (MMS). MMS OCS STUDY 2005-068 was confined to the southern Beaufort Sea and eastern Chukchi Sea for the time period 1993-2004. The current project extends the study area to cover the entire Chukchi Sea and includes new data since 2004.

The results of the current project supercede those of MMS OCS STUDY 2005-068. The aim of this continuing study is to map and document the spatial and temporal distribution of recurring lead systems, coastal polynyas and landfast ice in the Beaufort and Chukchi Seas. The expanded study region encompasses a large portion of the northern coast of Alaska and parts of the Russian and Canadian coasts and extends the analysis into 2010. The region and its sea ice cover are also of importance to protected marine mammals and bird species. Dramatic reductions in Arctic summer sea ice extent starting in 2005, with a record minimum extent in 2007 and another imminent at the time of this writing in 2012, lend urgency to the need for improved knowledge and understanding of the physical sea ice environment in this region of the Arctic.

The extent and duration of the landfast ice throughout the study region was analyzed with Radarsat Synthetic Aperture Radar (SAR) between November 1996 and April 2008. Radarsat data for the period since April 2008 are only available commercially and were not utilized for this study. Lead distributions were quantified from Advanced Very High Resolution Radiometer (AVHRR) data over two overlappoing subregions. In the eastern region, which covers the entire Chukchi Sea leads were analyzed for the period from January 1994 to April 2010. In the western region, which covers the southern Beaufort Sea and the northeastern Chukchi Sea, leads were analyzed for the period from November 1993 to June 2009. Monthly mean landfast ice edge positions and spatial statistics of lead distributions are derived from these data for the time period of stable, closed sea-ice cover. Longer-term spatio-temporal variations in landfast ice extent and lead patterns are assessed in the context of large-scale atmospheric and oceanic change. Project products and deliverables include ArcGIS grids and shapefiles of monthly landfast ice extents and lead distributions with accompanying metadata. Published articles and reports of relevance to the project were also compiled in an Endnote bibliography database.

EXECUTIVE SUMMARY

The Arctic Ocean region is in the midst of major environmental and socio-economic transformations. Summer minimum sea-ice extent has been reduced on average by more than 10% per decade since 1979, with record minimum ice extent attained in 2007 and 2012. This loss of summer sea ice and an associated reduction in multiyear ice concentration have been most pronounced in the western Arctic. This region has also experienced substantial increases in maritime traffic and exploration of offshore oil and gas resources in recent years. The present project builds on earlier work (MMS OCS Study 2005-068) to address data and knowledge gaps pertaining to the ice regime in the coastal and offshore Beaufort and Chukchi Seas, in particular in areas holding oil and gas leases and of importance to local communities and ecosystems.

Prior to MMS OCS STUDY 2005-068, little research had been completed on ice conditions in this region since the Outer Continental Shelf Environmental Assessment Program (OCSEAP) in the 1970s and 1980s. MMS OCS STUDY 2005-068 provided an updated baseline on Alaska coastal sea ice regions and found significant changes in the seasonality of landfast ice since the 1970s. However, in the context of broader sea ice characteristics, the most dramatic changes of recent decades have occurred since the conclusion of MMS OCS STUDY 2005-068. In addition commercial interest in the US Arctic has recently expanded into the Chukchi Sea, which is largely outside the study region of the MMS OCS STUDY 2005-068. This report aims to fill these knowledge gaps by extending the timeline and study domain of MMS OCS STUDY 2005-068 to take account of more recent changes and regions of growing importance in the Chukchi Sea.

To analyze the location, concentration and recurring patterns of leads and openings in the sea ice, this project conducted qualitative and quantitative analyses of all sufficiently cloud-free Advanced very High Resolution Radiometer (AVHRR) imagery from November-June for the period 1993-2010. By expanding the prior work done under the MMS OCS STUDY 2005-068 project, this study was able to demonstrate a clear regional contrast in the distribution and seasonality of lead patterns in the Beaufort and Chukchi Seas. In the Beaufort Sea, aside from a recurring lead pattern termed the “Barrow Arch”, most of the patterns identified were confined to a relatively narrow zone between the margins of the pack ice and the coast. Due to a number of inter-related differences in boundary conditions, wind forcing and ice concentration and thickness, lead patterns in the Chukchi Sea evolve relatively unconstrained and reflect an ice pack in a state of near-continuous transition.

As a result of the more dynamic ice conditions compared to the Beaufort Sea, Chukchi coastal polynyas and flaw leads are widespread and represent the most persistent lead pattern in the entire region. This includes lead systems forming off Wrangel Island, which are often linked to the same weather patterns responsible for open water off the Chukchi coast.

Small polynyas also form in the lee of grounded ice masses such as Katie’s Floeberg, which formed on Hanna Shoal in every year of the study period. These grounded floebergs play an important role as nucleation sites for leads under varying directions of ice movement. They also appear to act as stress concentrators such that they are often the point of origin of large-scale lead systems such as those developed along the margin of the Beaufort Gyre. Due to the substantial deformation associated with such grounded ice masses, they may serve as source areas of deep-draft floebergs later in the season. While the growth of these features is reasonably well understood, the probability of bottom contact by deep-draft ice or ice ridges as an important prerequisite to their formation is less well described. Findings from this project suggest that a delayed onset of grounding during the ice year reflects changes in the mass budget of the Beaufort and Chukchi ice pack over the past two decades. Since these features are associated with persistent open water, but at the same time massive grounding and presumably gouging of the seafloor, their ecological importance is far from clear.

The most substantial finding derived from the analysis of AVHRR imagery concerns the major transformation of lead patterns and ice deformation and movement apparent in the Beaufort Sea beginning with the 2006 ice season. Thus, compared to previous years with very few leads outside of the Barrow Arch and the Mackenzie flaw zone, the number, density and extent of leads in this region have increased substantially, likely as a result of the changing composition of the Beaufort ice pack.

In addition to AVHRR data, nearly 3,000 Radarsat synthetic aperture radar (SAR) images spanning the period 1996-2008 were analyzed to map landfast ice growth and decay over the entire Chukchi and Beaufort coasts of Alaska. This allowed a comprehensive comparison between the landfast ice in the Chukchi and Beaufort Seas, which shows that while landfast ice forms earlier and lasts longer in the Beaufort Sea than the Chukchi Sea, local variability in bathymetry and the configuration of the coastline have a greater influence on the timing of the annual cycle. In addition, it was found that the relationship between water depth and the location of the seaward landfast ice edge (SLIE) is not consistent between the Chukchi and Beaufort Seas. Unlike in the Beaufort Sea, where there is a relatively robust relationship between the stable location of the SLIE and isobaths near 20 m, the SLIE does not exhibit a strong preferred water depth throughout the Chukchi Sea. Hence, isobaths are poorly suited as proxies for the location of the SLIE in the Chukchi Sea, which has implications for current parameterization approaches in ice-ocean models of the region. Regional contrasts between Chukchi and Beaufort Sea ice regimes also depend on ocean heat transport through Bering Strait and local solar heating, both of which promote a thinner ice cover and milder conditions in the Chukchi Sea.

With respect to seasonal timing of the landfast ice cycle, we found statistically significant trends along specific stretches of coastline, but not at regional scales. Along the northern coasts of the Seward and Chukotka peninsulas, a trend towards a later date of landfast ice stabilization of 4 days per year was found. Between Cape Kruzenstern and Point Hope there has been a trend toward complete ice removal occurring around 3 days earlier per year. These trends are in the same direction as the longer-term changes reported in MMS OCS STUDY 2005-068, though this was not the case throughout the study area.

As with the analysis of lead patterns, the finding with the greatest potential significance concerns changes since 2006, which was the beginning of a period of pronounced multiyear ice loss in this sector of the Arctic. Unlike in MMS OCS STUDY 2005-068, which found little change in landfast ice extent since the 1970s, this study indicates a possible reduction in landfast ice extent since 2006. Analysis of additional data covering more recent years would be required to confirm these findings, but they point toward changes in the coastal ice regime of the Beaufort Sea that are unprecedented during the satellite record.

A further aim of this project was to develop alternative approaches to the mapping of landfast ice extent. Using interferometric SAR (InSAR) techniques, this study established that landfast sea ice along Alaska's coast remains interferometrically coherent in L-band SAR imagery over time intervals of at least 46 days. Hence, landfast sea ice can be distinguished from drifting ice or open water based on interferometric coherence at spatial resolutions comparable to or better than previously developed approaches. Further, an automated technique was developed to map landfast ice extent that agrees well with existing SAR-based techniques. L-band SAR interferometry also shows promise for investigating landfast ice displacement on meter to sub-meter scales. Such motion can have significant impacts on structures within or beneath the landfast ice and – based on a case study at Barrow, Alaska – provides important insight into the distribution of stabilizing grounded ridges. While spatio-temporal coverage of Arctic coasts by L-band InSAR data is currently limited, a larger fleet of upcoming low-frequency SAR systems with improved spatial coverage and temporal revisit cycle may render L-band SAR interferometry a promising tool for future assessments of pan-Arctic landfast ice areas.

ACKNOWLEDGEMENTS

This study was funded by the U.S. Department of the Interior, Bureau of Ocean Energy Management (BOEM), Alaska Outer Continental Shelf Region, Anchorage Alaska, under Agreement Number M09AC15191 through the Coastal Marine Institute at the University of Alaska Fairbanks, and with matching funds provided by Conoco-Phillips Alaska, Inc. and Shell International Exploration and Production, Inc.

The work reported on here came together with the help of many people. In particular, we would like to acknowledge the expertise and unflagging support of Kevin Engle, who passed away unexpectedly in January 2011. Kevin made this work (and life) easier for all us – we miss him. Others who contributed substantially to the project include Mette Kaufman, Dayne Broderson, Scott MacFarlane, Jason Grimes and Pete Hickman – thank you! We are grateful for matching funds support for this work from Shell and Conoco-Phillips; moreover, we appreciate the interest and helpful input from John Cologgi, Michael Macrander, Walt Spring and Mitch Winkler.

1. INTRODUCTION

1.1 Note on earlier project of same name

This project is the continuation and extension of an earlier project with the same title (MMS OCS Study 2005-068, active from 2004-2006), supported by the Minerals Management Service (MMS). MMS OCS Study 2005-068 was confined to the Beaufort and eastern Chukchi Sea and the time period 1993-2004. The current project extends the study area to cover the entire Chukchi Sea and integrates new data acquired since 2004. Radarsat Synthetic Aperture Radar (SAR) from November 1994 to April 2008 (at which point Radarsat data are only available commercially with a major change in the cost structure) are used to analyze landfast sea ice extent and duration. Lead distributions were quantified from AVHRR data over two overlapping subregions. In the eastern region, which covers the entire Chukchi Sea, leads were analyzed for the period from January 1994 to April 2010. In the western region, which covers the southern Beaufort Sea and the northeastern Chukchi Sea, leads were analyzed for the period from November 1993 to June 2009. The results of the current project supercede those of MMS OCS STUDY 2005-068, but the reader is directed to the final report for MMS OCS STUDY 2005-068 (*Eicken et al.*, 2006) for details that will only be summarized in this document.

1.2 Background

The Arctic Ocean region is currently undergoing significant, inter-related environmental and socio-economic change (*Perovich*, 2011). Summer minimum sea-ice extent has been subject to an average reduction of more than 10% per decade since 1979, with recent reductions faster than predicted by many climate models (*Stroeve et al.*, 2012), and a near-complete loss of summer ice projected by the late 2030s (e.g., *Wang and Overland*, 2009). The retreat of the summer Arctic ice cover has been and is projected to be most pronounced in the western Arctic, specifically the East Siberian, Chukchi and Beaufort Seas (*Comiso*, 2002; *Douglas*, 2010; *Hutchings and Rigor*, 2012). However it is the recent thinning and loss of old, multiyear sea ice that is of greatest significance for likelihood of a summertime ice-free Arctic in the near future. By definition, multiyear ice is more than one year old (note that we include second-year ice in the multiyear ice category) and in general, thickness increases with age (*Maslanik et al.*, 2007).The loss of Arctic's oldest and thickest ice (*Tucker et al.*, 2001; *Belchansky et al.*, 2004; *Rothrock and Zhang*, 2005; *Maslanik et al.*, 2011; *Polyakov et al.*, 2012) in recent years is therefore not a change that is likely to be reversed in the short term.

Partly as a result of these observed and predicted changes, marine traffic and activities related to offshore oil and gas development have grown substantially over the past decade and are projected to increase further (*Arctic Council*, 2009; *Schmidt*, 2011). This will create new societal and ecological risks. Commercial activities in areas of critical habitat may place greater stress on marine mammals already considered threatened by loss of habitat due to retreating sea ice (*U.S. Fish and Wildlife Service*, 2008). At the same time, increased maritime activity in this changing and remote region will generate new challenges for maritime and environmental security.

While there are few if any systematic direct observations of the extent and impacts of these changes in the Alaska coastal zone and inner-shelf waters, native communities have reported for some time about substantial changes in the sea-ice regime, including later onset of ice formation and a less stable and less predictable ice cover (*Huntington*, 2000; *Krupnik and Jolly*, 2002; *George et al.*, 2004; *Gearheard et al.*, 2006; *Kapsch et al.*, 2010). Given the importance of Alaska coastal and inner-shelf waters from an ecological, economic and sociological perspective, in particular in the light of recent sales of offshore oil and gas leases, there is a clear need for information on the current status of the coastal sea ice regime.

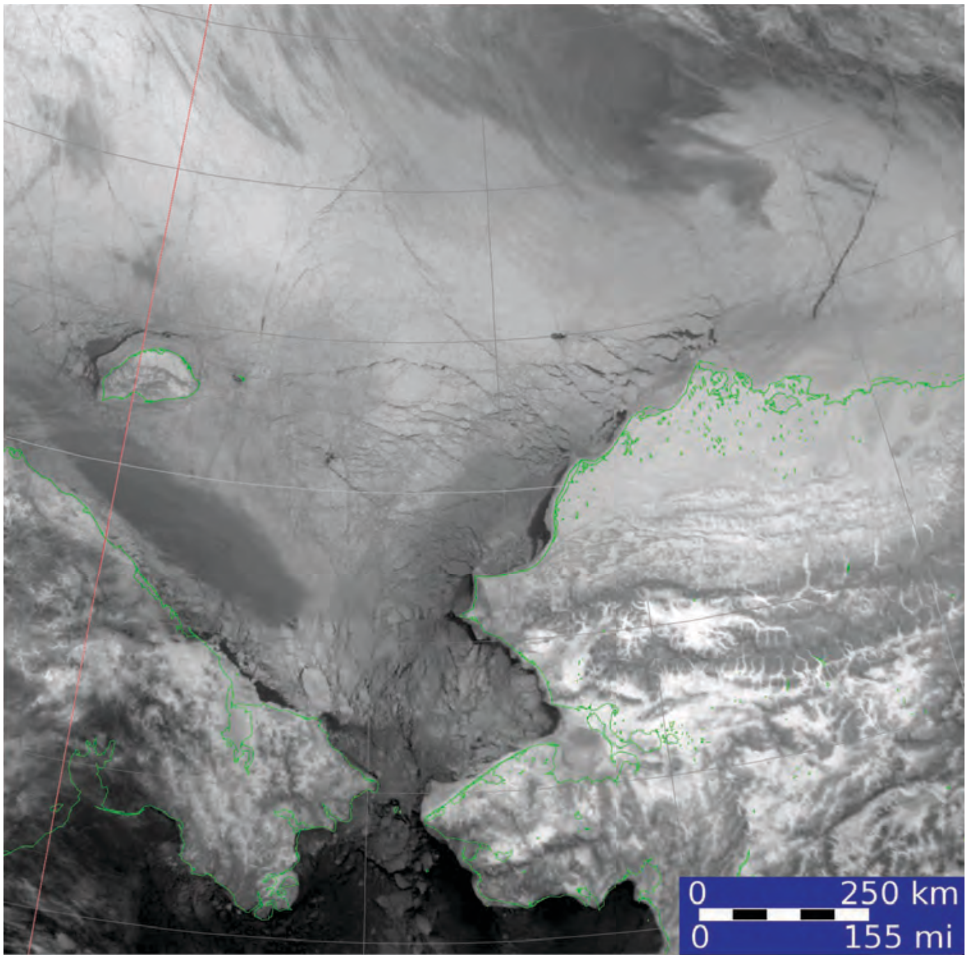

Figure 1.2.1 This figure emphasizes the difference between the "typical" level of deformation activity in the Beaufort and Chukchi Seas during the winter. The contrast in lead density across the east-west line from Wrangel Island (WI) through the grounded ice on Hanna Shoal (HAS) and then eastward to the northern edge of the zone of broken pack ice north of Point Barrow (PtB) is particularly clear in this image. The Chukchi Sea pack appears to be fragmented while the ice cover of the Beaufort Sea is relatively continuous. At other times during winter, the lead density in the Beaufort Sea ice cover is greater, so the boundary is less distinct. Also, as expected, ice conditions are more gradational across the boundary during the freeze up and melt seasons. (N14.97079.1550; 20 Mar 1997).

Prior to MMS OCS STUDY 2005-068, little research had been completed on ice conditions in this region since the Outer Continental Shelf Environmental Assessment Program (OCSEAP) in the 1970s and 1980s. MMS OCS STUDY 2005-068 provided an updated baseline on Alaska coastal sea ice regions, but the most dramatic sea ice changes of recent decades have occurred since the conclusion of MMS OCS STUDY 2005-068. In addition commercial interest in the US Arctic has recently expanded into the Chukchi Sea, which is largely outside the study region of the MMS OCS STUDY 2005-068. The sea ice literature seems to reflect a lack of interest in the ice over the Chukchi Sea shelf, since a literature search failed to produce any more recent publications on the Chukchi Sea ice pack. This leaves the impression that the Chukchi Sea ice cover is simply an extension of the Beaufort Sea pack ice. However, as will be described in this report, that is certainly not the case; the AVHRR image in Figure 1.2.1 illustrates this point. In terms of deformation processes and patterns, as well as physical and mechanical properties, the ice cover of the Chukchi Sea has a character of its own. This results from the particular geometry of the boundaries of the ice pack, the seasonal and areal patterns of freezing and melting that reflect the temperature gradient across the area, the effect of the prevailing winds off the northwest coast of Alaska, and the frequency and tracks of storms that traverse the area.

The aim of this study is to provide quantitative information on the seasonal and interannual variability in ice conditions in the Chukchi and Beaufort Seas for which such information is lacking. Specifically, this study presents data and results pertaining to the distribution and morphology of lead systems and to landfast sea-ice extent and stability (for definitions of these terms and in-depth discussions of previous work on these topics, please see Sections 3.1-3.3). The results of the analysis of lead systems covers the time from November, 1993 through June, 2010, while the landfast sea ice analysis spans the period 1996-2008. Further analysis of landfast ice was not possible due to changes in the availability of Radarsat data (after this date, the number of scenes required even for a single year would be associated with costs that exceed the scope of this project because of the large number of scenes required in the analysis). An additional aim of this work is therefore to investigate alternative approaches to identify landfast ice extent using other data sources.

The primary techniques used to identify and analyze leads and landfast ice are the same as those used in MMS OCS STUDY 2005-068 and can be regarded as operational methods. The alternative techniques for identifying and mapping landfast have been newly developed as part of this study and we present those results as case studies and comparisons. The study region encompasses the entire northern coast of Alaska and parts of the Russian and Canadian coasts. In addition to its commercial importance, this region and its sea ice cover are also of importance to protected marine mammals and birds. The resulting imagery and data sets (and ancillary data) have been compiled into geodatabases and are provided as part of this report. Upon formal release by the Bureau of Ocean Energy Management, they will also be made available online through established geodata distribution centers. As part of this project and in collaboration with the Geographic Information Network of Alaska (GINA) at the University of Alaska Fairbanks, we have also established a dedicated web site that serves as a clearinghouse and point-of-reference for project collaborators, program managers and others, with a separate, limited-access section that provides access to all resulting datasets (boem.gina.alaska.edu).

1.3 Regional hydrography and bathymetry

The Chukchi and Beaufort Seas lie north of Alaska and together contain the entire U.S. Arctic domain. Typically, Point Barrow, the northernmost point of the North American mainland, is taken as the demarcation between the two bodies. Away from the coast, the boundary between the Chukchi and Beaufort Seas is typically defined by the regional bathymetry (Figure 1.3.1). The Chukchi Sea is dominated by a broad, shallow shelf (the Chukchi Shelf) mostly less than 50 m deep with shoals such as Hanna Shoal and Herald Shoal rising to around 20 m. Conversely, water shallower than 50 m in the Beaufort Sea occupies only a narrow strip less than 100 km from the coast. Most of the Beaufort Sea is more than 1000 m deep and is part of the Canada Basin.

Figure 1.3.1 also shows the predominant current directions. In the Chukchi Sea, there is a net northward flow, which enters through Bering Strait and branches into different bathymetrically constrained currents (*Weingartner et al.*, 2005). The heat flux associated with this northward flow enhances the early loss of ice in the Chukchi Sea (*Woodgate et al.*, 2010). In contrast, circulation in the Beaufort Sea is dominated by the anticyclonic (clockwise) motion of the Beaufort Gyre (Figure 1), which transports some of the oldest and thickest ice in the Arctic from the region north of the Canadian Archipelago into the Beaufort Sea. This motion is driven by atmospheric circulation around a persistent region of high pressure (the Beaufort High). The strength of the Beaufort Gyre can vary from year to year and the ice motion can sometimes reverse for periods of a few days. However, in winter the average drift is approximately parallel to the coastline.

The differences in bathymetry and hydrography between the Chukchi and Beaufort Seas lead to marked differences in the character of sea ice in these two regions, as illustrated in Figure 1.2.1. Due to its more southerly location and the inflow of heat through Bering Strait, the Chukchi Sea experiences a longer open water season than the Beaufort Sea. In addition, the combination of a thinner ice pack and a coastline that offers the opportunity for open water creation under almost any drift direction, sea ice in the Chukchi sea is more mobile and changeable than sea ice in the Beaufort Sea. This is reflected in the more varied lead patterns in the Chukchi Sea and and in the greater extent of landfast sea ice in the Beaufort Sea.

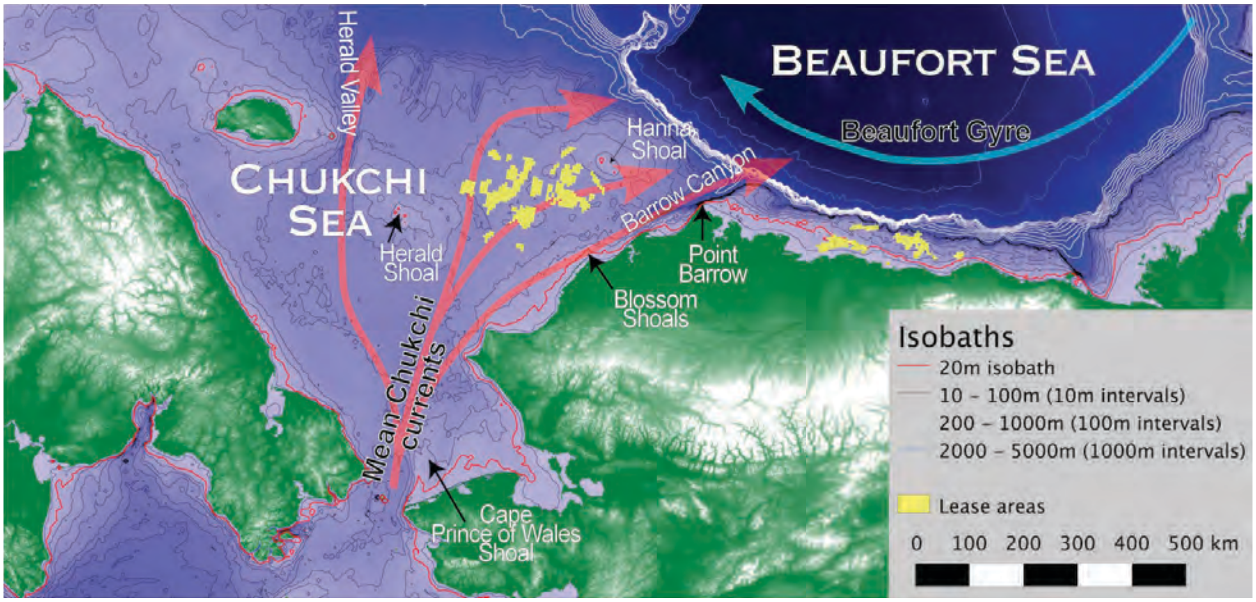

Figure 1.3.1: The bathymetry of the Chukchi and Beaufort Seas and the location of current OCS leases for oil and gas exploration. Bathymetry data from Danielson (2008). The red contour indicates the location of the 20 m isobath. Colored arrows are schematic represenations of mean surface currents, from Weingartner (2005)

1.4 Study regions

Figure 1.4.1 shows the study regions for the operational leads and landfast ice components of this study. To provide consistency with the results from MMS OCS STUDY 2005-068, we retained the study regions from the previous study and established additional regions to the west. From here on, we will refer to the study regions used in MMS OCS STUDY 2005-068 and those added for this study as the eastern and western regions, respectively.

For the leads component of the project, there is an area of overlap between the eastern and western study regions. This minimized the repetition of work from MMS OCS STUDY 2005-068 and allowed each study region to provide complete coverage of either the Chukchi or Beaufort Sea. For the landfast ice component of the project, the western study region is contiguous with the eastern region. Data were acquired and processed separately for each region, but in our analysis we treat both regions as a part of a single unit.

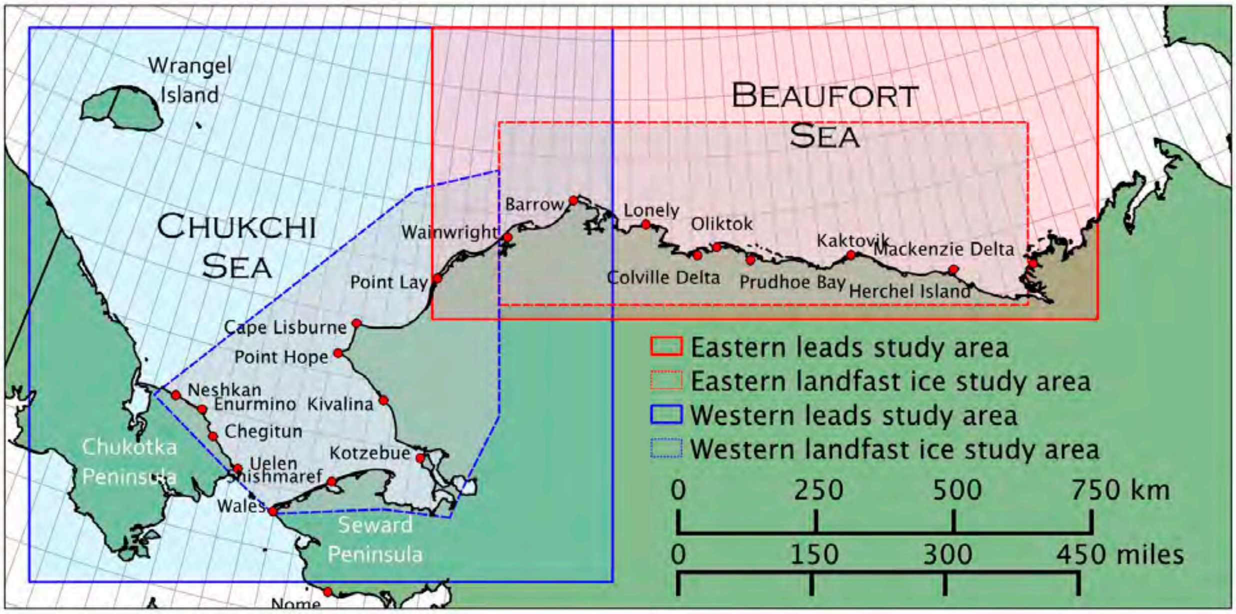

Figure 1.4.1: Map showing extent of the leads and landfast ice study areas for this project. The eastern study areas are the same as those used in MMS OCS STUDY 2005-068.

1.5 Lead distribution patterns

This study is based largely on the hypothesis that the deformation patterns of the pack ice in the Beaufort and Chukchi Seas generally, but not always, reflect the interaction of the moving ice with the fixed landmasses and, in some cases, grounded ice features. Differential motion in the sea ice pack is accommodated largely by the generation of leads. On some scales, the process can be modeled as if the ice is a continuum following some constitutive law. However, at the scales relevant to people and ecosystems and on the spatial and time scales of the satellite imagery used to study lead distributions, the deformation clearly depends on lead formation. The driving conditions repeat with the passage of weather systems and the consistency of ocean currents, and given that the coastal boundaries are rigid it is expected that many lead patterns would occur repeatedly in the same or different years. Some variations should occur because of differences in the configuration of the landfast ice and the composition of the pack ice. However, similar lead patterns should be recognizable. Descriptions and examples of recurring lead patterns and other deformation features constitute an important part of this report.

The interaction between the coast and moving ice is simplest in the Beaufort Sea, which is bounded to the east by the Canadian Arctic islands and to the south by the north coast of Alaska. As described in section 1.3, the mean sense of sea ice motion in the Beaufort Sea is clockwise around the Beaufort Gyre. Sea ice in the Beaufort Sea therefore moves generally southward and westward, approximately parallel to the Alaska coast. There can be occasional eastward excursions, but these are severely limited by the shapes of the coastlines. Northward and southward displacements also occur, but they too are limited in both time and distance.

The interaction between ice motion and the coast is more complex in the Chukchi Sea, where the configration of the coast is such that there is potential for the creation of open water under any drift direction. Along the northern Alaska Chukchi Sea coast, the prevailing winds from the northeast drive ice away from the shore giving rise to a recurring flaw lead. This ecologically important semi-permanent expanse of open water creates room for ice to spread into when wind conditions change. Other parts of the Chukchi Sea coast act similarly so that there is almost always open water somewhere for ice to drift into. This contributes to a highly mobile ice pack in the Chukchi Sea. Islands, such as Wrangel Island are able to create open water under any drift direction. Shoals, such as Hanna Shoal and Herald Shoal (see Figure 1.3.1), where the water is shallow enough for deep-keeled ice ridges to become grounded can act in a similar way and have a far-reaching effect on leads patterns.

In this report, we present quantitative analysis of lead distributions and morphology for the time period 1993 to 2010, which are complemented by a more general, qualitative analysis of deformation and lead patterns. Together, this study of recurring lead patterns in the Chukchi and Beaufort Seas provides tools for planning needs with respect to lead recurrence probabilities, lead morphology and size and linkages of lead distributions to large-scale atmospheric and ice-dynamics parameters.

1.6 Landfast ice extent and stability

Landfast sea ice, also referred to as shorefast or simply "fast" ice, is defined according to the World Meteorological Organization (1970) as "ice which remains attached to the coast". As such, it forms a rigid, immobile boundary that occupies the triple juxtaposition between the ocean, land and atmosphere, where it buffers the coast against the erosive action of waves (*Lantuit and Pollard*, 2008) and plays an important role in sediment dynamics (*Eicken et al.*, 2005a). By effectively isolating the coastal ocean from the atmosphere, shorefast ice (SFI) also effects the fate of river inflow when it enters the marine environment (*Kasper*, 2010).

The seaward landfast ice edge (SLIE) is marked by either open water or drifting pack ice. As a result, landfast ice provides important habitat for ringed seals and polar bears providing them with ideal denning locations in proximity to prey (*Laidre et al.*, 2008). As an extension of the land, landfast ice is used as a hunting and traveling platform by Arctic coastal communities (e.g. *Gearheard et al.*, 2006; *Krupnik*, 2010) and for the construction of ice roads (*Potter et al.*, 1981; *Masterson*, 2009) and runways. The presence and stability of landfast ice in Alaska is therefore of considerable economic importance for offshore oil and gas development (*Eicken et al.*, 2009) as well as for identifying potential places of refuge for maritime activities (*CRRC*, 2009). The extent and thickness of landfast ice was also a critical consideration during the recent wintertime delivery of fuel to the City of Nome in January, 2012.

Although stationary by definition, landfast ice is formed and deformed by a combination of dynamic and thermodynamic processes, which follow their own annual cycles and vary geographically in their presence and importance. Consequently, the extent and appearance of landfast ice differs significantly between regions of the Arctic. In much of the Russian Arctic, the landfast ice extends tens to hundreds of kilometers from the coast (*Zubov*, 1945; *Barnett*, 1991; *Eicken et al*., 2005b), which is one or two orders of magnitude greater than the typical width of landfast ice in Arctic Alaska (*Barry et al*., 1979; *Stringer et al*., 1980). Such basin-scale differences in spatial extent can be largely related to differences in nearshore bathymetry, but there is no Arctic-wide relationship between the water depth and the location of the landfast ice edge. Among the different water depths that have been cited as the limits of landfast ice extent are 25 m along the Siberian coast (*Zubov*, 1945; *Barry et al*., 1979), 10 m in the Kara Sea (*Barry et al*., 1979; *Divine et al*., 2004); between 18 m and 30 m in the Beaufort Sea (*Service*, 1968; *Kovacs and Mellor*, 1974; *Reimnitz and Barnes*, 1974; *Stringer*, 1974; *Shapiro*, 1975; *Kovacs*, 1976; *Weeks et al*., 1977; *Stringer et al*., 1980), 100 m near Severnaya Zemlya (*Divine et al*., 2004) and 180 m off the eastern coast of Baffin Island (*Jacobs et al*., 1975). One of the key outcomes of MMS OCS STUDY 2005-068 was the quantification of this relationship. In the Beaufort and northern Chukchi Seas it was found that the modal water depth at the seaward edge of the landfast ice varies between 16 m and 22 m (*Mahoney et al.*, 2007b).

In the Chukchi and Beaufort Seas, landfast sea ice is a seasonal phenomenon. The annual landfast ice cycle can be broadly characterized by a gradual seaward advance from the coast beginning in late fall or early winter (October - November) followed by a rapid retreat coinciding with the onset of spring (May-June). The range of dates comes from spatial differences in the arrival of the seasons as well as interannual variability in the behavior of the landfast ice. Landfast ice forms first in lagoons and sheltered embayments. To extend into deeper water and remain stable, landfast sea ice in the study area must be anchored by grounded ridges (*Mahoney et al.*, 2007a), which partly explains the relationship between extent and bathymetry. The availability of such ridges limits the timing of stabilization as ridges formed from thin, young ice tend to have shallower keels than ridges created from thicker ice, as found by Tin and Jeffries (2003) in Antarctic ridges. Another key finding of MMS OCS STUDY 2005-068 was that during the period 1996-2004, landfast ice in northern Alaska formed later and broke up earlier than it did during the1970s (*Barry et al.*, 1979; *Mahoney et al.*, 2007b). One of the aims of this study is to examine temporal trends in the extended dataset and test for evidence of further or accelerated change since 2004.

2. OBJECTIVES

The goal of this project is to update the results of MMS OCS Study 2005-068 (MMS OCS STUDY 2005-068) from its initial time span (1993-94 to 2003-2004 ice years) to the 2007-2008 ice year for the landfast ice and the 2009-2010 ice year for the lead distributions, and to extend the study area to include the Chukchi Sea coasts of Alaska and the Chukotka Peninsula of eastern Siberia over the entire time period. Note that the study area for MMS OCS STUDY 2005-068 included the Beaufort Sea coast from MacKenzie Bay to Point Barrow and then southwest along the Chukchi Sea coast to about Icy Cape (Figure 1.4.1).

The specific objectives for the entire study area and time period are to:

1. Document and map the spatial distribution and extent of recurring leads, lead systems and polynyas along the Alaska coast of the Beaufort and Chukchi Seas and their extension into the Chukchi Sea, and develop terminology to describe and classify lead patterns;
2. Document and map the extent of the stable landfast ice along the Beaufort and Chukchi Sea coasts of Alaska and the northern coast of the Chukotka Peninsula in eastern Siberia;
3. Determine monthly mean, minimum and maximum landfast ice extents;
4. Develop and evaluate efficacy of methods to delineate landfast ice extent and deformation based on interferometric synthetic aperature radar data analysis;
5. Determine and grid monthly lead and polynya occurrence probabilities;
6. Summarize statistics of lead morphology and recurrence;
7. Interpret the lead patterns and polynyas as indicators of ice dynamics;
8. Interpret landfast ice variability in the context of atmospheric and oceanic forcing and bathymetric constraints.

3. METHODS AND DATA SETS

3.1 Characterization of large-scale lead patterns

There is an extensive descriptive literature on the Beaufort Sea ice regime and other parts of the Arctic Ocean that goes back many years. Drifting ice camps and occupied ice islands, major projects such as AIDJEX and SHEBA, and numerous buoy deployments have provided much information about the typical movement and deformation patterns throughout the Arctic Basin on various time and spatial scales. However, aside from the occasional deployment of an isolated buoy, there has been little similar work done on the shelf of the Chukchi Sea. Pritchard (1978) and Colony (1979) reported on the results of buoy deployments in the Chukchi Sea in the spring of 1978. Later, six ARGOS data buoys were set out off the coast of Alaska in the winter of 1981-2 and the results were presented in Pritchard and Hanzlick (1987) and Pritchard (1991). The current interest in exploration for hydrocarbons on the Chukchi Sea shelf has undoubtedly produced more such deployments, but none of the results have yet appeared in the literature.

In MMS OCS STUDY 2005-068, we confirmed the hypothesis that, since neither the geometry of the coasts and landfast ice that bound the southern Beaufort Sea nor the progression of weather systems vary significantly over time, lead and deformation patterns in that area should recur frequently. This study therefore adopted the same hypothesis for both the Beaufort and Chukchi Seas. As will be shown, the hypothesis has proved to be useful, although the processes and interactions with the boundaries in the Chukchi Sea are clearly different from those in the Beaufort Sea. In addition, the overall deformation patterns in the Chukchi Sea tend to involve the entire ice cover over large areas, rather than being confined to narrow zones along the coasts.

As in MMS OCS STUDY 2005-068, the 'SwathViewer' application developed by the Geographic Information Network of Alaska (GINA) was used to study imagery from NOAA-AVHRR satellites stored in the GINA data archive. GINA acquires and archives virtually every available NOAA-AVHRR image of interest for Alaska studies and SwathViewer provides a simple and effective means of accessing the archive. It has the capability of displaying the AVHRR images at resolutions of from 20 km to 1 km per pixel. In addition, it provides methods to accurately locate observed features in the latitude-longitude grid, measure distances and, since the end of MMS OCS STUDY 2005-068, the capability for storage and capability of compare changes between images has been enhanced.

For this part of the project, an AVHRR image of the entire Chukchi Sea was selected and stored for each day of the ice year from 1993, when the GINA archive was established, through most of the 2011-2012 winter. The coverage for each year extends from the first appearance of ice in the Chukchi Sea through the last retreat of the ice from the area. The images were displayed in 1 km pixels, which is adequate for identifying and describing the deformation patterns and associated lead systems that are discussed here. Note that the collection of images includes many with extensive cloud cover, but even these were useful for the analysis when viewed in rapid sequences with clearer images. In addition, the catalog of images used in MMS OCS STUDY 2005-068, which ended with the 2003-2004 year, was also brought up to date. Note that for that project, the images were displayed at a resolution of 2 km/ pixel so that the entire area appeared in one scene. The same scale was used in the new images.

This project began by following the approach to data collection and organization used in MMS OCS STUDY 2005-068. However, it quickly became apparent that the processes and patterns in the southern Beaufort Sea are appreciably different from those that occur in the Chukchi Sea pack ice. Thus, instead of looking for particular lead forms, such at the tangent leads and lead fans that are prominent in the Beaufort Sea, it was necessary to look for large scale patterns ranging across the entire Chukchi Sea, rather than patterns that are confined to a relatively narrow zone where the pack ice interacts with the coast as occurs in the southern Beaufort Sea. This approach is explained further in sections 4.2.1 and 4.2.2 below, where the conceptual models that govern the approach to the analysis are described.

The analysis here is descriptive, and interpretations of driving forces that create the patterns assume that the deformation of the Chukchi Sea pack ice is primarily wind-driven. This is consistent with the observations that (1) deformation patterns change rapidly as weather systems move across the area, (2) the most common deformation patterns are readily interpreted in terms of the prevailing winds off the coast of Alaska, and (3) the coincidense of the directions of cloud streets that originate at openings in the pack ice with the displacement directions. There is evidence of floe displacements that are driven by currents in some areas. The data come from studies of the tracks of drifting buoys equipped to measure currents while in motion (*Pritchard and Hanzlick*, 1987; *Pritchard*, 1991). However, these effects appear to be local and there is no way to estimate the contribution of ocean currents to the deformation patterns observed here. As a result, the simplest way to classify and sort the deformation patterns is to simply relate them to the direction the pack ice is moving when the pattern appears, or to a simple descriptive feature of the pattern itself. This is a generic classification that relies only on observations although, in some cases, making the association of the displacement direction with the prevailing wind direction seems justified.

3.2 Mapping of lead distribution and morphology

3.2.1 Acquisition and processing of satellite imagery

The study area for the quantitative analysis of lead distribution and morphology is shown in Figure 1.4.1. The western and eastern regions cover the Chukchi and Beaufort Seas, respectively. Together, they provide a perspective on regional lead characteristics, capturing key geographic areas associated with specific lead patterns, such as the flaw lead along the Alaska Chukchi coast, leads over Hanna Shoal and in Mackenzie Bay. The western region for the leads study area covers approximately 1 million km^2 and spans the entire Chukchi Sea. The eastern subregion covers 540,000 km^2 and extends from Icy Cape in the west to the Mackenzie Delta in the east. For the exclusion of areas of excessive cloud coverage and to provide more localized results, we identified 4 subregions (A-D) within the western region and 12 subregions (1-12) in the eastern region. The locations and extents of these subregions are shown in Figures 3.2.1 and 3.2.2.

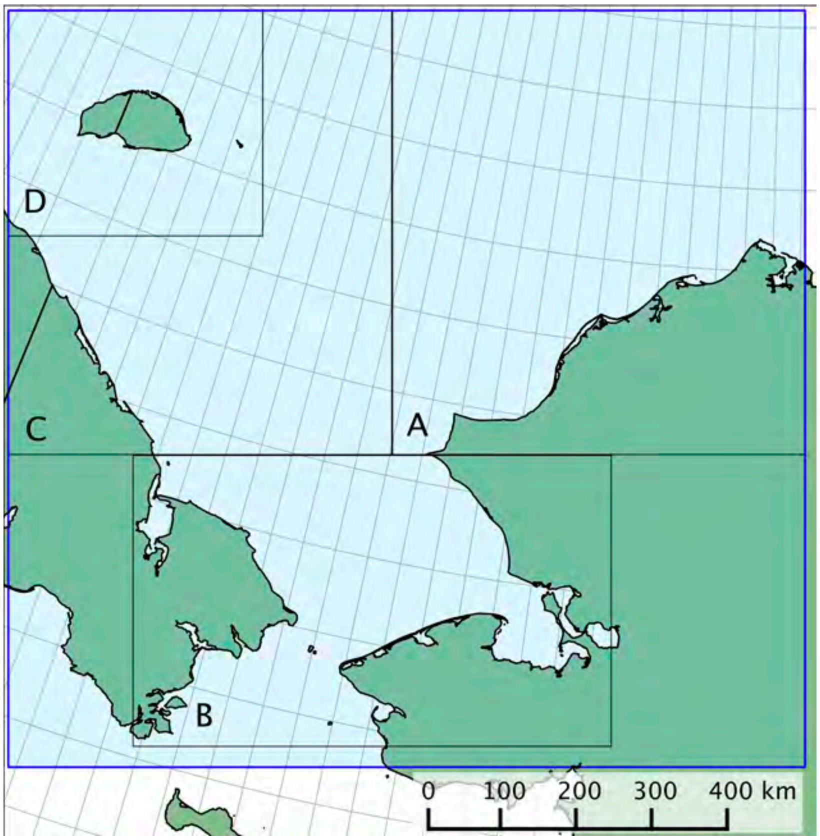

Figure 3.2.1: Study area and sub-regions for quantitative analysis of lead distribution and morphology in the western (Chukchi Sea) study area.

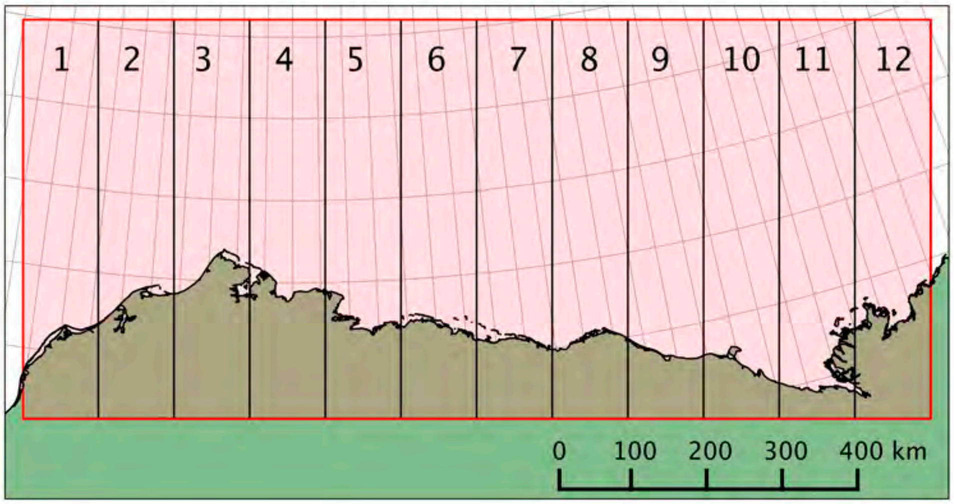

Figure 3.2.2: Study area and sub-regions for quantitative analysis of lead distribution and morphology in the eastern (Beaufort Sea) study area. This corresponds to the study area for MMS OCS STUDY 2005-068.

AVHRR data had been down-linked through the International Observatory of the North and its predecessors at the Geophysical Institute, UAF, and were acquired for this project through GINA. For the eastern (Beaufort Sea) study area, a total of 488 unique AVHRR scenes (including 385 from the previous study, MMS OCS Study 2005-068) were analyzed in either the thermal and visible ranges. Due to more frequent and extensive cloud cover in the Chukchi Sea than the Beaufort Sea, only 129 images were analyzed for the western study area. In addition to the image processing to extract lead fraction described below, each image was manually inspected to identify areas of cloud cover. Whole subregions of data were selectively eliminated if a significant fraction of their surfaces were obscured by clouds or if clouds were being misidentified as leads by the algorithm described below. Figure 3.2.3 shows the distribution of scenes across the different months for the eastern and western study areas. Cloud coverage is typically low over the Beaufort Sea throughout most of winter and roughly 5 images per month were analyzed for the eastern study area between January and May. In contrast, only 1-2 sufficiently cloud-free images were acquired in the western study area for all months except April, when skies were clearest over the Chukchi Sea.

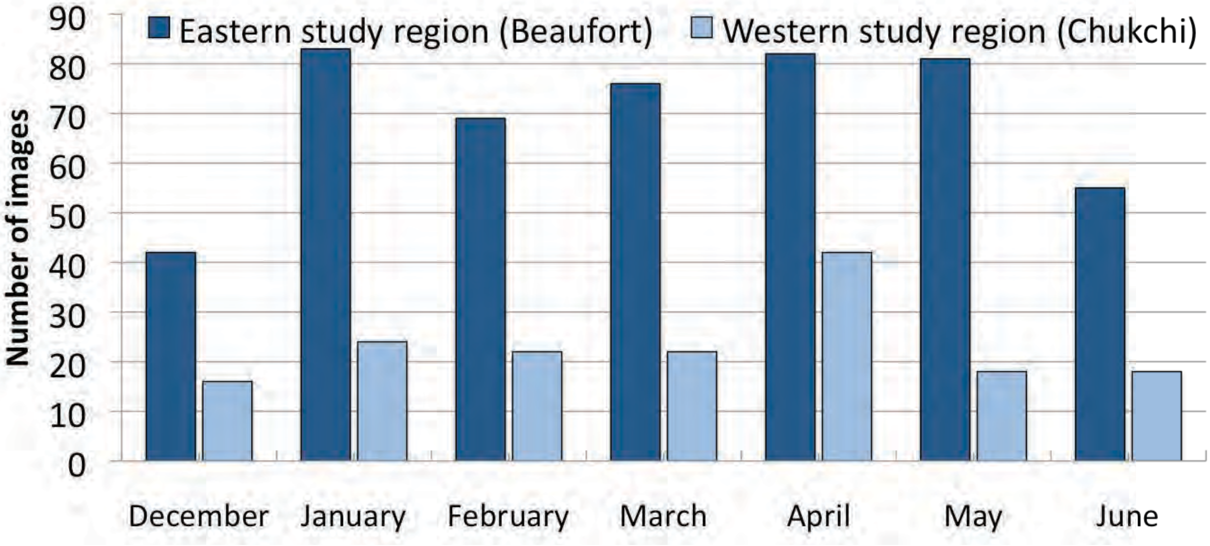

Figure 3.2.3 Number of AVHRR scenes analyzed for each month in the eastern and western study regions. Note that for the eastern (Beaufort) study region, data were acquired for the period December 1993- June 2009, and for western (Chukchi) study region, data were acquired for the period December 1993- June 2010.

Raw, High Resolution Picture Transmission (HRPT) data were ingested for each AVHRR scene and processed in TeraScan (SeaSpace, 2003). Calibration and conversion of visible and thermal channel data to surface reflectance and brightness temperature, respectively, was carried out as specified in the NOAA Polar Orbiter Data User's Guide (2003, www2.ncdc.noaa.gov/docs/podug/html/c3/sec3-3.htm).

Geo-location was accomplished by adjusting the pitch, tilt, roll, and yaw parameters within the XVU function of TeraScan until the image aligned with an overlain, georeferenced coast. Error was less than 3 kilometers, and generally within 1.2 kilometers. Georeferenced images in a polar stereographic projection were exported from TeraScan as HDF files.

These HDF files were subsequently imported into ENVI (Research Systems, Inc., 2003) where they were reprojected into an Albers Conical Equal Area (AK) projection using the NAD (1983) datum (see Section 3.5). Also using ENVI, the land area was masked, and the image was cropped to the study region. These files were exported as 16-bit integer files, with pixel values representing albedo in hundredths of percent and brightness temperature in hundredths of °C for channel 1 and channel 4 images respectively. Landmask values were set to 10001 (corresponding to 100.01%) and –5000 (corresponding to –50 °C) for channel 1 and channel 4 images respectively.

The fraction of leads within each pixel was determined based on the brightness temperatures or reflectances of open water and the surrounding thick ice, as described by Lindsay and Rothrock (1995). Here, we have corrected for regional differences in surface temperature and reflectance, as well as thin cloud cover, by determining the fraction of leads within a moving 50 by 50 (55 x 55 km, thermal channel) or 13x13 pixel (visible channel) square window, with the fraction of thick ice based on the upper and lower quartile reflectance and brightness temperature, respectively. For a few cases of more expansive stretches of open water, manual adjustments of open water extent have been made. The resulting image indicating the fraction of open water was then binarized about a threshold corresponding to an open water fraction of 25% in each pixel, (equivalent to a value of $\delta = 0.25$ deemed optimal based on work by Lindsay and Rothrock, 1995) with pixels containing less open water designated as ice and those at or above 25% designated as leads. The resulting binary images are then imported into the ImageJ software package (http://rsbweb.nih.gov/ij/) for derivation of lead location, shape and size statistics, open water fractions and other information for each subregion. Prior to analysis, single, isolated pixels which were found to be the result of noise in the data were removed from the segmented image. Lead statistics were exported from ImageJ into Microsoft Excel format. Data were eliminated from statistical analysis if the ice was obscured by clouds in a particular subregion as determined from manual inspection of images in both visible and thermal channels.

The binarized GeoTIFF images delineating leads, were converted to shapefiles using Geospatial Data Abstraction Library (GDAL) tools. Monthly lead probabilities were calculated for both the western and eastern regions by grouping and summing all binarized lead images by month. In the resulting images, the pixel value represented the number of images in which a lead was observed at the location during a particular month. Subregions identified as being cloudy were excluded. These were converted to probabilities by dividing by the total number of images stacked for each month, taking account of exluded regions.

3.2.2 Lead definitions

The World Meteorological Organization's Sea Ice Nomenclature defines a lead as "any fracture or passage-way through sea ice which is navigable by surface vessels" (1985). Expanding the definition from its original operational scope in the context of ice navigation, leads are commonly taken to be linear features of open water or thin ice present within the ice pack (*Lindsay and Rothrock*, 1994;1995). Their importance derives from the high rates of energy exchange that are sustained in areas of thin ice (*Maykut*, 1986), either as a result of heat conduction through an open-water or thin-ice surface (*Alam and Curry*, 1998) or as a result of absorption of shortwave radiation fostered by the low albedo of thin ice or open water (*Perovich*, 1990; *Pegau and Paulson*, 2001). At the same time, leads are of great ecological importance both as potential access points to open water for marine birds and mammals (*Stirling*, 1997; *Bump and Lovvorn*, 2004) and as a habitat (*Melnikov*, 1997). In the present study we are following common practice by applying a lead definition and corresponding lead detection criterion that does not distinguish between open leads and those covered by thin ice up to roughly 0.15 to 0.2 m thick (i.e., nilas and grey ice according to WMO nomenclature). This is motivated by the fact that thermally as well as optically, thin ice with albedos typically less than 0.2 and high surface temperatures is often indistinguishable from open water (*Perovich*, 1998). Furthermore, under freezing conditions, ice grows to several centimeter thickness within a few hours and even in cases of wind clearing leads of newly forming frazil ice, open water typically cannot be sustained for more than 24 hours (*Bauer and Martin*, 1983; *Alam and Curry*, 1998). Even after onset of surface melt, it is not uncommon to observe nighttime freezing of leads well into June.

Identification of leads in remote sensing imagery is complicated by a number of factors, including ambiguous signatures of open water and thin ice in SAR data(*Kwok and Cunningham*, 1994), atmospheric and resolution effects in visible-range and thermal IR AVHRR data (*Key et al.*, 1993) and lack of resolution in passive microwave data (*Fett et al.*, 1997). Several studies indicate that for analysis of lead patterns and distributions, AVHRR imagery provides for a dataset that represents the best compromise between resolution, coverage and discriminatory power (*Key et al.*, 1993; *Lindsay and Rothrock*, 1995; *Miles and Barry*, 1998; *Tschudi et al.*, 2002). In recent years, derivation of ice deformation fields from sequences of Radarsat SAR imagery has been used successfully to map pack ice openings at the scale of 5 km and upwards indirectly (*Kwok*, 1998; *Kwok and Cunningham*, 2002). However, this approach is only of limited value for a study in seasonal ice (where ice deformation fields are not easily obtained due to ambiguities in backscatter characteristics) and computationally intensive (so far only a limited number of years have been processed) and was hence not applicable in the current study. Here, we have followed the approach developed by (*Lindsay and Rothrock*, 1994;1995) for extracting lead distributions from AVHRR radiance data for the visible-range (channel 1) and thermal-IR (channel 4), converted to reflectances and brightness temperatures, respectively. Specifically, we can calculate the fraction of leads δ_T within each pixel based on the surface brightness temperature of the entire pixel T, that of open water ($T_w = -1.8$ ˚C) and that of surrounding thick ice (T_i):

$$\delta_T = \frac{T_i - T}{T_i - T_w} \qquad \textbf{Eqn 3.2.1.}$$

The surface brightness temperature of the surrounding thick ice is derived from the lower quartile brightness temperature determined for a 50x50 pixel window centered on each pixel. The corresponding approach is taken in the analysis of visible range data, with ρ_i, and ρ_w denoting the reflectances of open water (0.1) and the surrounding thick ice (upper quartile within the 50x50 pixel mask):

$$\delta_R = \frac{\rho_i - \rho}{\rho_i - \rho_w} \qquad \textbf{Eqn 3.2.2.}$$

The fraction of open water is then indicated by the magnitude of δ_T or δ_R. In following Lindsay and Rothrock's approach, we have chosen a value of 0.25 as the cutoff value, with cells (pixels) exhibiting a $\delta > 0.25$ designated as lead and those smaller designated as ice. Selecting a value smaller than 0.5 (i.e., a cell composed out of equal fractions of ice and lead) is driven by the fact that two processes tend to result in an underestimation of the fraction of lead present. First, thin ice in a lead will result in lowered surface temperatures and raised reflectances, thereby lowering δ. Second, atmospheric effects such as formation of vapor plumes further reduce detectability of leads (*Key et al.*, 1993).

The MMS OCS STUDY 2005-068 study included a more detailed validation of the lead detection approach through comparison with ship-based observations in the study area indicating good correspondence between the two types of data (*Eicken et al.*, 2006).

3.3 Mapping of landfast ice extent and stability from Radarsat data

3.3.1 Definition of landfast ice from remote sensing data

A detailed summary of different definitions of landfast ice and their applicability to remote sensing data is provided by Mahoney *et al.* (2006)in the final report for MMS OCS STUDY 2005-068 (*Eicken et al.*, 2006). Here we provide a brief summary of the definition used to distinguish regions of landfast ice from moving ice or open water in Radarsat SAR imagery.

Our definition of landfast ice encompasses two criteria:

1. the sea ice is contiguous with the shoreline
2. the sea ice lacks motion detectable in satellite imagery for approximately 20 days

We note that unlike definitions used in operational datasets such as the ice charts produced by the National Ice Center, our definition does not rely on a flaw lead and uses no remote-sensing signatures or textures of sea ice, other than to distinguish it from open water. The time period of 20 days was chosen to be short enough to capture both the annual cycle of advance and retreat as well as the higher frequency variability due to stable extensions and breakouts. It also spans more than a single synoptic period and so precludes sea ice that merely comes to rest temporarily and lacks a mechanism to hold it fast against offshore or alongshore forcing.

It is also important to note that we exclude islands from our definition of the coastline, with the exceptions of Herschel and Barter Islands, which are larger than most others and separated from the mainland by only a very narrow stretch of water. This decision was made to avoid complex topological problems that would result when trying to calculate distances from the coast. As a result, ice that is attached to barrier islands but is not contiguous with the mainland is excluded from the analysis. This usually only occurs late in the spring, however, when offshore ice operations have typically ceased.

3.3.2 Study area and SAR imagery

The study area for the landfast ice analysis is shown in Figure 1.4.1. It is composed of a rectangular eastern region, which was the study region from MMS OCS STUDY 2005-068, and an irregularly-shaped western region, which includes most of the Chukchi Sea. The combined study area covers the entire Chukchi and Beaufort coasts of Alaska together with parts of Canada and Russia. Moderate resolution Radarsat ScanSAR wide beam data were ordered via the Alaska Satellite Facility (ASF) electronic data gateway and were chosen to provide complete coverage of the study area approximately every 10 days between October and July for each of the 12 annual cycles between 1996 and 2008. Due to gaps in data availability, it was not possible to provide complete spatial coverage during the early stages of landfast ice formation in 1996 and 1997. Also, Radarsat data became a commercial product after April 2008 with prohibitive costs to achieve complete coverage of our region, hence our dataset does not capture break-up for 2008.

SAR data were provided by the ASF Advanced Product Design group in GeoTIFF format with a geolocation accuracy stated to be 5 pixels or 500 m. Each image covers an area 550 km by 550 km and is one of a group of parent scenes for a mosaic cropped to the boundaries shown in Figure 1.4.1. To provide products consistent with those of MMS OCS STUDY 2005-068 and to reduce filesizes, we generated separate SAR mosaics for the eastern and western regions of the study area. Each mosaic is made up of between 3 and 5 parent scenes representing a timespan of between 2 and 4 days. A total of almost 3,000 parent scenes were used to create 359 mosaics for the western region and 331 mosaics for the eastern region during the 12-year study period.

Prior to any landfast ice analysis in the images, the data were checked to ensure adequate coverage of the study area and each subregion. In addition, scenes with a large geolocation error were identified and either corrected with a simple horizontal translation or removed from the dataset. The stated geolocation accuracy could give rise to co-location errors of up to 10 pixels or 1 km between parts of two mosaics, though where possible this was reduced to less than 500 m.

3.3.3 Image processing to identify landfast ice

If the backscatter from a sea ice surface changed over time only through ice motion, then landfast ice ought to exhibit a constant backscatter, since it is stationary according to our definition (Section 3.3.1). However, due to the processes described in Section 3.3.1, the backscatter of landfast ice can still change over time while the ice remains stationary. This means that simple subtraction of collocated images is not sufficient to discern motion. However, the processes that change the backscatter from the ice surface act least strongly on ridges and areas of deformed ice and consequently the features of the SAR imagery that exhibit most consistency over time are stationary linear regions of high backscatter. These regions are typically a few hundred meters wide and parallel or sub-parallel with the coast. A technique for distinguishing landfast ice must therefore be able to recognize these features and their orientation.

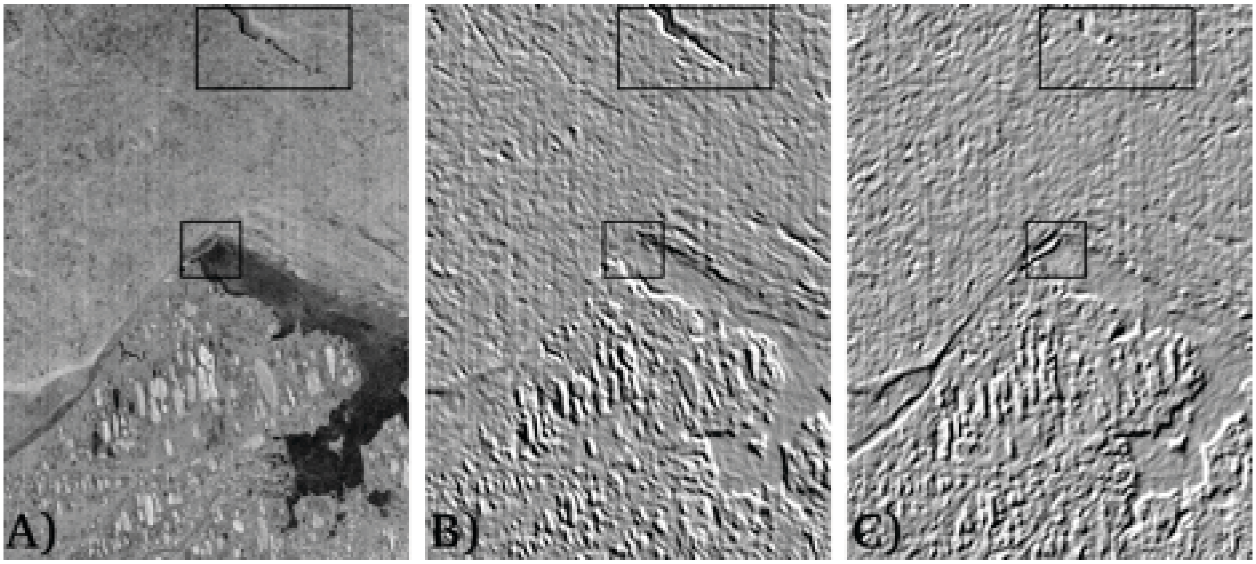

Figure 3.3.1. a) Calibrated Radarsat ScanSAR image over Barrow, Alaska, January 6, 2002. The image has been smoothed by 5x5 pixel (500 m) filter, b) Horizontal component of grayscale gradient field, c) Vertical component of grayscale gradient field. Bright areas are positive gradients and dark areas are negative gradients, with axes positive to the right and downwards. Note how features have different orientations in the horizontal and vertical component images, such as those indicated by the boxed regions.

The technique we used calculates the horizontal and vertical grey value gradient fields in 3 consecutive images and then calculates the magnitude of the difference in gradient fields. We call the result a gradient difference image. Calculation of the gradient fields is similar to the application of a Laplacian filter, which is commonly used to detect edges in images, except we only calculate first derivatives and treat the horizontal and vertical components separately in order to preserve the information regarding the orientation of the edge features.

The 2-dimensional vector gradient of a scalar field, Φ, is given by:

$$\nabla\Phi = \nabla_H \underline{i} + \nabla_V \underline{j}\text{, where } \nabla_H\Phi = \frac{\partial\Phi}{\partial x} \text{ and } \nabla_V\Phi = \frac{\partial\Phi}{\partial y} \qquad \textbf{Eqn 3.3.1}$$

where $\underline{i}$ and $\underline{j}$ are horizontal and vertical unit vectors respectively in the image plane. We can apply this to a digital SAR image, if Φ is the backscatter grey values and we approximate equation 3.3.1 with finite differences:

$$\nabla\Phi_{x,y} \approx \left(\frac{\Phi_{x-d,y} - \Phi_{x+d,y}}{2d}\right)\underline{i} + \left(\frac{\Phi_{x,y-d} - \Phi_{x,y+d}}{2d}\right)\underline{j} \qquad \textbf{Eqn 3.3.2}$$

where x and y are the image co-ordinates and d is the number of pixels between which the gradient is calculated.

By calculating the vector spatial grayscale gradient field of a single SAR image we generate two images that represent the horizontal and vertical components of the gradient field (Figure 3.3.1b and c respectively). The combination of both components describes the magnitude and orientation of edges in the original image.

To identify regions of the image that remained constant and therefore may represent landfast ice, we calculated the vector gradient fields of three (3) consecutive SAR images and derived the magnitude of net difference between them. In order to preserve the directional information during this calculation, the net difference of each component of the gradient fields is treated separately. Calculation of the net difference between horizontal components is described by:

$$\Delta_{net}\left(\nabla_H\Phi\right) = \left|\nabla_H\Phi_1 - \nabla_H\Phi_2\right| + \left|\nabla_H\Phi_1 - \nabla_H\Phi_3\right| + \left|\nabla_H\Phi_2 - \nabla_H\Phi_3\right| \qquad \textbf{Eqn 3.3.3}$$

Where Φ_1, Φ_2 and Φ_3 are the 3 consecutive SAR images and ∇_H is the horizontal gradient component, as defined in equation 3.3.1. The net difference between vertical gradient components is calculated in the same way. The final gradient difference image is the Pythagorean sum of the horizontal and vertical components:

$$\Delta\left(\nabla\Phi\right) = \sqrt{\Delta_{net}\left(\nabla_H\Phi\right)^2 + \Delta_{net}\left(\nabla_V\Phi\right)^2} \qquad \textbf{Eqn 3.3.4}$$

Figure 3.3.2 shows the gradient difference image that was derived from 3 consecutive SAR images. These images off Barrow, Alaska represent the coverage of one of ten subregions into which the whole study area was divided. In doing so, we were able to calculate the gradient fields of images that were free from mosaicking edges that contribute artificial gradients.

Landfast ice occupies the dark region of low gradient difference values adjacent to the coast. The seaward boundary of this zone, which corresponds to the seaward landfast ice edge (SLIE), is often marked by bright linear regions of high gradient difference, which are the result of a flaw lead existing at that location in one of the 3 parent images. However, no single threshold value of backscatter gradient difference was found to uniquely identify landfast ice and so the SLIE is discontinuous. An algorithm to locate and connect the SLIE was developed but this proved successful only during the middle of winter when the backscatter signatures of landfast ice are most constant. At other times, regions of high gradient difference could be found within the landfast ice particularly during the spring when surface flooding from rivers occurs. Different incidence angles between ascending and descendig orbits also introduced backscatter gradients.

As a result of these difficulties, the gradient difference technique failed to provide the automated and objective method of delineating the SLIE that we were looking for. However, the mosaics of the gradient difference images were still used in conjunction with manual examination of the parent images when image quality was poor and also to reduce some of the subjectivity in such a manual approach. This technique is described in section 3.3.4.

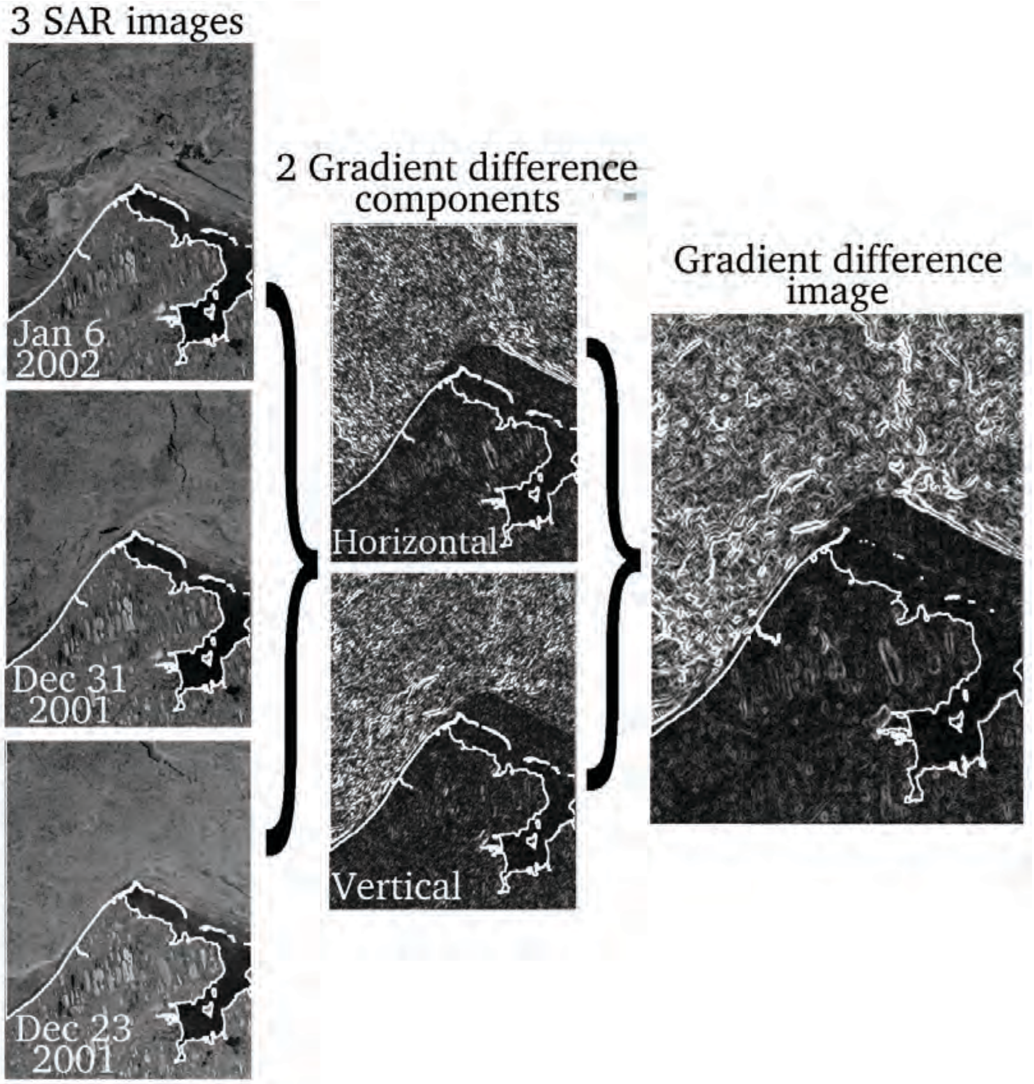

Figure 3.3.2. A gradient difference image and the 3 SAR images from which it was derived. Landfast ice appears dark since the ridges within it retain a more constant backscatter over time. The horizontal and vertical differences are calculated separately from the corresponding components of the vector gradient fields, which are not shown.

3.3.4 Delineation of landfast ice from consecutive SAR mosaics

Although a fully automated method for delineating the SLIE proved elusive (Section 3.3.3), a rigorous technique of manual examination of 3 consecutive SAR mosaics and a gradient difference image was used for the purposes of this study. Sets of 3 consecutive mosaics were examined together to identify regions of ice exhibiting a lack of motion determined by a constant backscatter signature. The georeferencing accuracy of the data allowed us to confidently identify motion greater than 500 m. This involved a detailed manual examination of each set of 3 mosaics by process of flickering on a computer screen. The gradient difference image was used to better discriminate changes in backscatter in low-contrast regions of the imagery.

Since the individual SAR images comprising a mosaic were not acquired simultaneously, each mosaic does not represent a single point in time. On occasions when the SLIE location is changing rapidly, this can introduce artifacts as illustrated in Figure 3.3.3. These are not strictly errors as the SLIE still accurately represents the extent of immobile ice. However, this serves to illustrate that the SLIEs delineated in this fashion do not represent a single point in time. This is discussed in more detail in section 3.3.6.

Figure 3.3.3. The landfast ice area for the period February 16 – March 8, 2000, overlain semi-transparently on the first of the 3 mosaics of period. This shows how mosaic boundaries, which effectively represent temporal boundaries in the image, lead to artifacts along the SLIE.

A SLIE delineated through analysis of consecutive mosaics is a line representing the minimum offshore extent of contiguous stationary ice during the period represented by the imagery. We distinguish between a seaward and an inshore landfast ice edge. The latter develops during break-up when river flooding and the development of an inshore lead, mostly in areas of bottomfast ice (*Reimnitz*, 2000), can result in open water inside of the SLIE, as identified in SAR and AVHRR imagery (see also Section 4.1). This delineation technique yields the shape of the SLIE and allows us to examine changes in landfast ice area over time. However, to analyze variability in extent over space and time, we need to determine the width of landfast sea ice relative to the coast throughout the study area.

3.3.5 Measuring landfast ice width

The measurement of landfast ice width is not as simple a task as it initially appears, since the value yielded depends upon the direction from the coast in which the measurement is taken. A direction normal to the coastline at the point of interest is preferable, but at convex regions of the coast with high curvature a single direction can be both difficult to define and misrepresentative. To overcome this, a set of transects was defined based on a fixed set of rules. First we defined an offshore line such that each point on the line is a fixed distance from the nearest point of land. It should be noted again that islands are excluded from this coastline, with the exception of Barter and Herschel Islands (see Section 3.3.1). Every 200 m along this offshore line, we defined a vector connecting the offshore line to the nearest point on the coast. If two consecutive points on the coast are more than 200 m apart, then intervening coastal points at 200 m intervals are connected to the closest point of the offshore line. The result of this process is a set of 8,889 approximately coast-normal transects located at approximately regular distance that serve as a curvilinear co-ordinate system for defining the location of the SLIE.

Figure 3.3.4 shows the SLIE coordinate vectors defined for the eastern and western regions of the landfast ice study area. The coordinate vectors are longer in the eastern region than in the western region, in part because landfast ice in the Beaufort Sea is typically wider than in the Chukchi Sea. Also, the shorter coordinate vectors in the western region allow mesurement of landfast ice in the more complex embayments found in the Chukchi Sea. Note that in addition to a set of coordinates defined from an offshore line, Kotzebue Sound is also represented by a set of coordinate vectors radiating from a point inside the Sound. This allows measurement of both the early- and late-season distribution of landfast ice in the vicinity of this complex coastal region. However, there are still a few isolated regions along the coast where landfast ice may not be captured by these coordinate vectors. This include the waters of Hotham Inlet and Eschscholtz Bay near Kotzebue, Admiralty Bay west of Point Barrow are other small "shadows" behind headlands where the vectors do not reach. Also, on rare occasions when the SLIE was more than 150 km from the coast (see Section 1.3.5) the measurement was truncated (deemed of negligible effect on the following analysis).

During spring breakup, areas of open water caused by flooding or breakup of nearshore ice may exist between the shore and landfast ice offshore. If the amount of landfast ice offshore is less than the amount of water separating it from the land, we treat this as zero landfast width. Otherwise, we ignore the open water and treat the landfast ice width as being equal to the distance from shore to the SLIE.

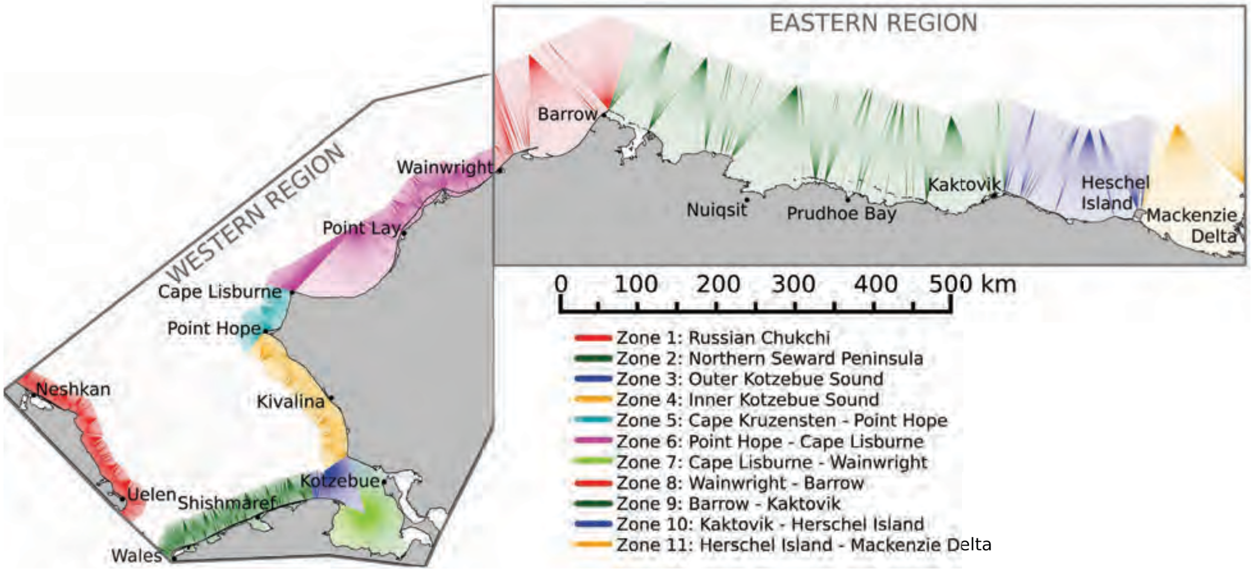

Figure 3.3.4. The 8,889 coordinate vectors along which landfast ice width is measured. The vectors are color coded by coastal zones used in later analysis of the SLIE data.

3.3.6 Assigning dates to SLIEs

Assigning a particular date to a SLIE requires thoughtful consideration of how information from the three mosaics is used during the delineation process. Since the SLIE represents the minimum landfast ice extent during the time period spanned by the three mosaics, its position will be defined by the first mosaic when it is advancing and by the last mosaic when it is retreating. Since different parts of the landfast ice may be advancing and retreating at the same time, it is not meaningful to attribute a single date to the entire delineated SLIE. In addition, since we take a mosaic to represent a snapshot in time, the observed position of the SLIE could have first occurred at any time between acquisition dates of the first mosaic in which it was observed and the susequent mosaic. In the analysis that follows, we assign dates to SLIEs on a point-by-point basis taking account of whether the SLIE along a particular vector is advancing or retreating. The date assigned is the date mid-way between the mosaic that defines the SLIE at that point and the preceding mosaic.

3.3.7 Identifying key events in landfast ice development

By measuring average landfast ice width along each coastal coordinate vector (Figure 3.3.4), during the 12 annual cycles between 1996 and 2008, we obtained over 100,0000 time series charting the annual development of landfast ice along the coasts of the Chukchi and Beaufort Seas. Figure 3.3.5 shows the time-series of landfast ice width and water depth at the SLIE along a vector starting near Nuiqsut for the 2001-02 cycle. Automated algorithms are then applied to these time series to determine the timing of 4 key events at each coastal location during each landfast ice cycle as defined below:

First ice on coasts. The first occurrence of more than 500 m of ice at the coast is taken to represent the time at which ice started forming, given the geolocation accuracy of the SAR imagery.

Stable landfast ice. Stability of the landfast ice is more difficult to define. Here, the stable period is defined as the longest period during which the SLIE occupies water 15 m or deeper. The onset of this period is used to define key event 2.

Break-up. This is characterized by a sharp decrease in landfast ice width toward the end of the season and its occurrence is defined by the most negative gradient in the tail of the season once the gradient remains less than or equal to zero. It should be noted that break-up does not necessarily coincide with the end of the stable period.

Ice-free coasts. Once the landfast ice width drops to less than 500 m, the coast is deemed ice-free.

The selection of these four criteria is illustrated in Figure 3.3.5 but we should note that not all annual time series fit this pattern and determination of all key events by these criteria was not possible for all locations in all years. The failure rates of these criteria to identify key events are discussed in section 4.3.4.

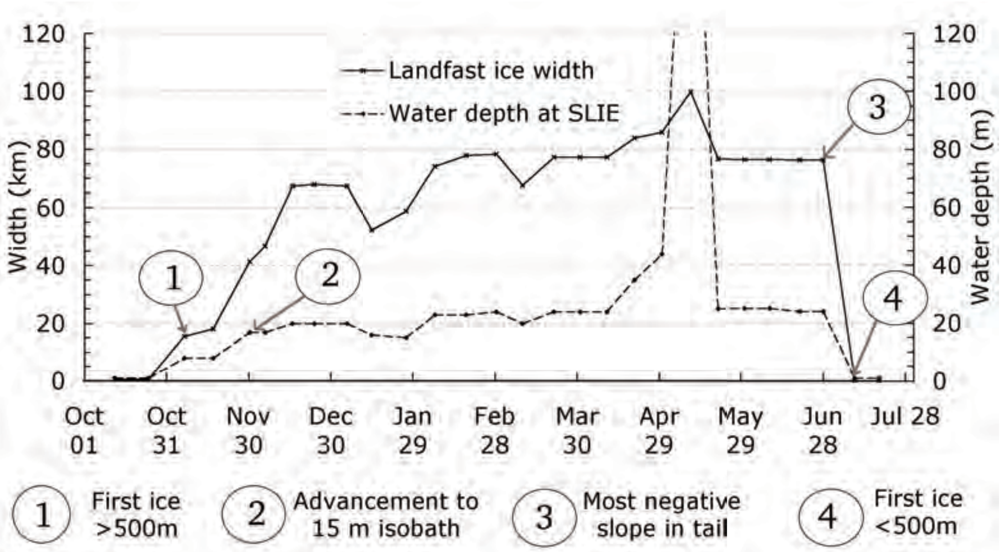

Figure 3.3.5: Development of landfast ice near Nuiqsut between October 2001 and July 2002, showing features of the time series that are used to determine the occurrence dates of four key events in the annual cycle. See text for explanation.

3.3.8 Calculation of monthly SLIE statistics

To construct monthly SLIE positions, we calculated the minimum, mean, median and maximum landfast ice width along each coastal coordinate vector for each calendar month. These points were then used as vertices to define the corresponding monthly SLIE. Figure 3.3.6 illustrates this method for the month of April in the vicinity of Barrow. The dots indicate all the landfast ice width data measured along the coastal coordinate vectors. The mininum, mean, median and maximum SLIE locations are calculated from all the data for each vector. Note however, the monthly maximum SLIE positions may not reflect the true maximum in cases where landfast ice extended beyond the range of the coastal coordinate vectors. Similarly, landfast ice in complex embayments that are not well captured by the coastal coordinate vectors (see section 3.3.5) may not be represented in the monthly minimum SLIEs. The mean and median SLIE positions typically lie close to each other and since the mean SLIE positions generate a smoother line, we omit monthly median SLIEs from our analysis.

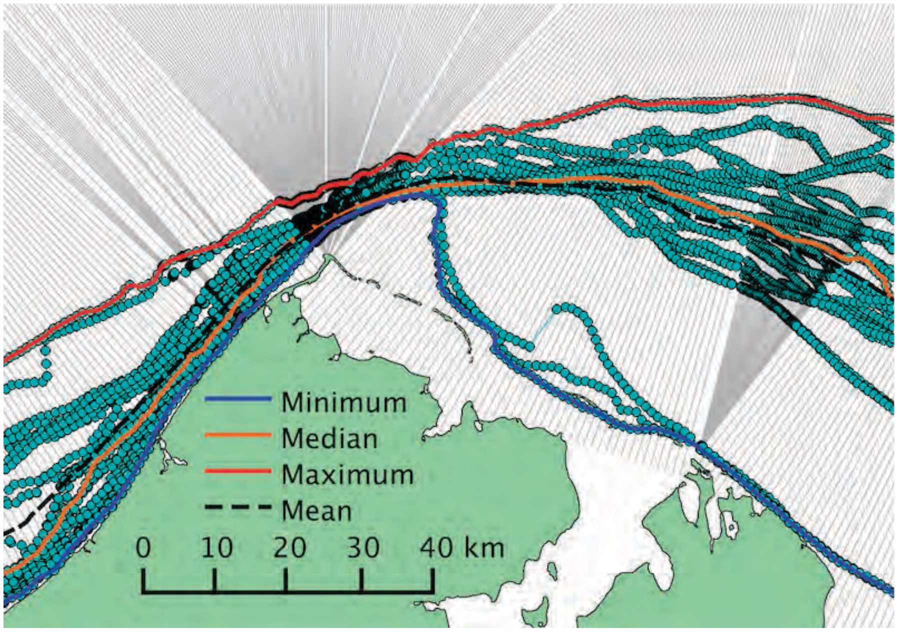

Figure 3.3.6. Minimum, mean, median and maximum SLIE positions near Barrow, calculated from all SLIE points corresponding to the month of April. The grey lines indicate the coastal coordinate vectors along which landfast ice width is measured.

3.3.9 Categorization of coastal morphology

In order to be able to investigate the effect of local coastal morphology on landfast ice behavior, we have categorized each coastal coordinate vector (Figure 3.3.4) according to whether it originates in a lagoon, an embayment, an open section of coastline or a headland. We designated lagoons and embayments according to color-coding of the coastline shown in Figure 3.3.7. Coastal coordinate vectors that diverged away from the coast were designated as originating at headlands. Other sections of coast were designated as open.

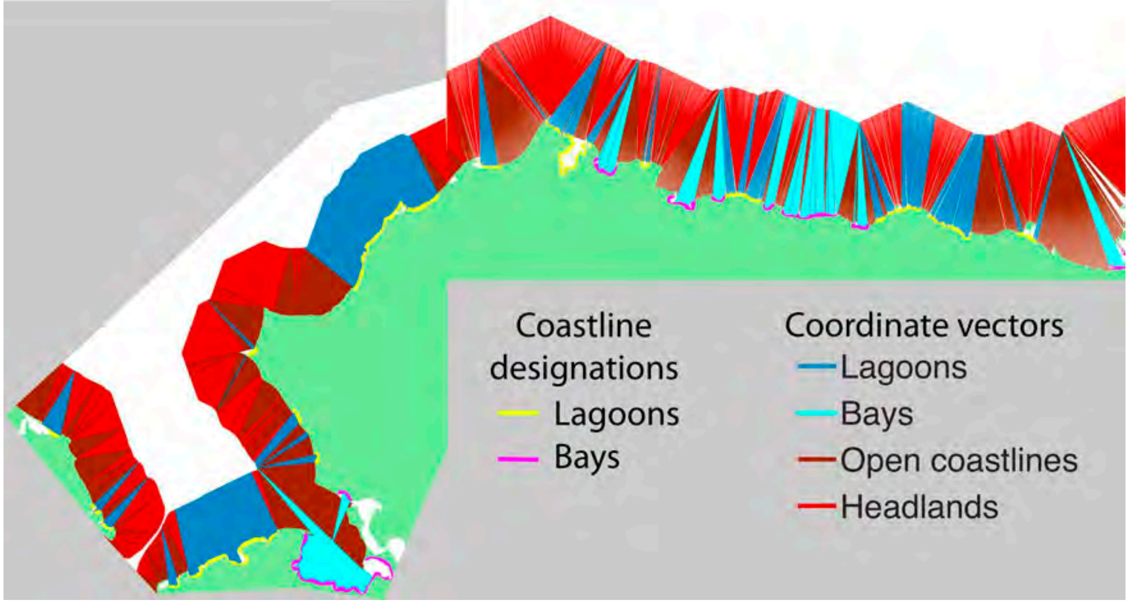

Figure 3.3.7: Categorization of coastal coordinate vectors by coastal morphology

3.4 Development of alternative approach for mapping landfast sea ice extent

3.4.1 Motivation for alternative approach

Automatic identification and delineation of the seaward edge of landfast ice from spaceborne remote sensing data is a non-trivial task, as described in Section 3.3.1. In this project, we have used a semi-objective method for delineating landfast ice from three consecutive ScanSAR images spanning a period of approximately 20 days (Sections 3.3.3 - 3.3.4). However, despite some initial success automating this process, in general the technique has to rely on visual interpretation and manual editing in conjunction with the three parent images. From an operational point of view, a higher degree of automation would be desirable to reduce laborious editing work and increase the throughput of the landfast ice analysis procedure. In addition, the Radarsat ScanSAR data used for this method ceased being readily available to academic researchers in April 2008.

Therefore, within the scope of this project, we investigated an alternative approach to landfast sea ice detection based on interferometric processing of image pairs acquired by spaceborne L-band Synthetic Aperture Radar (SAR) sensors such as PALSAR on board the Japanese Advanced Land Observing Satellite (ALOS). With interferometric phase and coherence, SAR interferometry (InSAR) comprises two measurements that have the potential for assessing both landfast ice extent and its stability. Here, stability is defined as the absence of motion or deformation that would compromise the integrity of the landfast ice, such as ridge building or ice break-out events. Interferometric coherence is an indicator of the degree to which surfaces remain unchanged, in particular with respect to scattering properties, potential movement, or deformation. Interferometric phase reveals information about cm- to dm-scale surface motion, and therefore provides very detailed information about surface stability.

The intent of this work was to present a technique for landfast ice mapping from L-band InSAR and demonstrate its suitability for automated landfast sea ice detection. To validate the performance of this alternative method, its results were compared to the results of the operational landfast ice detection method used in this project. For this comparison, we selected two different regions of the Alaska coast. These regions were chosen in part due to the availability of data through the Alaska Satellite Facility at the University of Alaska Fairbanks, but also due to the socio-economic significance and availability of background information on landfast ice in Alaska. The results of the validation of the newly developed landfast ice detection method are summarized in Section 4.4.1 of this report. They demonstrate the high performance of L-band InSAR for several stages throughout the sea-ice season and for different geographic and climatic settings. Generally, we conclude that L-band InSAR-based landfast ice mapping shows significant potential in reducing data and processing efforts, increasing reliability of landfast ice detection, as well as reducing processing complexity and required manual interaction. Moreover, we find that L-band InSAR has the potential to reveal additional information about small-scale ice dynamics and motion.

3.4.2 Use of interferometric SAR for landfast ice detection

The use of InSAR for landfast ice mapping was limited in the past (*Dammert et al.*, 1998; *Morris et al.*, 1999) as most spaceborne sensors operated at C-band. At this frequency range, scattering properties of landfast ice surfaces change rapidly resulting in a rapid degradation of the interferometric coherence over time. While earlier InSAR studies were successful at identifying landfast ice, they relied on the 3-day repeat interval of the European Remote Sensing satellite (ERS-1) during its two ice phases from 1991-92 and 1993-94. There are currently no widely available complex SAR products at this repeat interval. However, with the launch of the Japanese Aerospace Exploration Agency's (JAXA's) L-band SAR PALSAR on board of ALOS in 2006, InSAR data in L-band has become more widely available, promising improved coherence over time spans of tens of days, thus enabling the mapping of landfast ice areas.

One of the main limitations of interferometric techniques (*Meyer*, 2007) is temporal decorrelation of the SAR signals (*Zebker and Villasenor*, 1992). The average loss of signal correlation over time is, among other factors, dependent on the wavelength of the applied system. Decorrelation is especially pronounced for data acquired in the higher signal frequencies of C-band and X-band while appearing reduced in low frequency data as provided by the L-band SAR used in this study. Many studies of InSAR coherence confirm a generally improved coherence in interferometric L-band SAR data (*Rosen et al.*, 1996). Improved coherence in L-band over snow and ice areas is reported, e.g., by Lu et al. (2005).

3.4.3 Interferometric Coherence

The complex coherence between two complex SAR images u_1 and u_2 is defined as

$$\gamma = \frac{E\left\{u_1 u_2^*\right\}}{\sqrt{E\left\{\left|u_1\right|^2\right\} E\left\{\left|u_2\right|^2\right\}}} \qquad \textbf{Eqn 3.4.1}$$

where E{.} is the expectation value. A coherence value can be assigned to every pixel of an interferogram if the expectation values in Eqn 3.4.1 are known. Pixel coherence can be estimated from a suite of SAR observations through ensemble averaging. However, if only few repeated acquisitions are available, but ergodicity can be assumed, coherence can be estimated through spatial averaging over a uniform region. Under these assumptions, the maximum likelihood estimate of the coherence magnitude, $|\hat{\gamma}|$, can be derived using a small window *W* centered around pixel *[i,k]* (*Seymour and Cumming*, 1994):

$$\left|\hat{\gamma}[i,k]\right| = \frac{\left|\sum_W u_1[i,k]\, u_2^*[i,k]\right|}{\sqrt{\sum_W \left|u_1[i,k]\right|^2 \sum_W \left|u_2[i,k]\right|^2}} \qquad \textbf{Eqn 3.4.2}$$

Coherence values are ranging between [0, 1], with 1 indicating perfect correlation and 0 corresponding to complete decorrelation. Reduction in the magnitude of the coherence estimate $|\hat{\gamma}|$, also called decorrelation, can be caused by several factors summarized in Eqn 3.4.3

$$|\hat{\gamma}| = \gamma_{spatial} \cdot \gamma_{temporal} \cdot \gamma_{thermal} \cdot \gamma_{process} \qquad \text{Eqn 3.4.3}$$

In Eqn 3.4.3, the term $\gamma_{spatial}$ corresponds to signal decorrelation caused by the incidence angle differences between the two acquisitions of an interferogram that is proportional to the perpendicular baseline $B_\perp$ separating the two SAR antennas. As the satellite locations during image acquisition are known with high accuracy, $\gamma_{spatial}$ can be calculated and corrected. $\gamma_{thermal}$, the thermal decorrelation factor, is related to the signal-to-noise ratio (SNR). Due to the smoothness of the scattering interface and the associated low SNR, $\gamma_{thermal}$ can be low (<<1) for very smooth young sea ice and is smaller for L- than C-band. Lower SNR in SAR data can also be caused by the presence of melt water during spring and summer in the Arctic and snow load-related surface flooding events in Antarctic environments. $\gamma_{process}$ describes processing-induced decorrelation effects that may stem from errors in co-registration, image interpolation, or spectral filtering. For this study, it is assumed that $\gamma_{process} \approx 1$. $\gamma_{temporal}$ is the correlation factor associated with incoherent changes in the scattering medium between observations, and is in many cases the main driver for coherence loss in SAR interferometry. Mechanisms determining the amplitude of $\gamma_{temporal}$ over ice and snow surfaces include the movement of snow/ice particles on the surface due to wind, melting and refreezing processes, desalination of sea ice associated with aging processes, sea ice motion, deformation, or fracturing. Although temporal decorrelation generally increases with time and although attempts have been made to model the general trend of temporal decorrelation through empirical polynomial functions (e.g., Hoen and Zebker (2000)), a general model for $\gamma_{temporal}$ does not exist due to strong differences of $\gamma_{temporal}$ for different surface types and environmental conditions. It is, however, known that temporal decorrelation is dependent on the sensor's signal wavelength λ and is much smaller for L-band than for C-band.

Most of the aforementioned decorrelation factors show a dependence on signal frequency and are, with the exception of $\gamma_{thermal}$, less severe for low frequency systems, e.g. for L-band. Therefore, L-band systems ($\lambda \approx 0.25$ m) are preferred over C-band ($\lambda \approx 0.05$ m) or X-band ($\lambda \approx 0.03$ m) systems for monitoring natural environments and have been implemented with great success for many geodynamic studies. As landfast ice is per definition stationary over longer time spans, it is expected that coherence in L-band is high. Therefore, L-band InSAR coherence might provide a robust means for detection and delineation of the landfast ice extent.

3.4.4 Statistical Properties of Coherence on Landfast and Moving Ice

In order to verify the applicability of L-band InSAR for mapping landfast ice extent we performed an analysis of the average L-band coherence over landfast ice in 46 day ALOS PALSAR interferograms relative to the average coherence of non-stationary ice areas. To this end, InSAR pairs over several areas of interest and for several stages of the landfast ice season were processed to interferograms and interferometric coherence was derived. Based on independent knowledge of the landfast ice extent at the respective InSAR acquisition times, the coherence in landfast ice areas was compared to the coherence in areas of moving ice. Table 3.4.1 summarizes the parameters of the L-band ALOS PALSAR interferograms that were used in this analysis. All images used here were ALOS PALSAR Fine Beam Single-Polarization data sets with a swath width of 70km. The data were acquired from the data holdings of the Alaska Satellite Facility's Americas ALOS Data Node (AADN). Test sites include the area around Barrow, Alaska, and Alaska's Seward Peninsula. These two regions represent a broad range of sea ice conditions, with landfast and offshore ice at Barrow consisting of a mixture of level and deformed first- and multiyear ice representative of the marginal seas of the Arctic Basin. Ice along the Seward Peninsula is more representative of somewhat milder, dynamic ice regime of sub-Arctic seas.

Figure 3.4.1a shows the coherence probability density functions (PDFs) for areas of moving ice (gray lines) and for landfast ice regions (black lines) for the interferograms listed in Table 3.4.1. (first interferogram: bold line; second: dashed line; third: dotted line; fourth: dash-dotted line). The coherence was calculated based on Eqn 3.4.2 from full-resolution single-look interferograms and using a 5x5 estimation window size. The 5x5 estimation window size was chosen as a compromise between spatial resolution, coherence estimation bias, and shape of the coherence PDF. Large window sizes reduce biases in coherence estimation and produce coherence PDFs with small standard deviation and Gaussian shape (*Bamler and Hartl*, 1998). Both effects are favorable as they minimize the overlap of PDFs of different coherence regimes. However, large window sizes also reduce the spatial resolution of resulting coherence maps.

Table 3.4.1: Image pairs used to study the coherence of landfast ice areas in 46 day ALOS PALSAR interferograms.

		Interferometric Processing Parameters				
		Orbit/Frame	Resolution	Acquisition Dates	Δt	$B_\perp$
Geographic Location	Barrow, Alaska	10171/1430	range: 9.4 m	12/22/2007	46 days	910 m
		10842/1430	azimuth: 18.5 m	02/06/2008		
		10842/1430	range: 9.4 m	02/06/2008	46 days	630 m
		11513/1430	azimuth: 18.5 m	03/23/2008		
		11265/1430	range: 9.4 m	03/06/2008	46 days	570 m
		11936/1430	azimuth: 18.5 m	04/21/2008		
	Seward Peninsula, AK	10186/1320	range: 9.4 m	12/23/2007	46 days	950 m
		10857/1320	azimuth: 12.5 m	02/07/2008		

As expected, the coherence distributions of the moving sea ice samples show the typical pattern of total decorrelation with very consistent probability density functions and an average coherence of $\mu_\gamma \leq 0.08$. Total decorrelation is expected for drifting sea ice, as sea ice moves with speeds of tens of kilometers per day causing the ice surface captured in the interferometric partner images to change completely over a 46 day interval. Figure 3.4.1a also indicates that the L-band coherence over landfast ice areas is significantly higher than the coherence over moving ice. While some variability can be observed between different realizations, all the samples presented here have significantly higher average coherence values of $\mu_\gamma = \{0.2;\ 0.28;\ 0.31;\ 0.38\}$. It is worth noting that lowest coherence was observed in early winter, where low SNR as well as growth and deformation of the thin ice layer may be contributing to coherence degradation. As shown in previous studies (*Sandwell et al.*, 2008), spatial phase pattern can be visually discerned and analyzed if the average coherence is $\mu_\gamma \geq 0.2$. Thus, in all of the presented test cases, the coherence over landfast ice areas is high enough to identify phase pattern, and both phase and coherence images can be used to identify and map landfast ice extent.

While this initial analysis verifies that landfast ice can be identified in interferometric coherence images, Figure 3.4.1a also shows significant overlap between the coherence PDFs of moving and stationary ice. Hence, a simple pixel-based thresholding operator will produce misclassifications for pixels with coherence values close to the detection threshold. To improve the separation between landfast ice and background coherence, an additional adaptive phase filter is applied, whose filtering function is based on the local fringe spectrum. The applied filter, presented by Goldstein and Werner (1998), significantly reduces phase noise for areas with sufficiently reliable phase information, while high phase noise areas are minimally affected. Therefore its application maximizes the contrast between de-correlated and coherent areas in both the interferometric phase and coherence image and enhances the detectability of the landfast ice extent. The non-linear filter is described by an exponent α that determines the filter strength, with larger values leading to greater filtering. The application of this filter raises the coherence in landfast ice areas considerably, while the coherence PDFs of the decorrelated moving ice remain largely unchanged (see Figure 3.4.1b). Figure 3.4.1b presents the coherence PDFs for the moving ice (gray lines) and landfast ice (black lines) samples after the application of the adaptive phase filter. As predicted, the PDFs of the moving ice samples changed only minimally, while the coherence over stationary ice increased dramatically. It is obvious that, after the phase filter was applied, the identification of landfast ice areas appears vastly improved and a statistical thresholding operation of L-band coherence images will be a useful first step in a landfast ice detection scheme.

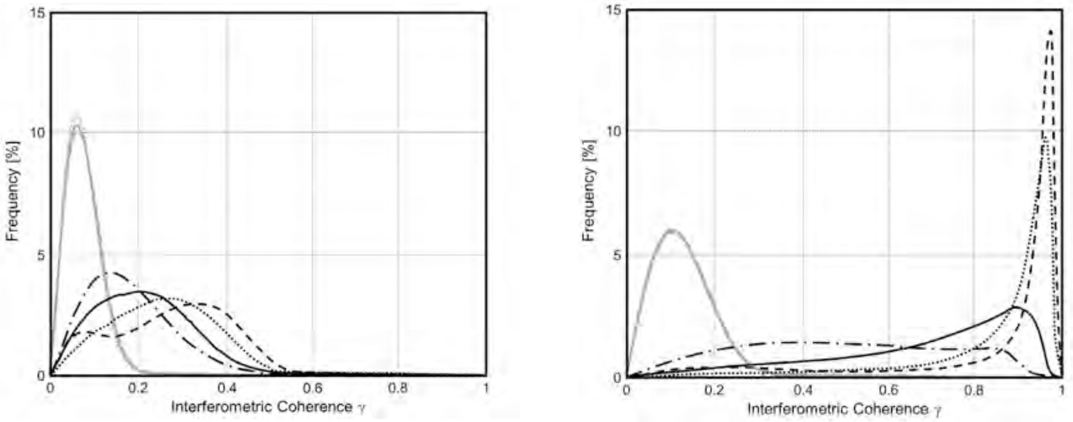

a) b)

Figure 3.4.1: a) Coherence PDFs for moving (gray lines) and stationary ice (black lines) calculated from full-resolution interferograms and using a 5x5 estimation window. PDFs are shown for the four interferograms listed in Table 1 (first interferogram: bold line; second: dashed line; third: dotted line; fourth: dash-dotted line). Significantly higher coherence is evident for stationary ice, yet PDFs overlap strongly; b) Coherence PDFs for drifting and stationary ice after an adaptive phase filter was applied. The separation of drifting and stationary ice PDFs appears greatly enhanced.

In the following section, we will demonstrate that L-band InSAR is a convenient base layer for landfast ice detection in both manual and automatic detection procedures. Whereas landfast ice edge detection is currently performed manually for operational applications, a proof of concept of an automated procedure for landfast ice delineation is presented that uses coherence information as a base layer in a work flow that adds in additional operators like morphological filters, patch size analysis, and linear feature extraction for robust landfast ice edge detection.

3.4.5 Workflow for Manual Landfast Ice Edge Extraction from InSAR

The workflow for manual extraction, depicted in Figure 3.4.2, is essentially a three-step procedure including data ordering, interferometric SAR processing, and GIS analysis. For ordering we take advantage of the data selection and ordering utilities provided by the Alaska Satellite Facility's User Remote Sensing Access (URSA) interface, which, in its latest edition, provides convenient tools for identifying InSAR pairs over an area of interest. These URSA tools are available to every ASF data user and can be readily used to identify InSAR data available in the ASF archives for any area on the globe. In a second step, an automated InSAR workflow is applied that takes interferometric partner images, processes them to interferograms, applies adaptive phase filters and geocodes coherence, phase, and amplitude images to a geographic projection of choice. The InSAR processing can be done with freely available community software tools such as the Repeat Orbit Interferometry Package (ROI_PAC) (*Rosen et al.*, 2004).

The end products of the InSAR processing chain are GeoTIFF images that can be easily imported into GIS software such as ArcGIS, for analysis by operators. For best analysis results and to aid image interpretation, the operator is provided with a composite image that includes both interferometric coherence and interferometric phase information. Additional land masking is applied to improve orientation and clarity.

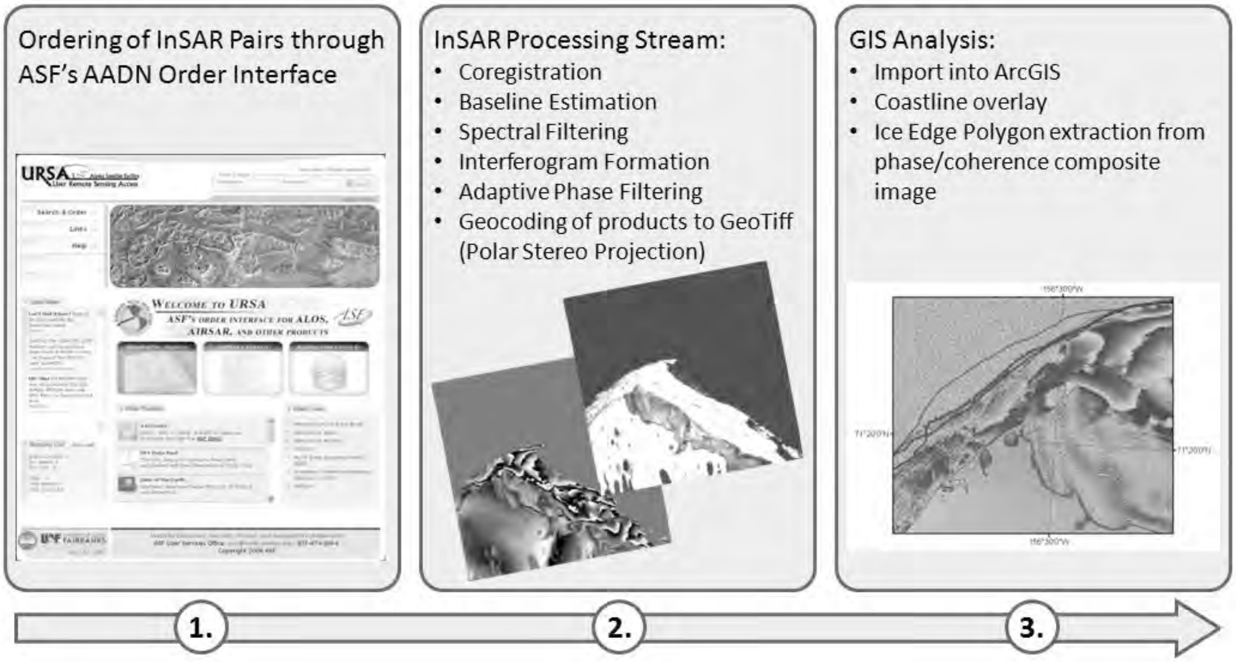

Figure 3.4.2: **Workflow for manual extraction of landfast ice extent from L-band InSAR data obtained from ASF, and using ASF-based tools.**

3.4.6 A Workflow for Automated Landfast Ice Edge Extraction from InSAR

Although the manual workflow presented in Section 3.4.5 has proven to be quick and robust, a routine mapping of Arctic landfast ice extent over large areas would still benefit from an automated or semi-automated workflow to reduce manual labor and speed up the processing flow. Below, we introduce an approach to automate landfast ice extraction from L-band InSAR data and illustrate its performance in an example.

Although the separation of stationary and moving ice areas in the coherence image is significant, the coherence PDFs depicted in Figure 3.4.1a still show overlap, causing errors in a pixel-by-pixel threshold-based landfast ice detection. To provide robust landfast ice detection, we therefore implemented a processing chain that combines a statistical constant-false-alarm-rate (CFAR) classification with subsequent spatial image processing steps. Within the multi-step procedure, a final classification decision is made based on the following characteristics: statistical coherence thresholding, morphological image analysis, image segmentation and patch size analysis, final morphological closing procedure, and outline extraction (see Figure 3.4.3 for an example). In the following sections we explain the motivation and process behind the individual processing steps. This explanation is assisted by a processing example of an L-band InSAR scene covering part of the Seward Peninsula, Alaska (see Figure 3.4.3). Starting from the interferometric coherence image (Figure 3.4.3a), the results of the individual processing steps are illustrated to provide a first visual assessment of the extraction quality.

Step 1: Pre-Classification by Statistical Coherence Thresholding

As explained above, areas of moving sea ice will decorrelate in 46-day ALOS PALSAR interferograms, such that the statistical properties of the interferometric coherence over drifting sea ice areas is consistent and predictable (see gray lines in Figure 3.4.1). This allows application of CFAR detection methodology for pre-classifying interferograms into landfast and drifting ice classes. In CFAR classifiers, the classification threshold can be set statistically to yield constant and pre-defined false detection probabilities , where α corresponds to a pre-defined acceptable false alarm rate. Therefore, CFAR classifiers have the advantage of producing statistically consistent results as they do not require a manual and somewhat arbitrary choice of the detection threshold. More information in CFAR classification methods can be found in (*Gandhi and Kassam*, 1988; *Meyer et al.*, 2006).

For the application at hand we empirically determined a false alarm rate of $P_{fa} = 0.1$ to be most suitable for pre-classifying the data into candidate classes. Figure 3.4.3b, shows the coherence mask created using the CFAR detection step. Areas in white indicate areas classified as landfast ice. At this stage, this class also contains all landmasses in the image, which are masked for final landfast ice area assessment after landfast ice edge extraction. Land masking was performed by overlaying coastline information onto the geocoded SAR products. The accuracy of the land masking approach depends on the geocoding quality of the SAR data and the accuracy of the coastline information. The geocoding accuracy of PALSAR data can be quantified with ~10 m (*Rosenqvist et al.*, 2007). The coastline information used in this study was digitized from USGS 1:63,360 topographic maps ranging in date from 1950's to 1990's. The quality of the extracted coastline is not precisely known due to the varying coastline retreat that was observed along the Alaskan Arctic coast. As this study focuses on a relative analysis of landfast ice detection methods, absolute errors introduced by uncertainties in the coastline location are of lesser importance.

The initial CFAR classification covers most of the landfast ice areas but leaves holes in some isolated decorrelated regions both inland and offshore. The decorrelated patches are partly caused by temporal decorrelation on not-yet-frozen fresh water lakes and by low signal-to-noise ratios on some very low-backscatter sea ice patches. In addition to these holes, the mask also shows a larger amount of isolated false positive detections in areas of drifting ice (white speckles in lower right part of Figure 3.4.3b). The number of false detections is defined by our choice of $P_{fa} = 0.1$. As the false positives are isolated pixels rather than clusters, they can be easily removed in subsequent morphological filtering steps.

Step 2: Morphological Operations

In an intermediate step, morphological filters (median, erosion and dilation filters) are used to fill small holes in the existing mask and to remove small patches of false detections, which originate from the speckle pattern in the SAR data (see Figure 3.4.3c). This leads to a reduction of false positives and closes some holes in the landfast ice class. Background information on the morphological filters applied in this study can be found in (*Haralick and Shapiro*, 1992).

Step 3: Patch Size Analysis

After the morphological filtering the mask is segmented into connected sub-regions, each of which is assumed to cover parts of the total landfast ice area. The segmentation process follows an approach presented by Haralick and Shapiro (1992). From an analysis of several segmentation results we have empirically determined that patches of false positives cover less than 500 m^2 per piece, and segments smaller than this are rejected. The remaining segments are combined and handed over to the next processing step. The improvement in landfast ice mask accuracy can be seen in Figure 3.4.3d, where many of the false alarms in the drifting ice regions have been discarded.

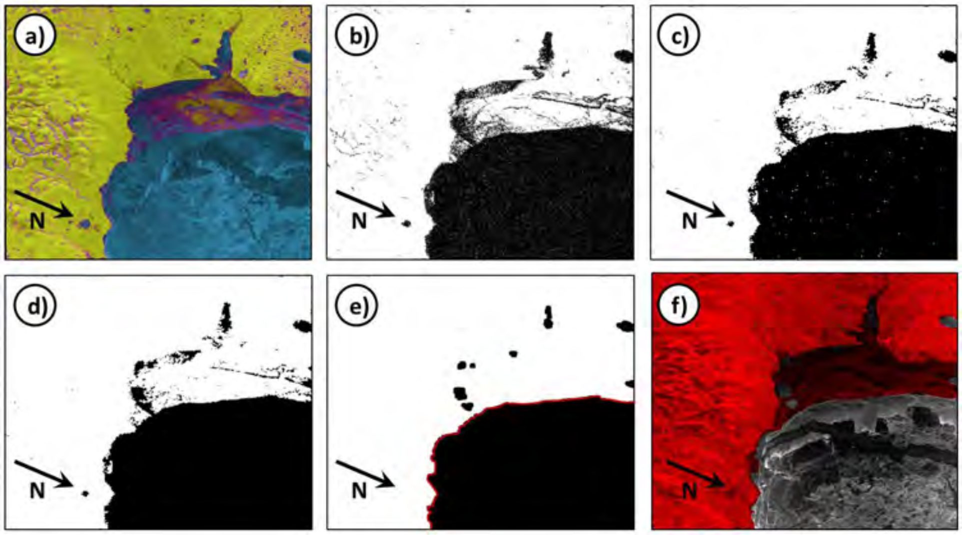

Figure 3.4.3: Progression of landfast ice mask derivation for an example covering the Seward Peninsula, Alaska. Detected masks are shown starting with the original coherence image, progressing through steps 1 to 4, and ending with an overlay of the final mask over a SAR amplitude image. For a detailed description of the significance of different colors and shading, please see text.

Step 4: Creation of Closed Outline and Outline Tracing

A morphological closing procedure is applied to create a closed outline for the generated mask. Closing is performed using a flat linear structuring element. To fix the orientation of these linear elements, gradients are calculated from the mask and their local orientation is extracted (*Haralick and Shapiro*, 1992). This last processing step provides a closed mask whose outline can easily be traced using line extractors. In our case, linear features are extracted in a first step. The individual line segments are then connected and tested for closed loops. Closed loops are rejected as they do not represent the landfast ice edge. The final extracted line is shown in Figure 3.4.3e. Figure 3.4.3f also shows the final landfast ice mask superimposed on a SAR amplitude image to provide a visual for a first validity test of the mask. A quantitative accuracy analysis of landfast ice extent extracted from L-band InSAR data is provided in section 4.4.4.

3.5 Ancillary data sets

3.5.1 Bathymetry

Two bathymetry datasets were used in this project in conjunction with the analysis of landfast ice data. The first dataset was compiled from a variety of sources (see Table 3.5.1) and is the one that was used for MMS OCS STUDY 2005-068. It therefore covers only the eastern landfast ice study region (see Figure 1.4.1). The second bathymetry dataset was used for the western landfast ice study region and consists exclusively of data from the Alaska region bathymetric digital elevation model (ARBDEM) (*Danielson et al.*, 2008). These data are shown in Figure 1.3.1.

Table 3.5.1: Summary of bathymetric datasets acquired in the process of developing a gridded bathymetry of the landfast ice study area.

	Dataset	Source	Region
1	GEODAS depth soundings	NGDC	Nearshore Chukchi and Beaufort Seas
2	ENC sounding data	NOAA	Chukchi Sea
3	ENC sounding data	NOAA	Beaufort Sea
4	Nautical chart #16082	NOAA	Point Barrow
5	Outer Continental Shelf Study MMS 2002-017	MMS	
6	Digital Ocean Chart 7662	NDI	Mackenzie Bay
7	Digital Ocean Chart 7661	NDI	Demarcation Bay To Philips Bay
8	IBCAO Sheet 3	IBCAO	Arctic Ocean

The data from both sources were gridded to 100 m pixel sizes, corresponding to the same grid as the SAR imagery used for the landfast ice analysis. However, the spatial distribution of datapoints used in the MMS OCS STUDY 2005-068 bathymetry dataset are significantly better than that for the ARBDEM, especially near the coast, and comparison of results between the two study regions should bear this in mind. In particular, any inaccuracy in the location of the 15 m isobath will affect the determination of the data of landfast ice stabilization (Section 3.3.7). This effect will be most noticeable along sections of coast where the SLIE does not extend far offshore, such as zone 5 from Cape Krusenstern to Cape Lisburne.

3.5.2 Surface air temperature reanalysis data

Daily mean surface temperature fields were acquired from the National Centers for Environmental Prediction (NCEP) over the entire study area for the period 1993-2010. These data were used to generate daily timeseries of temperature at each of the 8,889 points on the coast defined by the coastal coordinate vectors (Figure 3.3.4). From these timeseries, we indentified the onset of freezing temperatures each year, as defined by the first day with a daily mean temperature below 0 °C that was also the first day of a 15-day period with a mean temperature below 0 °C. The onset of thawing was calculated in a similar way using positive temperatures.

3.6 Dissemination and archival of resultant data sets

All project data were processed to the standard Alaska Statewide Albers map projection and federal datum standard to promote data integration. These project data include remotely sensed imagery, specifically AVHRR scenes and Radarsat mosaics in GeoTIFF format plus ArcGIS grids, shapefiles and vector-based geodatabases. Following are the detailed projection and datum parameters:

Map Projection Name: Albers Conical Equal Area
Standard Parallel: 55.000000
Standard Parallel: 65.000000
Longitude of Central Meridian: -154.000000
Latitude of Projection Origin: 50.000000
False Easting: 0.000000
False Northing: 0.000000

Planar Coordinate Information
Planar Distance Units: meters
Coordinate Encoding Method: coordinate pair

Coordinate Representation
Abscissa Resolution: 0.002048
Ordinate Resolution: 0.002048

Geodetic Model
Horizontal Datum Name: North American Datum of 1983
Ellipsoid Name: Geodetic Reference System 80
Semi-major Axis: 6378137.000000
Denominator of Flattening Ratio: 298.257222

This project required processing a large volume of imagery and derived data. Almost 3000 Radarsat data granules were acquired and processed into image mosaics in GeoTIFF format covering the eastern and western study areas. Radarsat mosaics, derived GIS SLIE delineations and monthly averages total nearly 100 GB worth of data for the ice seasons beginning in the Fall of 1996 through Spring of 2008. 644 AVHRR scenes were acquired and processed into GeoTIFF format as well. A total of nearly 3 GB of AVHRR imagery and derived GIS data were produced for 1993-2010 ice seasons.

The final deliverables for the project utilize the standard naming conventions developed for the previous study. These deliverables include data as ArcGIS file geodatabases, shapefiles, and grids (which impose a 13-character file limitation that was taken into consideration in developing the naming conventions.) The data were divided between the Chukchi Sea and Beaufort Sea portions of the study area. The file names rely on the use of the directory structure to organize the files in folders by year. Individual file names incorporate the number associated with the day of that year for each of the data sets. Detailed information on the file naming conventions is available on the project web site and in the metadata files.

Final deliverables are provided in formats compatible with ArcGIS as requested in the RFP. The geodatabases organize the SLIE and lead data by ice season, plus include monthly SLIE minimum, mean, and maximum data. Summary data sets are also available in GeoTIFF and text formats. FGDC XML metadata templates have been associated with each data set. Bathymetry data (1 km resolution) was acquired from Seth Danielson of UAF's School of Fisheries (http://mather.sfos.uaf.edu/~seth/bathy/) for use in our analysis.

These geospatial data sets and associated metadata, plus lead statistic summaries, are available on a password protected web site hosted by the Geographic Information Network of Alaska (GINA) at the University of Alaska Fairbanks. This project web site organizes resultant data sets by ice season and is accessible at: http://boemre-new.gina.alaska.edu. The site proved to be a useful tool for sharing data products and ongoing progress with the BOEM contracting officer. After the final products have been reviewed and accepted, the project deliverables will be made available to clearinghouses and data catalogues at the Geographic Information Network of Alaska, Alaska Ocean Observation System, National Oceanographic Data Center (NODC) and National Snow and Ice Data Center (NSIDC) to foster dissemination.

4. RESULTS

4.1 Mapping of lead distribution and morphology

4.1.1 Seasonal, interannual and regional variability in lead areal fractions

The total lead fraction averaged by month for the eastern (Beaufort Sea) and western (Chukchi Sea) regions is shown in Figures 4.1.1 and 4.1.2. While there is substantial interannual and regional variability, most years nevertheless exhibit a distinct seasonal cycle with lead fractions between 0.02 and 0.07 throughout the winter and early spring, increasing to well above 0.1 in June (Figure 4.1.3). Minimum lead fractions in February coincide roughly with the lowest temperatures, typically found in the second half of February or the first week of March based on Barrow surface air temperature climatology (Alaska Climate Research Center, 2012, climate.gi.alaska.edu). The distribution of leads in the Beaufort Sea shows a distinct regional pattern, with lower values between Point Barrow and Barter Island. The highest values were found in the Mackenzie region, in particular in late spring in association with river and coastal landfast ice break-up (Figure 4.1.1, see also Table 4.1.1 and Section 4.3). Thus, in May and June, the landfast ice adjacent to the Mackenzie Delta is inundated by spring flood waters that contribute to rapid melt and decay of the landfast ice in this region, reflected in greater open water areas (*Dickins et al.*, 2011). The sensible heat advected into coastal waters also contributes to ice retreat further offshore. In the Chukchi Sea, highest lead fractions are found in the southern subregion (Bering Strait, region B), as well as just west of Point Barrow, with the lowest lead fractions in the East Siberian Chukchi Sea (Table 4.1.2 and Figure 4.1.2).

Table 4.1.1: Mean and standard deviation (σ) of lead areal fractions, numbers, and size parameters for all years for the eastern study region (Beaufort Sea), Dec 1993 – Jun 2009.

Eastern study area (Beaufort Sea)	All subregions		West Subregions 1-3		West-Central Subregions 4-6		East-Central Subregions 7-9		East Subregions 10-12	
Parameter	Dec-Apr	May-Jun	Dec-Apr	May-Jun	Dec-Apr	May-Jun	Dec-Apr	May-Jun	Dec-Apr	May-Jun
Areal Fraction %	2.6	9.1	3.7	8	1.8	4.7	1.9	6.3	2.1	16.4
σ	2.4	8.5	3.3	5.3	2.1	5.4	2.7	7.7	2.7	16.8
Number of leads	312	1109	111	212	96	269	94	350	58	292
σ	338	667	118	135	126	199	138	249	66	213
Area (km^2)	36.5	37.0	55.4	59.8	34.7	44.6	45.3	61.7	64.0	162.4
σ	203.6	465.6	235.3	410.1	263.0	164.5	183.6	549.9	145.4	700.1
Perimeter (km)	23.4	18.1	28.4	21.5	18.3	25.0	23.0	19.4	21.1	24.0
σ	57.6	61.0	65.1	74.4	58.7	51.6	49.3	62.4	46.0	91.3
Major Axis (km)	7.4	5.7	8.3	6.3	5.7	5.7	7.0	5.9	7.6	9.2
σ	11.4	10.7	12.7	13.6	10.5	10.7	9.5	10.7	11.0	19.3
Minor Axis (km)	2.5	2.4	2.9	2.5	2.3	2.4	2.2	2.4	2.5	3.4
σ	2.5	3.0	2.9	3.3	2.4	2.0	1.8	3.1	2.5	5.2
Number of Scenes	302	108	321	111	316	115	315	116	315	118

Areal fraction: total surface area of leads divided by total surface area of the subregion; Number: total number of leads in subregion; Area: surface area of individual leads; Perimeter: perimeter (circumference) of individual leads; Major and minor axis: major and minor axis of an ellipse that provides the best fit to the lead outline; Number of scenes: number of scenes in which subregions were cloud-free and could be analyzed.

As indicated in Figures 4.1.4 and 4.1.5, there is substantial interannual variability in the lead areal fraction in all regions and for all seasons. In the Bering Strait region and the southern Chukchi Sea this variability is largely driven by the fact that during May and June the region begins to exhibit seasonal ice retreat which skews the open water fraction (as opposed to the lead numbers, for example) towards the open water associated with the marginal ice zone and open water outside of the ice pack. Differences in cloud cover and availability of imagery suitable for analysis, in particular in the Chukchi Sea with consistently higher cloud cover also play a role. However, the broader regional patterns, such as minimum interannual variability in the Smith Bay sector (subregion 4) and maximum variability west of Point Barrow off the Mackenzie Delta, or comparatively low variability around Wrangel Island, hold up to further scrutiny. These regional variability patterns are also manifest in monthly mean lead distributions (Figures 4.1.2 and 4.1.1)

Table 4.1.2: Mean and standard deviation (σ) of lead areal fractions, numbers, and size parameters for all years for the western study region (Chukchi Sea), Dec 1993 – Jun 2010.

Western study area (Chukchi Sea)	All subregions		East (A)		Bering Strait (B)		West (C)		Wrangell Island (D)	
Parameter	Dec-Apr	May-Jun	Dec-Apr	May-Jun	Dec-Apr	May-Jun	Dec-Apr	May-Jun	Dec-Apr	May-Jun
Areal Fraction %	4.5	21.7	3.7	15.1	7.8	48.2	2.9	13.6	4.0	9.0
σ	4.5	22.4	2.8	10.1	7.4	27.4	2.2	13.3	2.7	2.3
Number of leads	1605	1841	552	840	341	159	496	754	195	265
σ	851	783	349	411	168	100	365	431	137	145.1
Area (km^2)	16.5	18.2	14.7	13.2	18.7	30.4	14.1	16.9	19.4	25.5
σ	77.2	224.4	58.7	113.2	68.9	148.8	48.0	115.0	66.0	178.3
Perimeter (km)	16.0	13.6	15.5	11.8	16.9	19.2	15.3	13.9	17.7	15.6
σ	29.9	36.7	27	22.7	29.3	40.8	24.2	30.7	30.0	40.5
Major Axis (km)	5.5	4.5	5.4	4.2	5.6	5.8	5.4	4.6	5.9	5.0
σ	6.7	6.6	6.1	4.8	6.5	8.0	6.0	6.0	6.8	7.2
Minor Axis (km)	2.2	2.1	2.1	2.0	2.3	2.6	2.1	2.2	2.3	2.3
σ	1.6	2.2	1.4	1.5	1.8	2.9	1.4	1.9	1.7	2.6
Number of Scenes	61	24	95	31	77	29	92	32	82	20

Areal fraction: total surface area of leads divided by total surface area of the subregion; Number: total number of leads in subregion; Area: surface area of individual leads; Perimeter: perimeter (circumference) of individual leads; Major and minor axis: major and minor axis of an ellipse that provides the best fit to the lead outline; Number of scenes: number of scenes in which subregions were cloud-free and could be analyzed.

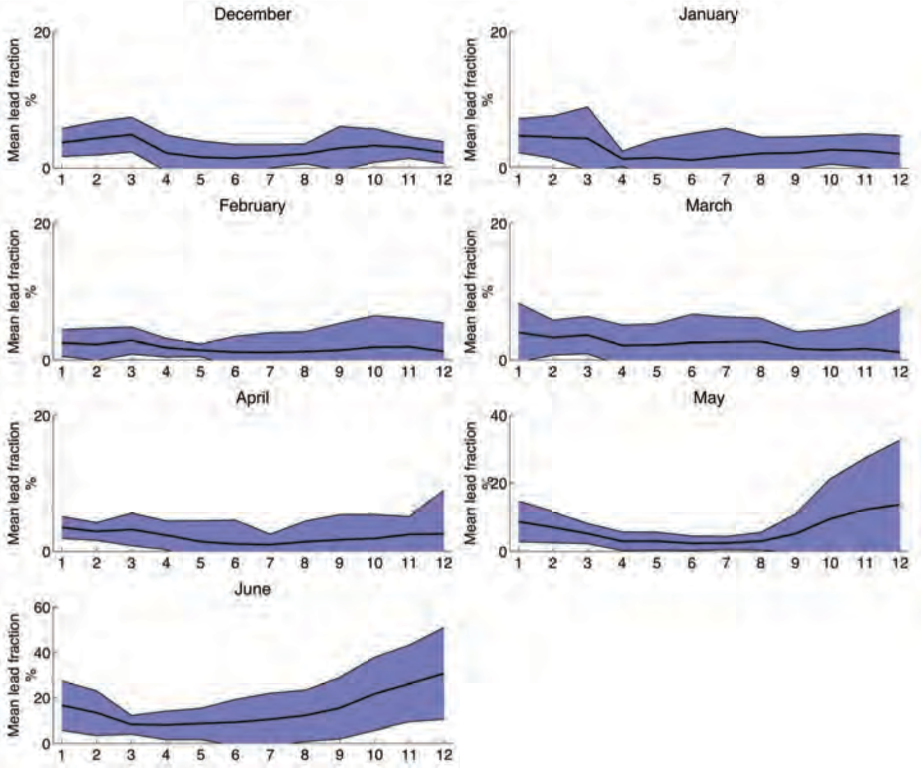

Figure 4.1.1: Monthly mean lead fractions (bold black lines) for the different subregions in the eastern study area (Beaufort Sea) for the period December 1993 – June 2009. The blue regions indicate 1 standard deviation either side of the mean. Note the different y-axis scales for the June panel.

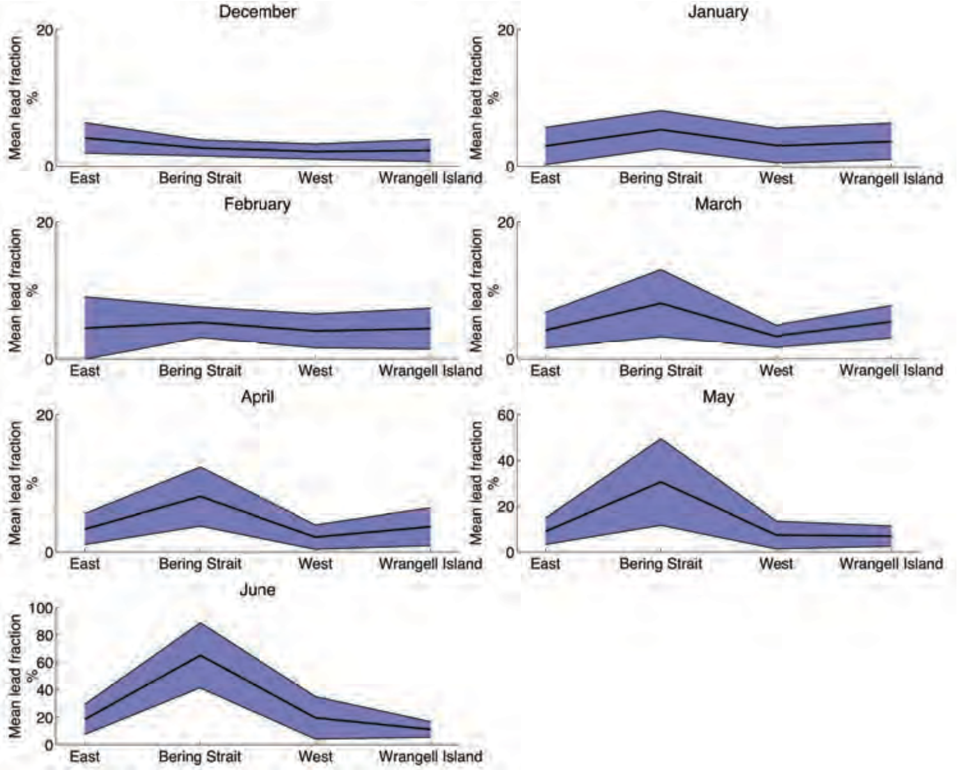

Figure 4.1.2: Monthly mean lead fractions (bold black lines) for the different subergions in the western study area (Chukchi Sea) for the period December 1993 – June 2010. The blue regions indicate 1 standard deviation either side of the mean. Note the different y-axis scales for the May and June panels.

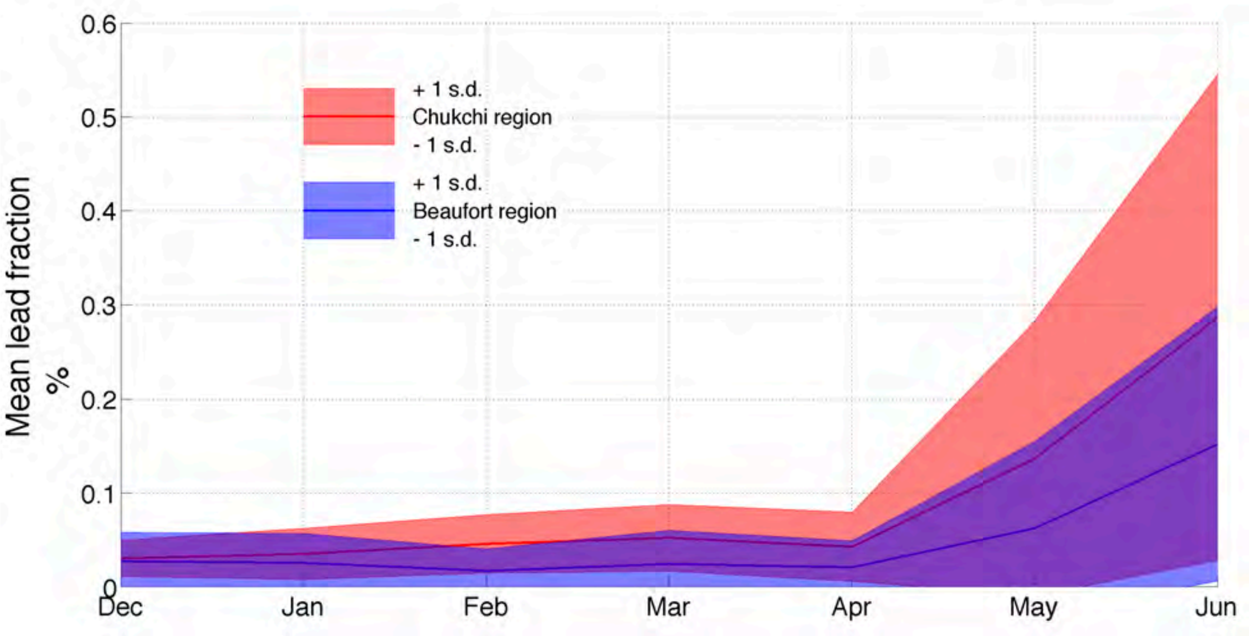

Figure 4.1.3: Mean and standard deviation of lead fractions in the eastern and western study areas (Beaufort and Chukchi Seas, respectively) for December through June.

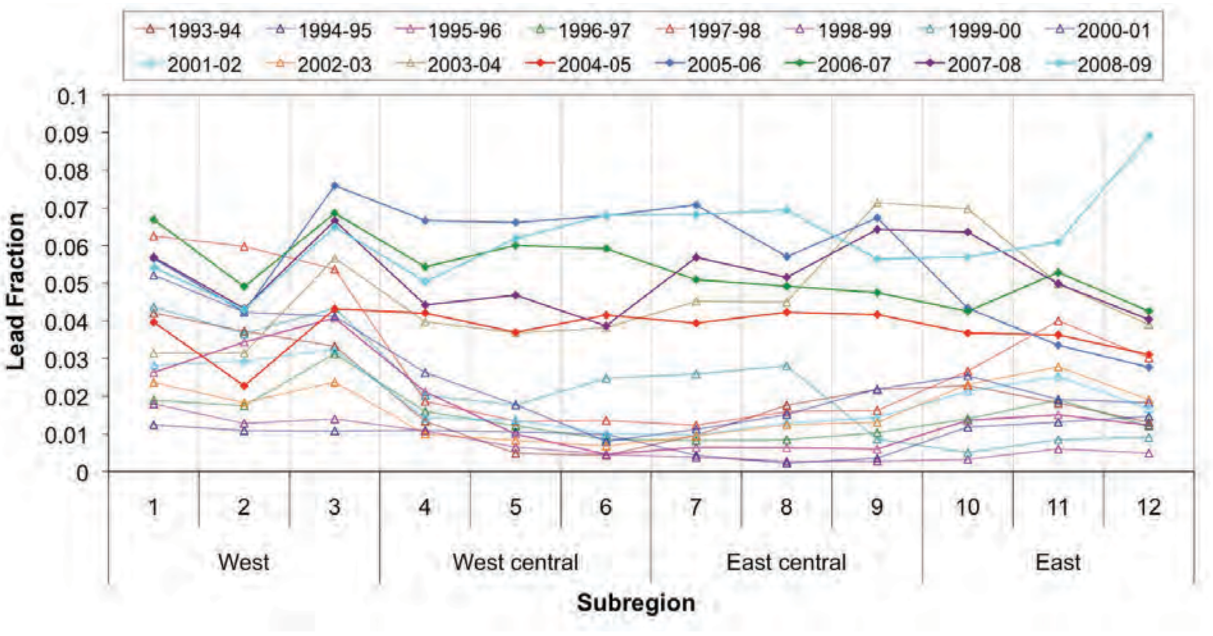

Figure 4.1.4: Mean lead fractions in the eastern study area (Beaufort Sea) for December through June shown by subregion for all years (December 1993- June 2009). Data from previous study (MMS OCS Study 2005-068) are drawn in paler colors with triangular markers, whereas new data from this study are drawn in darker colors with diamond-shaped makers.

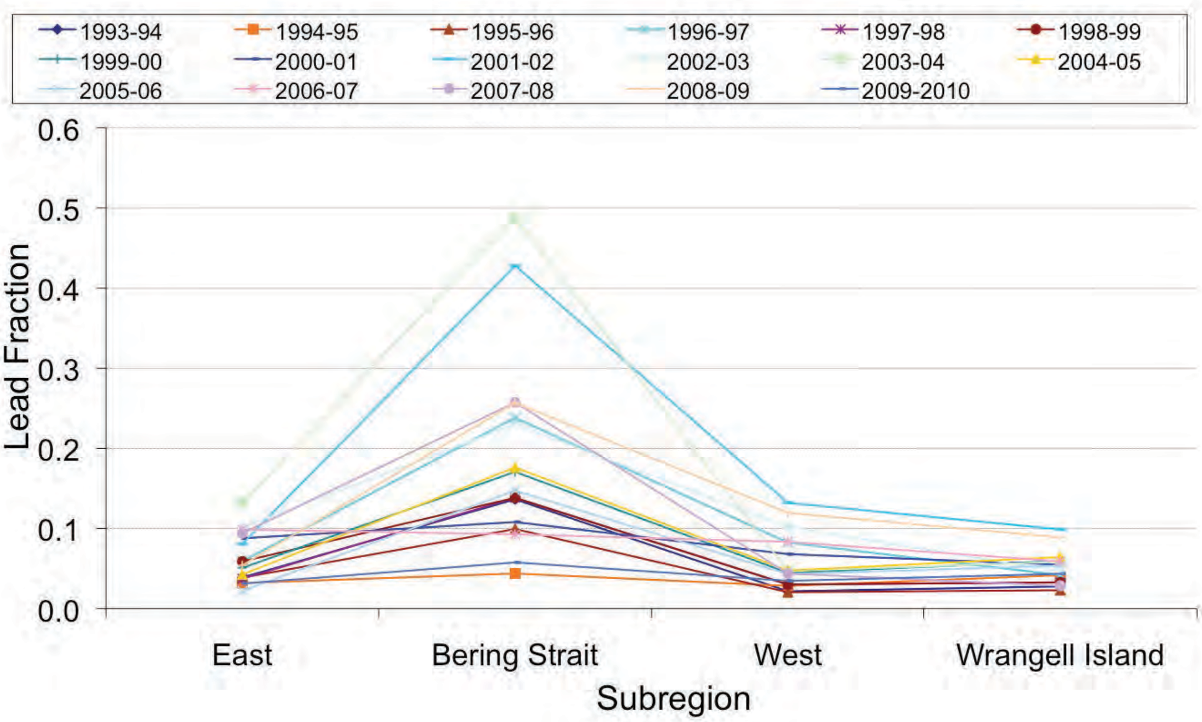

Figure 4.1.5: Mean lead fractions in the western study area (Chukchi Sea) for December through June shown by subregion for all years (December 1993 – June 2010).

4.1.2 Regional and seasonal variability in number and size of leads

The number of leads was determined for each subregion through automated counting of contiguous lead areas. Each lead was only considered once based on the location of its centerpoint (center of ellipse fit to lead outline). Typical lead numbers for the in the eastern and western study areas ranged between hundreds for the Beaufort Sea during the peak of the ice growth season (around one thousand for the Chukchi Sea region at this time), to a few thousands in fall and late spring (Figures 4.1.6 and 4.1.7). A striking feature in all data is the near-absence of a pronounced seasonal cycle. In the Chukchi Sea this is in line with the dynamic nature of the ice pack and is observed throughout the study period (1994-2010). In the Beaufort Sea, however, there is a clear difference between the years after 2006 and those prior, with much higher lead numbers and lead number densities in the last few seasons as compared to the earlier years analyzed (Figure 4.1.6 and Eicken et al., 2006).

Several variables have been determined to describe the morphology and size of individual leads. These include the lead area, perimeter, and the major and minor axis lengths of a best-fitting ellipse as shown in Tables 4.1.1 - 4.1.2. With leads typically narrow and irregular in shape, lead minor axes exceed the pixel size only by a factor of two to three, with lead (ellipse) aspect ratios averaging between 2 and 3 for the Beaufort and Chukchi Seas, respectively. These numbers reflect the fact that the number distribution of leads is dominated by small features which are different in shape from the large, elongated leads apparent in the imagery but constituting only a few percent at most of the total number of leads. The regional contrasts apparent in Tables 4.1.1 - 4.1.2 are marginally significant and mostly reflect the appearance of large coastal leads and polynyas in the western and eastern subregions of the study area.

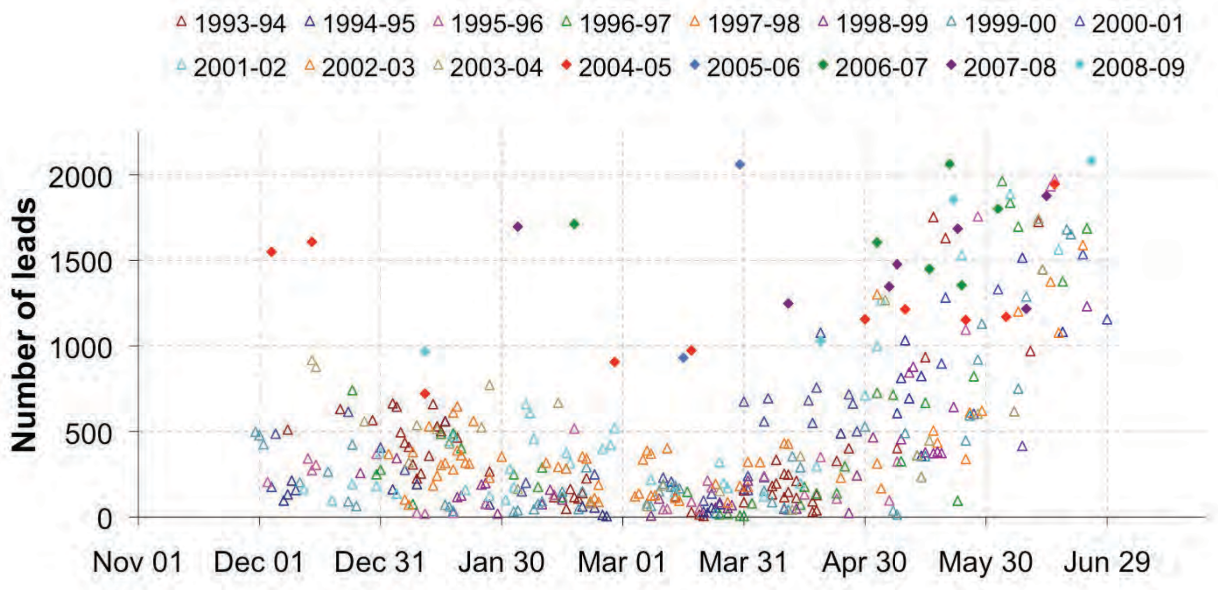

Figure 4.1.6: Seasonal cycle of lead number in the Beaufort Sea for the period December 1993 – June 2009. Data from the previous study (MMS OCS Study 2005-068) are drawn with triangular markers, whereas new data from this study are drawn with diamond-shaped makers.

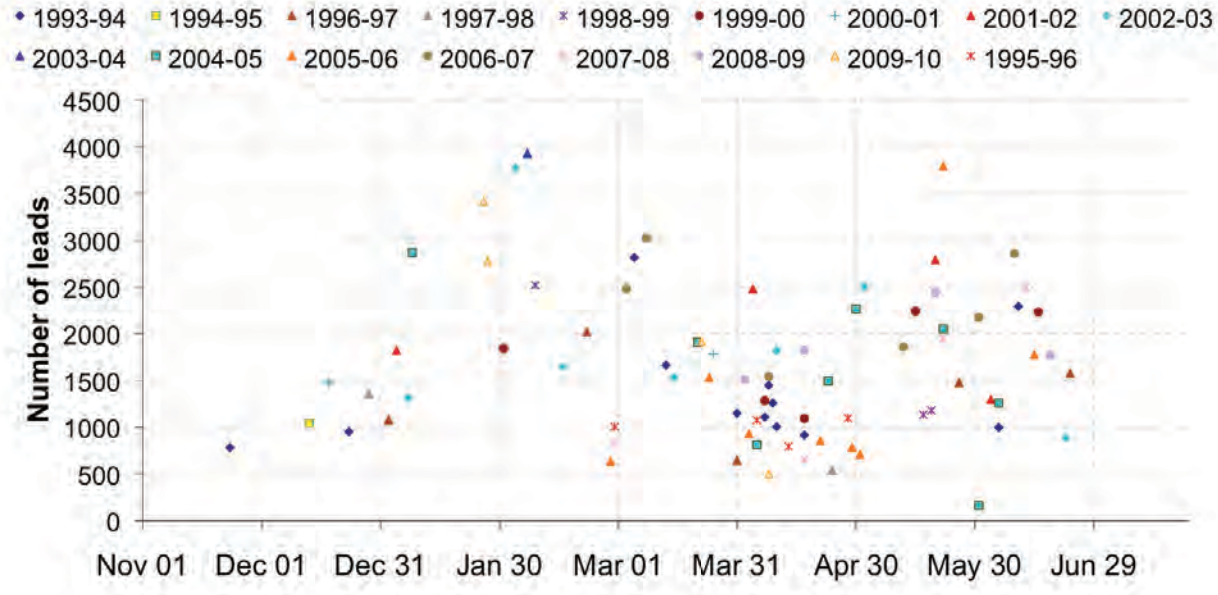

Figure 4.1.7: Seasonal cycle of lead number in the Chukchi Sea for the period December 1993 - June 2010.

4.2 Identification and description of pack ice lead patterns

Since this reports builds on but does not explicitly reiterate the findings of the MMS OCS STUDY 2005-068 report, readers are referred to the earlier report (Eicken et al., 2006) for a more detailed description and discussion of lead patterns in the Beaufort Sea. The focus of the section below is on the Chukchi Sea and any patterns that had not been evident in the data analyzed for Beaufort Sea for the time period 1994-2004.

4.2.1 Definitions

In MMS OCS STUDY 2005-068, the term "lead pattern" was used to identify both (1) a lead along the landfast ice edge and (2) a lead or series of leads that occur in a repeatable configuration or relationship at different times …" The first usage can be dropped for this study, because assemblages of leads in the Chukchi Sea are often tied to deformation episodes that involve most, if not all, of the ice pack. Thus, a "lead pattern" could involve leads of different shapes and orientations on opposite sides of the Chukchi Sea. This contrasts with the Beaufort Sea where, except for the Barrow Arch and the frequent occurance of long leads extending to the north or northeast from Point Barrow, leads and lead patterns occur mainly in a narrow zone between the pack ice and the landfast ice edge. Note that some of the long leads from the Point Barrow areas were included in the pattern called "Chukchi Offshore Leads" in MMS OCS STUDY 2005-068.

The lead patterns described here were all observed several times on the AVHRR imagery so they recur often enough to be identified and named. However, it should be noted that there are variations of every pattern and the patterns are transitory and change constantly. The description of a lead pattern is, therefore, essentially based on a snapshot taken of a process and there is no certainty that the processes will continue until all the possible components are formed. Thus, no attempt was made to systematically compare the appearance and characteristics of any particular pattern for different times of the year. The physical and mechanical properties of the pack ice vary with both time and location across the area and, to some extent, the boundaries change as the position of the landfast ice edge changes and ice grounds on Hanna and Herald Shoals. Thus, it is reasonable to expect there to be differences in the details of any pattern depending on the time of year and the state of the ice. However, it is not difficult to recognize particular patterns whenever they occur. This is because the basic features of any pattern (i.e. the typical shapes and orientations of leads) are generally consistent for any particular direction of pack ice displacement.

4.2.2 Chukchi Sea pack ice boundaries and patterns of motion

In MMS OCS STUDY 2005-068 a working hypothesis was adopted that lead and deformation patterns in the southern Beaufort Sea exhibit characteristic, recurring patterns. Two sets of observations support this conjecture. First, the coastlines that bound the area are fixed and their shapes as modified by the attachment of landfast ice provide rigid boundaries that are generally consistent from year to year. Second, pack ice motion in the southern Beaufort Sea is dominantly westward, reflecting the rotation of the Beaufort Gyre and the prevailing northeasterly to easterly winds across the area. (Figure 4.2.1a). Displacement to the north is restricted by the presence of the main Beaufort Sea ice pack, and the most common weather patterns also tend to keep the pack ice close to the Alaska coast. These constraints and influences on the motion of the southern Beaufort Sea pack ice justify the assumption that lead patterns should be repeatable within those rigid boundaries. In fact, many of the lead forms and patterns identified in MMS recur often, reflect the westward sense of displacement and are mainly confined to a relatively narrow zone where the pack ice and coast interact. The Barrow Arch, the prominent arch structure that is common near Point Barrow, develops because the Point itself is a sharp corner in the boundary. It acts as a stress concentrator in the flow field of moving ice and fractures would be expected to form there. In addition, the frequent westward drift of the Chukchi Sea pack ice off the coast of Alaska usually provides space for some of the west-drifting ice from the Beaufort Sea to diverge into as it moves west of Point Barrow.

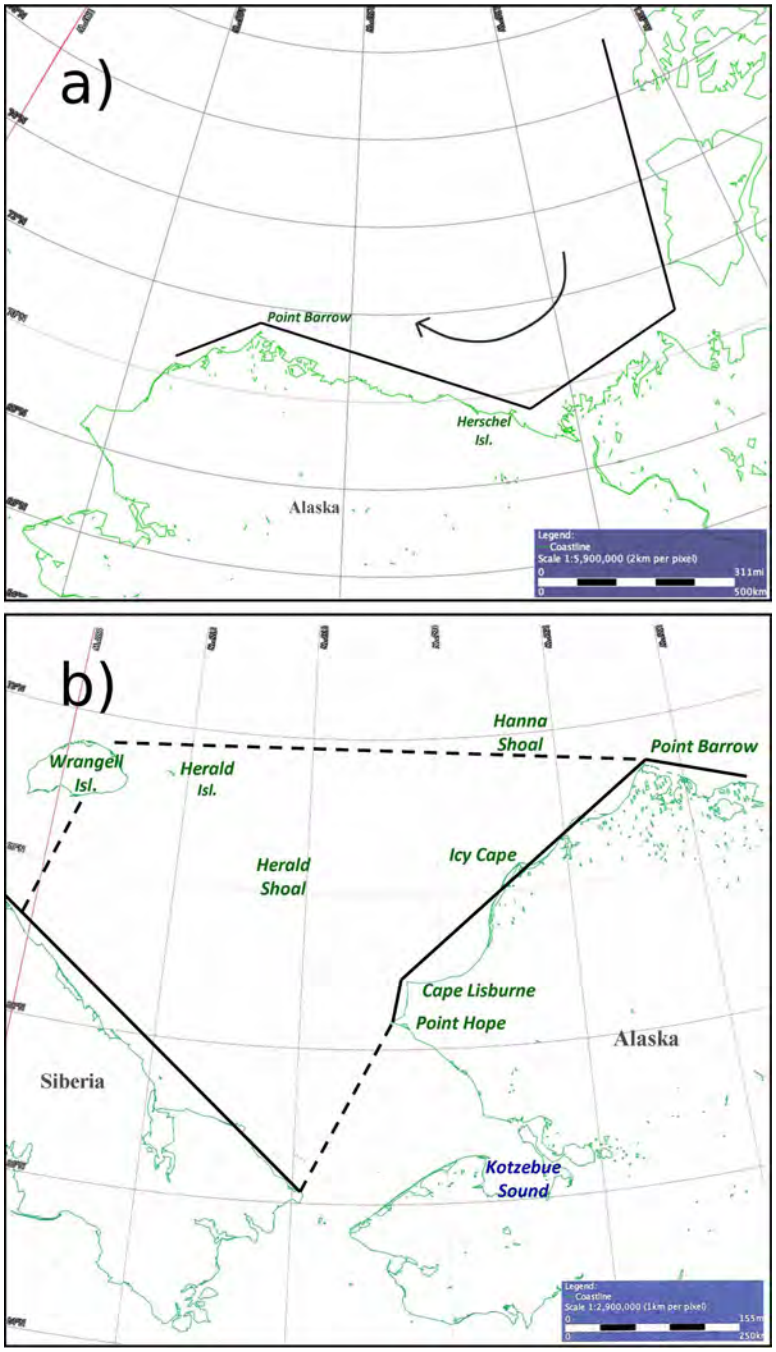

Figure 4.2.1. Boundaries to ice motion in the region covered in this study. a) Rigid boundaries in the eastern Beaufort Sea. The heavy lines approximate the offshore limit of the landfast ice where interactions with the pack ice take place. The arrow indicates the dominant drift direction of the pack ice; b) boundaries in the Chukchi Sea. Solid lines represent rigid boundaries imposed by the coastlines or offshore limits of the landfast ice. Ice can potentially cross the dashed lines in either direction although most examples of significant reverse motion occur near Point Barrow.

A similar hypothesis regarding boundary influences was assumed to apply in the Chukchi Sea, anticipating that consistent, recurring lead and deformation patterns would be identified. As will be shown, this has proved to be the case, although the processes and interactions with the boundaries are clearly different from those in the Beaufort Sea. In addition, the overall deformation patterns in the Chukchi Sea tend to involve large segments of the ice cover, rather than being confined to narrow zones along the coasts.

The Chukchi Sea pack ice fills what can be described as a roughly triangular-shaped confined basin (Figure 4.2.1b) bounded on two sides mainly by the rigid coasts of Alaska and Chukotka. There is a gap in the Alaska side that opens into the area north of Bering Strait and outer Kotzebue Sound as shown by a dashed line in Figure (Figure 4.2.1b). The third side of the triangle is bounded by (1) the Beaufort Sea ice pack, (2) a rigid segment represented by Wrangel and Herald Islands and the landfast ice between them and (3) a short open gap between Wrangel Island and Chukotka.

The coast of Alaska trends generally to the northeast from Cape Lisburne to Point Barrow, and the short reach of the coast from Point Hope to Cape Lisburne is oriented a few degrees east of north. Thus, overall the coast is roughly aligned with, or at a high angle to, the prevailing winds. The coast from Point Hope to the southeast is approximately at a right angle to the overall trend of the remainder the Alaska coast and that is important for some of the deformation patterns involving Bering Strait (see section 4.2.9). The coast of Chukotka also trends at approximately a right angle to the northeast trending coast of Alaska and helps define a route for southward-drifting pack ice toward Bering Strait and outer Kotzebue Sound. Finally, when the Chukchi Sea pack ice drifts in a westward direction, the space between the coast of Chukotka and Wrangel Island provides a gap for pack ice to move out of the Chukchi Sea. However, there is generally little space west of the opening to accommodate ice moving in that direction.

During winter, the cumulative ice drift through the Bering Strait is southward, so some ice is exported from the Chukchi Sea into the Bering Sea. The drift direction generally reverses in spring, and northward drift through the eastern side of Bering Strait is common during melt season.

The boundary between the Chukchi and Beaufort Sea ice packs changes with changes in weather systems. Under some conditions there is no visible boundary and the pack ice is continuous, but at other times, the transition is shown by the increase in the number and density of leads in the Chukchi Sea pack ice as compared to the Beaufort Sea as shown in Figure 1.2.1. At other times the grounded ice mass on Hanna Shoal helps define the boundary. The shoal is located at approximately 72° N, 162° W (see Figure 4.3.2) where the shallowest depth contour is 25 m (*Grantz and mullen*, 1992) and, under some conditions, a zone of leads from there to Herald Island, about 500 kilometers to the west, provides a recognizable boundary between the Chukchi and Beaufort Sea ice packs (Figure 4.2.2). The time that grounded ice first appears on the shoal varies, but once in place it has a significant influence on the pattern of leads in the northeastern Chukchi Sea (Table 4.2.1).

The most prominent features of the landfast ice along the Chukchi Sea coast of Alaska are the masses of ice that ground on Blossom Shoals. The shoals lie along a line that projects about 20 km northward from Icy Cape (see Figure 1.3.1) and the grounded ice creates a node that projects into the pack ice. Leads extending into the pack ice can originate at the node under some conditions and the direction of pack ice motion parallel to the coast is often shown by openings on the downstream side of the node. This node is highlighted as a region of high SLIE occurrence probability in Figure 4.3.1).

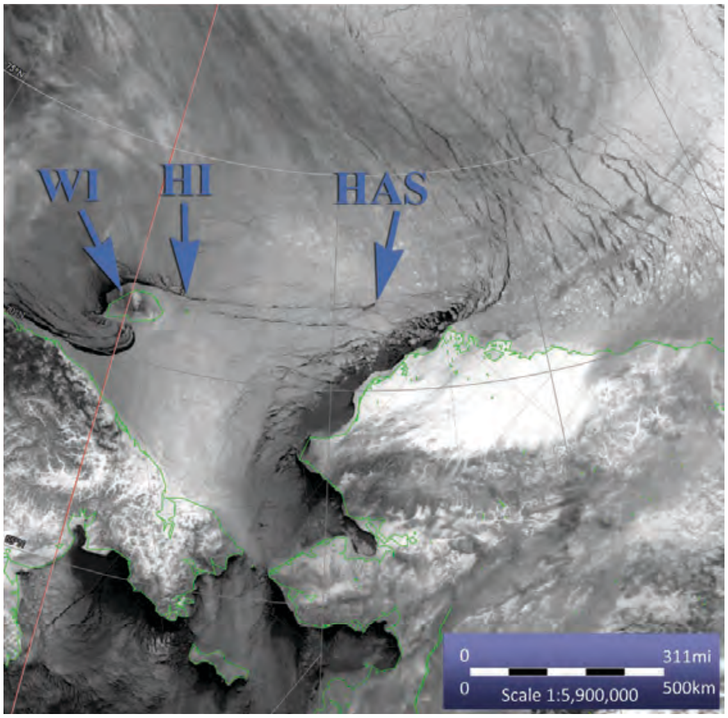

Figure 4.2.2: The Chukchi Sea-Beaufort Sea boundary as defined by a lead system from Hanna Shoal (HAS) to near Herald Island (HI). (n18.09076.1430; 03 April 2009).

Table 4.2.1: Date of first observation of open water or thin ice around grounded ice on Hanna Shoal shown as a dark spot on the IR imagery. The terms "probable" and "possible" express the degree of certainty when the definite identification of grounding on the shoal is not possible. The use of these terms may reflect the cloud cover or image quality. Question mark indicates that the first observation was made after a period when the shoal area was under cloud cover.

Ice season	First positive observation of Hanna Shoal polynya	Comments
93-94	1/6	
94-95	11/25	Probable 11/17
95-96	12/28	
96-97	12/24	
97-98	1/9	Possible 1/3
98-99	1/17	Possible 1/6
99-00	12/5	
00-01	1/27(?)	Cloudy since 1/13
01-02	12/12	
02-03	12/18	Possible 12/15
03-04	1/24	Probable 1/15
04-05	2/13(?)	Cloudy 1/29 to 2/13
05-06	12/11	Possible 12/3
06-07	2/18	
07-08	3/15	
08-09	1/7	Probable 12/27
09-10	2/19(?)	Bad data/cloud since 1/29
10-11	1/18	Cloudy since 1/15
11-12	12/20	Probable 12/14

One other element that is not part of the boundary, but can be important in determining the overall lead pattern in the Chukchi Sea pack ice, is the grounded ice mass that forms on Herald Shoal (at approximately 70.5° N, 171.5° W) in some years (Table 4.2.2). The bathymetric map (Grantz and Mullen, 1992) indicates that the shallowest closed contour at the shoal is 20 m below the surface. When present, the grounded ice mass is a point of origin for leads with various orientations, depending on the direction of pack ice motion. In addition, the ice tends to stay in the area of the shoal until late in the melt season. Unfortunately, there is no information in the open literature on the source and nature of the ice that grounds on the shoal.

Table 4.2.2: Observations of open water or thin ice around grounded ice on Herald Shoal. If a positive observation was made and there was no remnant, then the grounded ice mass was probably small enough to melt and/or drift off unnoticed as the pack ice deteriorated during melt. Note that in some years, large remnants remained in place until late July.

Ice season	First positive observation of Herald Shoal polynya	Comments
93-94	None	
94-95	(?)	Possible present for a few days about 5/10
95-96	4/11	
96-97	2/21	Last observed Jul 2
97-98	3/1	Last observed Jul 30
98-99	5/14	Last observed Jul 7, cloudy afterward
99-00	4/5 (?)	Probable 4/5; Last obs Jun 30
00-01	2/20	Probable 2/14 Large remnant 7/12
01-02	3/9	No remnant observed
02-03	(?))	Possible 4/23 to 5/5; No remnant
03-04	No data 2/20 - 6/9	Grounded ice 6/9; Large remnant 7/8
04-05	None	
05-06	None	
06-07	3/8	Last observed Jul 22
07-08	None	
08-09	3/12	Cloudy since 2/28; No remnant observed.
09-10	3/17	Cloudy from 2/1 to 3/17; Last obs. 6/25
10-11	None	
11-12	1/22	Cloudy since 1/17.....

The deformation patterns of the Chukchi Sea pack ice appear to be less influenced by the coastal boundary conditions than are those in the Beaufort Sea. This is because, as noted, there is usually open space for the Chukchi Sea pack ice to move into so deformation is not restricted to narrow zones along the coast. In additon, there are clear connections between local lead patterns that are large distances apart but still part of the same ocean-wide pattern. These will become clear in the descriptions of patterns later in this section.

4.2.3 <u>Chukchi Sea ice features and motion</u>

The ice cover in the Chukchi Sea is easily put into motion. Changes in lead patterns indicate shifts in the displacement direction of the pack ice, and major changes often take place within the day between the AVHRR images studied. The time of year appears to make little difference in the rate of response of the pack ice to environmental forcing. Rapid changes in pack ice configuration occur even in the coldest months when the ice is strongest and the ice cover is most densely packed. The reason appears to be that there is almost always some space available for at least part of the pack ice in the Chukchi Sea to move into, regardless of the displacement direction.

The area of the Chukchi Sea that is most consistently open is off the northwest coast of Alaska, where the pack ice is frequently driven away from the shore (Figure 4.2.3), leaving behind wide areas of thin ice or open water. Similar patterns develop off the southeast coast of Wrangel Island, the south-facing part of the Alaska coast southeast of Point Hope and, to a lesser extent, along the northeast-facing coast of Chukotka. As a result, there are often free, unrestrained boundaries to pack ice motion in any direction and the motion is not retarded until resistance builds up against a rigid boundary. The resulting convergence then increases stresses in the pack ice, creating ridges along the boundary and in thin ice within the tightening pack. Few leads can form in the convergent areas near the rigid boundaries, but the trailing part of the moving ice pack is often marked by arcuate leads concave in the direction of motion. However, as noted, patterns rapidly change as the displacement shifts, and the open spaces created in the up-drift direction during any displacement regime are quickly filled.

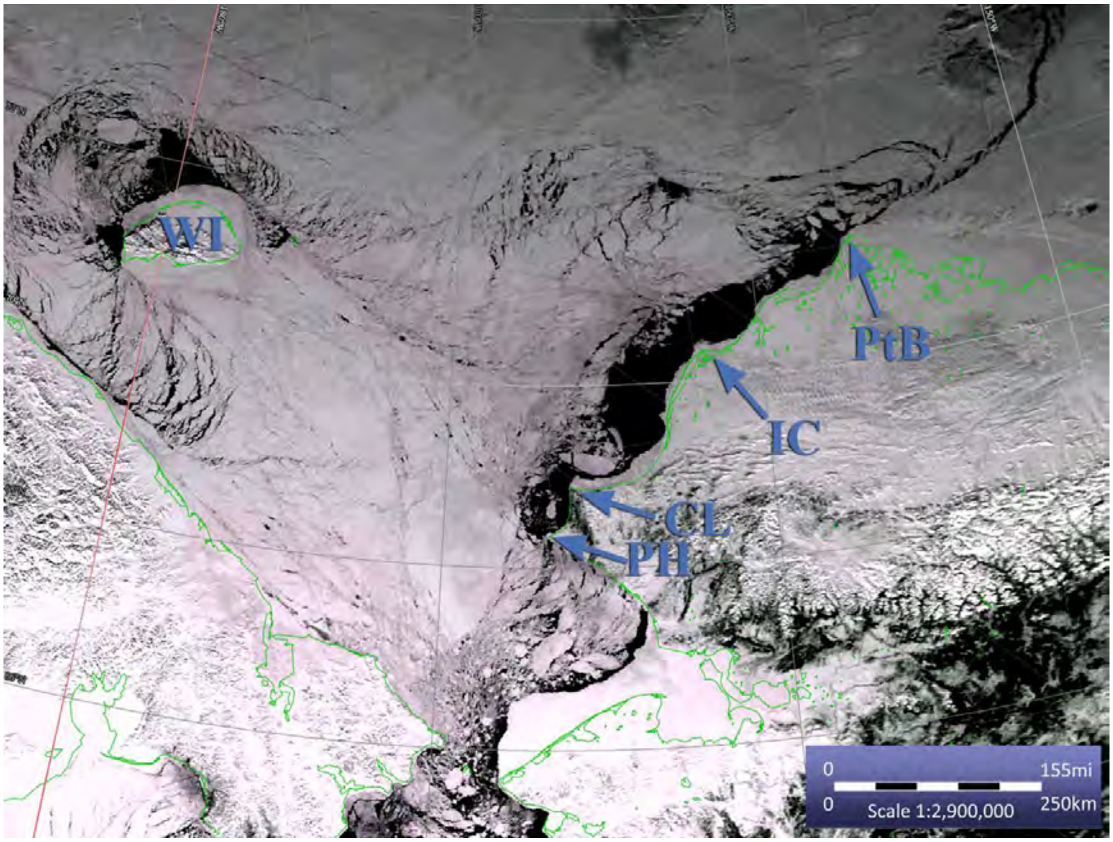

Figure 4.2.3: Wide zone of open water or thin ice off the Alaskan Chukchi Sea coast. The pack ice is displacing westward under widespread winds from the east. The entire coast of Alaska between Point Barrow (PtB) and Point Hope (PH) is open, and ice is clearing from the bight between Cape Lisburne (CL) and Icy Cape (IC. Note the arcing leads near Wrangel Island (WI) indicating ice displacement toward the gap between the island and the mainland. (N19.10082.2350; 23 Mar 2010)

The most common lead patterns observed in the Chukchi Sea pack ice involve displacements to the southwest, west and northwest, and probably reflect the prevailing northeast to east winds that range along or across the coast of Alaska. Reversals must obviously occur, but patterns associated with movements in other directions are less commonly seen. However, this may reflect a bias in the data since the prevailing winds in this area are often associated with clear, cloud-free weather, while clouds often accompany weather systems coming from other directions.

In general, the sense of pack ice displacement and convergence or divergence in any area can be determined by the shape and configuration of leads. In fact, once the overall characteristics of a particular pattern have been established, it is often possible to recognize the pattern if only a small part of it is visible in cloud free sections of an image. However, rapidly moving weather systems often cross the area creating confusing arrays of leads so some care is necessary in making such identifications.

The situation in the Beaufort Sea is much simpler. As described in MMS OCS STUDY 2005-068 and noted above (section 1.5), the deformation and lead patterns in the Beaufort Sea are mainly determined by the interaction of the pack ice with the coast or landfast ice edge along the North Slope. The predominant pack ice drift direction is to the west, and the infrequent shifts to the east or north are generally of small magnitude. As a result, with the exception of the Barrow Arch, the repeatable "patterns" described in MMS OCS STUDY 2005-068 are mainly leads of a particular shape, orientation relative to the coast, or clusters of leads originating a point. This contrasts with the patterns defined in the Chukchi Sea pack ice, which involve leads of different orientations dispersed over large areas.

4.2.4 Deformation patterns from westward displacement

The two most common deformation patterns reflect the prevailing northeast to east winds off the Alaska coast. The first pattern is associated with a generally southwestward displacement direction that is roughly parallel to the Alaska coast north of Point Hope and reflects the interaction of the drifting pack ice with the coastline ice. Its defining feature is an arcing lead or shear zone that extends northward from the coast of Chukotka east of Bering Strait and bounds a wide zone of broken floes between itself and the Alaska coast. The shape of the lead and its location suggest the name "West Coast Arc Lead (WCAL). The second of the two patterns reflects a more westward displacement direction. It is called here the “Open East” (OE) pattern to signify that the most obvious feature of the pattern is the area of thin ice and/or open water in the eastern Chukchi Sea off the Alaska Coast that was shown in Figure 4.2.3. A third pattern that reflects a westward displacement direction is expressed by leads close to the coast of Chukotka and westward drift from outer Kotzebue Sound is also described below. The name "Chukotka Parallel" (CP) denotes the sense of the displacement relative to the coastline in this pattern.

The WCAL and OE patterns are the most frequently visible of all patterns in the AVHRR imagery. This could reflect a bias in the data because, as noted above, the weather systems that bring the prevailing northeast to east winds that drive these patterns generally bring clear weather to the area. We note that there must be intervals of eastward pack ice displacement that bring the ice back against the Alaska coast.

The following subsections provide discussions of each patterns individually as well as a summary of the relationship relationship between these three patterns. The development of the WCAL will be discussed first because it is brings up several ideas and features that will enter into other descriptions.

4.2.4.1 West Coast Arc-Lead (WCAL)

The process of developing a WCAL pattern can occur over a few days, so the final shape and features of the pattern depend on the persistence of the driving system. However, for purposes of discussion it is useful to identify intermediate steps in the development of the pattern and there are enough examples available to give credence to the generalized description of the process presented here. Also, note that term "phases" is used as a device to facilitate the discussion aand doesn't necessarily imply that the various features always appear in order, or even appear at all depending on the duration of the process.

Phase 1: The result of the first series of events in forming a WCAL is shown in Figure 4.2.4. The Beaufort Sea pack ice has been displaced southward and tightened the ice cover in the Chukchi Sea by closing leads and compressing the ice against the coast of Chukotka. Concurrently, the pack ice along the coast southeast of Point Hope moved southward opening a lead along the coast, and ice started moving southward through Bering Strait. The latter is indicated by open water south of the Diomede Islands and by the curving leads, concave to the south, across the openings in Bering Strait. These leads are the first elements of a structure, called here the "Bering Strait Arch," which is visible in almost all examples of the WCAL pattern and occurs in other patterns as well. These are described and illustrated in subsequent sections.

Phase 2: Phase 2 is represented in Figure 4.2.5, which was acquired on the day following the image in Figure 4.2.4. In this example, the area north of Bering Strait is marked by a series of arcing leads, concave to the south, that terminate against two leads that trend north from near the east and west margins of Bering Strait. However, regardless of the lead or deformation pattern in that area, the processes create a stream of southward moving ice that appears to be funneled into the opening of the Strait. In the WCAL pattern, the eastern lead of the pair terminates southeast of the Point Hope either against the coast or in thin ice while the western lead continues to the north and becomes the arcing lead (the "WCAL") that gives the pattern its name. As the arcing lead extends, new leads form between it and the coast. Most are curved and concave to the south, and contribute to creating the zone of broken floes along the pack ice edge that was noted above as important habit for marine mammals.

Phase 3: Figure 4.2.6 shows the WCAL structure in the third day of the sequence following Figures 4.2.4 and 4.2.5. At its northern end, the WCAL structure often extends into the west limb of the Barrow Arch (Figure 5.2.7) or it can terminate at Hanna Shoal when the ice is grounded there (Figure 5.2.8). Occasionally, a lead extends to the west from the grounded ice on Hanna Shoal and develops into an arch structure. This structure, in turn, widens the zone of leads to include most of the eastern Chukchi Sea (Figure 4.2.9).

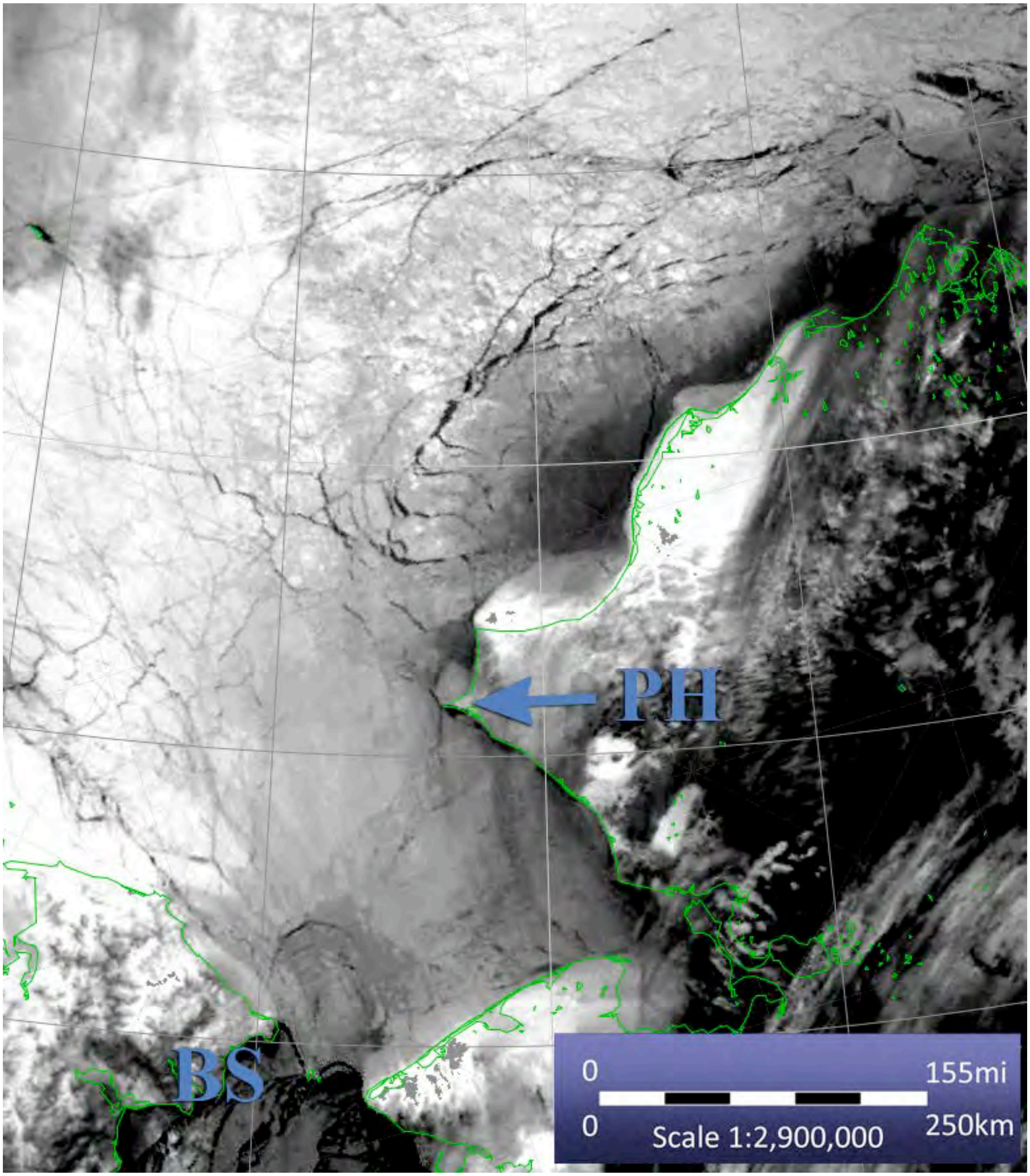

Figure 4.2.4. Eastern Chukchi Sea at the end of Phase 1 of forming a WCAL. Comparison with the image for the previous day shows that the "leads" shown as dark linear features are relics of an earlier deformation episode. The only new openings on this image are the two small arcs ("double arches" of Torgerson and Stringer, 1985) bridging the openings at Bering Strait (BS) and the thin dark band along the coast southeast of Point Hope (PH) which is the start of a coastal lead. (N14.97052; 21 Feb 1997)

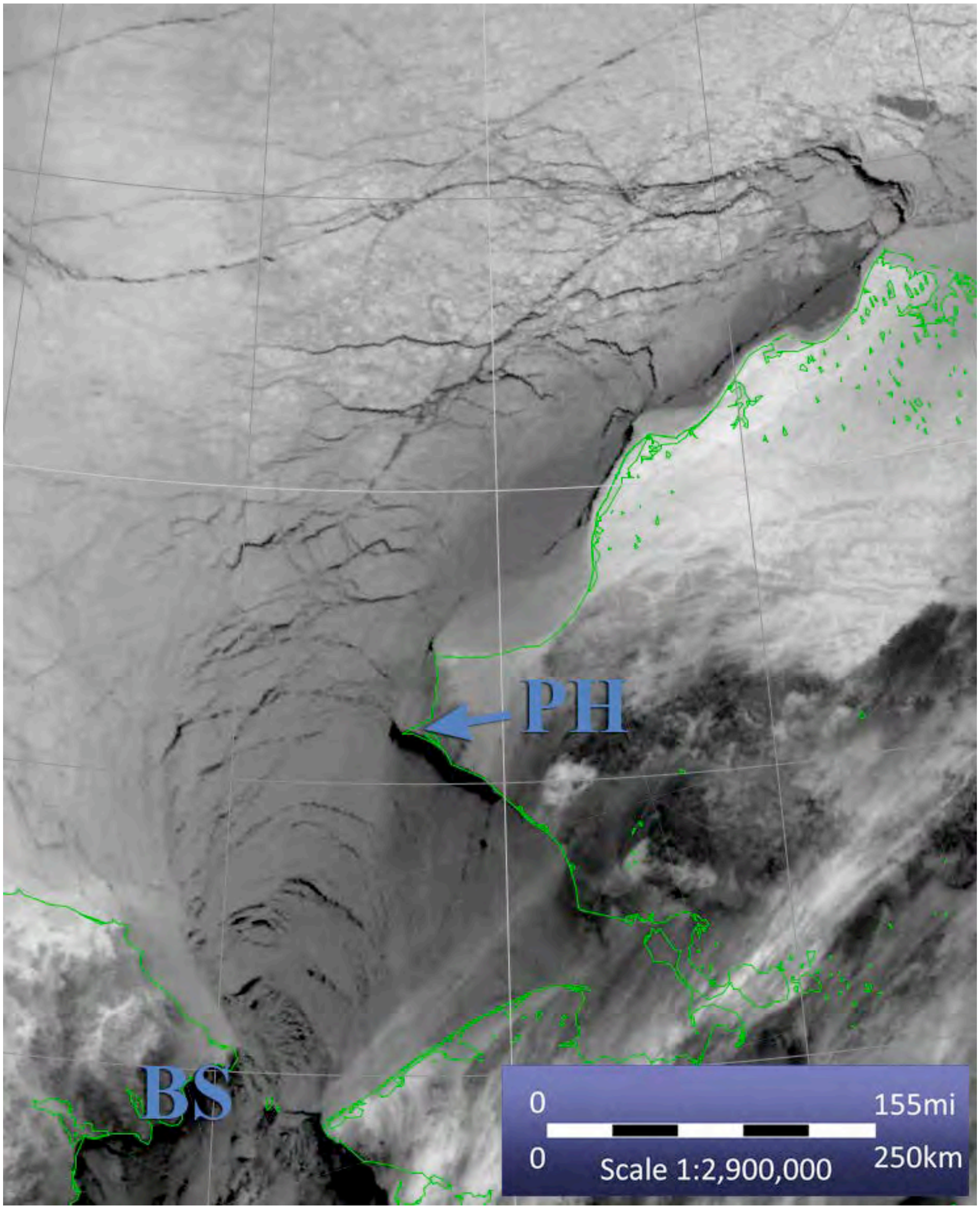

Figure 4.2.5. Eastern Chukchi Sea on the day following the scene in Figure 4.2.4 showing the end of phase 2. The zone of arc leads north of Bering Strait (BS) has extended, and the western ends of those leads are tangent to the zone that will become the WCAL proper. Note that the eastern ends of the arc leads appear to terminate at a less distinct boundary, and that the opening along the coast southeast of Point Hope (PH) has widened. (N14.97053.1352; 22 Feb 1997)

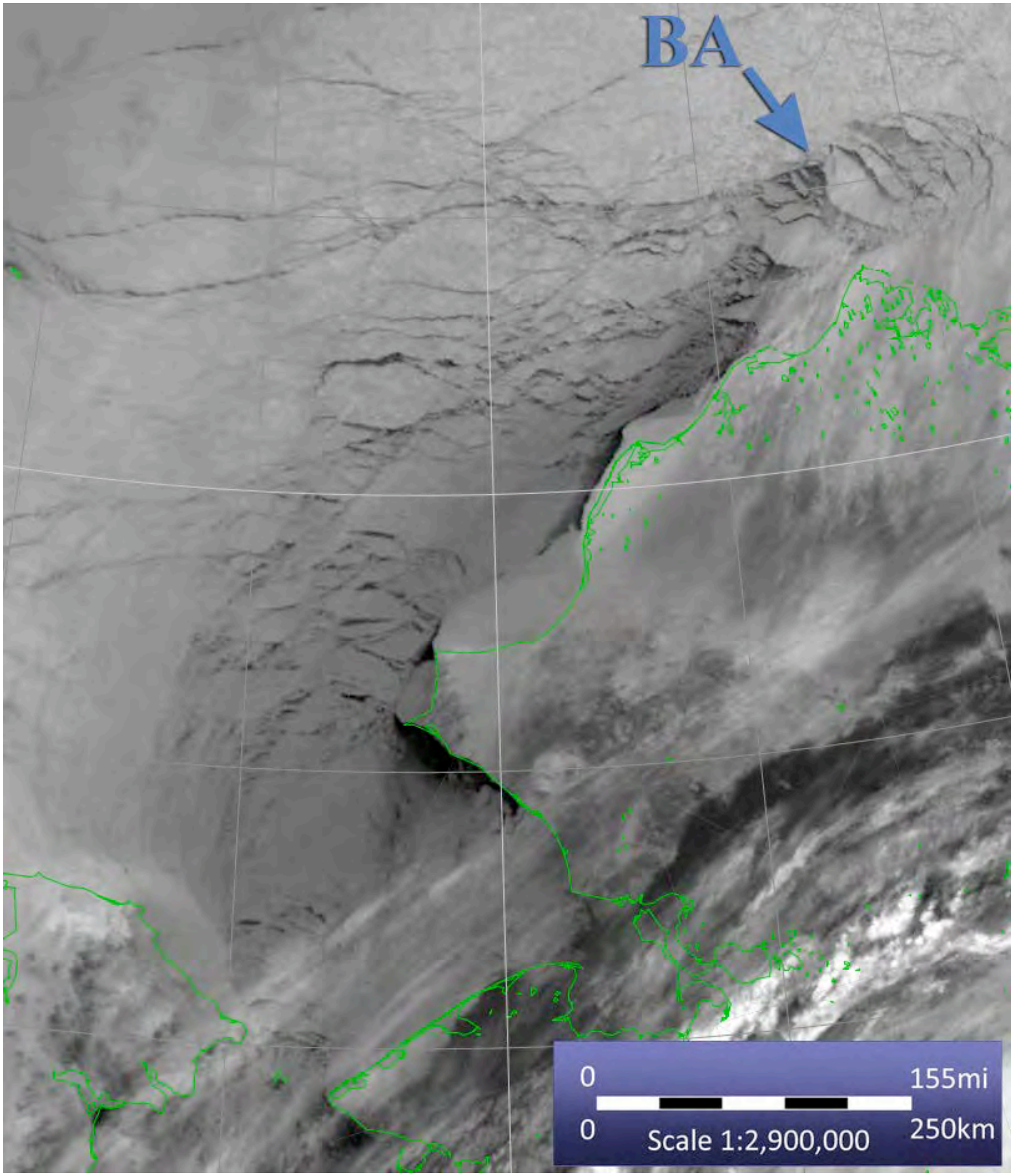

Figure 4.2.6 Eastern Chukchi Sea on the day following the scene in Figure 4.2.5. The WCAL has lost some definition, but can be identified by the change from relatively continuous pack ice in the west to broken ice closer to the coast. Note that the floes from the Barrow Arch (BA) are starting to move southwest along the Alaska coast. (N14.97054.1341; 23 Feb 1997)

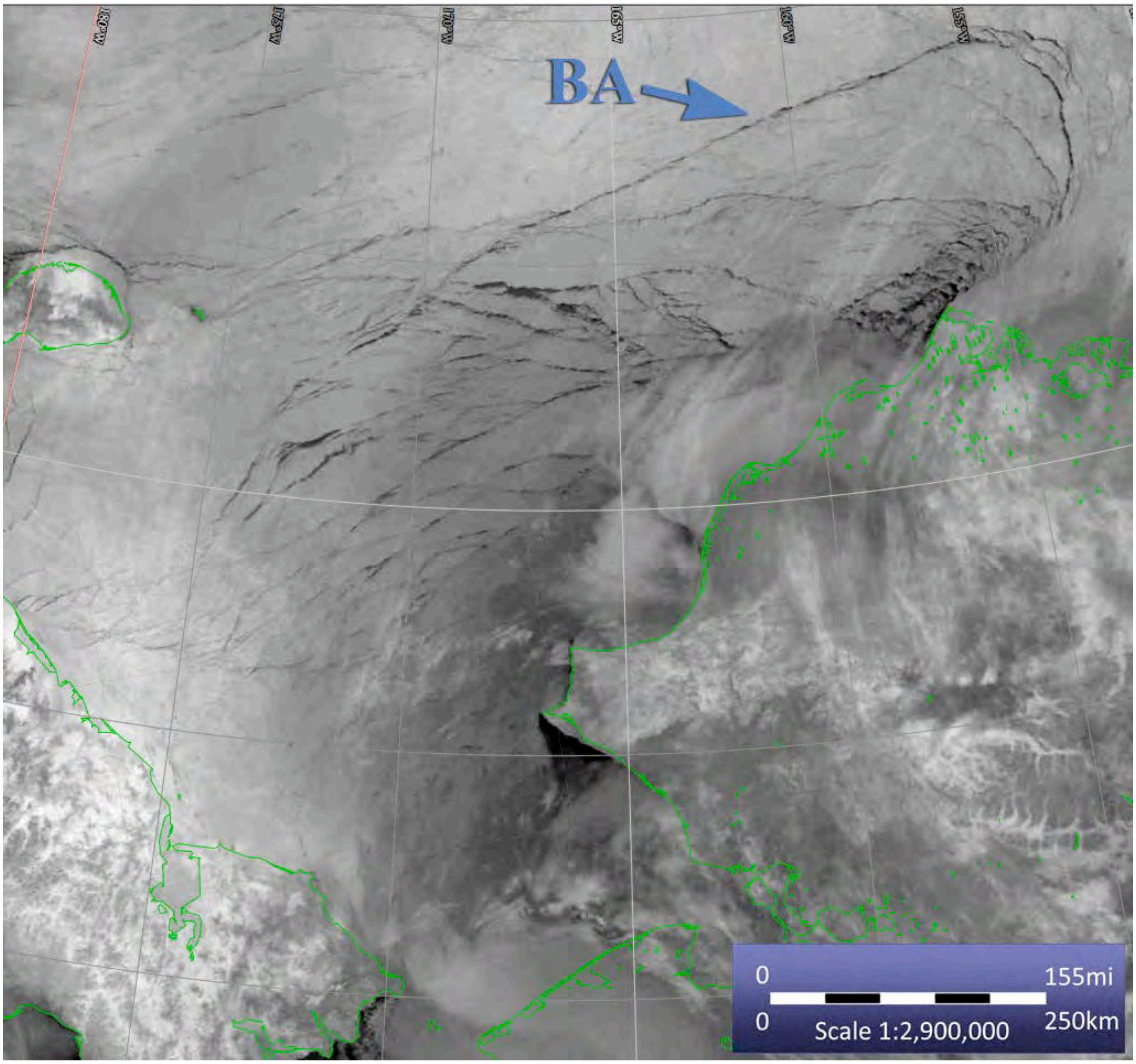

Figure 4.2.7. WCAL lead pattern before ice has grounded on Hanna Shoal. The Barrow Arch (BA) structure is wide and the lead that bounds its northwest side is long and straight trending to the southwest. Compare with Figures 4.2.8 and 4.2.9. (N18.07023.1447; 23 Jan 2007)

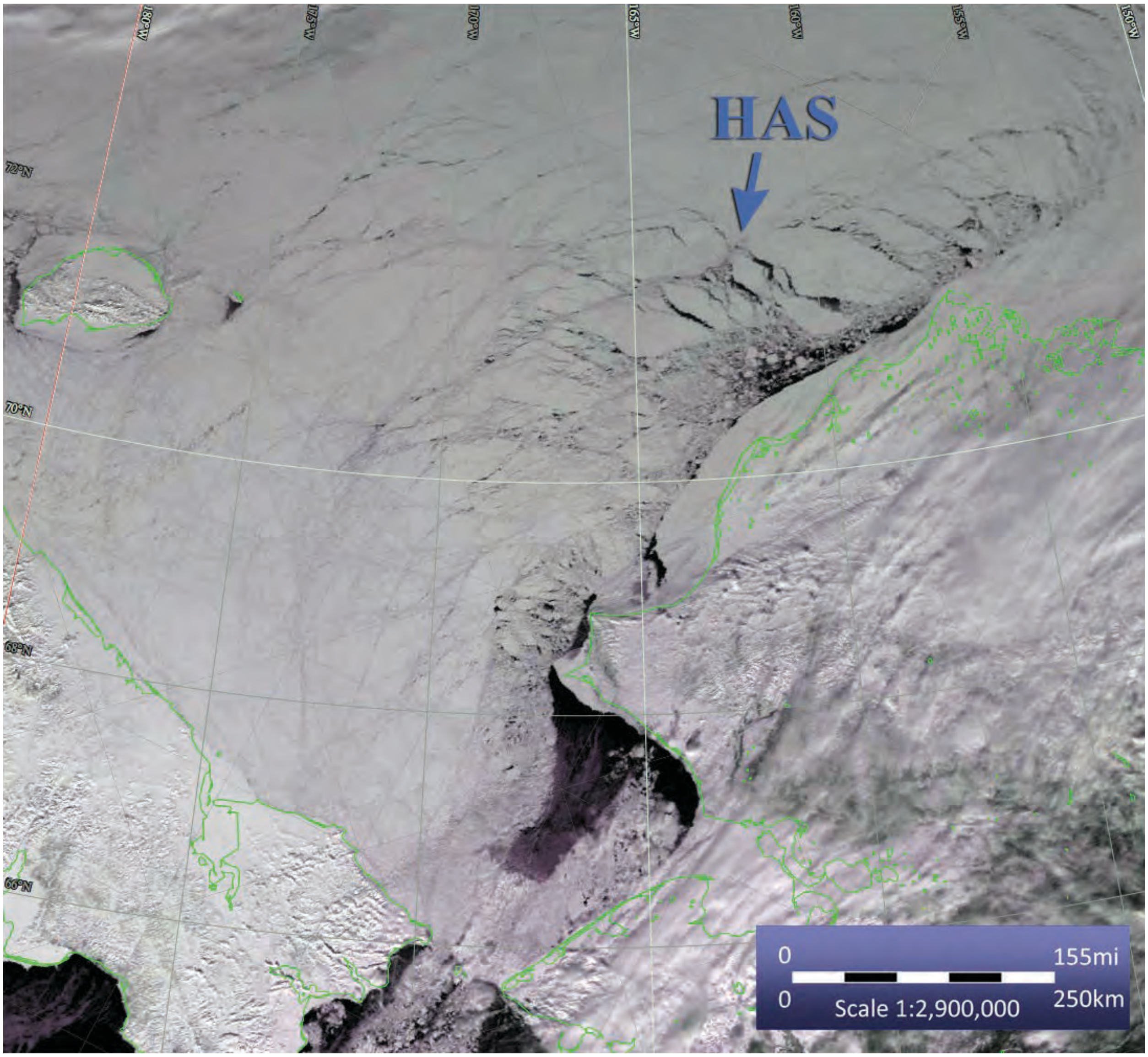

Figure 4.2.8. WCAL pattern after ice has grounded on Hanna Shoal (HAS). The Barrow Arch structure is narrower than in Figure 4.2.7 because the lead bounding the northwest side of the arch is directed to Hanna Shoal, where it terminates. Note the lead arcing to the northwest from the grounded ice. Compare to Figure 4.2.9 next. (N18.07099.2325; 09 Apr 2007)

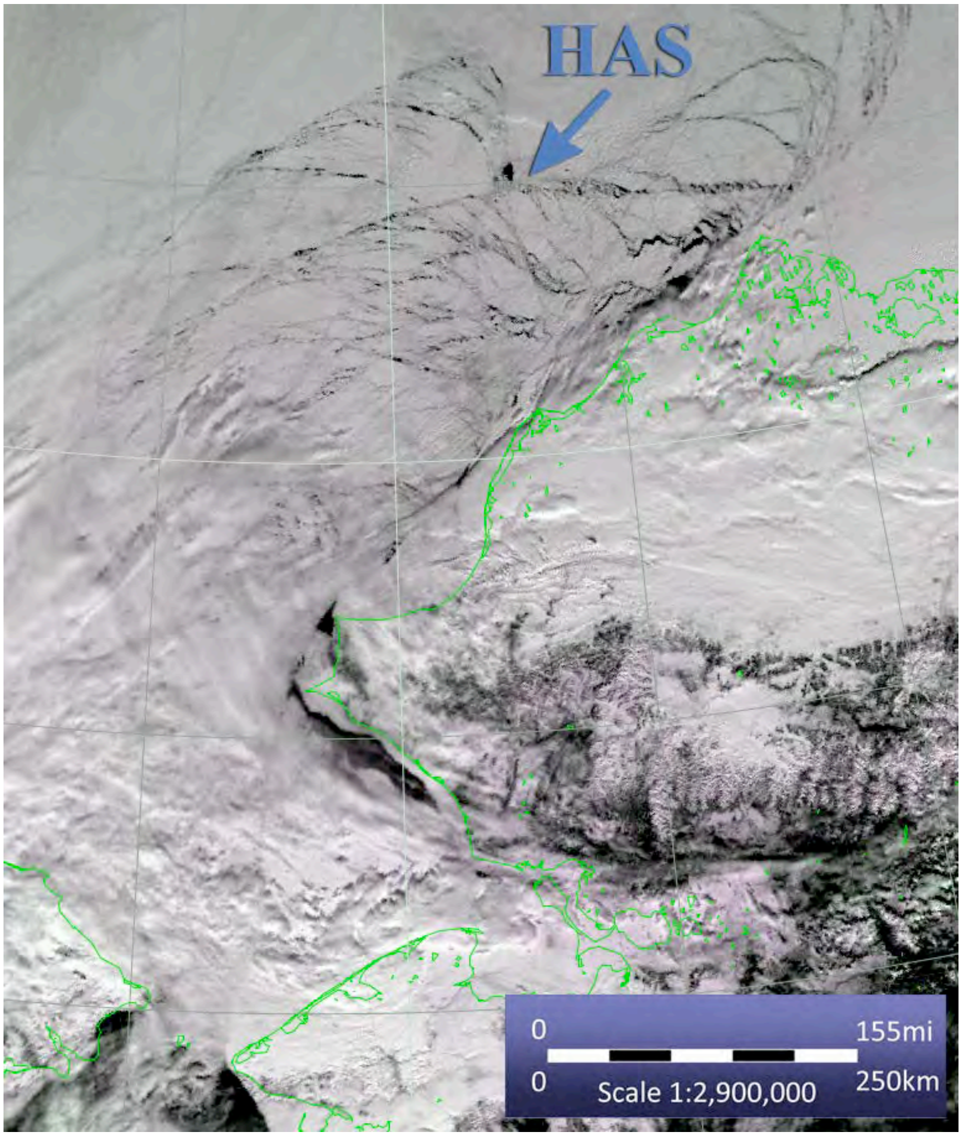

Figure 4.2.9. If the lead extending northwest from Hanna Shoal (HAS) in Figure 4.2.8 continues to extend, it may curve into an arch structure as shown in this figure. This has the effect of enlarging the area in which new leads can form in both the Chukchi and southern Beaufort Seas. (N18.06126.2239; 6 May 2006)

The WCAL shown in Figures 4.2.4 - 4.2.6 developed over a three to four day period. The question of how representative this is of the process in general is still open, but other examples of the pattern have been observed to remain in place for several days. During those times, the motion of the pack ice is probably roughly parallel to the Alaska coast and new leads continue to form inshore of the bounding arc lead zone. The floes that form then interact with each other and with the coast causing breaking and reduction of average floe sizes. The rapid change in size, shape and orientation of the floes makes it difficult to identify and follow any particular floe on the AVHRR images for more than a day or two. However, the orientation of the leads in the WCAL pattern suggests that displacement is generally southwestward along the coast when the pattern is active. The frequent intervals of displacement to the northwest in the buoy data from

Pritchard and Hanzlick (1988) and the floe displacement measurements in Norton and Graves (2004) probably occur during times when patterns other than the WCAL are active.

As the WCAL pattern develops, the pack ice remains tight against the coast of Chukotka where it occupies a dead space in the deformation field. This is shown by the general absence of leads in that area in Figures 4.2.4 - 4.2.8 (note that the area is cloud-covered in Figure 4.2.9). In fact, there are few other openings in the remainder of the Chukchi Sea pack ice during these times, except possibly on the west sides of Wrangel and Herald Islands, and Herald Shoal when ice is grounded there (Figure 4.2.8).

The process of developing the WCAL pattern can be idealized as leading to the flow of ice along the coast and exiting into the Bering Sea through Bering Strait. It resembles the flow of a granulated material moving in a chute formed by the arcing lead that bounds the pattern and the coast until it can exit into the gap between Point Hope and Chukotka. However, there are no data available on the cumulative southwestward drift of ice that could be used to estimate how much pack ice can move out of the Chukchi Sea in to the Bering Sea as a result of this process. Pritchard and Hanzlick (1988) described the motion of two buoys, deployed in what would be the area where WCAL patterns form, as moving back and forth over about 10 day intervals. The cumulative displacement of the buoys was about 200 km/month during the six months they were tracked, but the difference between the start and end points of the each track was less than 100 km. Shapiro and Burns (1975), used Landsat imagery to measure the daily southward displacement of floes in the Bering Strait area during a 3 day period of strong northerly winds. Displacements of more than 50 km/day were measured close to and into Bering Strait, but the magnitudes decreased rapidly with distance to the north.

These results would seem to indicate that there is only a small chance that ice originating in the central or northern Chukchi Sea would ever exit through Bering Strait.

4.2.4.2 Open East (OE) pattern and variations

The WCAL pattern apparently depends on the continuity of pack ice displacement to the southwest. However, a change to a more westward drift direction produces a new pattern in which the pack ice moves off the Alaska coast and leaves an expanse of open water and thin, new ice (Figure 4.2.10). The name "Open East" is adopted for this pattern. The displacements that create the pattern close or reorient many of the leads of the WCAL pattern and, occasionally, the ice in the bight between Cape Lisburne and Icy Cape is also involved and moves offshore.

The basic drift pattern associated with the OE is a partial clockwise rotation of the entire Chukchi Sea ice pack toward Chukotka and Wrangel Island (Figure 4.2.10). Initially, the displacement closes any openings along the southern or eastern coasts of Wrangel and Herald islands and as the pattern develops, openings form on the opposite coasts of those islands. When the pack ice converges to the west, a set of arcuate leads, concave to the northwest, forms between Wrangel Island and the coast of Chukotka indicating that the drift of the pack is to the northwest through the gap. The southern ends of these leads often terminate against a long lead or shear zone that is concave to the north and projects towards the area of Point Hope and Cape Lisburne (Figure 4.2.10). This lead or zone is tangent to the edge of the landfast ice, or to the coast if landfast ice is not present. However, it does not reach the Alaska coast, because it only forms when the pack ice is moving away from that coast. As the displacement to the west continues, the axis of the zone of arcuate leads tends to turn toward the east as shown in Figure 4.2.11 (which was acquired the day after the image in Figure 4.2.10). An example with the bounding lead tangent to the coast of Chukotka is shown in Figure 4.2.12.

In this configuration, the long, concave-north lead is a shear lead (or shear zone) that separates the west-drifting pack ice to the north, from the stationary wedge of ice along the coast of Chukotka to the south. It is also the southern boundary of the segment of the Chukchi Sea pack ice that rotates clockwise during these deformation episodes. Its appearance under different ice conditions is shown in Figures 4.2.13 - 4.2.15, which illustrate the repeatability of the OE pattern throughout the ice year. Figure 4.2.13 is a late spring scene in which the pack ice is in the process of breaking up. There is open space northwest of Wrangel Island so the spaces between the arc leads between Wrangel Island and the mainland are open and filled with loose floes. In contrast, Figure 4.2.14 is an early winter scene and suggests that the bounding lead forms before the arc leads between Wrangel Island and the mainland. Finally, Figure 4.2.15 shows the Chukchi Sea pack ice late enough in the year to have been reduced to "spring ice" consisting of discrete floes so that leads, as fractures, can no longer form in it. However, the bounding "lead" is still visible as a discontinuity in the field of moving floes. The role of the bounding lead can therefore be considered as analogous to a shear zone in a two-dimensional flow field of a plastic material. Examples are shown in analyses of the deformation of materials during die-casting and deformation of fields of loose aggregates.

Note that in some years ice grounds on a shoal northwest of Wrangel Island that constrains the form of openings in that area to a roughly triangular shape (Figure 4.2.16) in which the legs appear to be bounded by shear zones.

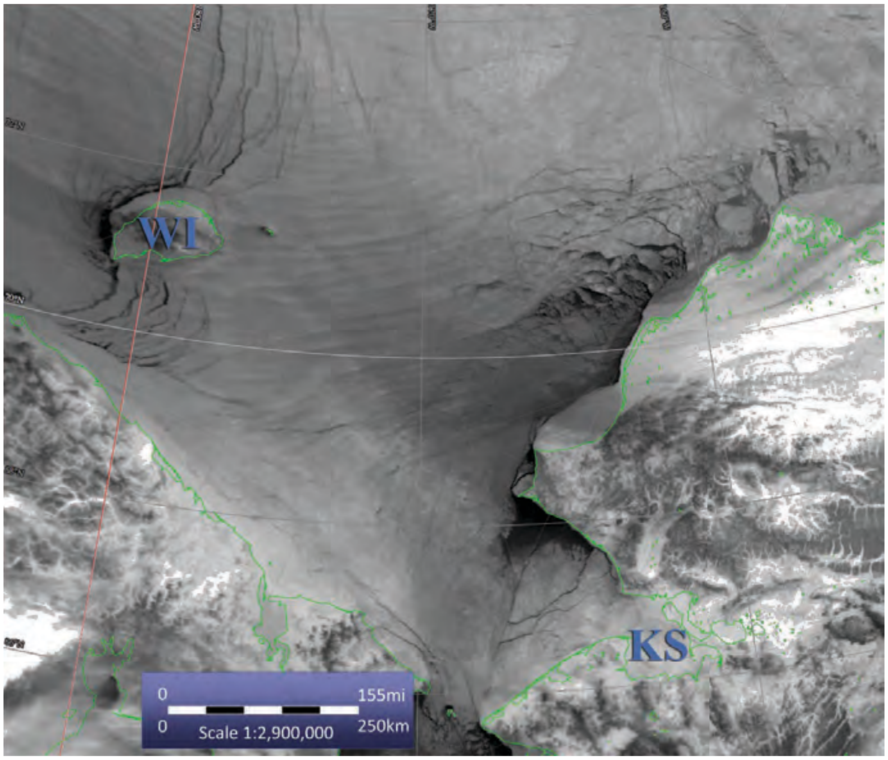

Figure 4.2.10. General westward shift of Chukchi Sea pack ice, opening the Alaska Coast. Note the leads crossing the ice in outer Kotzebue Sound (KS) and the boundary where the arc leads between Wrangel Island (WI) and Chukotka terminate. The boundary is offshore from the edge of the landfast ice and is visible projecting toward the east. It separates the moving pack ice to the north from a stationary wedge to the south. In this image, the distribution and shape of the clouds mimics the clockwise rotation of the pack ice noted in the text. (N14.97061.1405; 02 Mar 1997)

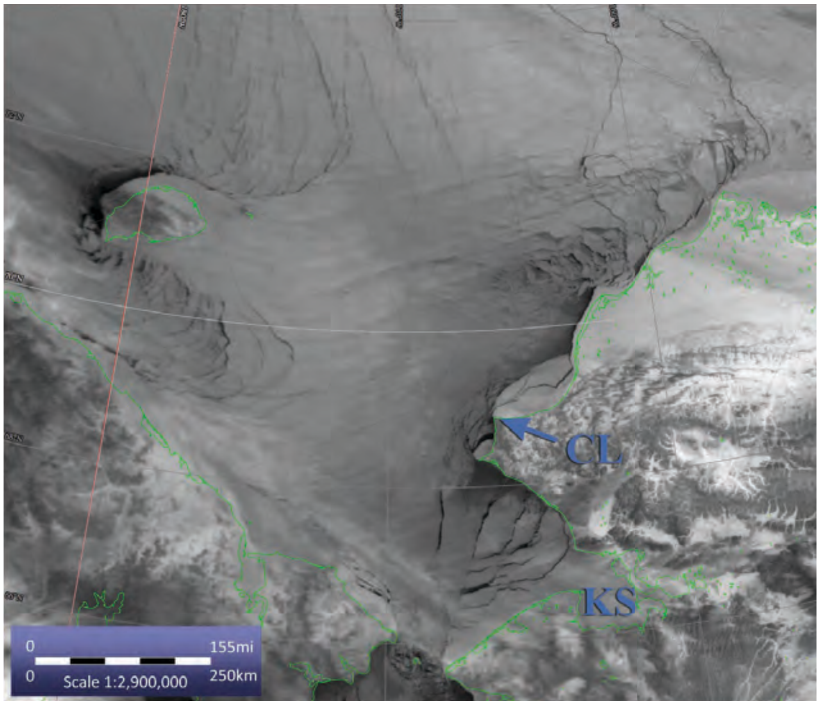

Figure 4.2.11 Lead pattern on the day after the image shown in Figure 4.2.10 was acquired. Note that the axis of the zone of arcing leads and the boundary have extended and turned further to the east. There are also new leads in outer Kotzebue Sound (KS) that show the ice is diverging to the west, and the new leads in the bight north of Cape Lisburne (CL) indicate that the ice in that area is unstable. (N14.97062.1354; 03 March 1997)

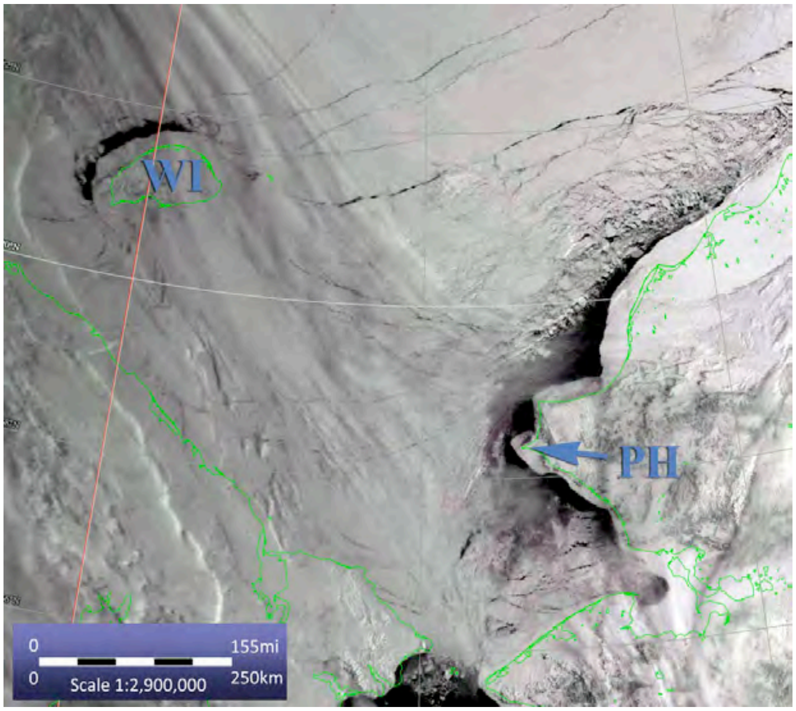

Figure 4.2.12 Arcuate leads between Wrangel Island (WI) and the coast of Chukotka. The leads are tangent to the coast near the origin of the arcuate lead that trends towards the area of Point Hope. (N12.96119.1845; 28 Apr 1996)

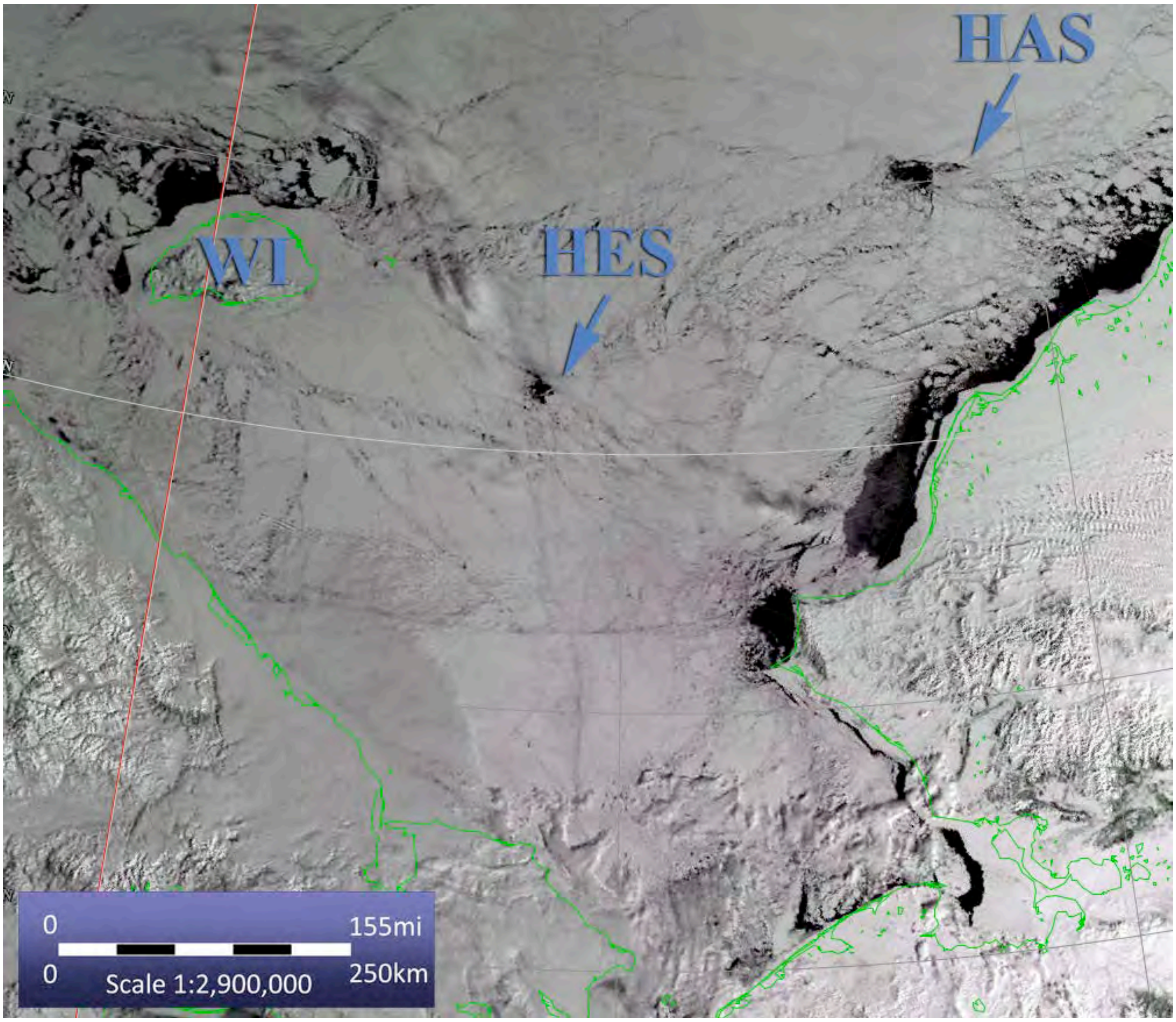

Figure 4.2.13 Example of the pattern in Figures 4.2.10 - 4.2.12 but early in the break up process. Pack ice is deteriorating and moving through the gap between Wrangel Island (WI) and Chukotka. Note the possible evidence of a left-lateral offset across the long, curving lead, as indicated by the mismatch of the refrozen leads that cross it. Dark areas in the pack ice east of Wrangel Island and in the northeast corner of the image are open areas around Herald Shoal (HES) and Hanna Shoal (HAS) respectively. (N15.01108.1955; 18 Apr 2001)

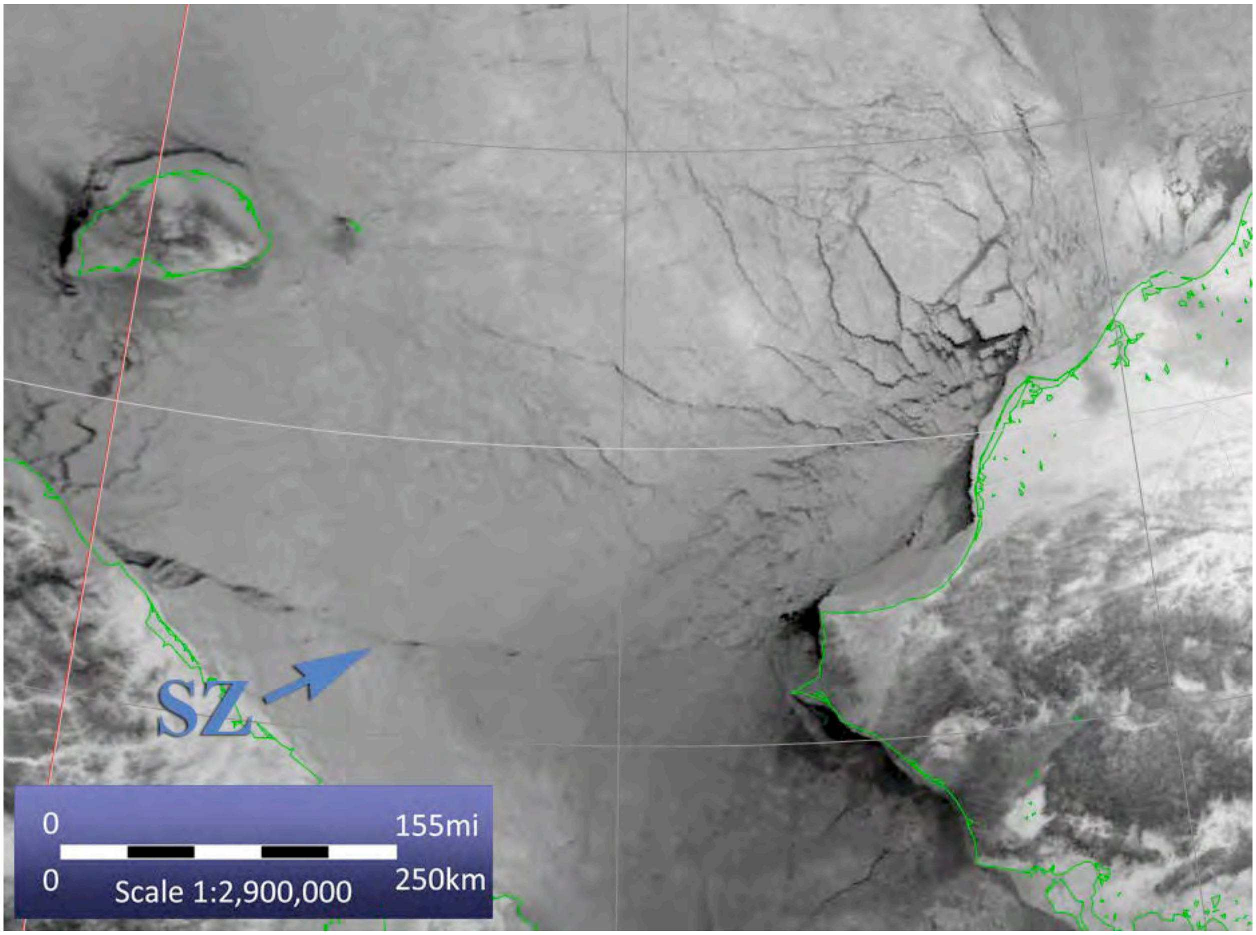

Figure 4.2.14 The arcuate shear zone (SZ) early in the process of westward displacement of the pack ice. The sequence of scenes around this date shows that the Chukchi Sea pack ice was rotating clockwise so as to move it parallel to the shear zone. (N16.05027.1422; 27 Jan 2005)

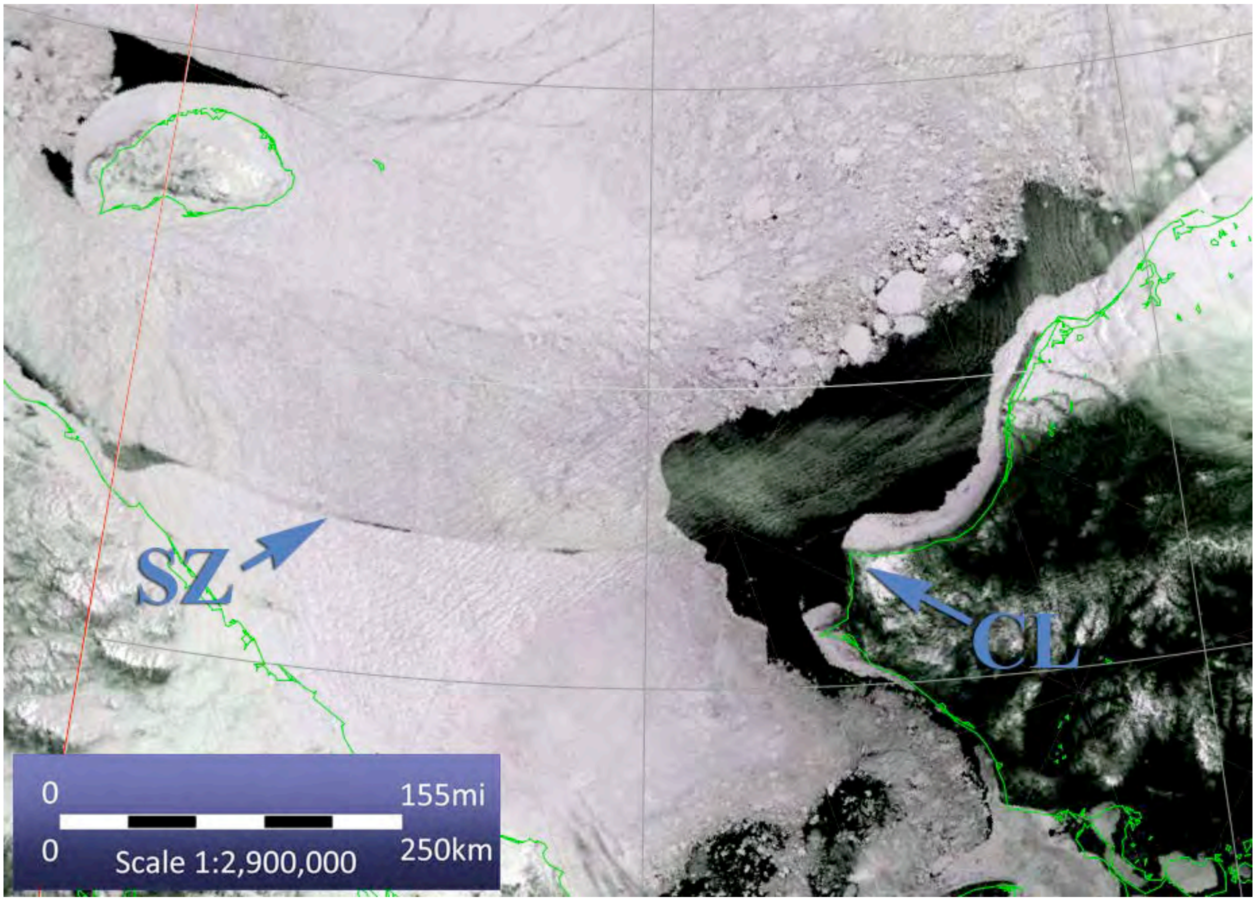

Figure 4.2.15 In this scene, the pack ice has deteriorated into "spring ice" so that it is an aggregate of discrete floes, rather than a continuous ice sheet. The shear zone (SZ) from the coast of Chukotka toward Cape Lisburne is then a discontinuity in the deformation field of the aggregate as described in the text. (N12.95142.1929; 22 May 1995)

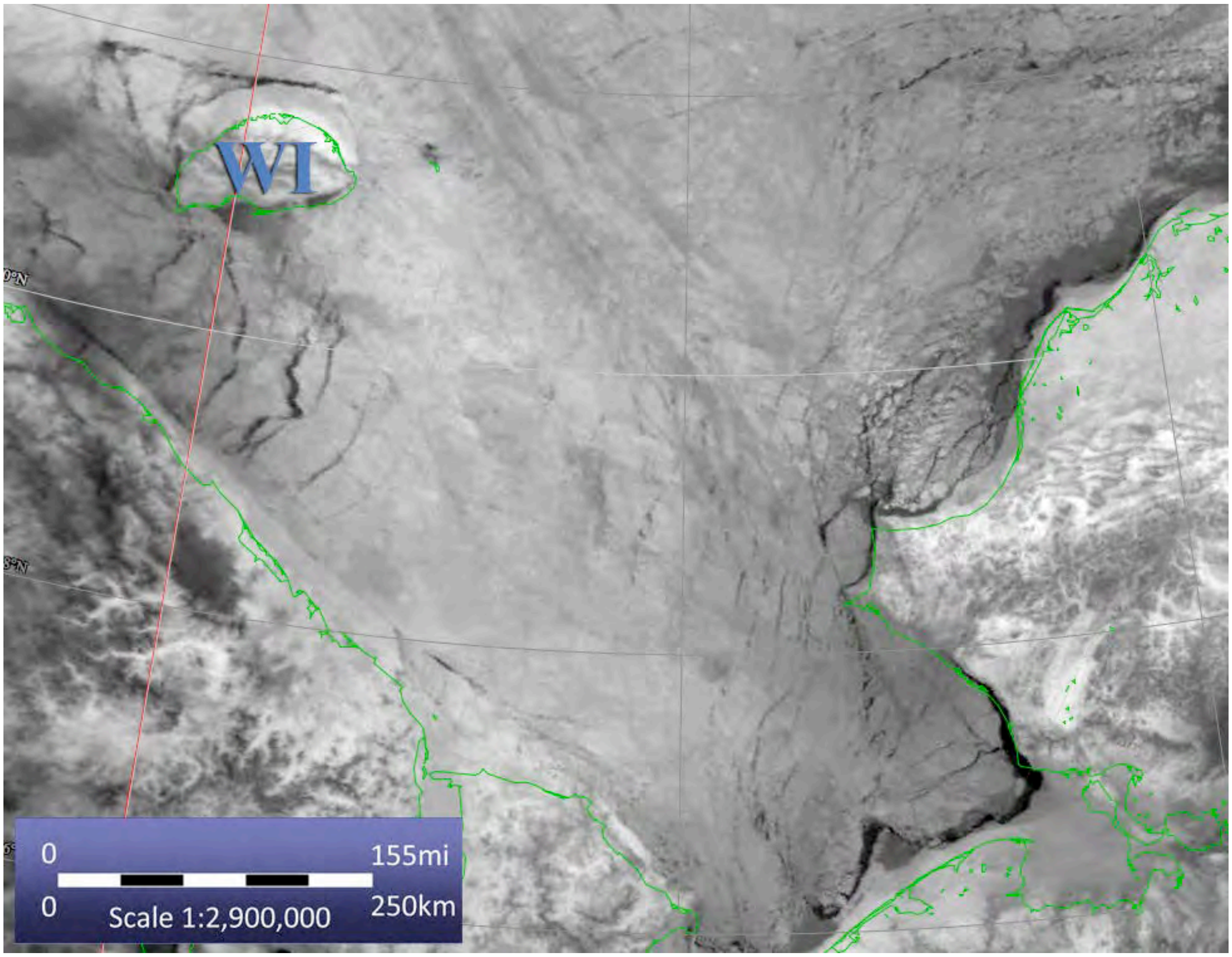

Figure 4.2.16. Grounded ice mass northwest of Wrangel Island (WI) shown early in an episode of general westward pack ice displacement. The ice in the triangular-shaped area is held in place by the grounded ice, while shear zones form along the westerly-trending edges of the triangle. (N12.02028.1643; 28 Jan 2002)

4.2.4.3 Chukotka Parallel (CP)

A relatively small change of the displacement direction to a more northwestward direction produces a variation of the OE deformation pattern called here the Chukotka Parallel (CP) pattern. An example is shown in Figure 4.2.17. The pack ice drifts off the Alaska coast, but in a more northwestward direction than in the OE, and the opening on the northwest side of Wrangel Island is also present. In the southern Chukchi Sea the displacement is also to the northwest, nearly parallel to the coast of Chukotka. Displacement in that direction creates openings along the fast ice edge on the northwest side of promontories, and leads appear in the ice cover in outer Kotzebue Sound as the pack ice in that area displaces to the northwest.

Arc leads concave to the northwest are present in the gap between Wrangel Island and the mainland. Their shoreward ends terminate against the landfast ice edge, and their seaward ends appear to merge into a shear boundary that trends roughly sub-parallel to the coast of Chukotka. There is a similarly oriented shear zone extending a short distance southeastward from Herald Island, as shown by the change from continuous pack ice on the south to broken floes north of the zone. These two apparent shear zones define the boundaries of a segment of the pack ice that is being pushed against the southeast coast of Wrangel Island and into the gap between Wrangel and Herald Islands. The arc lead between the islands is a result a result of that forcing mechanism.

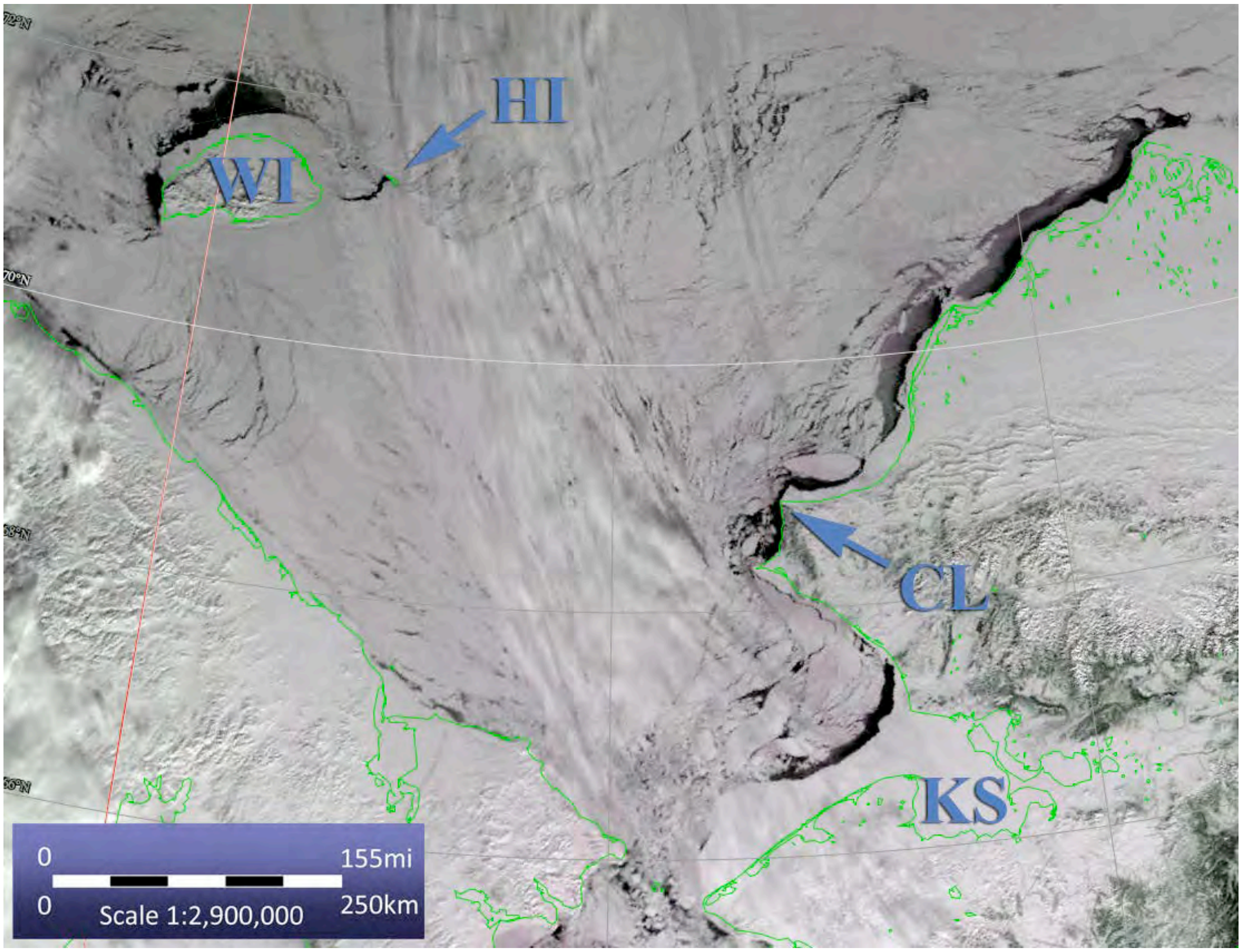

Figure 4.2.17. Northwest displacement parallel to the coast of Chukotka. The sense of displacement is indicated by (1) the arcs which are concave to the gap between Wrangel Island (WI) and Chukotka, and between WI and Herald Island (HI) (2) the opening on the northwest side of WI, (3) the pack ice moving out of Kotzebue Sound (KS) and (4) pack ice is displacing away from the coast of Alaska in a northwestward sense, rather than westward as it was when Figures 4.2.10 - 4.2.16 above were acquired. Note that the ice sheet moving out of the bight north of Cape Lisburne (CL) is rotating clockwise, following the same sense of motion. For reference, this image was acquired 2 days prior to the one shown in Figure 4.2.3. (N19.10080.2229; 21 Mar 2010)

4.2.4.4 Summary of patterns resulting from westward pack ice displacements

It is interesting to note that the three patterns described here reflect only minor changes in the displacement directions so it is reasonable to look for a relationship between them. A possibility follows from the idea that a large, high-pressure system crossing the area could produce surface winds that swing from the north through northeast, east and southeast across the Chukchi Sea. That progressive change of wind directions would generate the sequence of patterns from WCAL to OE to SP and, in fact, the complete sequence was once observed during this study to occur during a few cloud free days. However, examples of a direct change from WCAL to SP, reverses in the sequence, and changes to patterns reflecting winds from other directions were also noted. As a result, while some regularity in this sequence of patterns is possible, the actual events do not necessarily follow in order.

Another point of interest is that in both the OE and SP patterns, some of the pack ice drifts to the northwest out of the Chukchi Sea. Thus, as noted in the Final Environmental Impact Statement for lease sale 193, in the event that oil might be trapped in the Chukchi Sea pack ice, these patterns would be responsible for moving it into the Beaufort Sea. However, note that the limited buoy data available in the literature [Colony (1979), Pritchard (1979), Pritchard and Hanzlick (1988)] suggest that buoys deployed north of the boundary between the Chukchi and Beaufort Seas in winter are likely to track to the west and northwest as predicted by the rotation of the Beaufort Gyre. However, buoys deployed south of the boundary in winter tend to stay in the Chukchi Sea until Spring when they drift northwest into the Beaufort Sea. This implies that the boundary is a real barrier to northward transport of ice during winter, which may be significant in the event that it is necessary to follow the path of oil entrapped in ice.

Above, we noted that there must be intervals of easterward ice motion that close the coastal lead systems that characterize the WCAL and OE patterns. The repeated opening and closing of the pack ice against the Alaska coast and the frequent shifts parallel to the coast combine to continuously create new leads in the near shore area. As a result, even when the pack ice is close to the coast, there is often a zone of broken ice that extends at least a few tens of kilometers offshore. This zone is important as habitat because, on a large scale, it almost always provides openings that marine mammals use for migration and access to the ice surface.

4.2.5 Southeast Shift Along the Coast of Chukotka (SE)

There is a generally short-lived pattern that occurs with some frequency (designated here as SE), in which the pack ice along the coast of Chukotka shifts to the southeast. The displacement may be restricted to the pack ice south of an east-west lead that sometimes forms across the Chukchi Sea pack ice and connects Herald Island with the coast of Alaska in the area of Point Hope/Cape Lisburne. If the lead is present then there will probably be no new leads to the north because the pack ice in the eastern Chukchi Sea is converging against the Alaska coast.

Three examples of this pattern are shown in Figures 4.2.18 - 4.2.20. Note that the Bering Strait Arch structure formed in all three examples, but the axis of the structure turned to the northwest. This, again, is typical of the way the arch structure extends by growing into the direction of the advancing pack ice. The figures also show that in this pattern the pack ice moves off the southeast coasts of Wrangel and Herald Islands, and arcuate leads, concave to the southeast, may be present between the islands and between Chukotka and Wrangel Island. In addition, a small, east-facing arch structure sometimes forms on the south side of the tip of Point Hope with the broken floes drifting southeastward along the coast.

In Figures 4.2.18 and 4.2.20, there are prominent leads extending northwestward across the Chukchi Sea from Cape Lisburne toward Herald and Wrangel Islands, but there is no such lead in Figure 4.2.19. Also, at the time the image in Figure 4.2.18 was acquired, ice was grounded on Herald Shoal, which apparently had some influence on the lead crossing the Chukchi Sea, but there was no ice grounded on the shoal when the image in Figure 4.2.20 was acquired. These observations point out the difficulty of identifying details of cause and effect relationships between the patterns and their environment.

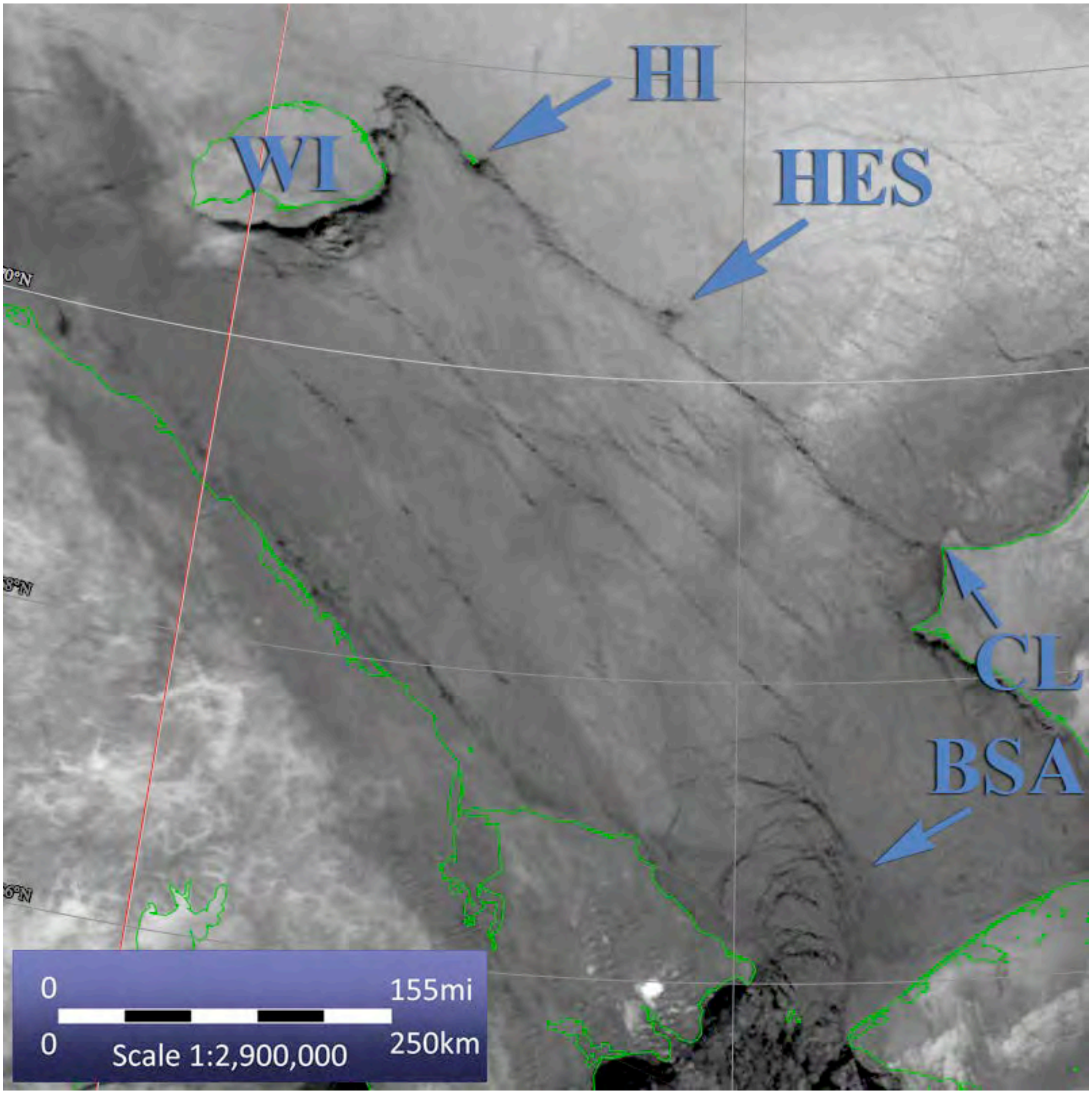

Figure 4.2.18. Start of an episode of southeast displacement in the southern Chukchi Sea. Note that the lead connecting Herald Island (HI) and Cape Lisburne (CL) probably also intersects the grounded ice on Herald Shoal (HES). However, this can't be verified since the boundary of the grounded ice on the shoal cannot be determined from this image. The lead creates a discontinuity between the pack ice southwest of the lead and the remainder of the pack ice to the northeast. The Bering Strait Arch (BSA) structure has formed and its axis is orienting into the direction of the approaching pack ice. It is likely that the entire Chukchi Sea pack ice is closing against the Alaska coast to the north of the lead, but the part south of the lead is less constrained and can displace further. This is suggested by the opening on the southeast coast of Wrangel Island (WI). (N12.97090.1350; 30 March 1997)

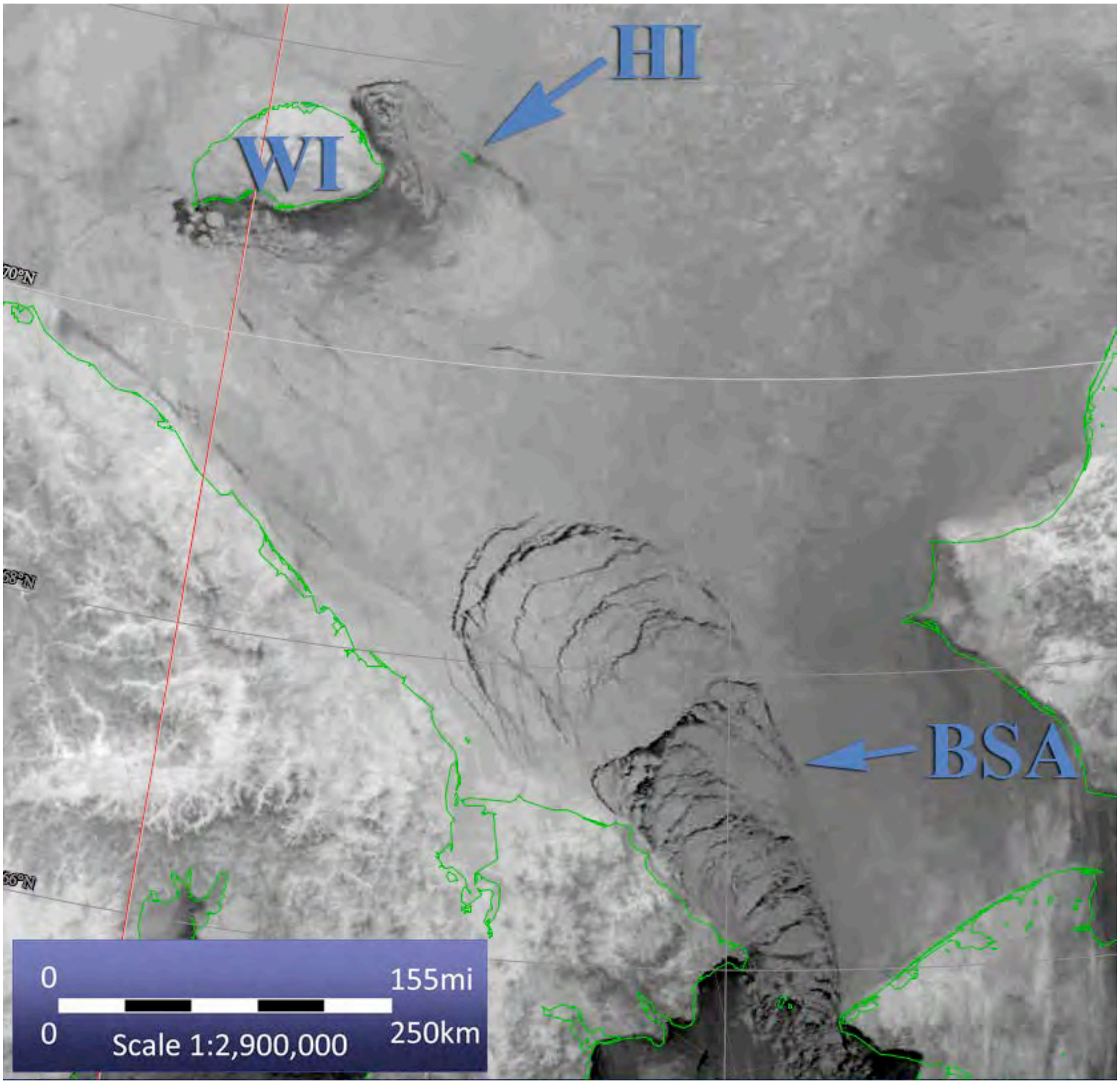

Figure 4.2.19. Southeast displacement along the coast of Chukotka when there is no ice grounded on Herald Shoal and no leads crossing the Chukchi Sea. Note the curvature of the Bering Strait Arch (BSA) structure into the approaching pack ice. Also, note the absence of openings in the pack ice over most of the area except the southeast coast of Wrangel Island and the arc leads between Wrangel Island (WI) and Herald Island (HI) as in Figure 4.2.18. Also, as in Figure 4.2.18, there is differential displacement to the southeast between the northern and southern segments of the pack ice However, there is no clear indication of the mechanisms involved. (N19.10020.1422; 20 Jan 2010)

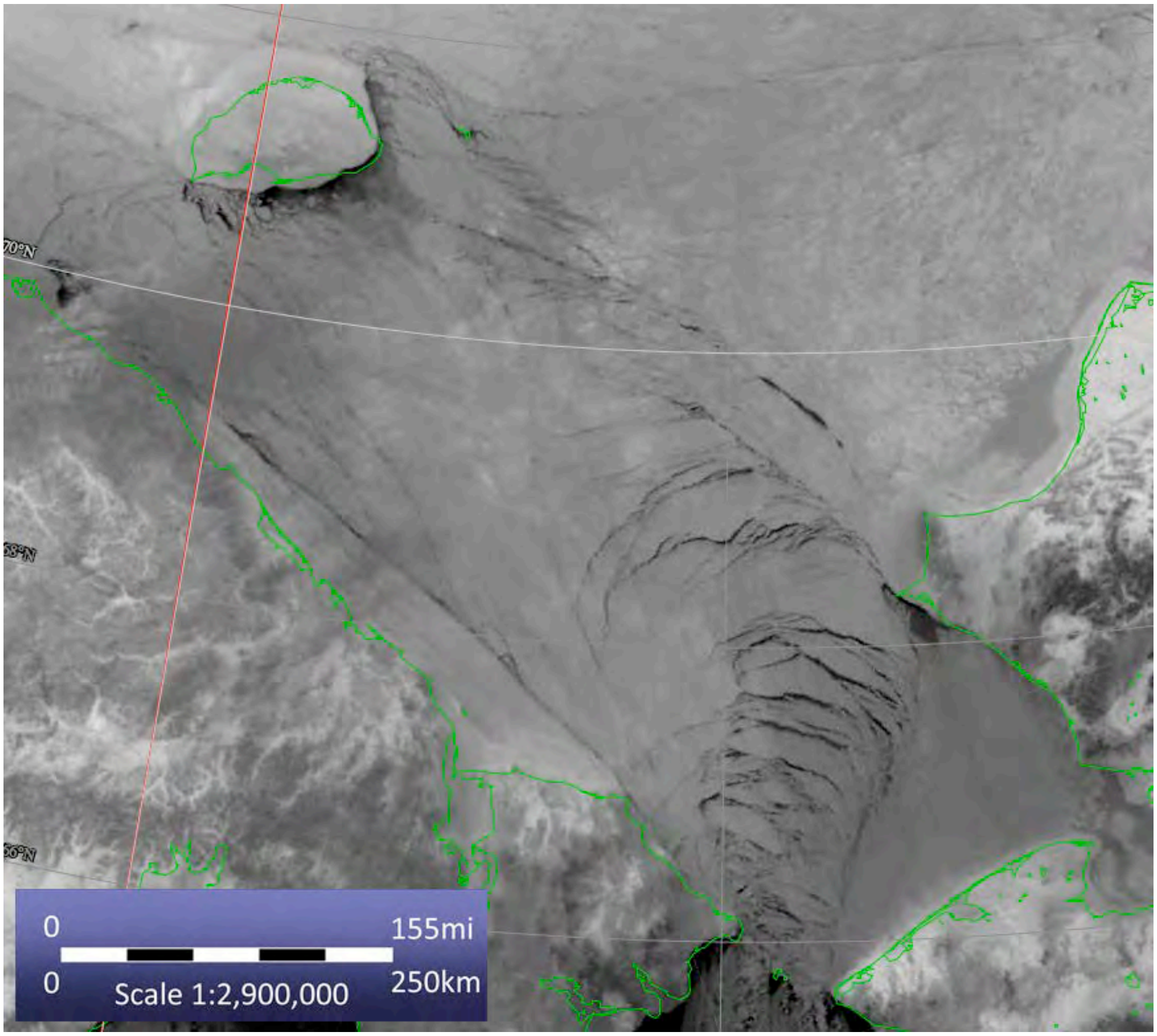

Figure 4.2.20. Southeast displacement along the coast of Chukotka after development of a lead system similar to that in Figure 4.2.18, but in the absence of ice grounded on Herald Shoal. In this case, the discontinuity is created by the differential ice displacement across the lead system as dictated by the geometry of the surrounding rigid boundaries. Note that in Figures 4.2.19, the Bering Strait arch structure curves to face the direction of the approaching pack ice and there are no apparent openings in the pack ice northeast of the lead zone so it is probably compressing against the Alaska coast. (N14.95030.1422; 30 Jan 1995)

4.2.6 Chukchi Straight South (SS)

In the Chukchi Straight South pattern the Chukchi Sea pack ice is displaced essentially straight to the south, and the axis of the Bering Strait Arch is directed to the north into the dominant displacement direction. Nested arc leads, concave to the south, may cross most of the width of the Chukchi Sea (Figures 4.2.21 and 4.2.22). However, a variation on this pattern was found in which the arch structure extends north of the latitude of Cape Lisburne, but there are no leads visible in the pack ice further north (Figure 4.2.23). In fact, the only openings in the Chukchi Sea visible in that figure are a narrow polynya along the coast southeast of Point Hope, and on the south-facing coasts of Wrangel and Herald Islands. That degree of continuity in the Chukchi Sea pack ice is rare.

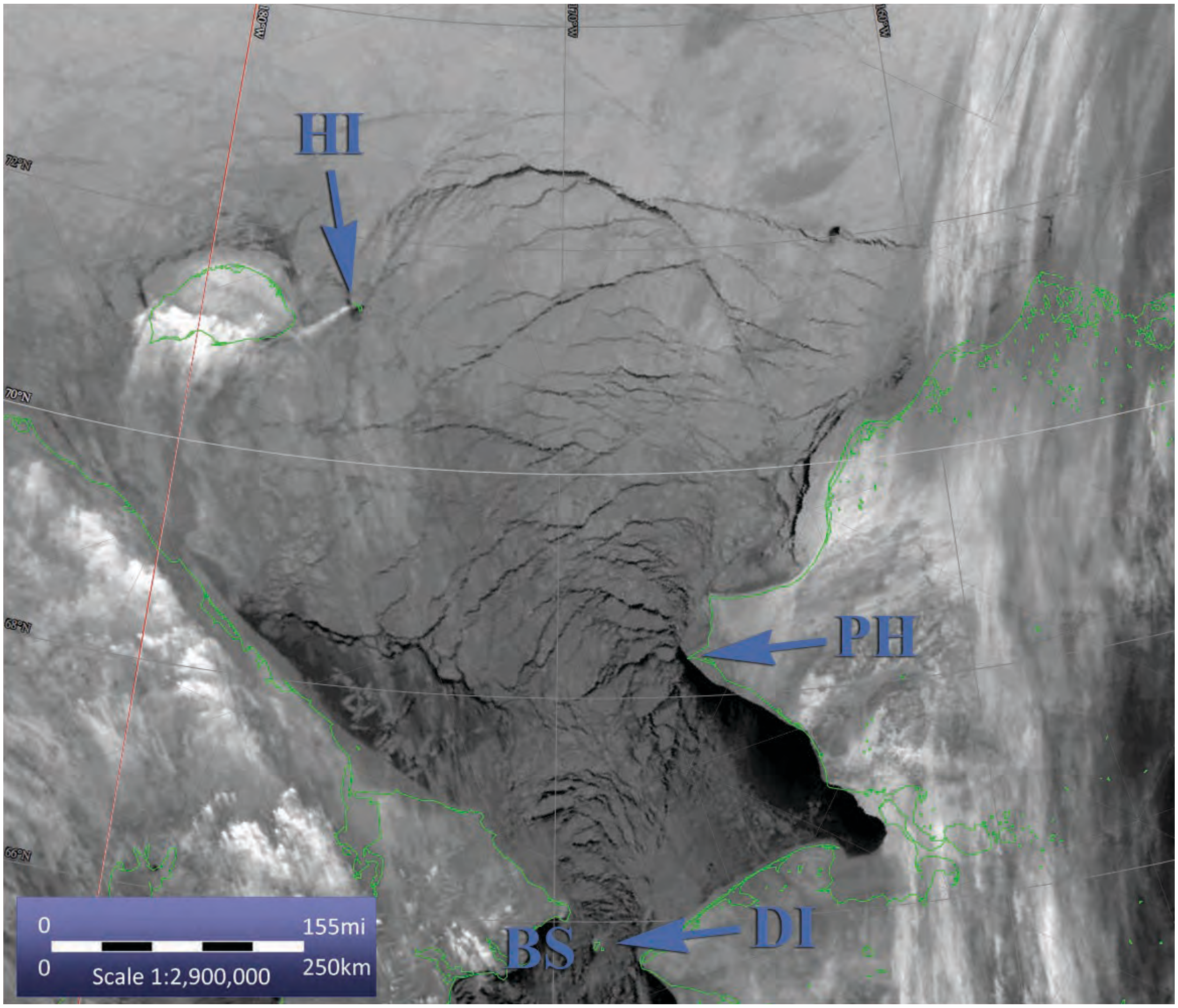

Figure 4.2.21. Example of straight southward movement of the Chukchi Sea pack ice with wide arcing, leads concave to the south crossing from Herald Island (HI) to the east. Note that the opening extending southward from the Diomede Islands (DI), the expanse of open water or thin ice off the coast southeast of Point Hope (PH), and the leads arcing from Point Hope all indicate that the entire Chukchi Sea pack ice south of the leads from Herald Island is displacing to the south toward Bering Strait (BS). (N14.96096.1350; 5 Apr 1996).

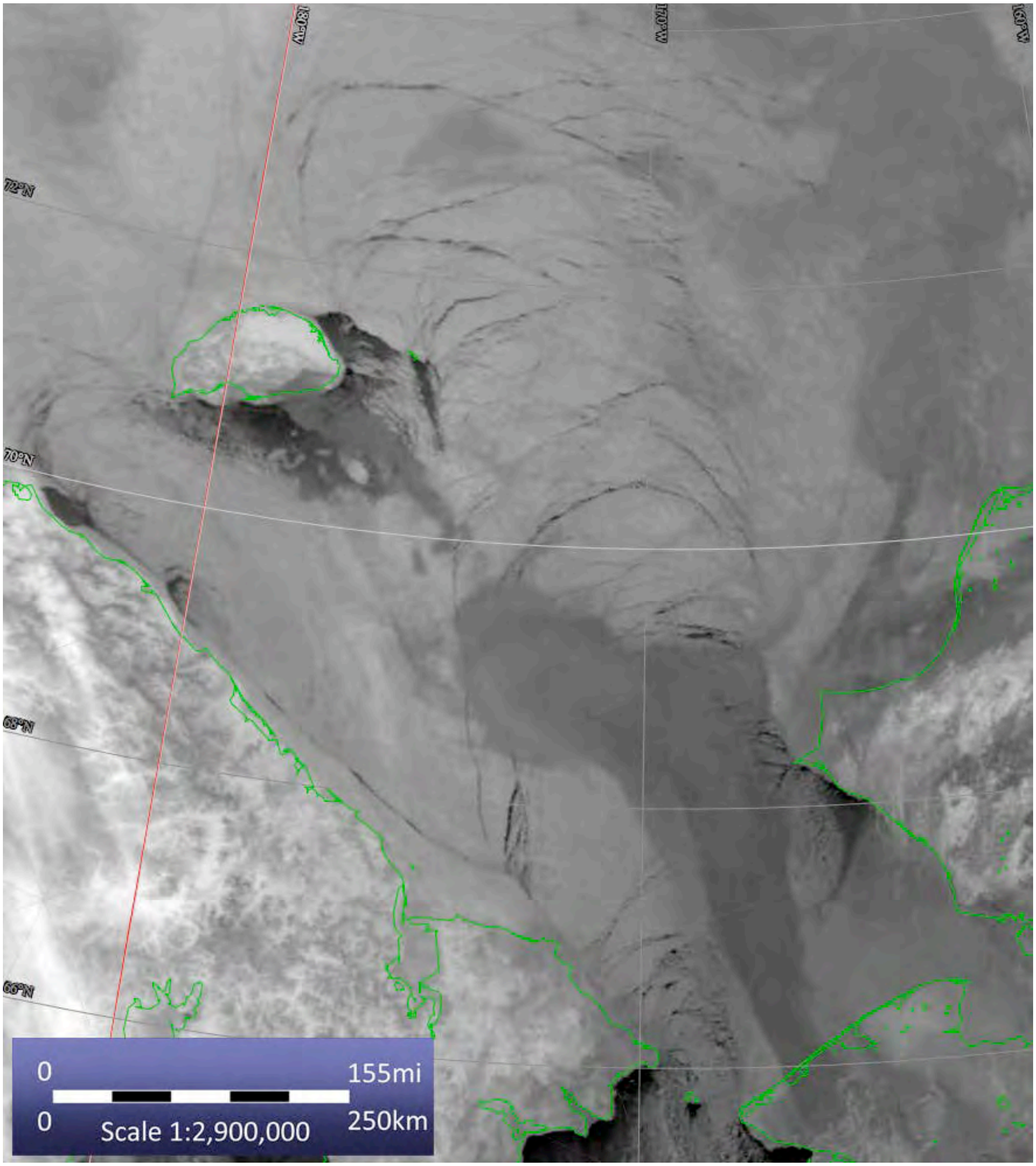

Figure 4.2.22. Another example of the southward displacement of the Chukchi Sea pack ice indicated by the pattern of concave southward arcing leads. (N12.00010.1722; 10 Jan 2000)

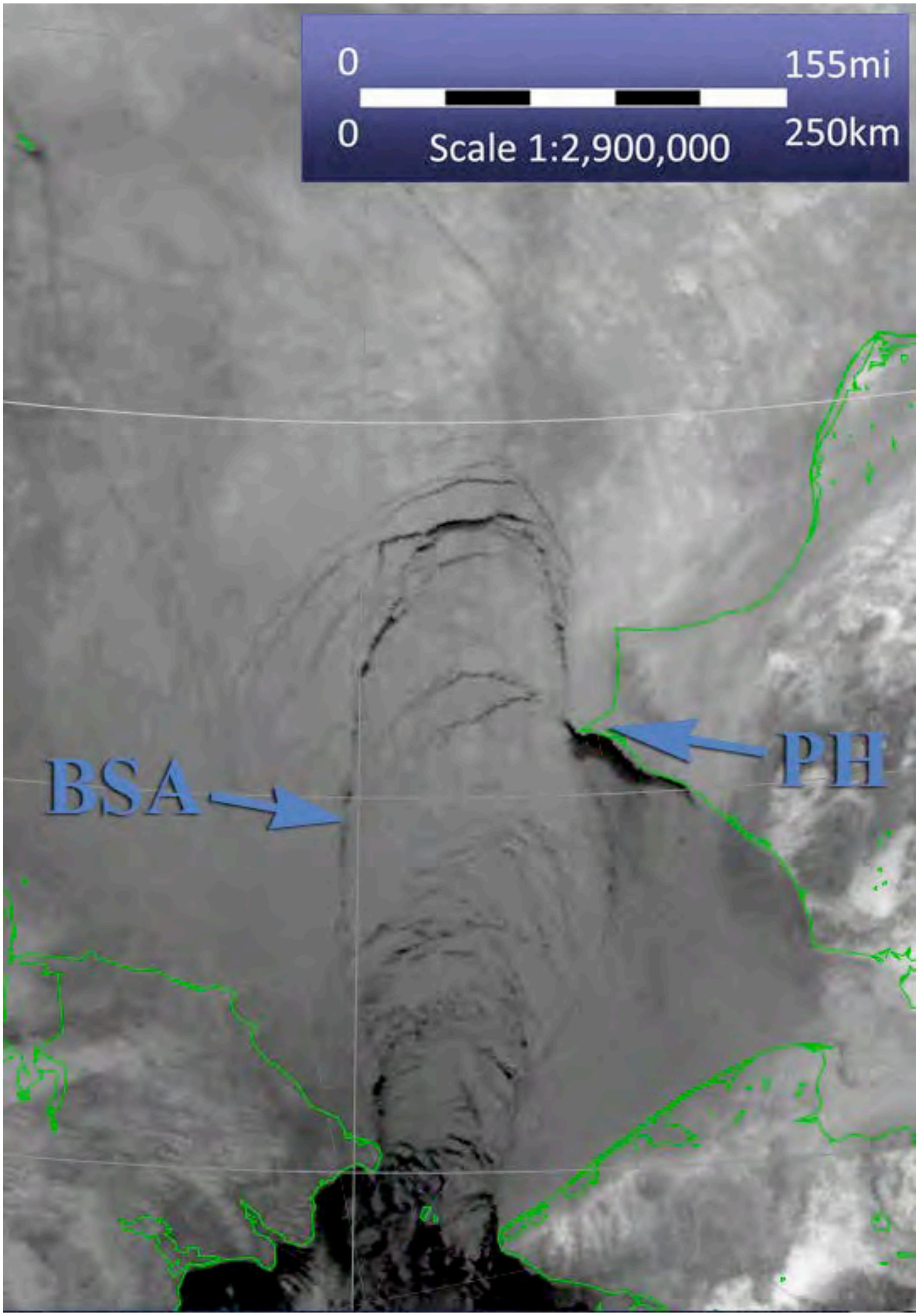

Figure 4.2.23. Southward displacement of the Chukchi Sea pack ice indicated by the direction of the Bering Strait Arch (BSA) structure. The pattern is probably unusual in that there are no leads visible on the scale of the imagery other than those in the arch, the opening southeast of Point Hope, and the arcing leads originating at Point Hope (PH). Compare to Figure 4.2.24 next. (N12.06030.1634; 30 Jan 2006)

4.2.7 Northward Displacement of the Chukchi Sea pack ice (ND)

Several patterns with dominantly northward displacement direction are shown in Figures 4.2.24 - 4.2.30. There are similarities between some but their only commonality is the dominant displacement direction.

Figure 4.2.24 shows the same arch structure in Figure 4.2.23, but the next day (January 31) after the arch had extended some distance to the north under continued southward ice motion. However, the new leads in the northwestern part of the figure are precursors to a change in the direction of displacement of the Chukchi Sea pack ice. This is clear in Figure 4.2.25, which was acquired the day after Figure 4.2.24 (February 1). By that time the direction of pack ice displacement had reversed and was directed northward. This is shown by the presence of several wide arcing leads, concave to the north, that cross most of the area. Note that there are no new leads in the southern Chukchi Sea or along the coast of Chukotka. This is interpreted here as implying that the first northward movements took place in the northern Chukchi Sea with new leads forming progressively to the south as space became available.

In Figure 4.2.26 the displacement is toward the northeast. The lead pattern suggests that the movement began near the coast of Chukotka, because the widest leads are near the coast and the arcing leads decreasing in number to the north. A similar pattern is shown in Figure 4.2.27 in which the displacement is to the northeast, but the openings are generally close to the coat of Chukotka. However, in this case, the openings north of Point Hope, Cape Lisburne, Icy Cape and east of Point Barrow suggest that the ice pack moved as a unit. Finally, the lead pattern in Figure 4.2.28 shows a more regular distribution of open leads in a pattern that shows a northward displacement direction.

Figures 4.2.29 and 4.2.30 illustrate two other styles of deformation patterns during northward displacement of the Chukchi Sea pack ice. In Figure 4.2.29 there is a clear separation along the lead from Herald Island to Point Hope, passing through the grounded ice mass on Herald Shoal. The triangular wedge between the lead and the coast of Alaska moved northward as a single unit. No new leads formed in the wedge, or in the pack ice to the south. In contrast, the pattern in Figure 4.2.30, developed over two days, beginning with the formation of the arc leads in the north and ending with the appearance of the lead from the west side of Bering Strait to near Herald Island.

Figures 4.2.25 - 4.2.30 show that there are different patterns and mechanisms through which northward displacements of the Chukchi Sea pack ice can take place. It is likely that small variations in displacement direction can create large variations in the resulting pattern. Similarly, the state of the ice and the time of year must also contribute to the final lead pattern.

4.2.8 Chukchi Coast Shoreward (CS)

There are several displacement patterns that can bring ice against the Chukchi Sea coast of Alaska. The southward pack ice displacement in the early stages of WCAL formation (Figure 4.2.4) was described above. In addition, other patterns that have similar results are illustrated in in Figures 4.2.31 - 4.2.33, which show patterns of curving leads that that are concave toward the coast. In addition to closing the pack ice against the coast, episodes such as these create openings along the Beaufort Sea coast as can be seen in the figures. One addtional pattern in this catagory is not illutrated here because it involves the clockwise rotation of part of the northeastern Chukchi Sea pack ice. There is no particular lead pattern associated with the movement, but it can be recognized by rapidly scanning through successive images so the motion appears in a "time-lapse" sequence.

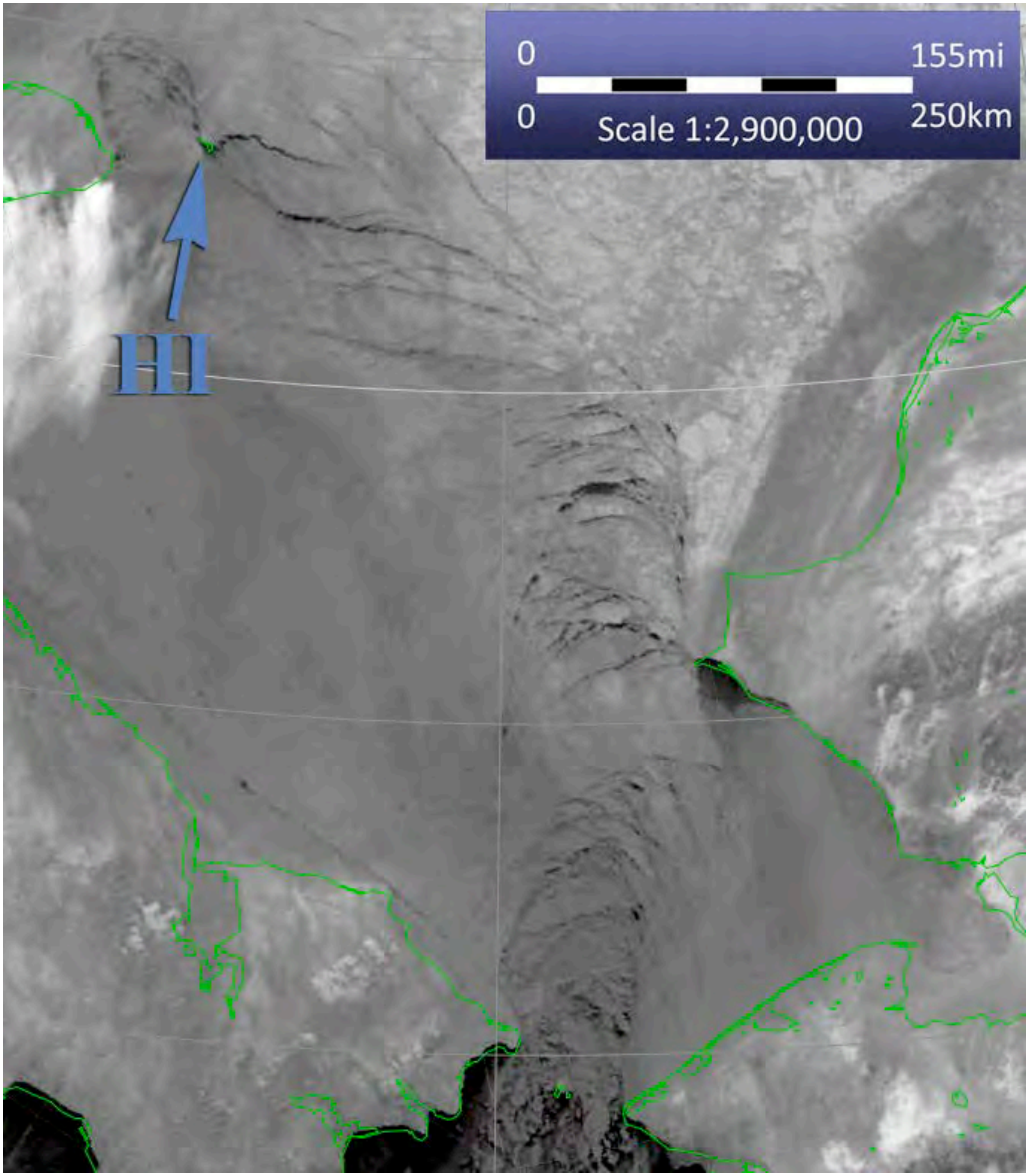

Figure 4.2.24. Extension of the arch structure in Figure 4.2.23 on the following day. The structure has lengthened slightly northward and some of the contained arcing leads have opened wider. However, the new leads near Herald Island (HI) suggest that the direction of pack ice motion is changing. (N18.06031.1345; 31 Jan 2006)

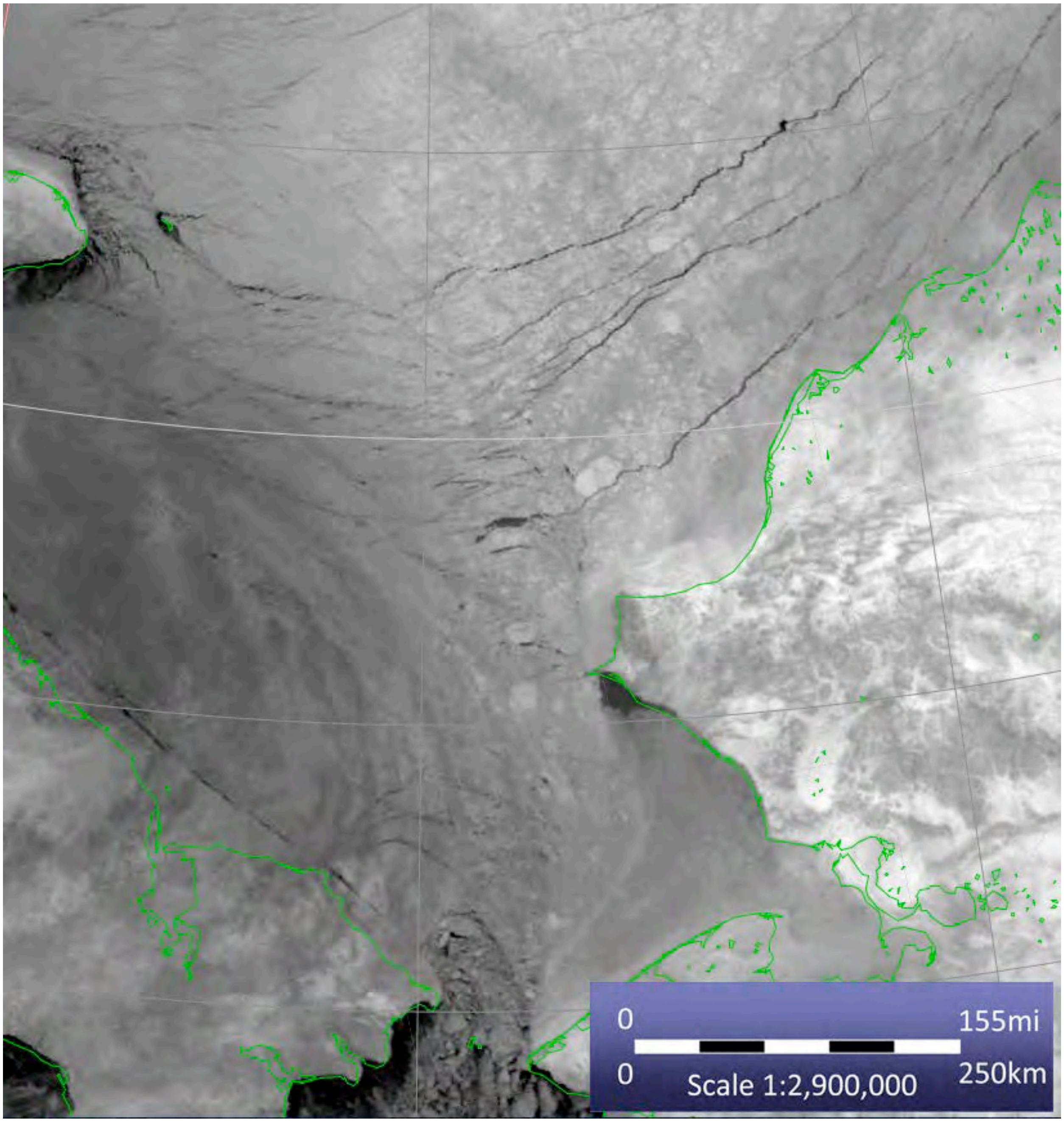

Figure 4.2.25. Image on the day following that in Figure 4.2.24. The sense of displacement is fully reversed from that in Figure 4.2.23 and is now directed toward the north in the central Chukchi Sea. This is indicated by the new concave-north leads crossing the area. However, the pattern was short-lived and the displacement reversed to southward again on the next day. (N18.06032; 1516; 1 Feb 2006)

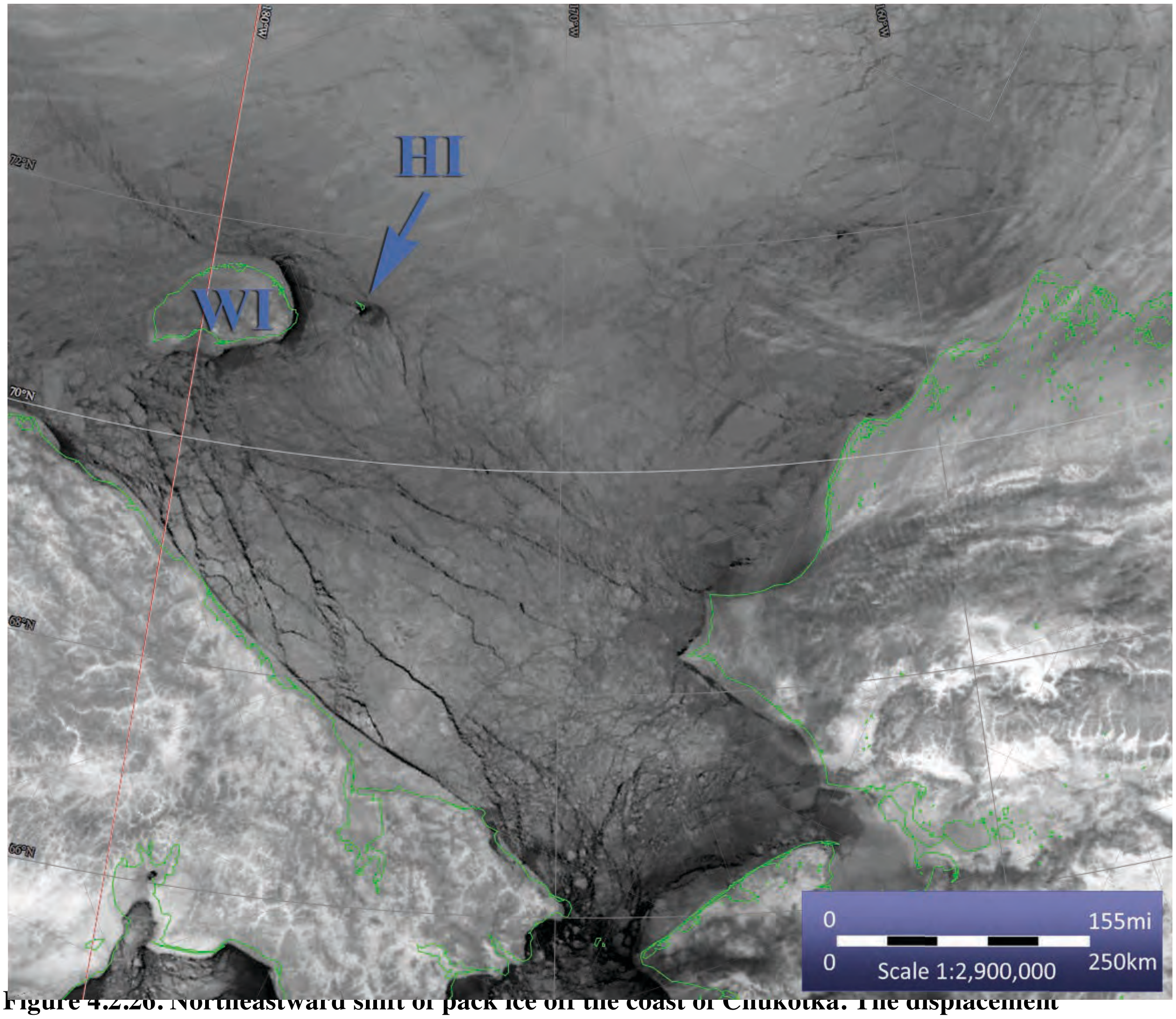

Figure 4.2.26. Northeastward shift of pack ice off the coast of Chukotka. The displacement direction is indicated by the open polynya on the northeast side of Wrangel Island (WI), the arcs concave north between the Alaska coast and Wrangel Island and Herald Island (HI), and the lead along the Beaufort Sea coast of Alaska. Note that the widest leads are along the coast of Chukotka and the number of leads decreases to the north. This is interpreted as suggesting that the displacement progressed differentially from south to north. (N14.96054.1443; 23 Feb 1996)

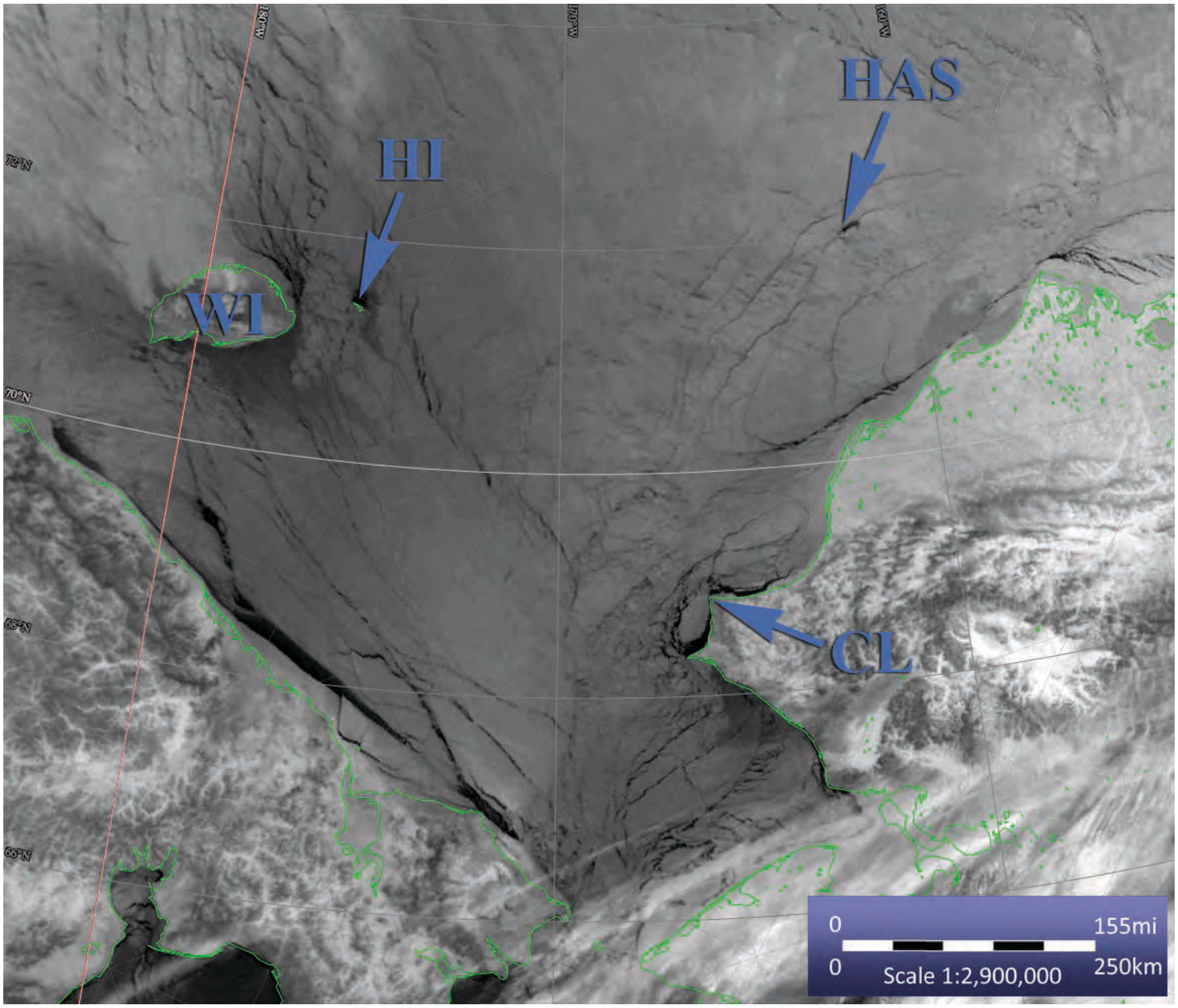

Figure 4.2.27. Early winter shift of pack ice to the northeast off the coast of Chukotka. Note the openings along the coasts of Wrangel Island (WI) and Herald Island (HI), in the bight north of Cape Lisburne (CL), and along the Beaufort Sea coast. The northeastward trending opening at Hanna Shoal (HAS) shows the direction and magnitude of the displacement at that latitude. The opening north of Cape Lisburne and along the Beaufort Sea coast of Alaska and the lack of leads in the northern Chukchi Sea suggests that the pack ice displacement is relatively uniform over the entire area. (N12.03008.1658; 08 Jan 2003)

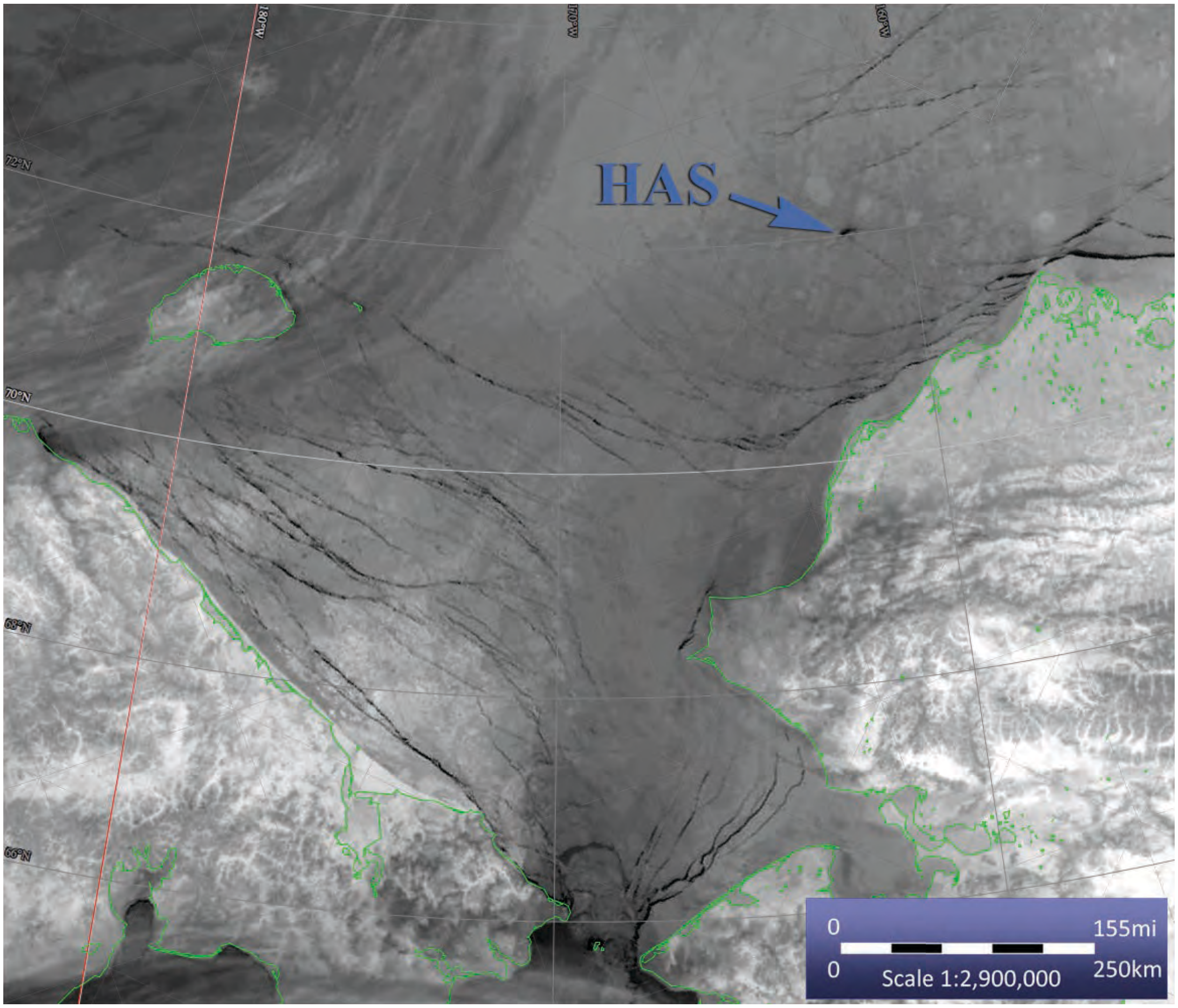

Figure 4.2.28. North to northeast shift of pack ice in the Chukchi Sea as indicated by the track to the northeast at Hanna Shoal (HAS). Comparison with Figures 4.2.25 - 4.2.27 shows that the leads in this figure are more uniformly distributed across the area than those in the earlier examples. (N12.99040.1822; 9 Feb 1999)

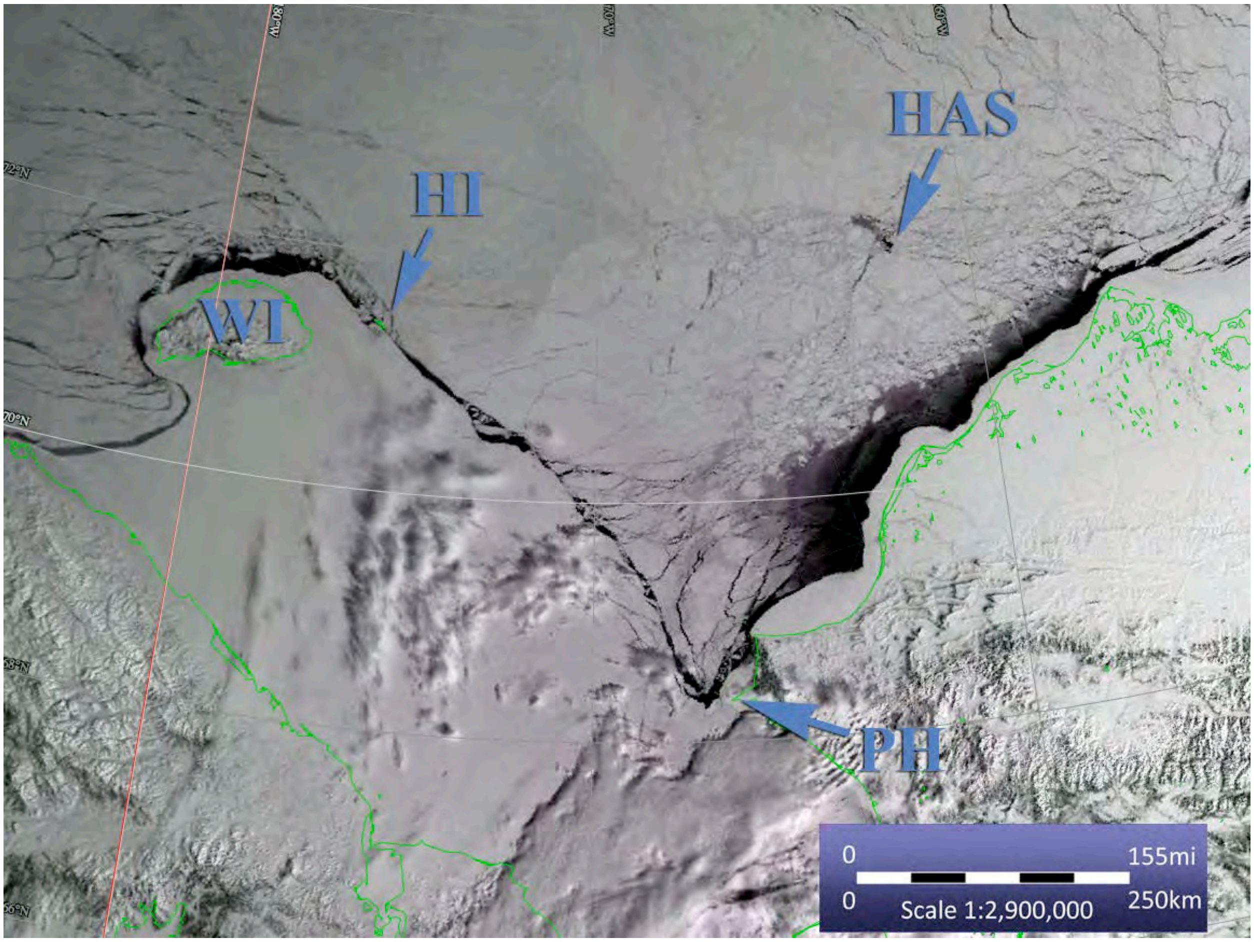

Figure 4.2.29. A wedge of the northern Chukchi Sea pack ice separated from the ice to the south along a lead from Point Hope through the grounded ice on Herald Shoal (HES) and on to Herald Island (HI). The pack ice also moved off the Alaska coast. The initial displacement was to the north, but it quickly changed to the northwest as shown by the drift track at Hanna Shoal (HAS). Note the general absence of other leads in both the pack ice of the wedge and in the pack ice to the south that remained stationary. (N15.00102.1946; 11 Apr 2000)

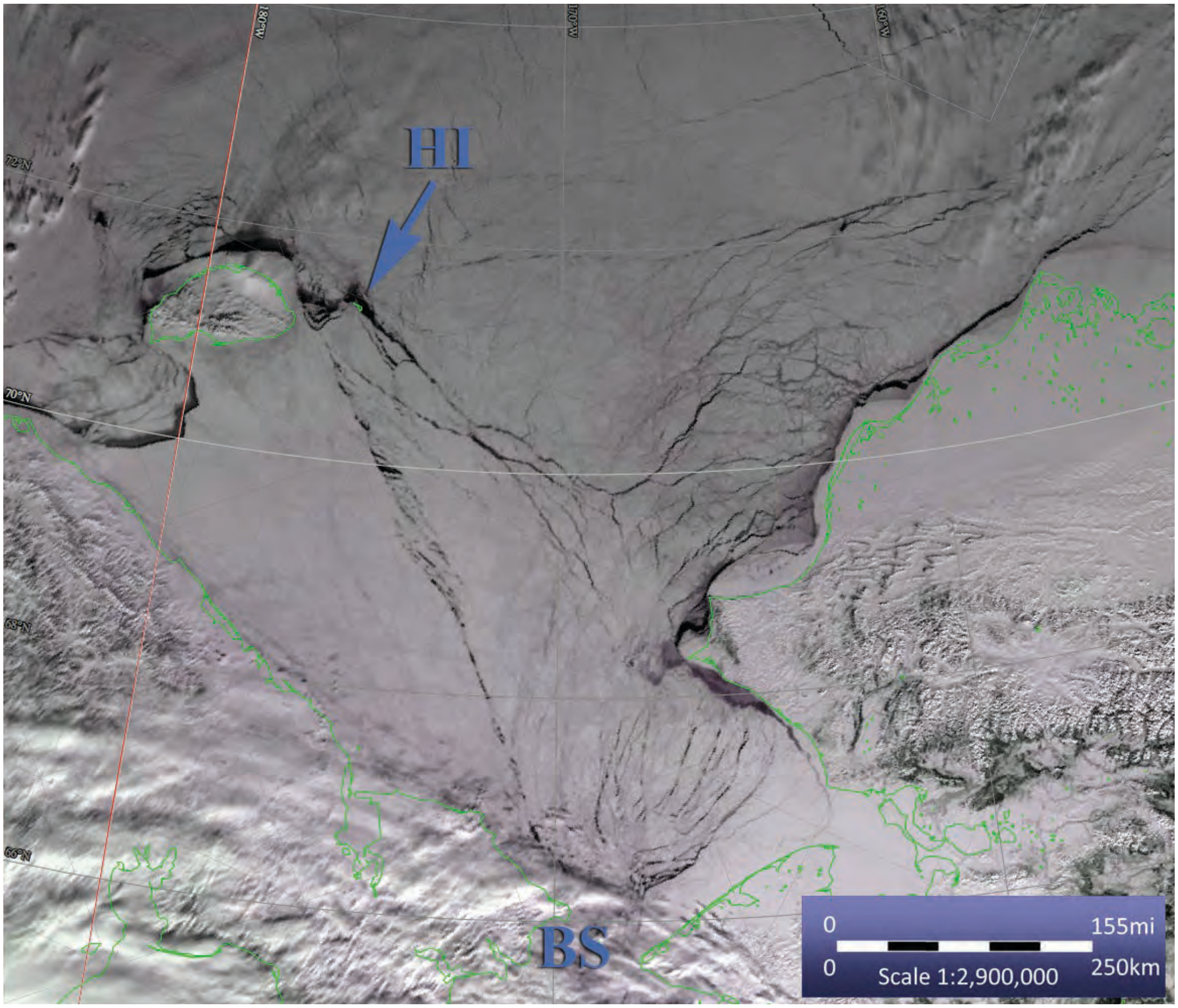

Figure 4.2.30. Northward displacement of pack ice in the Chukchi Sea that resulted from progressive displacement beginning in the north. This was shown from examination of the images from the two days prior to the image shown here. The arcing leads in the north appeared first, and the boundary of the wedge [the lead from Bering Strait (BS) to Herald Island (HI)] was added later. Note however that there are no new leads in the ice to the southwest of the wedge. (N16.03086.2227; 27 Mar 2003)

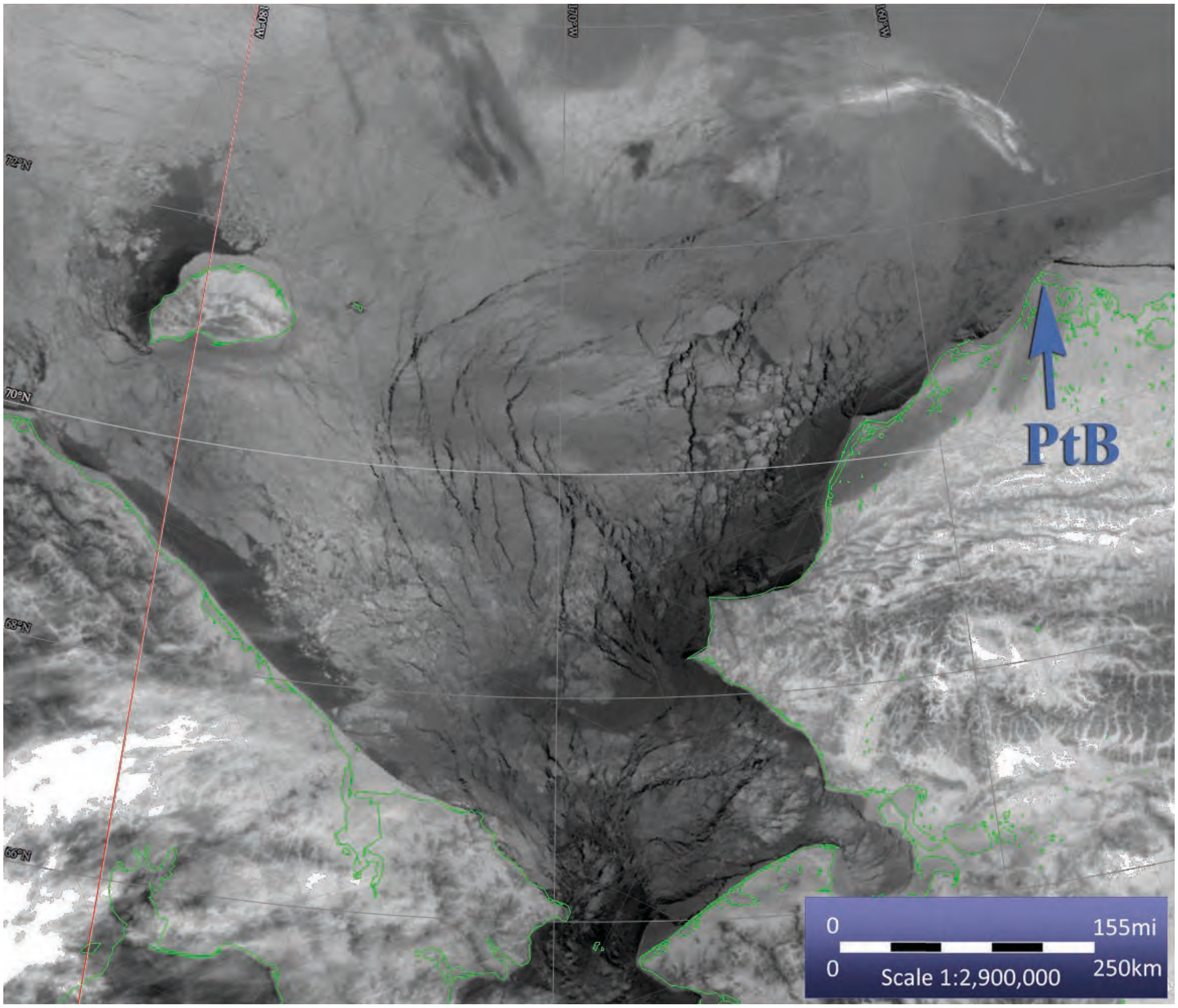

Figure 4.2.31. Lead pattern during eastward pack ice displacement toward the coast of Alaska. The concave east curvature of the leads indicates the displacement direction. Note the narrow lead along the Beaufort Sea coast east of Point Barrow (PtB). (N12.99004.1819; 4 Jan 1999)

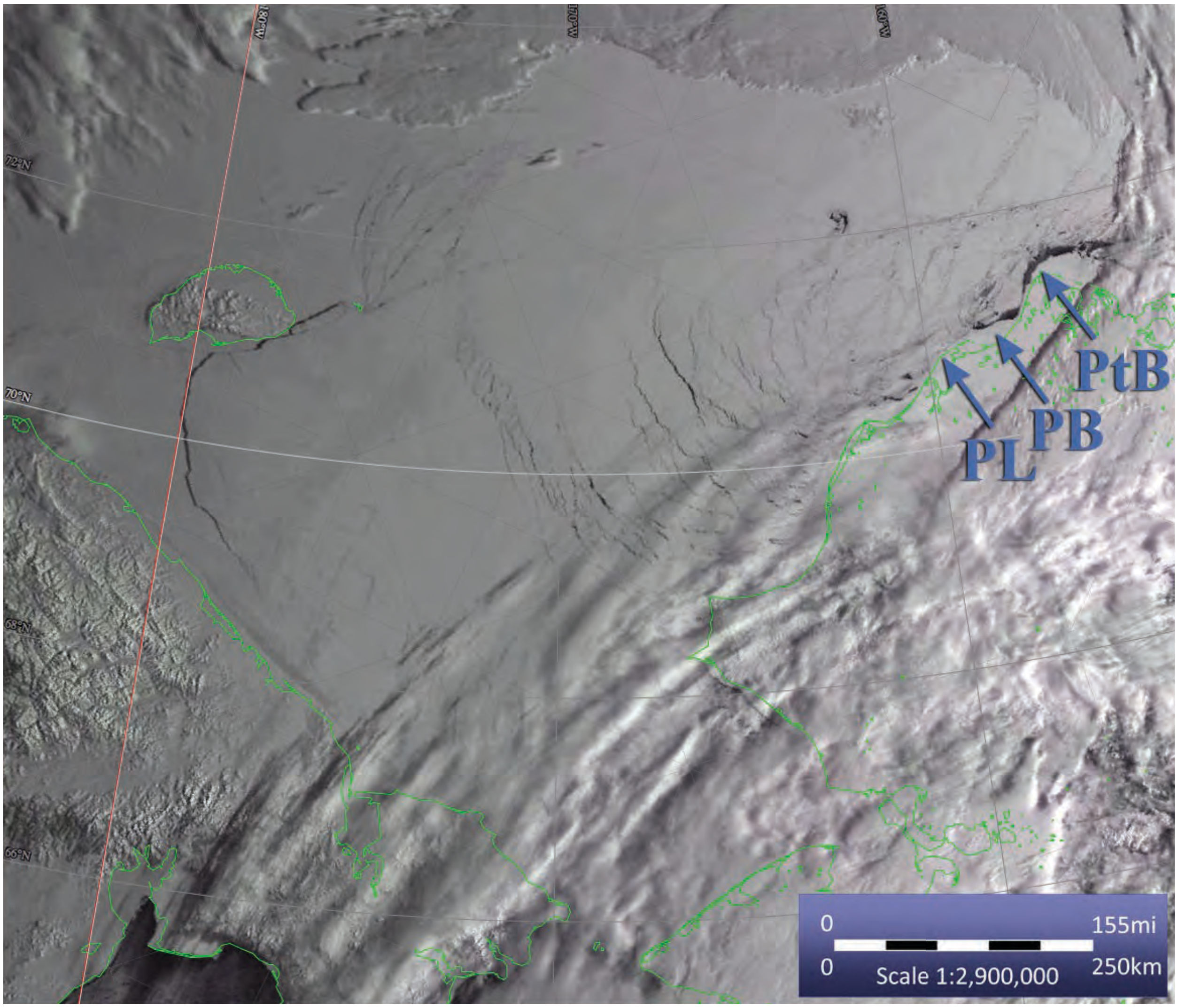

Figure 4.2.32. Pattern of arcing leads concave to the northeast. The displacement in this example is at a low angle to the coast as shown by the openings north of Point Lay (PL), in Peard Bay (PB), and north of Point Barrow (PtB). (N12.99108.1814; 18 Apr 1999)

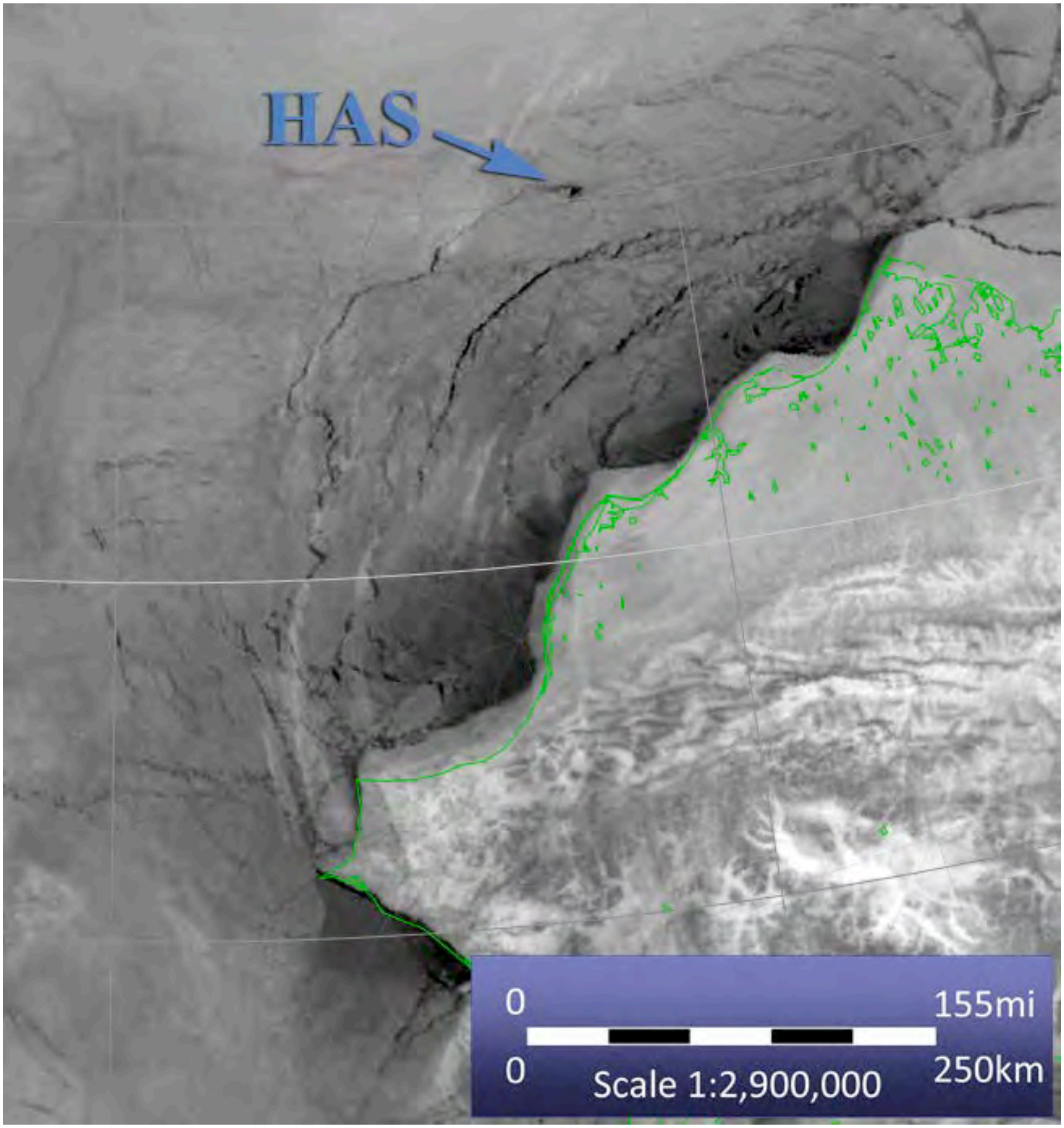

Figure 4.2.33. Pattern of arcing leads indicating pack ice motion at a high angle to the coast, as opposed to the lower angle of impact shown in Figure 4.2.32. Note the lead terminating at the mass of grounded ice on Hanna Shoal (HAS). (N12.03052.1730; 21 Feb 2003)

4.2.9 Bering Strait Arch Structure

The Bering Strait Arch is a common lead pattern in the pack ice in the southeastern Chukchi Sea. It forms when the ice is being driven southward into Bering Strait and was first described by Shapiro and Burns (1974) from study of ERTS-1 (later Landsat) imagery acquired on March 6, 7 and 8, 1973. The sequential imagery permitted the daily changes in the lead pattern to be mapped, so that the sequence in which it formed could be described. The arch structure extended to the north over all three days captured by the ERTS-1 imagery and visible and IR imagery from the Air Force DAPP system (an early element of the DMSP) acquired over the next several days showed that fracturing and lead formation continued to progress northward. The final pattern was similar to the WCAL described in this report.

Tracking the floes on the ERTS-1 imagery over the 3-day period provided data on the displacement pattern of the ice as it approached, and then drifted southward through Bering Strait. The data from the lead and displacement patterns then led to the hypothesis that the geometry of the process could be described by a slip-line field model of the extrusion of a perfectly plastic material through a die or a granular material through a constricted channel. The idea that pack ice deformation could be considered in that way is the basis for the approach adopted for interpreting the patterns identified in both this study and MMS OCS STUDY 2005-068.

The initial stages of the Bering Strait Arch structure are often the "double arch" structures described by Torgerson and Stringer (1985). The development of the main structure, which ultimately extends to become the WCAL pattern, follows as illustrated in Figures 4.2.4 - 4.2.6. The process requires the formation of longer leads projecting to the north from either side of Bering Strait. Their initial length and orientation varies but they serve as boundaries within which the pack ice breaks up and displaces southward toward the Strait. In some examples, this is accomplished by the formation of a series of arcing leads that are concave to the south and may be tangent to the bounding leads (Figure 4.2.5) but in others, the pack ice within the arch structure breaks into smaller floes so the longer leads are not recognizable. Subsequently, the lead or shear zone that gives the WCAL its name extends northward and new leads form between it and the coast to complete the pattern.

Another sequence of images of the formation of a Bering Strait Arch is shown in Figure 4.2.34. In this example the arch developed over a few days, so some intermediate steps were captured. Note that the sequence shown is the result of southeast displacement along the coast of Chukotka, so the axis of the arch structure is directed to northwest. The next step in the sequence is shown in Figure 4.2.19.

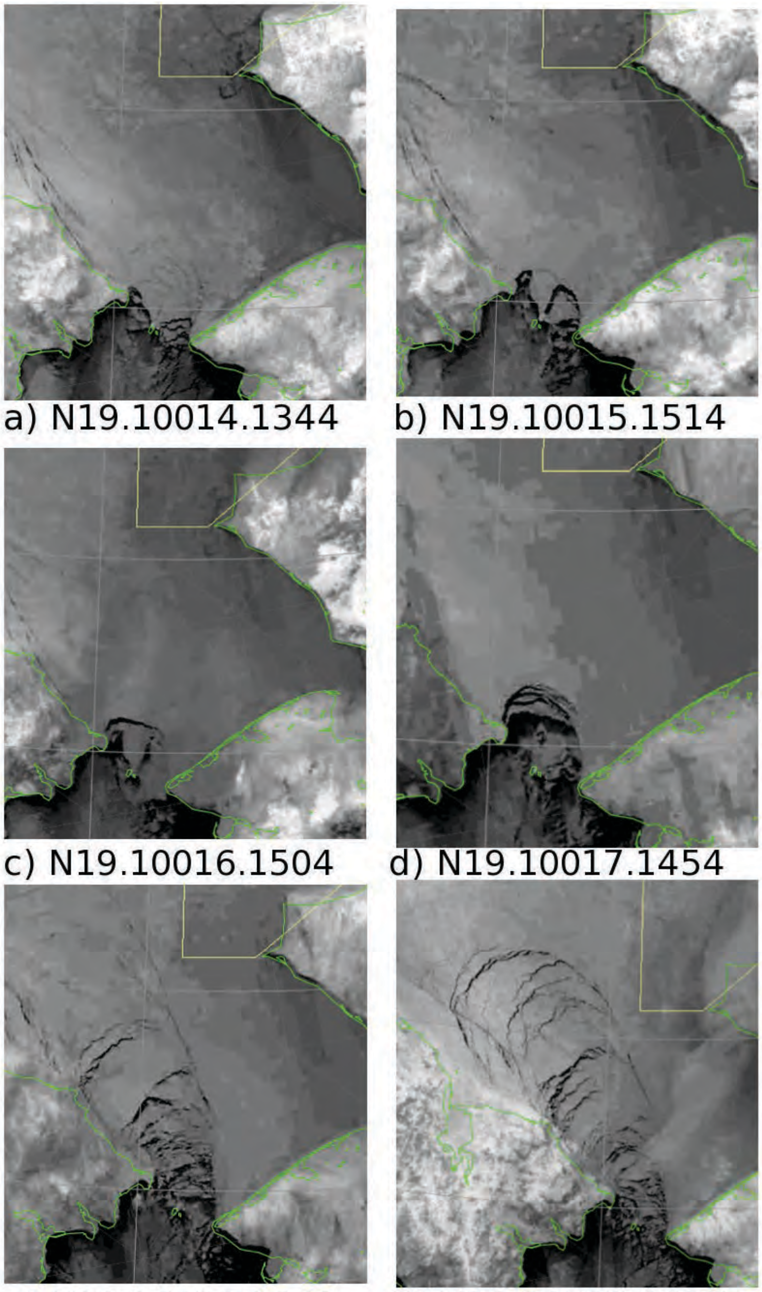

a) N19.10014.1344 b) N19.10015.1514

c) N19.10016.1504 d) N19.10017.1454

e) N19.10018.1443 d) N19.10019.1433

Figure 4.2.34. Sequence of clips from images acquired at about 24 hour intervals showing stages of formation of leads in the Bering Strait Arch structure. In this case, the axis of the arch is turning to the northwest and results in the pattern shown in Figure 4.2.19. The sequence is representative of arches formed in other displacement patterns which often begin with small arches across the gaps in Bering Strait and then progress to wider arcing leads that merge into leads/shear zones, that bound the structure.

4.3 Landfast ice variability and stability

4.3.1 Location of the SLIE

As described in section 3.3.4, SLIEs were delineated using a combination of 3 consecutive Radarsat mosaics and the corresponding gradient difference mosaics. Consequently, for each season, there were 2 fewer SLIEs identified than there were mosaics available yielding a total of 312 and 326 SLIEs for the western and eastern landfast ice regions, respectively, over the study period from 1996-2008. Figure 4.3.1 illustrates the distribution of all these SLIEs, stacked such the color scale indicates the probability of SLIE occurring within 500km of a given point. A near-continuous dark blue zone indicates where the SLIE commonly stabilizes. Within this zone are red “nodes” where the SLIE was observed more frequently. Dashed ellipses highlight the locations of nodes some distance from the coast where the SLIE occurs with greater frequency and which indicate probably locations of recurring grounded ice features.

Figure 4.3.2 shows the landfast ice area shoreward of each SLIEs stacked by year such that the shade of blue indicates the number of occasions when landfast was observed. This provides a measure of the relative probability with which landfast ice was observed at any point in the study area during the period from October to July. The individual SLIEs for each year are overlain in black and thus have the appearance of probablity contours. The nodes shown in Figure 4.2.1 are indicated by regions at which SLIEs converge and it can seen that there are some nodes that appear each year while others move or are absent in some years. Figures 4.3.1 and 4.3.2 show that there are strong contrasts in landfast ice extent and variability across the whole study region. We will assess local and regional variability later, using the coastal zones identified in Figure 3.3.4

The maximum extent of landfast ice in each year is indicated by the palest blue areas, which show significant interannual differences. In the Beaufort Sea, there were four annual cycles in which we identified vast extents of motionless ice (1998-99, 1999-00, 2000-01 and 2003-04). We refer to these phenomena as *stable extensions* following Stringer et al. (1980). Although others have also observed similar features (*Barry*, 1979; *Barry et al.*, 1979) they have not typically been considered part of the landfast ice. We include them here in keeping with our definition (Section 3.3.1) and discuss them in more detail in Section 4.3.5. Figure 4.3.2 shows stable extensions in most years along the northern Seward Peninsula and one such occurrence was observed along the Chukotkan coast. Some SLIEs in Figure 4.3.2 appear to have irregular and jagged edges. These are often the result image boundaries within the parent images, as discussed in section 3.3.4 and illustrated in Figure 3.3.3.

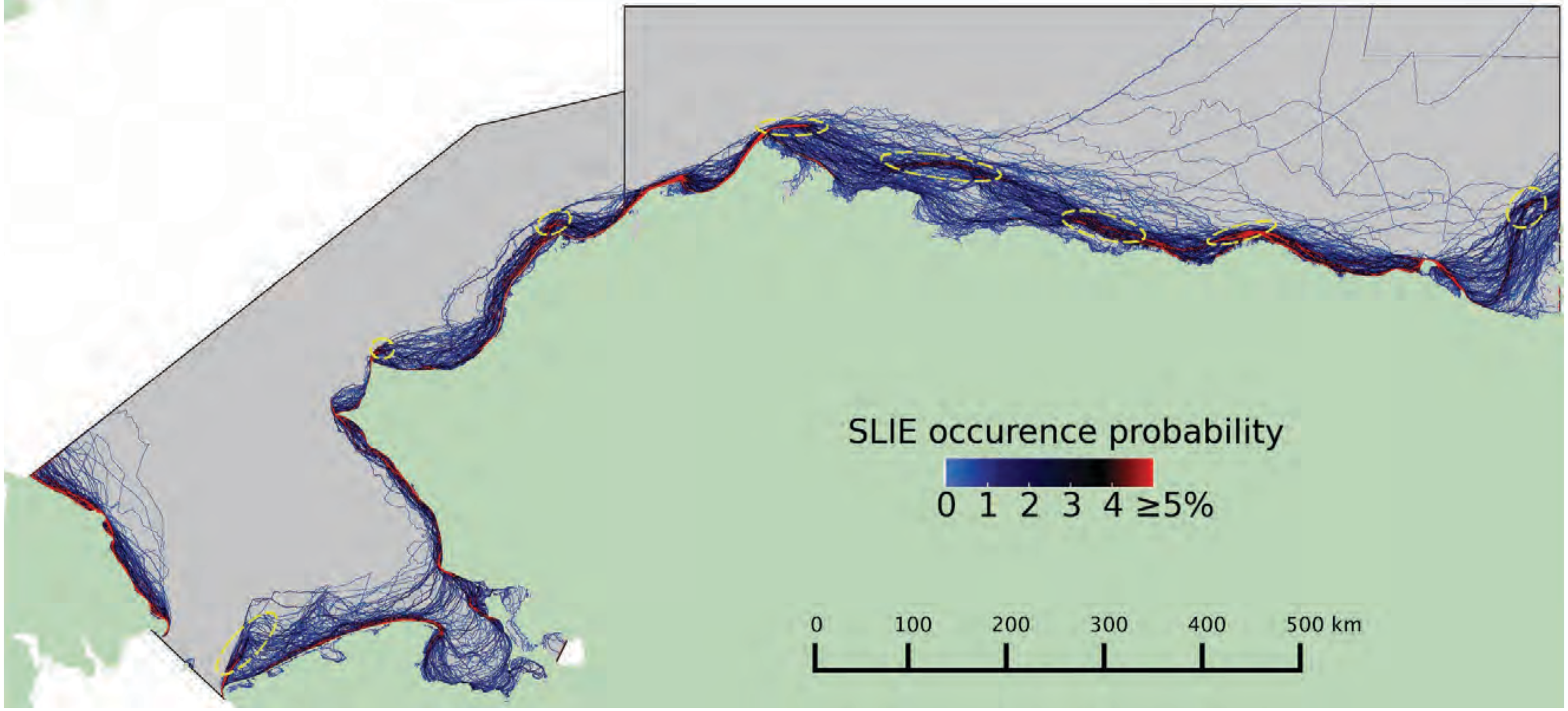

Figures 4.3.1: All the SLIEs delineated for the period 1996-2008 stacked so that the color value of a line indicates the probability of the SLIE lying within 500 m of a given point between October and July. A near-continuous dark bue zone indicates where the SLIE commonly stabilizes. Within this zone are red "nodes" where the SLIE was observed more frequently. Dashed ellipses highlight the locations of nodes some distance from the coast where the SLIE occurs with greater frequency and which indicate probable locations of recurring grounded ice features.

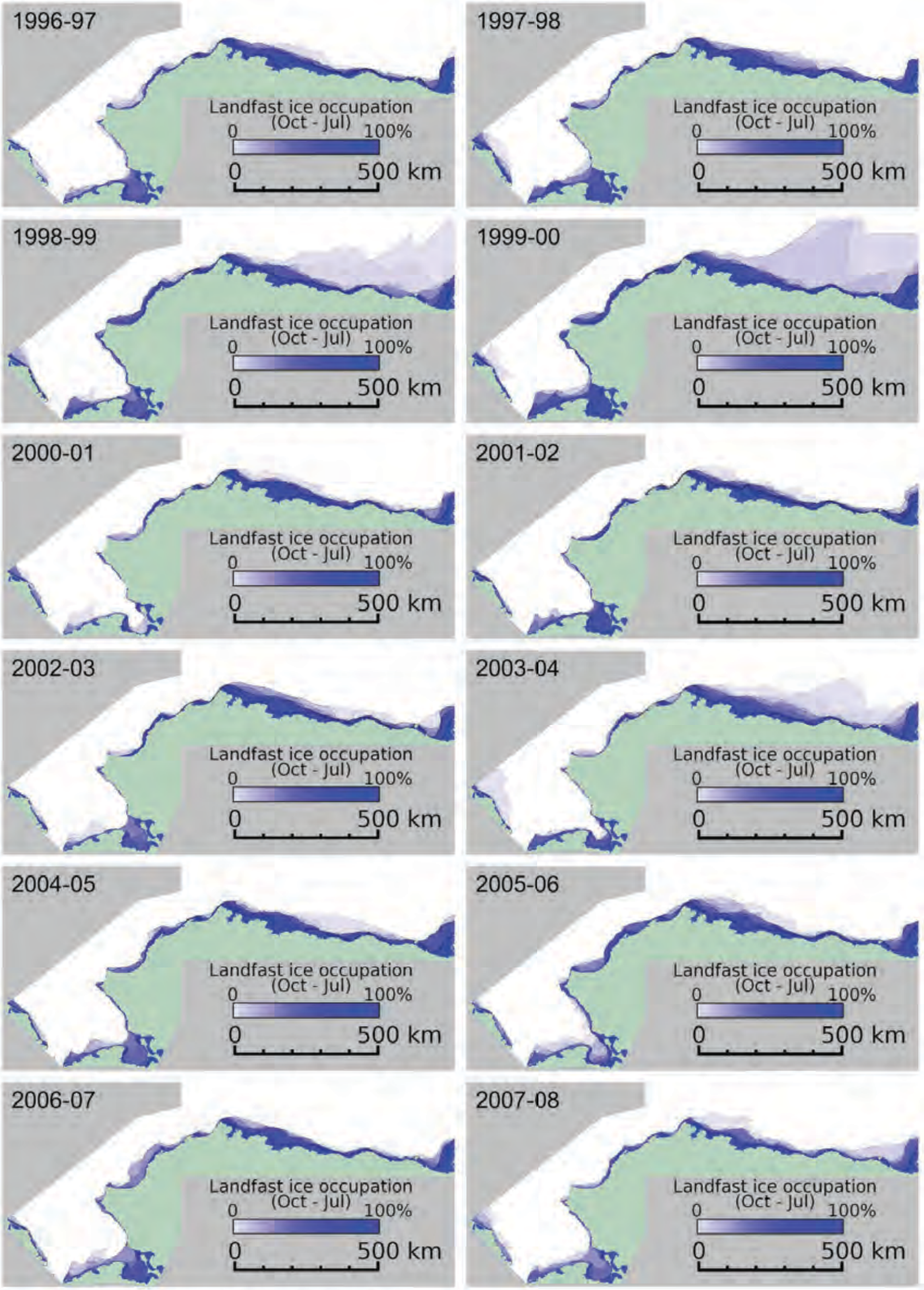

Figure 4.3.2: The extent of landfast ice shoreward of the SLIE stacked for each year, such that the shade of blue represents the fraction of the annual cycle (October-July) for which that area was occupied by landfast sea ice. White areas indicate where landfast ice was never observed, but may have been occupied by drifting sea ice. Black lines indicate locations of individual SLIEs**.**

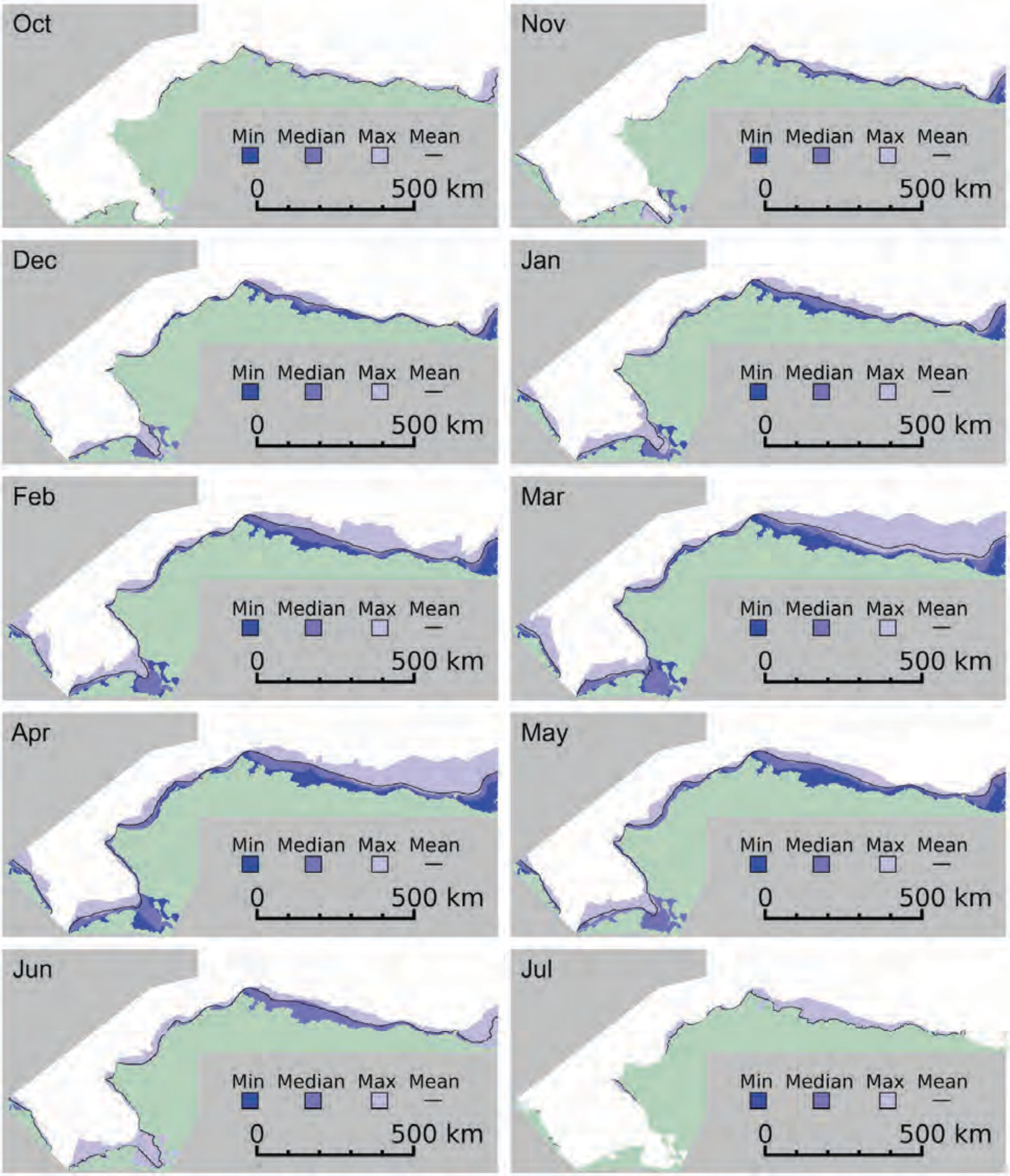

Figure 4.3.3.: Minimum, median, maximum and mean monthly mean landfast sea ice extents showing the change in landfast ice distribution in the study area through the annual cycle. See text for details on calculating these SLIE positions.

4.3.2 Monthly landfast ice extents

Fgure 4.3.2 shows interannual variability in the location of the SLIE, but it provides no information on the changes that take place during the annual cycle. Such information is partly contained in maps of monthly minimum, median, maximum and mean landfast extent (Figure 4.3.3). The method used to calculate these maps is described in section 3.3.8. The reader is reminded that measured landfast ice widths are truncated by the maximum length of the coastal coordinate vectors. This will affect the maximum extents and, to a lesser degree, the mean extents during those months when vast stable extensions occurred beyond the range of the coordinate vectors.

Figure 4.3.3 illustrates the mean annual cycle and its variability across the study area. It can be seen that the landfast ice grows gradually from October through to February and the monthly median extent is greatest in March and April for most of the study area except for the section of the Beaufort coast between Point Barrow and Nuiqsut, where the median extent is greatest in May. The advance of landfast ice is not a continuous process and can involve many stages of formation, break-up and reformation. Hence, except in October when the landfast may not have had time to form and break-up, the monthly minimum SLIE corresponds to most severe break-out that was observed in any month. In the Beaufort Sea, the minimum SLIE position advances behind the mean up until April, indicating that break-outs become less severe. The minimum SLIE position begins retreating again in April, indicating that in the Beaufort Sea, landfast ice most stable in March. In contrast, along most of the Chukchi coast outside of Kotzebue Sound, the minimum SLIE position never extends far offshore indicating the possibility of a severe breakout occurred in any month of the year.

4.3.3 Water depth at the SLIE

In figures 4.3.1 and 4.3.2, the relative stability of the SLIE position can be inferred from the probability and spatial density of SLIEs. Similarly, we assume that water depths in which the SLIE is most frequently observed correspond to depths in which the SLIE is most stable. Using the bathymetric data discussed in Section 3.5.1, we generated a dataset of over 2.8 million measurements of water depth at the SLIE. From these data we calculated the distribution of water depth at the SLIE for each calendar month and for each of the coastal zones shown in Figure 3.3.4. These distributions are shown in Figure 4.3.4.

Zones 8-11 were the subject of MMS OCS STUDY 2005-068, which demonstrated that the distribution of water depths at the SLIE evolved toward a uni-modal distribution as the landfast ice extended away from the coast.. This evolution is evident in Figure 4.3.4, but the pattern is not clear in all zones, particularly those along the Chukchi Sea coast. For example, the northern Chukotka Pensinsula (zone 1) and between Cape Cruzenstern and Point Hope (zone 5) show a multi-modal distribution. Also, with the exception of the northern Chukotka Peninsula, landfast ice in the Chukchi Sea occupies shallower water overall than in the Beaufort Sea.

Table 4.3.1 lists the modal depths in each coastal zone and the month in which they are achieved. These depths are useful indicators of stability of the landfast ice, since the histograms do not change significantly once the mode has reached such a depth. However, the determination of when a modal depth has been achieved can be highly subjective. For example, the Northern Chukotka Peninsula (zone 1) and Outer Kotzebue Sound (zone 3) both exhibit their modal depths as early as October, although the distributions are not fully developed at this time. Therefore, in keeping with the work of Barry et al. (1979) and to reduce the sensitivity of the criterion, a depth of 15 m was chosen to the indicate the onset of stabilization (Section 3.3.7)

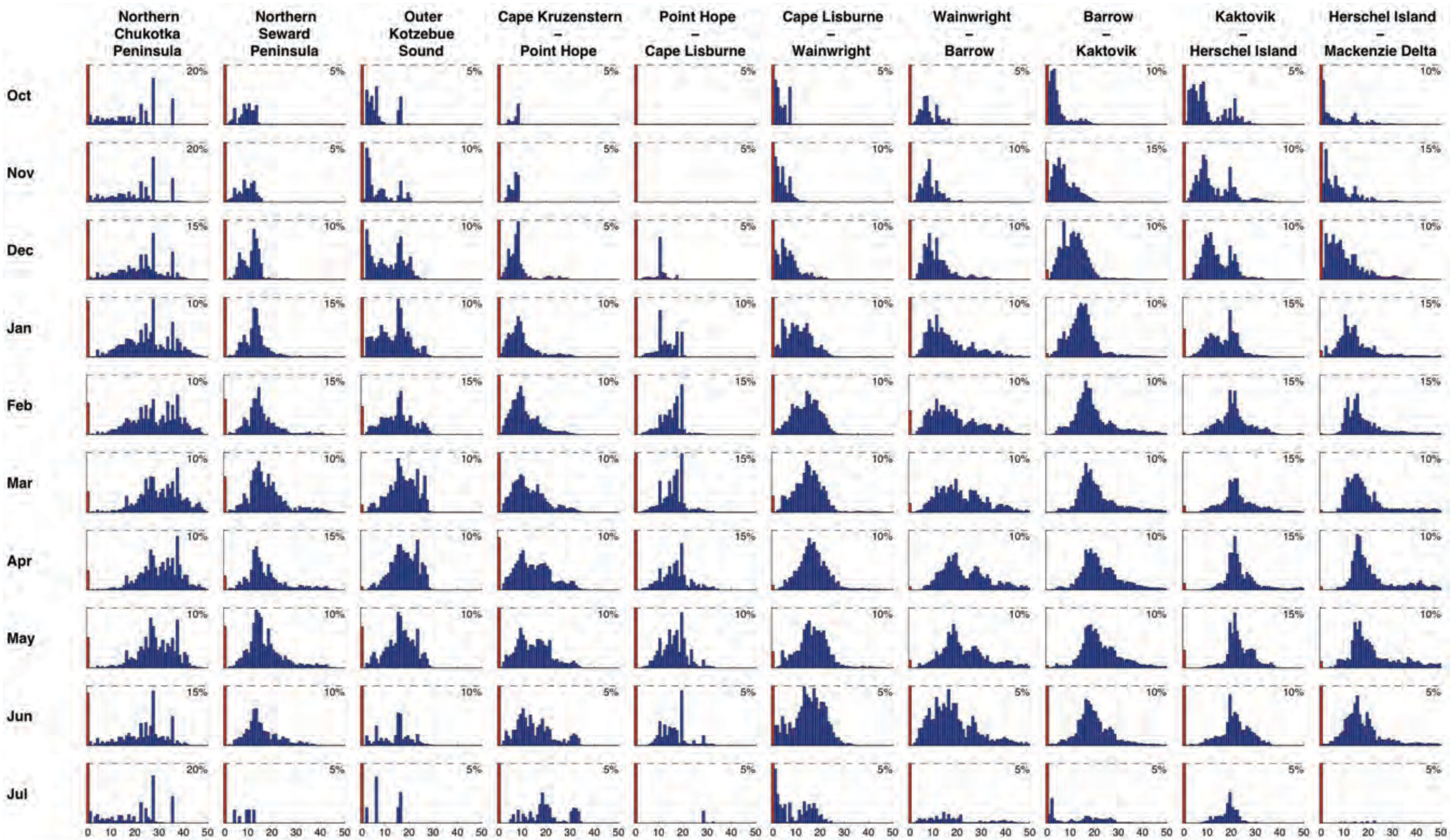

Figure 4.3.4. Monthly histograms of water depth at the SLIE for the coastal zones shown in Figure 3.3.4. Zone 4 (inner Kotzebue Sound) is not shown as the data are not meaningful once Kotzebue Sound freezes over the SLIE does not lie within the Sound. The y-axes are scaled different for each panel and the percentage and the top right corner of each panel indicates the maximum frequency density for that panel. Water depths are binned into 1 m bins. Data indicating water depths <1 m are shown in red and may extend beyond the axes.

Table 4.3.1. The modal water depth at the SLIE at the end of winter for each zone and the month in which this distribution is achieved

	Zone	Modal water depth at SLIE (m)	Month achieved
1	Northern Chukotka Peninsula	26 & 37	October
2	Northern Seward Peninsula	13	November
3	Outer Kotzebue Sound	16	October
4	Inner Kotzebue Sound	-	-
5	Cape Kruzenstern - Point Hope	9 & 18	January & February
6	Point Hope - Cape Lisburne	11 & 19	December & January
7	Cape Lisburne - Wainwright	15	January
8	Wainwright - Barrow	18 & 28	February & March
9	Barrow - Kaktovik	16	January
10	Kaktovik - Herschel Island	19	December
11	Herschel Island - Mackenzie Delta	15	January

As with the development of landfast ice area, the advance of the SLIE into deeper water is more gradual than its retreat at the end of the annual cycle. Also, advancement to these water depths is not a continuous process. At the beginning of the annual cycle, the distributions in all zones are multi-modal with the strongest modes in shallow water. Through the first few months, however, deeper modes develop at the expense of the shallow modes. Hence, the SLIE appears to advance from one stable water depth to the next in order to reach its final modal depth. The retreat of the SLIE into shallow water is rapid, though along many sections of coast the modes become more distinct in May and June, indicating that places where the SLIE occupies these depths are the last to retreat.

4.3.4 Key events within the annual cycle

The mean annual cycle can be described by the monthly averages as in Figure 4.3.3, but it is also informative to examine the variation in width at individual points along the coast. In doing so, we can examine the annual cycle in finer detail and also consider interannual variability. As described in section 3.3.5, we calculated landfast ice width at 8,889 locations along the coast. Time series at 5 of these locations over the period 1996-2008 are shown in Figure 4.3.5. Twelve annual cycles are clearly seen, each with an asymmetric shape showing a gradual advance and rapid retreat (although the final cycle in 2008 is incomplete due to data availability). Short-term variability observed in many of the profiles is discussed in Section 4.3.5.

For each of the 5 time series shown in Figure 4.3.5 and the 8,884 others throughout the study area, we have derived mean occurrence dates of the 4 key events as described in Section 3.3.7. These are presented in Figure 4.3.6, which shows how the timing of the annual cycle varies along the coast. Interannual variability is indicated by the width of the colored swaths, which represent 1 standard deviation from the mean. Gaps in the lines and swaths indicate where identification of the key events failed. Table 4.3.2 lists the percentage of cases where this occurred. The relatively high failure rate in the identification of the date of stabilization reflects the difficulty in defining a single criteria to apply uniformly, as evidenced by the variability in water depth at the SLIE (section 4.3.3). The majority of failures to calculate the date of ice-free conditions occur in 2008, when SAR data were unavailable after April due to budget constraints.

Table 4.3.2: Percentage of cases where calculation of date of key landfast ice event failed

Event	First ice	Stable ice	Break-up	Ice-free
Failure rate (%)	1.4	30.7	5.8	12.0

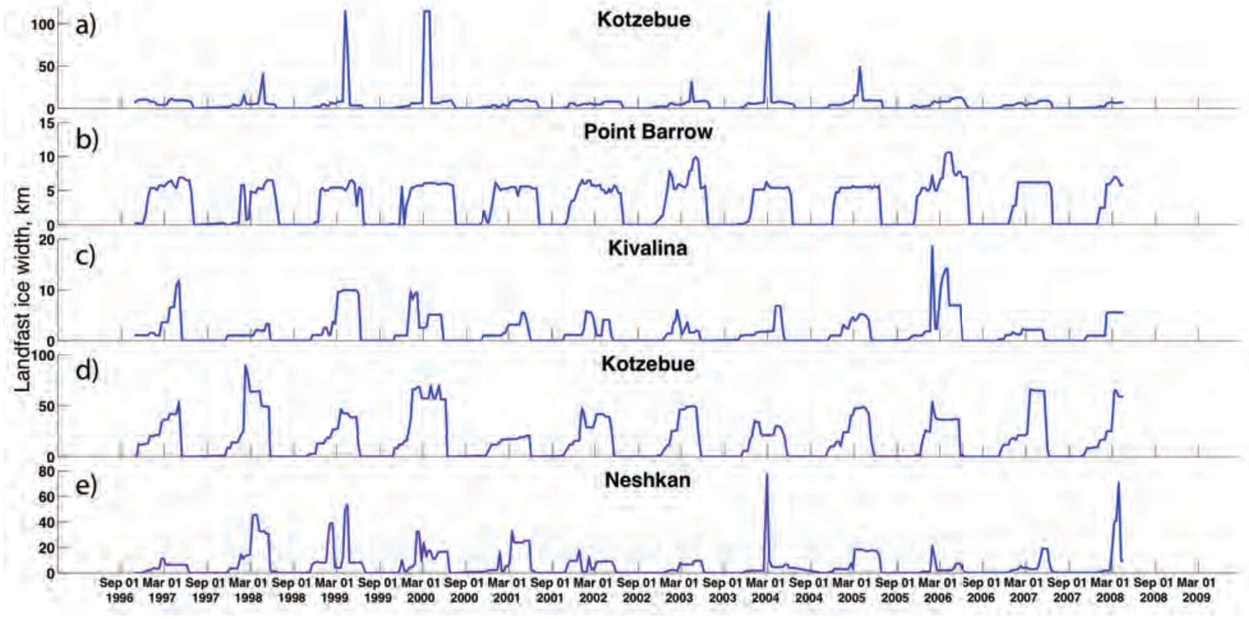

Figure 4.3.5: Time series of landfast ice width at 5 locations along the coast, showing interannual variability, but recurring patterns of growth and retreat over 12 annual cycles. Note the different scales on the width axes. Locations of the profiles are shown in Figure 3.3.4.

Figure 4.3.6 shows that there is both regional and local variability. Broadly, it can be seen that the landfast ice forms earlier and breaks-up later in the Beaufort Sea than it does in the Chukchi Sea (with the exception of some lagoons along the Chukchi coast). This broad pattern reflects the regional variability in freezing and thawing onset dates. The first landfast ice to form along any section of coast forms inside lagoons, where they are present. This is clearly seen in Figure 4.3.6, which shows that lagoon freeze-up is closely related to the onset date of freezing temperatures (section 3.5.2). The timing of ice-free conditions shows a more consistent relationship with the onset of thawing temperatures throughout the study area. Figure 4.3.7 shows the mean occurrence date for each event calculated for each coastal zone taking account of coastal morphology (see section 3.3.9 and Figure 3.3.7). Note that not all coastal morphology types are found in all zones. This reinforces the fact that lagoons and bays are the first to acquire a landfast ice cover, but indicates that coastal morphology is less important for later events in the landfast ice cycle.

Although there are latitudinal gradients evident in Figure 4.3.6, the degree of local variations is much greater than the broad differences between the Chukchi and Beaufort coasts. This implies that at the local scale, the landfast ice regime is controlled by the configuration of the coast and bathymetry. Outside of barrier islands, coastal orientation appears to play an important role. The last landfast ice to form in our study area is found not along the southernmost coastlines, but between Cape Kruzenstern and Point Hope, along the only section of coast that does not face north.

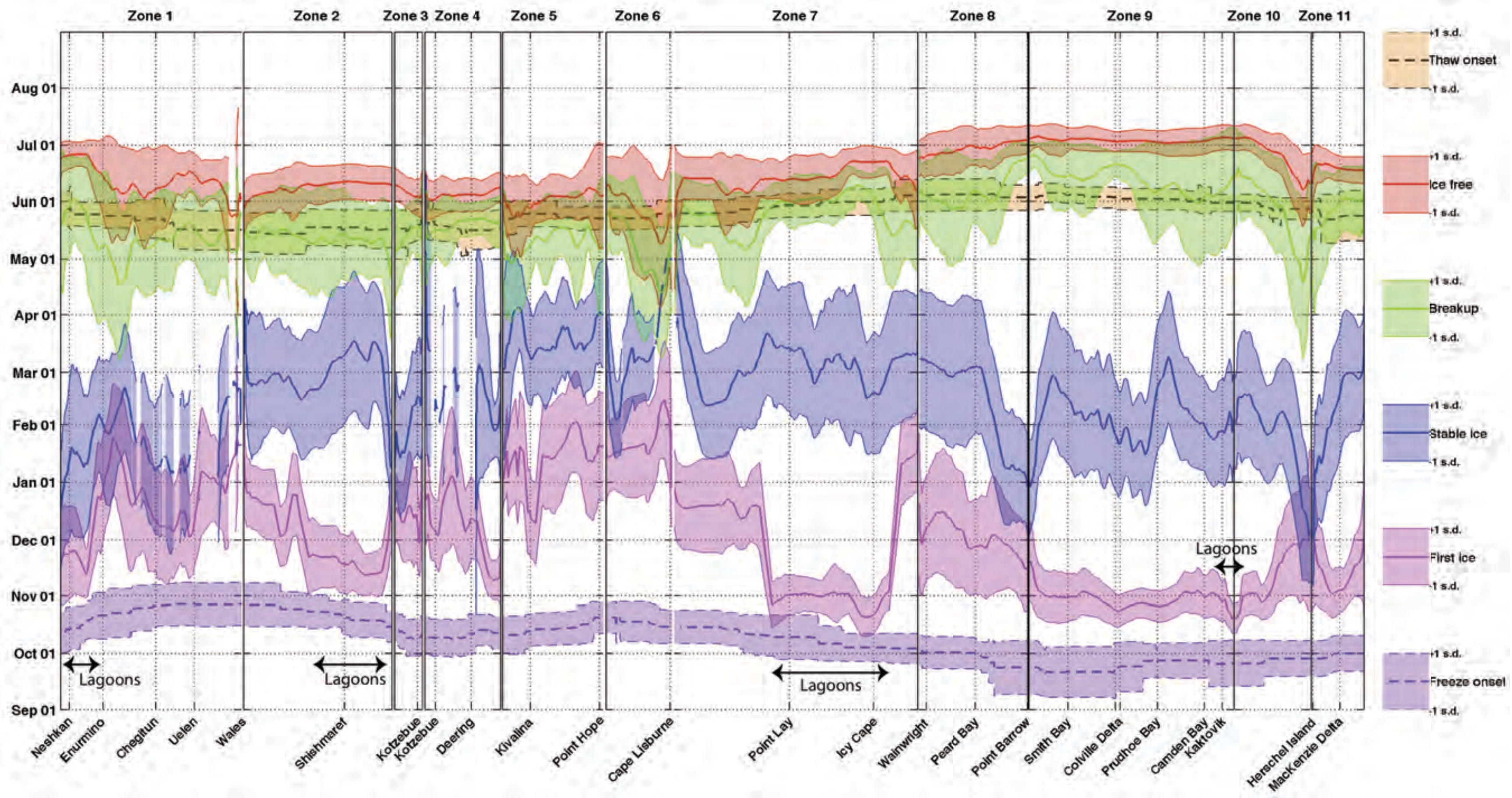

Figure 4.3.6: Spatial variability in the dates of occurrence of 4 key events in the annual cycle and the onsets of freezing and thawing derived from NCEP reanalysis data. The bold lines indicate the mean of the 8-year study period and the transparent colored regions indicate ±1 standard deviation from the mean. The x-axis represents the 8,889 coast locations from west to east (see Figure 3.3.4). Arrows indicate sections of coast with lagoons.

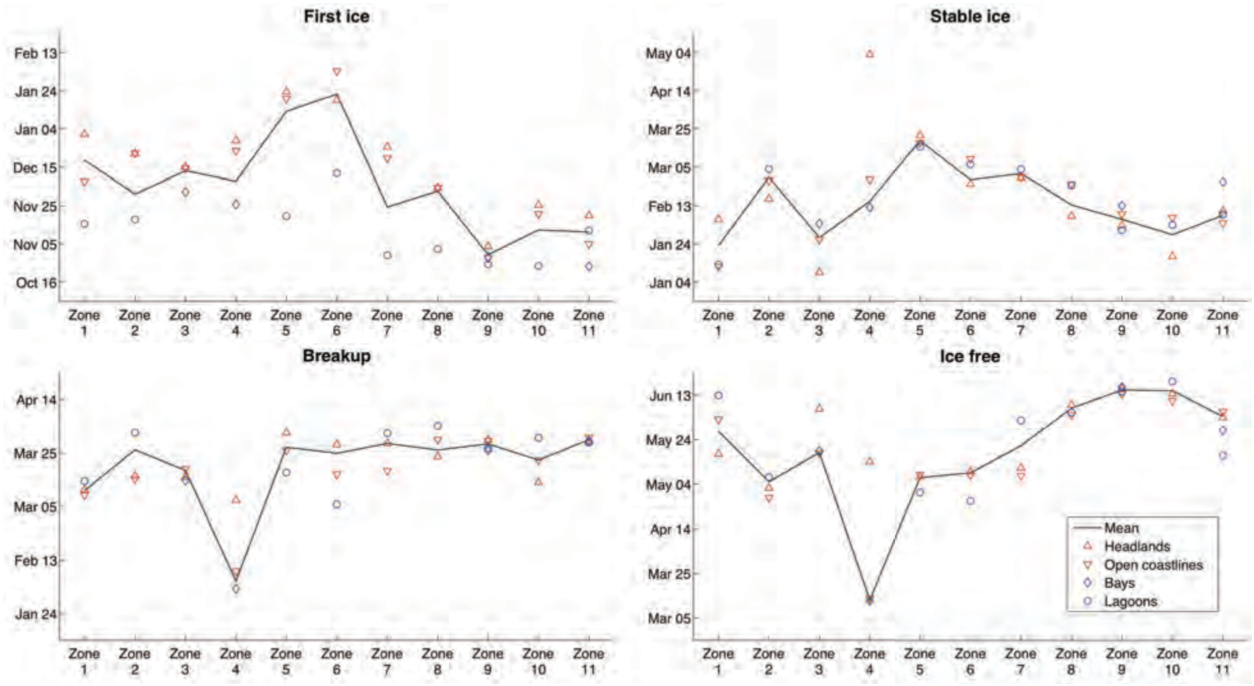

Figure 4.3.7: Variability in the mean occurrence date of key landfast ice events in different coastal zones. The symbols indicate the mean dates calculated separately for headlands, open sections of coast, embayments and lagoons.

4.3.5 Episodic Events

We use the term episodic events to refer to the brief events that occur at irregular intervals and result in a deviation of the SLIE position from the mean annual cycle. These may take the form of breakouts, where the SLIE retreats toward the coast; or stable extensions, where the SLIE occupies a region unusually far offshore. Breakouts are potentially hazardous events for those on the landfast ice and the susceptibility of a region to breakouts may be a limiting factor for ice-based operations. The significance of stable extensions is less clear. Though the pose no direct hazard, they have the potential to inhibit hunting activities at the SLIE and they preclude momentum transfer from the atmosphere to the ocean for the time that they persist, which may effect under-ice currents. In the time series of landfast ice width (e.g., Figure 4.3.5) extensions appear as abrupt peaks and breakouts and indicated by sharp troughs.

Small stable extensions appear to be a ubiquitous feature of the annual cycle through the Chukchi and Beaufort Coast. However, during the period 1996-2008 there were a number of exceptional stable extensions where the landfast ice extended far beyond the modal location of the SLIE. For example, Figure 4.3.5a shows three occasions when the landfast at Kaktovik was over 100 km wide. To identify the occurence of significant stable extension we analyzed the SLIE data using two criteria:

i) the SLIE is positioned at least 5 times further offshore than the modal landfast width

ii) the extension occurs along a section of coast that spans at least 100 consecutive coastal coordinate vectors (~200 km)

Using these criteria, we identified 24 separate stable extensions, which are listed in Table 4.3.3. The coverage of each extension can be seen by examining the corresponding season in Figure 4.3.2.

During these stable extensions, particularly those that occur in the Beaufort Sea, the SLIE occupies water deeper than that of any keel, which suggests that their existence is related to regional-scale dynamical ice conditions that compress the ice against the coast with minimal shear. The possible exception to this is the recurring extension that forms in coastal zone 2 along the northern Seward Peninsula between Wales and Shishmaref in the vicinity of the Cape Prince of Wales Shoal (Figure 1.3.1). This is the most commonly occurring stable extension in the study region and based on local observations and traditional knowledge is driven by the grounding of ice in the nearby shallow water (C. Nayokpuk, personal communication, 2012).

Table 4.3.3: Occurrences, duration and location of stable landfast ice extensions. Dates correspond to the dates of the first and last SAR mosaics in which the extension was observed.The termination of the extensions highlighted in red are linked to corresponding breakout events in Table 4.3.4.

			Coastal zone (see Figure 3.3.4)										
Year	Period	Duration	1	2	3	4	5	6	7	8	9	10	11
1998	Jan 12 - Mar 12	60 days							▨				
1998	Jan 22 - Feb 26	36 days	▨										
1998	Feb 26 - Mar 29	32 days	▨										
1999	Mar 25 - Apr 26	33 days									▨	▨	▨
1999	Mar 30 - Apr 24	26 days	▨										
1999	Mar 30 - Apr 14	16 days							▨				
2000	Feb 23 - Apr 08	46 days									▨	▨	▨
2000	Mar 14 - Apr 03	21 days	▨										
2000	Mar 24 - Apr 11	19 days	▨										
2000	Mar 24 - Jun 22	91 days		▨	▨								
2001	Mar 02 - Mar 27	26 days	▨										
2003	Mar 16 - Apr 10	26 days		▨									
2004	Feb 15 - Mar 11	26 days	▨										
2004	Feb 15 - Mar 08	23 days									▨		
2004	Feb 25 - Mar 18	23 days										▨	
2005	Mar 14 - Apr 09	27 days									▨	▨	
2005	Mar 28 - May 27	61 days		▨									
2006	Jan 19 - Feb 05	18 days					▨						
2006	Feb 21 - Jun 05	105 days			▨				▨				
2006	Apr 17 - May 12	26 days		▨									
2007	Mar 09 - Mar 31	23 days		▨									
2007	Mar 29 - Jun 10	74 days							▨				
2007	Apr 12 - May 31	50 days		▨									
2008	Feb 26 - Mar 24	28 days	▨										

To identify breakouts, we used the following criteria:

i) the SLIE retreated by at least half of the modal landfast width

ii) the retreated SLIE lies less than one third of the modal landfast width from the coast

iii) the breakout affects along a section of coast that spans at least 100 consecutive coastal coordinate vectors (~200 km)

Using these criteria, we identified 63 significant breakout events during the middle of the annual landfast ice cycle between January and April. These events are listed in Table 4.3.4, which indicates that the regions most succeptible to breakouts are coastal zones 1 and 2, which lie in the southernmost part of the Chukchi Sea and face northward. The lack of observed breakouts in zone 6 (between Point Hope and Cape Lisburne) is largely due to the fact that landfast ice does not often form in long continuous sections in this zone and so criterion iii) was never satisfied. The criteria listed above were chosen to highlight the most significant breakout extents captured by the SLIE dataset. Less extensive breakouts can still impact human activities, but they are too numerous to list in this report. Reducing the number of consecutive coast vectors by half in criterion iii) leads to approximately twice as many breakout events.

During 1996-2008, there were two breakout events that were notable for their extent. These are highlighted in red in Table 4.3.4 and correspond to the termination of stable extensions listed in 4.3.3. Between February 23 - April 8, 2000, a vast stable extension of landfast ice occupied the majority of the southeastern Beaufort Sea. This extension broke up during the period April 8-18 leaving the SLIE within approximately 15 km of the coast along much of zones 9-11. In 2006, landfast ice broke out almost everywhere in the Chukchi sometime between February 5 and February 22. This terminated the only stable extension of landfast ice observed in zone 5 and constituted the only occasion when landfast ice in Kotzebue Sound broke up during winter. However, it should be noted that there were two seasons (2000-01 and 2003-04) when Kotzebue Sound never acquired a complete landfast ice cover.

Table 4.3.4: List of significant breakout events and coastal zones affected. Dates correspond to the last date of the SAR mosaic in which the breakout was observed. The two events highlighted in red were widespread breakouts related to the break-up of stable extensions indicated in Table 4.3.3.

	Coastal zone (see Figure 3.3.4)										
Date	1	2	3	4	5	6	7	8	9	10	11
Feb 10, 1997		■									
Mar 17, 1997	■	■					■				
Apr 10, 1997		■									
Jan 23, 1997		■									
Feb 26, 1998	■				■						
Mar 26, 1998							■				
Mar 29, 1998	■										
Apr 21, 1998		■									
Apr 29, 1998		■									
Feb 11, 1999	■	■									
Mar 07, 1999	■										
Apr 26, 1999									■		
Apr 24, 1999							■				
May 08, 1999	■										
May 08, 1999										■	■
Mar 08, 2000	■	■									
Apr 18, 2000									■	■	■
Apr 25, 2000	■	■									
Jan 24, 2000	■										
Feb 07, 2001	■						■				
Feb 18, 2001										■	
Feb 17, 2001	■	■					■				
Apr 11, 2001										■	
May 01, 2001										■	
Jan 19, 2001	■										
Mar 02, 2002									■		
Mar 22, 2002					■						
May 02, 2002	■	■									
May 03, 2002									■		
Feb 10, 2003								■			
Feb 14, 2003	■										
Feb 27, 2003								■			
Mar 06, 2003		■									
Apr 10, 2003							■				
Apr 20, 2003	■	■									
May 05, 2003									■	■	
Mar 21, 2004	■										
Mar 18, 2004									■		
Mar 29, 2004									■	■	■
Mar 28, 2004							■				
May 08, 2004	■										
May 08, 2004										■	■
Feb 20, 2005							■				
Feb 27, 2005		■									
Apr 23, 2005			■		■		■				
May 03, 2005	■										
Jan 22, 2005		■									
Jan 29, 2006							■				
Jan 29, 2006									■		
Feb 22, 2006	■	■	■	■	■		■				
Mar 01, 2006									■		
Apr 18, 2006									■		
Apr 18, 2006					■						
Apr 28, 2006	■										
Mar 10, 2007									■	■	■
Apr 06, 2007										■	
Apr 06, 2007		■									
Jan 26, 2008							■				
Mar 31, 2008		■									
Apr 06, 2008		■									
Apr 07, 2008									■		
Apr 17, 2008	■										
May 01, 2008	■	■									
Total # events	22	20	2	1	5	0	12	1	13	10	5

The susceptibility of different parts of the coast to landfast break-out is further illustrated in Figure 4.3.8, which shows where landfast ice is most likely to retreat during each month. The regions closest in color to white indicate where landfast ice is most stable. Red colors indicate increasing likelihood of ice retreating in a given month. Areas shaded with blue were never observed to retreat in a given month. Darker blue areas indicate decreasing probability of the landfast ice occupying that location. These values were calculated by comparing consecutive SLIE delineations to identify areas where landfast ice retreated. We calculated the likelihood of retreat by counting the number of times ice retreat was observed and dividing by the total number of times landfast ice was observed at given location. This analysis highlights areas of the coast where landfast ice is more dynamic and more susceptible to breakouts.

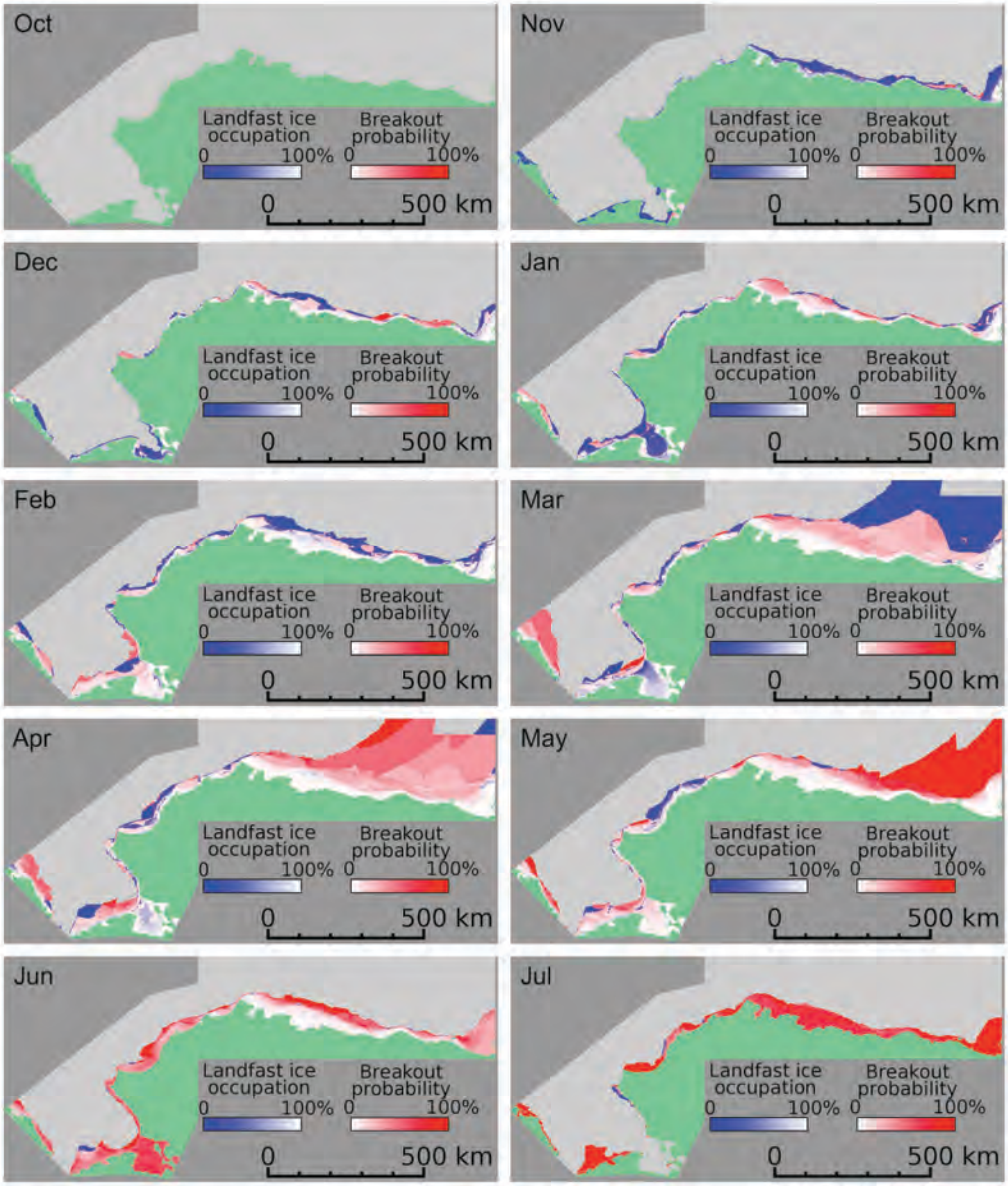

Figure 4.3.8: Monthly maps indicating the probability of landfast ice retreating from a given location. White regions indicate stable landfast ice. Red regions indicate a high likelihood of retreating while blue regions indicate areas where no retreat was observed, but which were rarely occupied by landfast ice.

4.4 Validation of landfast ice mapping from L-band InSAR

For evaluating the performance and reliability of the landfast ice detection from L-band InSAR that was introduced in Section 3.4, several SAR interferograms were processed over two test sites, the area around Point Barrow, Alaska, and the coastline of the Seward Peninsula, Alaska. These two test sites were selected to cover different climatic zones of the arctic environment, with longer, colder, and more stable landfast ice conditions in Barrow. Also, the test sites offer varying conditions in terms of general ice drift, wind exposure, and ocean currents, all factors that influence landfast ice development and stability. The InSAR data sets shown in the following were chosen to represent different conditions throughout the landfast ice season in order to enable an assessment of performance as a function of landfast ice age and thickness, and dependent on changing weather conditions. The Barrow, Alaska examples were acquired later in the landfast ice season at a time where both the weather conditions and the landfast ice itself were rather stable. The data sets over Seward Peninsula, Alaska stem from a time early in the landfast ice season with more variable climatic conditions and less stable landfast ice extent. Both sets of examples were randomly chosen from all data covering the respective season at the respective geographic location and are representative for the total bulk of available data.

Radarsat-1 ScanSAR data was processed using the techniques presented in Section 3.3 to provide reference data for evaluating the relative performance of the L-band InSAR-based method. To minimize errors in the reference data, the landfast ice edge was extracted manually from the Radarsat-1 ScanSAR imagery processed to gradient difference images. For mapping the landfast ice edge from L-band InSAR, the automated workflow described in Section 3.4.5 was used. In the following, relative performance analyses are presented for several InSAR pairs over both test sites to provide prove for the consistency, suitability, and accuracy of the presented methods.

4.4.1 Approach for Data Harmonization and Comparison

To facilitate a comparison of landfast ice extents derived from L-band InSAR and the reference technique, the temporal sampling of the individual data sources has to be unified. Due to the long repeat interval of currently available L-band SAR data, L-band InSAR-derived landfast ice edges correspond to sea ice areas that remained stable over a time span of *46 days*. Due to a shorter repeat interval of the sensor Radarsat-1 and because of the large spatial coverage of Radarsat-1 ScanSAR images and the resulting large overlap of neighboring scenes, the reference technique defines landfast ice as sea ice that remained stationary over a time interval of about *20 days*. Hence, the landfast ice extent mapped by both techniques follows different physical definitions, and an approach has to be defined to transform derived results to a common temporal sampling.

The extent of landfast ice, detected by the different methods, decreases with the length of the observation window. For InSAR data, only ice that remained stationary over an entire 46-day interval will be classified as landfast ice, corresponding to the minimum landfast ice extent during the observation period. To ensure intercomparability, all landfast ice edges extracted by the reference approach within a 46-day period are compared and their minimum extent is extracted manually as the representative ice edge for that period. An example for the extraction of the 46-day reference landfast ice edge from all 20-day outlines is shown in Figure 4.4.1 for an area near Barrow, Alaska, where Figure 4.4.1a shows the original 20-day reference outlines as colored lines on top of a phase filtered L-band interferogram. In Figure 4.4.1b the minimum ice extent has been extracted from the set of 20-day edges. A visual comparison of the coherent area in the SAR interferogram and the 46-day reference ice edge shows good agreement

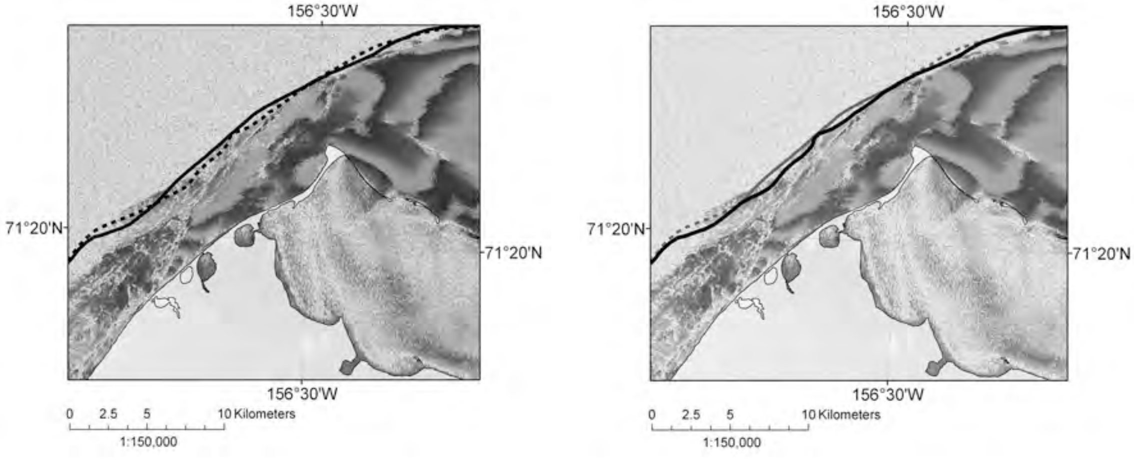

a) b)

Figure 4.4.1: Interferogram showing fringes over landfast sea ice near Barrow, Alaska, over a 46-day period. Acquisition dates for this interferogram are listed under "Interferogram B" in Table 4.4.1. a) The dashed and solid lines indicate two different SLIEs derived for this period using the methodology described in section 3.3. b) The black solid line indicates the minimum area encompassed by the two lines shown in panel a), which are shown in gray.

4.4.2 Application to Test Area near Barrow, Alaska

4.4.2.1 Available Datasets

An overview of the Radarsat-1 and ALOS PALSAR data sets used for the area of Barrow, Alaska is shown in Table 4.4.1. Out of all available SAR data, two representative interferograms (A and B in Table 4.4.1) were selected for a demonstration of the performance of InSAR-based landfast ice mapping. For the periods covered by both interferograms, four Radarsat-1 ScanSAR acquisitions were available (See Table 4.4.1, left side), from which two ~20-day landfast ice edges were derived using the reference technique.

Table 4.4.1: Data sets used for a relative performance analysis of InSAR-based landfast ice mapping and reference technique.

	L-band InSAR Data				Radarsat-1 Data			
	Orbit/Frame	Acquisition Dates	Δt	$B_\perp$	Orbit/Frame	Acquisition Dates	Δt	
Interferogram A	10842/1430	02/06/08	46 days	630 m	63986/273	02/16/08	18 days	
					64129/273	02/27/08		17 days
					64268/273	03/05/08		
	11513/1430	03/23/08			64529/273	03/15/08		
Interferogram B	11265/1430	03/06/08	46 days	570 m	64386/273	03/15/08	20 days	
					64529/273	03/25/08		18 days
					64672/273	04/04/08		
	11936/1430	04/21/08			65058/273	04/12/08		

4.4.2.2 Performance Analysis

From the original gradient difference image-based outlines, covering a time span of ~20 days each, a representative reference outline for comparison to the SAR interferograms was derived following the approach presented in Section 4.4.1. This derived reference outline was then compared to InSAR-based landfast ice edges for an evaluation of relative performance. This comparison has been carried out for both interferograms A and B (see Table 4.4.1). Figure 4.4.2 shows a segment of interferogram B to showcase the comparison procedure. In Figure 4.4.2a the reference outline and the InSAR-derived outline are projected onto interferogram B as red and blue lines, respectively. A first comparison of these lines indicates that the two methods produce very comparable results.

Figure 4.4.2b shows the results of a quantitative comparison between landfast ice areas extracted by the two techniques. Differences in coverage are classified into two classes: i) reference extent smaller than InSAR-based extent (red areas in Figure 4.4.2b), and ii) reference extent larger than InSAR-based extent (blue regions in Figure 4.4.2b). Regions of coherence in the interferograms must correspond to areas that remained stationary over the entire 46 day interval. Red segments therefore indicate underestimation of landfast ice extent by the reference technique. On the other hand, blue areas indicate regions that did not remain coherent over the 46-day interval and yet remained stationary according to the reference technique. Reduced coherence, and therefore an underestimation of landfast ice area by InSAR-based techniques, can appear in regions dominated by very smooth young sea ice, whose low backscatter gives rise to poor SNR. A relative comparison of extracted landfast ice areas will provide insight into the relative performance of the applied methods. While we are lacking accurate, dedicated ground-truth information, a coastal radar covering much of the area shown in Figure 4.4.2 (*Druckenmiller et al.*, 2009) indicates ice to be stable, though varying in backscatter strength, throughout the time period covered by interferogram B.

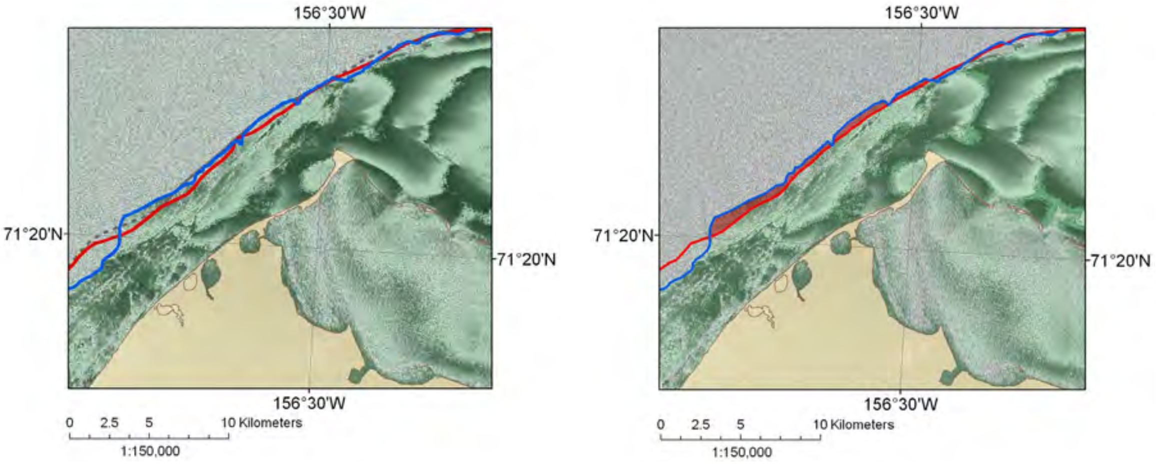

a) b)

Figure 4.4.2: a) Reference landfast ice edge in red compared to InSAR-based landfast ice edge in blue derived from interferogram B (Table 4.4.1); b) differences in landfast ice area between the two techniques. Red areas correspond to a relative underestimation by reference technique; blue area shows relative underestimation by InSAR-based technique.

An areal analysis of relative extraction errors is presented in Figure 4.4.3 for interferogram B spanning March 3 to April 21, 2008. The interferogram together with reference and

InSAR-derived landfast ice edge are presented in Figure 4.4.3a. Areal differences between the outlines are analyzed in Figure 4.4.3b where the entire outline is broken up into 20 segments of positive and negative area differences for which statistical parameters were derived. As before, negative (red) segments indicate relative underestimation by the reference technique while positive (blue) segments indicate a relative underestimation of landfast ice extent by the InSAR-based approach. From the visual representation in Figure 4.4.3a as well as the statistical analysis in Figure 4.4.3b, it is evident that both techniques provide very consistent results with landfast ice area differing by only over a coastline length of 95km. In a relative comparison, areal biases are slightly lower for the new InSAR-based method confirming its suitability for the task of landfast ice mapping.

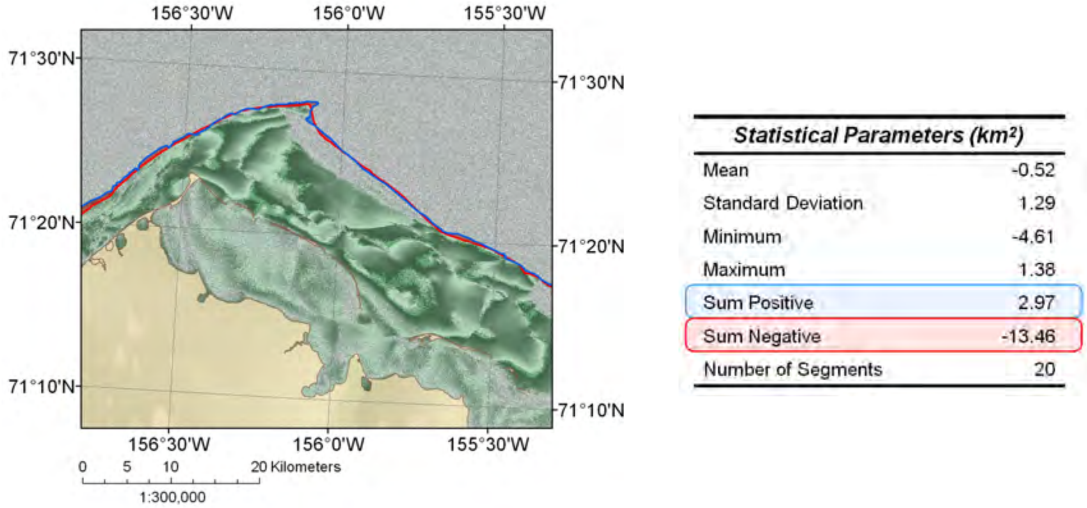

Statistical Parameters (km²)	
Mean	-0.52
Standard Deviation	1.29
Minimum	-4.61
Maximum	1.38
Sum Positive	2.97
Sum Negative	-13.46
Number of Segments	20

a) b)

Figure 4.4.3: a) Interferogram B together with reference and InSAR-derived landfast ice edges for the period spanning March 3 – April 21, 2008; b) analysis of areal differences between the outlines where the entire outline is broken up into 20 segments of positive and negative area differences.

Results for the interferogram A, spanning February 6 to March 23, 2008, (see Table 4.4.1) are presented in Figure 4.4.4. While this example also demonstrates generally consistent results from both methods, it reveals some minor but important differences, in particular at the center of the scene where the coherence image is significantly underestimating landfast ice extent relative to the reference technique (see blue area in Figure 4.4.4a), limiting the detected landfast ice area to a narrow ice bridge. For a statistical comparison of the techniques, two tables are shown in Figure 4.4.4b and c. The first one (Figure 4.4.4b) presents an analysis of areal differences based on all segments along the analyzed part of the coastline, indicating a significant relative underestimation of ice area by $\Delta a \approx 3.25 km^2$ committed by InSAR-based mapping. As this difference is largely caused by one segment, a second table is added (see Figure 4.4.4c) to analyze the relative performance of the techniques outside of this anomalous region. This second comparison shows very little difference between the techniques ($\Delta a < 0.15 km^2$) and verifies their general comparability.

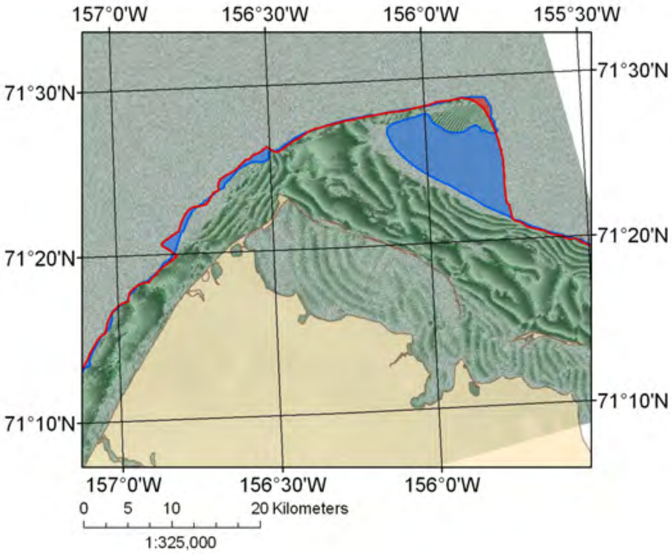

a)

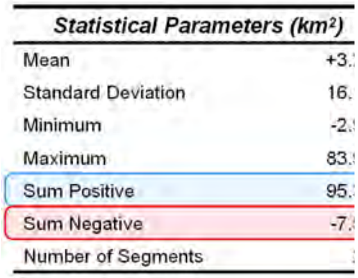

Statistical Parameters (km²)	
Mean	+3.
Standard Deviation	16.
Minimum	-2.
Maximum	83.
Sum Positive	95.
Sum Negative	-7.
Number of Segments	

b)

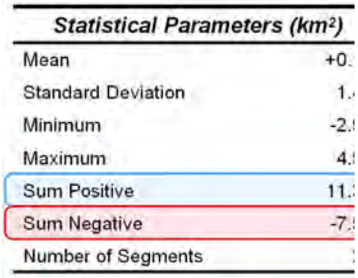

Statistical Parameters (km²)	
Mean	+0.
Standard Deviation	1.
Minimum	-2.
Maximum	4.
Sum Positive	11.
Sum Negative	-7.
Number of Segments	

c)

Figure 4.4.4:a) Interferogram A together with reference and InSAR-derived landfast ice edges for the period spanning February 6 – March 23, 2008; b) and c) analysis of areal differences between the outlines. In c), the anomalous region of large areal differences is ignored in the statistics.

To understand the observed differences in Figure 4.4.4 we conducted a closer analysis of both a time series of Radarsat-1 ScanSAR scenes covering this time span and the ALOS PALSAR imagery contributing to the L-band interferogram. This detailed inspection showed two main features contributing to extraction errors: 1) variation of the landfast ice edge over the 46 day period introduced by hinging motion of parts of the ice close to the shore (see Figure 4.4.5a and b), and 2) very low radar backscatter cross-section for a part of the landfast ice identified as area "A" in Figure 4.4.5b. Figure 4.4.5a shows four landfast ice edges extracted by the reference technique together with their respective time intervals. The evolution of the landfast ice edge is shown by colored lines overlaid on a superposition of a Radarsat-1 ScanSAR scene and the ALOS PALSAR interferogram. Note that the colored lines were derived using additional SAR data outside of the 46-day period of the interferogram.

From Figure 4.4.5a it can be seen that the landfast ice extent varied extensively especially in areas to the east of the coherent ice bridge. This strong variation is caused by a hinging motion of large parts of the landfast ice area between the beginning of February and the middle of March, 2008. The rotational motion was centered about a point to the northeast of Point Barrow, causing a lead to open up. The width of this lead increases with distance from Point Barrow and reaches a maximum of about two miles at the eastern edge of the coastline segment shown in Figure 4.4.5a. The affected landfast ice patch is indicated in Figure 4.4.5b where the dashed white line represents the location of the ice before the hinging motion, while the solid white line shows its location after the displacement occurred. This motion led to an underestimation of landfast ice extent by both the reference technique and the InSAR-based method (see also Figure 4.4.5a as a reference). The decorrelation of the InSAR phase was due to motion-induced co-registration mismatch. Additional coherence loss that can be observed to the west of the area affected by ice motion (area “A” in Figure 4.4.5b) is caused by a very low SNR on smooth ice patches. The combined effect of both factors gave rise to the underestimation of landfast ice extent in this example.

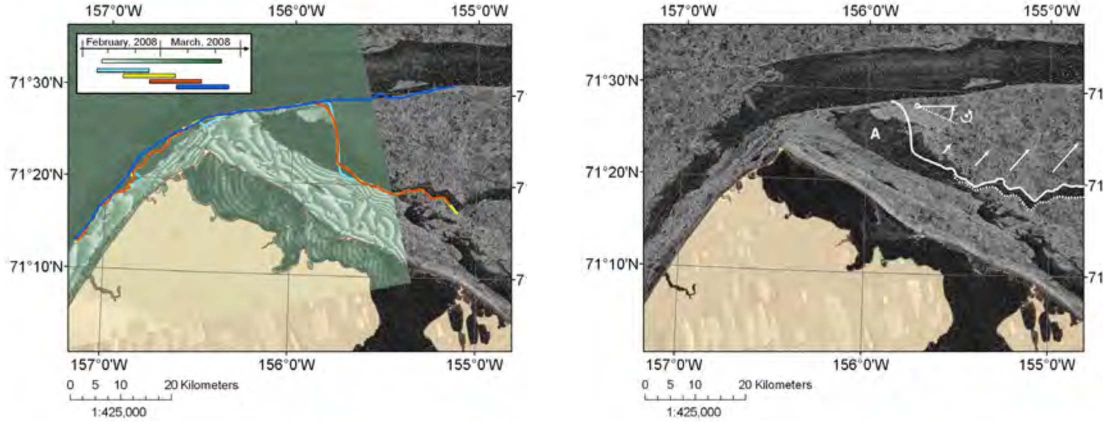

a) b)

Figure 4.4.5: a) The interferogram from Figure 4.4.4a shown with four landfast ice edges identified using the reference technique spanning a similar time period (time spans indicated by insert at top left); b) an analysis of a time series of Radarsat-1 ScanSAR images revealed a hinging motion of large parts of the landfast ice area as the main cause for errors in landfast ice estimates by both the reference and the InSAR-based techniques. Area “A” marks a low backscatter region causing SNR-based coherence loss.

4.4.3 Application to Test Area Seward Peninsula, Alaska

4.4.3.1 Available Datasets

As stated above, the northern Seward Peninsula, Alaska has been added as a second test site to increase the level of generality of the derived performance measures. The Seward Peninsula is characterized by shorter landfast ice seasons governed by more dynamic environmental conditions. Also, drift patterns and velocities of drifting sea ice differ compared to test site Barrow, Alaska, resulting in different landfast ice dynamics. An overview of the Radarsat-1 and ALOS PALSAR data sets used for Seward Peninsula, Alaska is shown in Table 4.4.2. Two neighboring InSAR frames of the early landfast ice season are shown along with several Radarsat-1 ScanSAR acquisitions for both data sets (See, Table 4.4.2 left side).

4.4.4 Performance Analysis

Results for both neighboring InSAR frames are presented in Figure 4.4.6 indicating a high general consistency between the results of the applied methods. As in the previous examples, reference outline and InSAR-derived outline correspond very well for most areas. Larger differences occur only along the northern tip of the captured area of the Seward Peninsula, where changes of the sea ice drift field and ocean currents result in highly dynamic landfast ice conditions. Hence, for the statistical comparison of the techniques (see Figure 4.4.6b), these anomalous features were ignored. The areal differences between both techniques are presented in Figure 4.4.6b and are again very small, with an average difference of only $\Delta a \approx 0.2 km^2$. Therefore, both test sites show a high consistency between the results provided by both detection techniques and suggest the suitability and sufficient performance of L-band InSAR for automated landfast ice mapping.

Table 4.4.2: Data sets used for a relative performance analysis of InSAR-based landfast ice mapping and reference technique.

	L-band InSAR Data				Radarsat-1 Data				
	Orbit/Frame	Acquisition Dates	Δt	$B_\perp$	Orbit/Frame	Acquisition Dates	Δt		
Interferogram C	10186/133	12/23/07	46 days	950 m	63343/28	01/02/08	14 days		
					63486/28	01/09/08		17 days	
					63586/28	01/16/08			17 days
					63829/28	01/26/08			
	10857/133	02/07/08			63929/28	02/02/08			
Interferogram D	10186/132	12/23/07	46 days	952 m	63343/28	01/02/08	14 days		
					63486/28	01/09/08		17 days	
					63586/28	01/16/08			17 days
					63829/28	01/26/08			
	10857/132	02/07/08			63929/28	02/02/08			

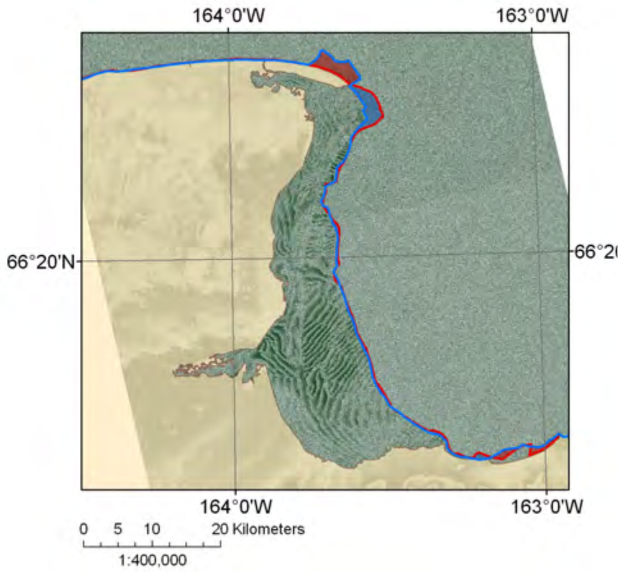

a)

Statistical Parameters (km²)	
Mean	0.21
Standard Deviation	1.34
Minimum	-2.73
Maximum	3.83
Sum Positive	9.40
Sum Negative	-6.40
Number of Segments	24

b)

Figure 4.4.6: a) The interferogram together with reference and InSAR-derived landfast ice edge for an interferogram spanning December 23, 2007 – February 7, 2008; b) statistical analysis of areal differences between the outlines where positive differences correspond to relative errors of the reference outlines and negative differences indicate relative underestimation by InSAR-based mapping efforts.

5. DISCUSSION

5.1 Potential analysis errors and biases

The most significant sources and magnitudes of geolocation, detection and classification errors both for leads and landfast ice are described in detail in Sections 3.2 and 3.3. Outside of these, the most important potential source of errors and in particular bias is the limitation of the lead analysis to cloud-free regions and periods. As outlined in previous sections, with limitations in resolution and other problems, AVHRR still remains the most relevant source of data on lead distributions and morphology, at least in the context of studies such as this. Nevertheless, since leads are in significant part driven by atmospheric processes, lack of data on lead morphology and distribution during cloudy periods may result in a bias towards atmospheric conditions favoring cloud-free skies. In the study area, these conditions are associated with a Beaufort Sea high pressure system, with winds predominantly out of the east and northeast (see also Section 4.2.3). The penetration of low-pressure systems is associated with winds veering to southerly and westerly sectors. Such weather situations are increasingly common in the summer and fall months in the study region (*Lynch et al.*, 2003), and the summer weakening of the Beaufort high pressure system in part explains increasing cloudiness. At the same time, reductions in summer sea ice in the region may increase cloudiness as well (*Liu et al.*, 2012). In general, as illustrated in Figures 3.2.3 and 3.2.4, the Chukchi Sea is cloudier than the Beaufort Sea, with more frequent incursions of storms and greater prevalence of stratus in summer. In winter, passage of individual storms is typically followed by clearer weather. Since leads have an average lifetime that extends over several days, analysis of the first cloud-free scene available after such periods still contains information about the morphology and size of leads that developed. Furthermore, direct inspection of daily scenes and qualitative comparisons between highly obscured lead patterns and cloud-free conditions suggests that the resulting cloud bias is small.

5.2 Lead patterns

5.2.1 Distribution of leads in the context of large-scale ice motion and deformation: Recurrence of observed patterns

Building on the work conducted for MMS OCS STUDY 2005-068, we expanded on the quantitative analysis of lead recurrence patterns conducted in the previous study by calculating the probability of lead occurrence based on the entire data set of binarized lead data, displayed for the two subregions by month in Figures 5.2.1 and 5.2.2. Focusing first on the entire data set, shown in the left column in each figure, it is clear that many of the features described at length in Section 4.2 express themselves as high lead occurrence probabilities in the monthly maps. For the Chukchi Sea, and less so for the Beaufort Sea, high cloud cover and the migration of the marginal ice zone into the region in May and June limit the value of data for the latter two months, as well as for the month of November when freeze-up is still progressing. The recurrence maps reproduce in a quantitative fashion the recurrence and co-location of key large-scale lead and polynya features that represent the response of the ice pack and landfast ice to atmospheric forcing as constrained by the regional topography and bathymetry as well as the rheology of the ice pack. The distribution of (i) flaw leads and coastal polynyas, (ii) arced and linked lead patterns, (iii) lead systems associated with shoals, and (iv) the transition from winter to spring lead conditions will be discussed in more depth below. A key aspects of the data is the regional contrast between ice conditions in Chukchi as opposed to the Beaufort Sea, clearly expressed in the summary figures. Moreover, the new study in comparison to MMS OCS STUDY 2005-068 reveals a striking contrast in the distribution of lead patterns in the Beaufort Sea for recent years compared to the period prior to 2005. This difference is also expressed in the two panels at center and right in Figure 5.2.2.

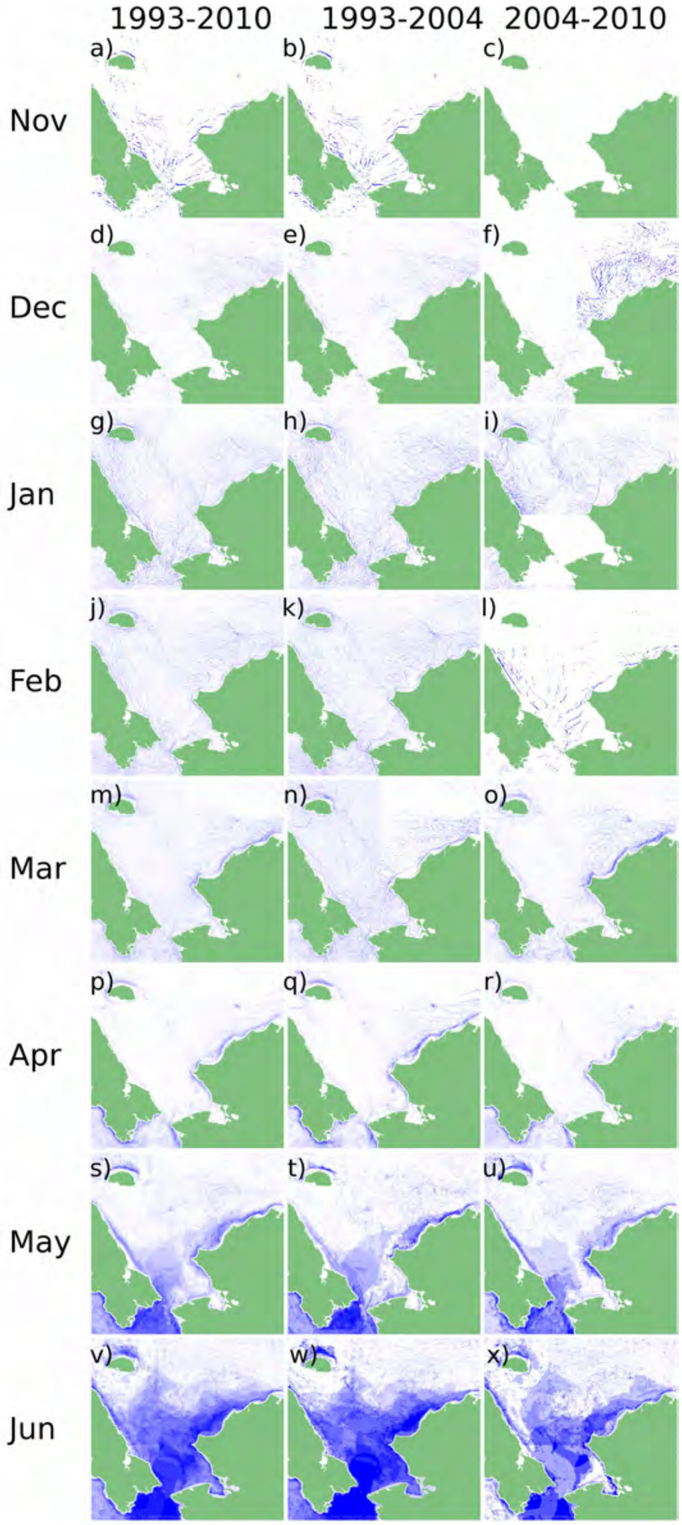

Figure 5.2.1: Monthly recurrence probability of leads in the Chukchi Sea subregion, derived from all images for each month during the time periods 1993-2010 (left), 1993-2004 (middle) and 2005-2010 (right) for each grid cell. Subregions with partial or complete cloud cover have been excluded from the analysis. The significance of different patterns evident in the data is discussed in detail in the text.

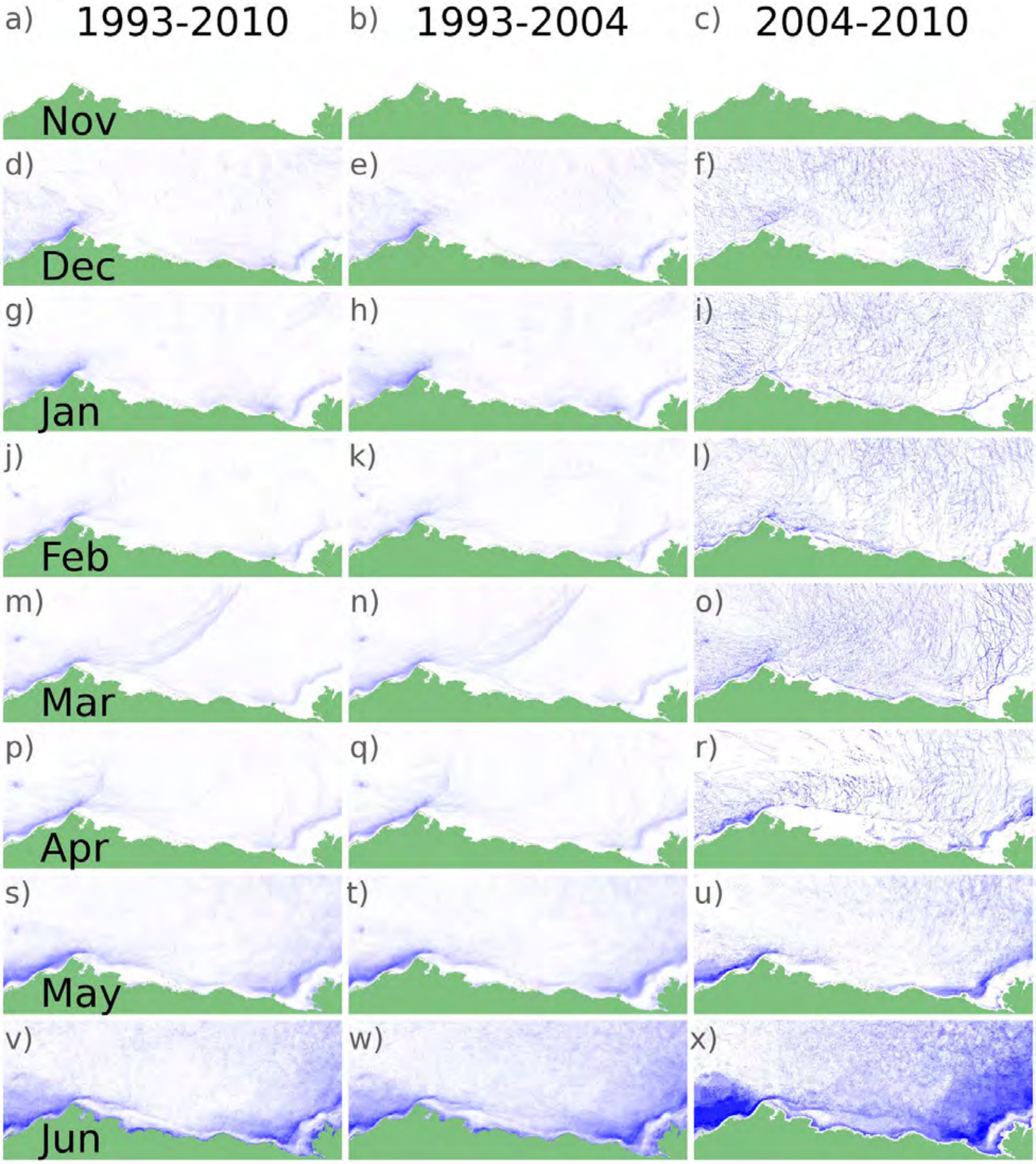

Figure 5.2.2: Monthly recurrence probability of leads in the Beaufort Sea subregion, derived from all images for each month during the time periods 1993-2009 (left), 1993-2004 (middle) and 2005-2009 (right) for each grid cell. Subregions with partial or complete cloud cover have been excluded from the analysis. The significance of different patterns evident in the data is discussed in detail in the text.

(i) Flaw leads and coastal polynyas

The Chukchi Sea, and to a lesser degree the Beaufort Sea, is characterized by recurring coastal lead patterns that are particularly prominent in the months of March through May (Figures 5.2.1 and 5.2.2). Polynyas are defined as openings in the ice with a non-linear shape and the polynyas occurring adjacent to the landfast ice or coast are referred to as flaw or coastal polynyas (*World Meteorological Association*, WMO, 1983). According to WMO Sea Ice Nomenclature, the flaw zone is a narrow zone between pack ice and landfast ice "where the pieces of ice are in a chaotic state" as a result of (shear) deformation. *Norton and Graves Gaylord's* (2004) analysis of ice motion in the Barrow region indicates that the flaw zone, as defined by high, shore-parallel ice velocities, can extend several tens of kilometers offshore between March and June. In both the Chukchi and the Beaufort Sea, the extent of the flaw zone as defined by interannual monthly lead recurrence larger than approximately 20 % does in fact range between about 10 km and more than 100 km when it appears at its widest. Note, however, that the seasonal variation in flaw zone extent based on lead distribution also depends on ice growth rates, as these define the transition between thin lead ice and thicker pack ice.

Along the Beaufort coast, such persistent leads and polynyas are limited to the Mackenzie Delta, Herschel and Barter Island (Figure 5.2.2). In the Chukchi Sea, the most prominent coastal polynyas and flaw leads form along the eastern Chukchi Coast between Point Hope and Point Barrow, as well as to the north and west of Wrangel Island, with less distinct flaw leads appearing off the northern coast of Chukotka. While outside of the main study area, coastal polynyas are also noteworthy along the southern coast of Chukotka and southeast of Cape Prince of Wales. The location of these flaw and coastal leads and polynyas is an indication of their mode of formation, as they a show a clear pattern of preferential occurrence downdrift of promontories or lee coasts as typical of so-called "latent heat" polynyas generated by offshore winds (*Gordon and Comiso*, 1988). The prevailing winds in the study area are out of ENE at Barrow and E at Barter Island. With a typical turning angle of 20 to 30° to the right of the local wind (*Hibler*, 1986; *Kottmeier et al.*, 1992), this explains the recurrence patterns of flaw leads or polynyas as well as the absence of such openings in much of the western and central Beaufort Sea and the coast of Chukotka of the western Chukchi Sea.

The extent of the flaw zone or the flaw-lead/polynya zone is of significance in the context of potential oil-spill clean-up efforts. The high ice velocities, complex ice motion patterns, and mix of open water, thin ice and highly fragmented ice floes as a result of shear between landfast ice and ice pack result in a challenging environment in the context of oil-spill mitigation. It is notable, however, that in the central portions of the Beaufort Sea, the orientation of the coast with respect to the prevailing wind patterns results in very small lead recurrence probabilities and instead favors the formation of shear ridges.

Beginning in May, the recurrence maps reflect coastal flooding as a result of the onset of ice break-up and over-flooding. For the Beaufort Sea, the geographic extent and timing of such flooding have been analyzed in great detail by *Dickins et al*. (2011) and are not further considered in the context of this study.

(ii) Arced and linked lead patterns in the Chukchi Sea

As apparent from the results presented in Section 4.2, the topography of the Chukchi Sea works in concert with prevailing wind direction to generate a range of lead distribution patterns. Nevertheless, both the analysis based on specific features identified in Section 4.2, as well as the examination of lead recurrence maps allows us to identify a few key patterns that are of relevance in the context of activities in the broader region of the Chukchi Sea. These patterns are shown schematically in Figure 5.2.3 for the lead occurrence probability in April (based on the entire time series 1993-2010). As apparent from this map, the lease area is bounded by two linear lead systems associated with shear deformation that link Herald Island with the Alaska mainland at Cape Lisburne or the grounded ice on Hanna Shoal. The northernmost of these, termed Chukchi Boundary (CB) in the analysis in Section 4.2, is also apparent in ice deformation maps derived from Radarsat SAR data for selected time periods between 1996 and 2000 (*Eicken et al.*, 2006; *Kwok*, 2006). Both, the Chukchi Boundary and the Southeast Shift (SE) pattern indicate differential movement between the Chukchi and Beaufort ice pack and the ice cover of the southern Chukchi Sea, with arrays of stacked leads or potentially stagnant ice associated with these patterns.

Under more dynamic, somewhat open conditions with prevailing northeasterly winds the West Coast Arc Lead (WCAL), the Barrow Arch or the Bering Strait Arch dominate and result in stacked leads throughout the eastern Chukchi Sea (Figure 5.2.3). Such lead patterns can be associated with rapid increases in the lead fraction due to clearing of ice packed against the coast and creation of open water as ice is exported into the northern Bering or western Chukchi Sea. Southward displacement of sea ice results in long, arcuate leads that extend from Herald Island across to Hanna Shoal and beyond.

The third, key pattern is associated with easterly flow and strong displacement of ice from the coast and termed Open East (OE). Under such circumstances coastal leads and polynyas open all along the Chukchi coast all the way down into Kotzebue Sound.

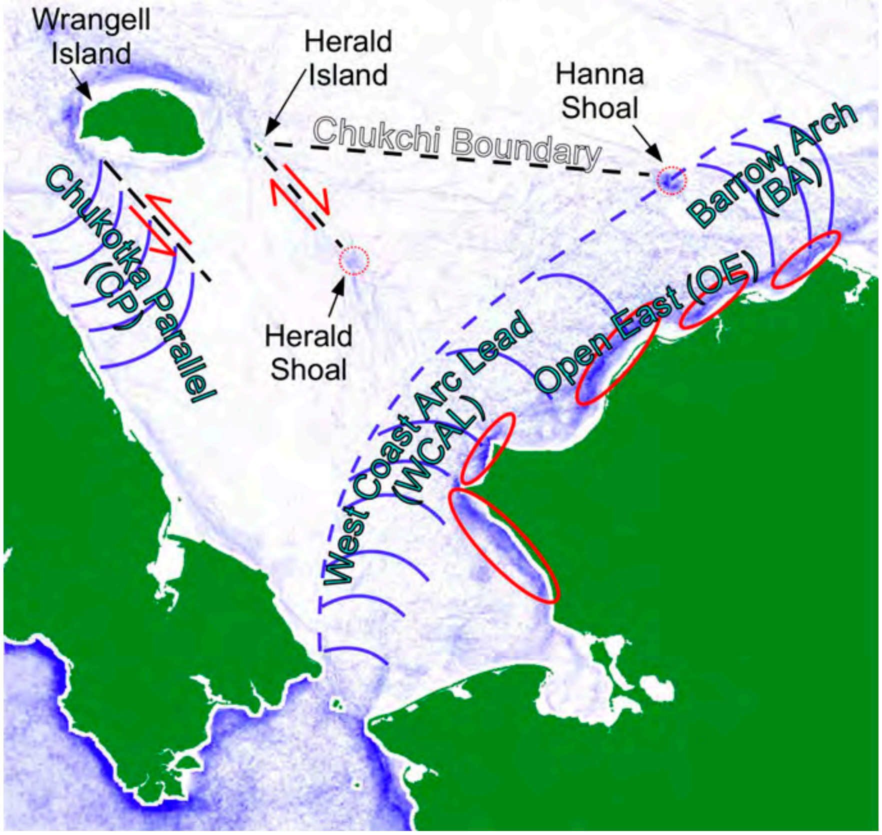

Figure 5.2.3: Schematic of key lead patterns of relevance for the Chukchi Sea, sketched onto a map of recurrence probability of leads in the Chukchi Sea subregion. The map has been derived for the month of April from all images for each month during the time periods 1993-2010 for each grid cell. Subregions with partial or complete cloud cover have been excluded from the analysis. Note that the color shading has been manipulated to enhance the visibility of different lead features and does not conform with the scale shown in Figure 5.2.1.

(iii) Leads associated with Hanna and Herald Shoals and Herald Island

Herald Island and grounded sea ice features associated with Herald and Hanna Shoal play an important role as sources of open water or leads and points of origin for more extended lead systems (Figure 5.2.3). As apparent from the lead recurrence maps, they are the only offshore features that are consistently associated with open water and thin ice. A shoal to the northwest of Wrangel Island at the very margin of the study region also falls into this category. Hanna and Herald Shoals require the grounding of ice in water depths of 20 m or more. As evident from the analysis of AVHRR imagery for the time period 1993 through 2012 (Tables 4.2.1 and 4.2.2), such grounding occurs every year at Hanna Shoal, typically starting in December or January and persisting into the break-up season, as apparent from the monthly lead recurrence maps (Figure 5.2.1). At Herald Shoal, in contrast, grounding was confirmed to be absent in five out of 18 years and doubtful in another two years (Table 4.2.2).

What constrains the formation of these grounded features? The formation of "Katie's Floeberg" at Hanna Shoal has been examined based on satellite data by Barrett and Stringer (1978b; 1978a) who postulate but do not examine grounding of deep-draft ice as a prerequisite to its formation. If one assumes that the date of onset of grounding depends in part on the probability density function of ice draft in the region, then the interannual variations in the first observation of open-water features associated with the shoal are in part explained by interannual variations in the ice thickness distribution. It is noteworthy that the latest date of onset was observed on March 15 in 2008, following on the record minimum ice extent and hence substantial reduction of multiyear ice in the study region (see also discussion below). Similarly, in spring of 2008 no grounding of ice was observed at Herald Shoal. In an airborne thickness survey, (see Appendix 3), we found ice over Hanna Shoal grounded at water depths of up to 26 m, with no evidence of multiyear ice present.

5.2.2 Variability and change: Lead patterns prior to and after 2004

A major aspect of the present study in relation to MMS OCS STUDY 2005-068 (*Eicken et al.*, 2006) is the fact that the present analysis includes the winters following on a sequence of record minimum summer ice extent years beginning in 2005, with 2007 the lowest on record for the modern satellite era starting in 1979 and summer minima well below average for the subsequent years (*Stroeve et al.*, 2008; *Maslanik et al.*, 2011). The regional expression of these changes is highlighted in Figure 5.2.4 which shows a time series of multiyear ice extent in the Beaufort Sea (*Maslanik et al.*, 2011). The figure demonstrates how from 2006 to 2008 the multiyear ice extent for March and September in the Beaufort Sea has dropped by 30 and 60%, respectively. Since, values have remained at a much lower level than prior to the 1980s and 1990s.

As evident from Figure 5.2.1, which shows the lead distribution in the Chukchi Sea prior to 2005 and from 2005 through 2010, there are no significant differences between lead patterns prior to this major transformation of ice conditions in the region. This is likely explained by the fact that the fraction of multiyear ice in the Chukchi Sea has been low throughout the study period (ranging between 0.02 and 0.1 x 10^6 km^2 from 1996 onwards; *Maslanik et al.*, 2011) with a much larger area of first-year ice present. In contrast, the Beaufort Sea experienced a substantial change in lead patterns when comparing the period 1993-2004 and 2005 through 2009 (Figure 5.2.2). Thus, throughout winter, lead number densities are high (also borne out by the data presented in Section 4.1) and leads occur throughout the entire Beaufort Sea, with the exception of a comparatively narrow belt of stagnant or landfast ice between Point Barrow and Prudhoe Bay and off the Mackenzie Delta. While some of the features, such as the Barrow Arch, the flaw lead of the Mackenzie Delta and arcuate leads trending to the northeast are still apparent, they are embedded within an extensive distribution of smaller leads that occupy the entire study region. These lead patterns that were largely absent in prior years are also associated with greater variability and translation of leads on synoptic time scales than in prior years (see discussion in Section 4.2).

These contrasting patterns are explained in terms of a thinner, more mobile ice pack in the Beaufort Sea. Thus, as demonstrated by *Maslanik et al*. (2011, see also Figure 5.2.4) and apparent from ice thickness surveys conducted in the region as part of the Seasonal Ice Zone Observing Network (www.sizonet.org) from 2007 onwards, the winter ice pack of the Beaufort Sea is both thinner and contains much smaller areal fractions of (high-strength) multiyear ice than in years prior to 2006 (e.g., comparison to data compiled by *Tucker et al*., 2001). In the Beaufort region, this reduction is driven by a combination of factors, with increased solar heating and resultant thinning of ice a major factor (*Perovich et al.*, 2008). However, as pointed out by *Hutchings and Hibler* (2008) and *Hutchings and Rigor (2012)*, ice dynamics and changes in Beaufort Gyre circulation also reduced the influx of thick multiyear ice into the region. At the same time, changes in the large rheology of the region have resulted in greater divergence and increased ice velocities that explain the changes in lead patterns (*Hutchings and Hibler*, 2008; *Spreen et al.*, 2011; *Hutchings and Rigor*, 2012). *Spreen et al*. have shown that in the Beaufort Sea, ice speed has been increasing at rates of around 2 cm s^{-1} per decade (i.e., by 10 to 20 %) between 1992 and 2009, mostly as a result of changes in ice rheology.

As an indication of the complex connection between lead patterns, ice motion and the boundary conditions at the coast, the extent of landfast sea ice in the Beaufort Sea showed a marked reduction in the season 2006-07 and 2007-08. This is discussed in more detail in section 5.3.2 together with changes in the seasonality and the occurrence of episodic events.

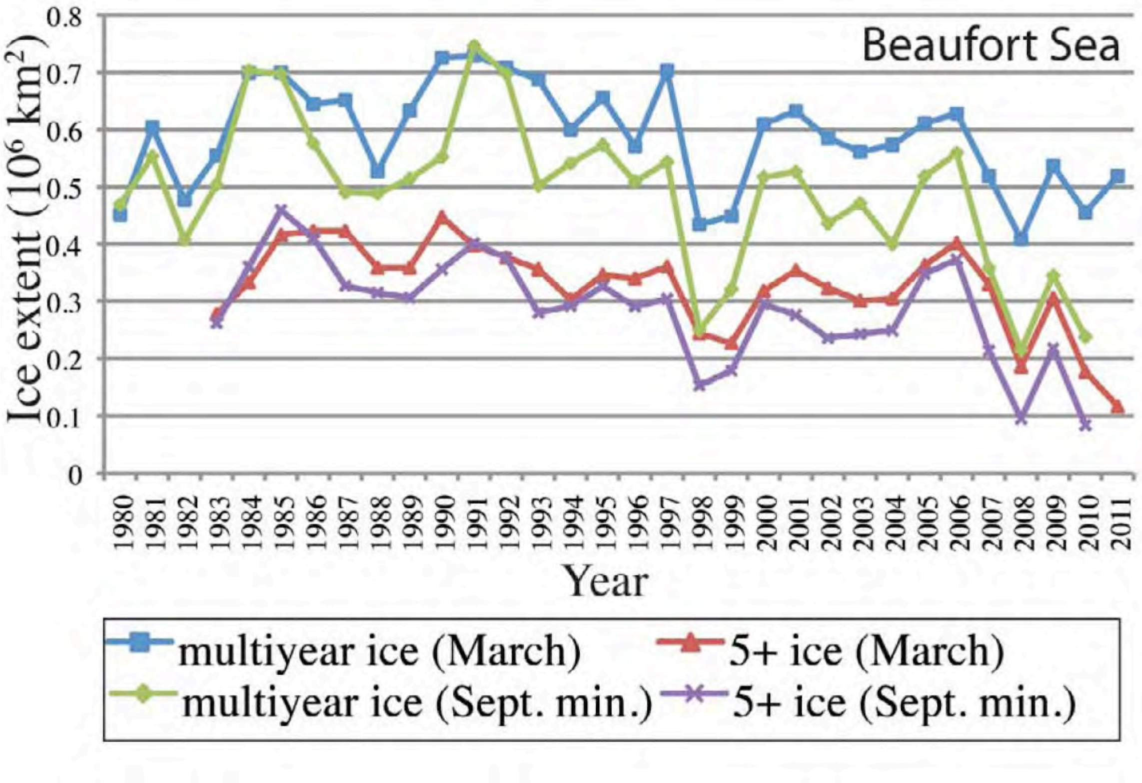

Figure 5.2.4: Extent of multiyear ice of different age classes for the Beaufort Sea, derived from ice velocity maps obtained through analysis of passive microwave remote sensing data (figure from Maslanik et al., 2011). Note the substantial drop between 2006 and 2008.

5.3 Discussion of landfast ice conditions in the Chukchi and Beaufort Seas

5.3.1 Comparison between Chukchi and Beaufort landfast ice regimes

In MMS OCS STUDY 2005-068, we reported on the relationship between the location of the SLIE and configuration of the coast and bathymetry in the southern Beaufort Sea and northeastern Chukchi Sea. By including a new study region to the west, our analysis now spans the entire Alaska coast of the Chukchi and Beaufort Seas and includes parts of eastern Russia and western Canada (Figure 1.4.1). We are therefore now in a position to make a comprehensive comparison between the landfast ice regimes of the Chukchi and Beaufort Seas and explore the relationships with bathymetry and coastal configuration.

When comparing landfast along the whole Chukchi and Beaufort coasts, the most marked difference between the two seas is the mean width of landfast ice. This contrast is readily seen in Figures 4.3.1 - 4.3.3. There are locations along the Chukchi coast where landfast ice is as extensive as that in the Beaufort Sea, but there are no locations along the Beaufort coast where the landfast ice is as persistently narrow as in the Chukchi. In addition, although we observed some stable extensions of landfast ice in the Chukchi Sea, they were not nearly as extensive as those in the Beaufort (section 4.3.5).

As discussed in section 1.3 and illustrated in Figure 1.3.1, the bathymetries of the Chukchi and Beaufort Seas are markedly different. Moreover, in our analysis of water depth at the SLIE, we find notable differences in the relationship between landfast and bathymetry in the two seas. Figure 4.3.4 shows the distributions of water depth of the SLIE in each of the 11 coastal zones shown in Figure 3.3.4. These results show that the SLIE-bathymetry relationship differs in two ways between the Chukchi and Beaufort coasts. First, landfast ice tends to occupy deeper water in the Beaufort Sea than in the Chukchi Sea. It is important to note that this is not simply due to the Beaufort Sea being deeper than the Chukchi since landfast ice is also more extensive in the Beaufort Sea as discussed above.

The second way in which in the relationship between landfast ice and bathymetry differs in the Chukchi and Beaufort Seas is in the shape of the water depth distrisbution and how this evolves over the annual cycle. In the Beaufort Sea (zones 9-11), the SLIE advances progressively into deeper water such that by January or February, the histograms of water depth (Figure 4.3.4) exhibit a well-defined mode. In contrast, most of the coastal zones in the Chukchi Sea (zones 1-8) exhibit multi-modal distributions and do not show a consistent progression into deeper water over the course of the annual cycle. The significance of these findings is that in the Chukchi Sea the SLIE is not as well represented by a particular isobath as it is in the Beaufort Sea, where the 20 m isobath is commnly used to approximate the location of the SLIE. Also, our depth-dependent definition of landfast ice stabilization (section 3.3.7) may not be appropriate in the Chukchi Sea.

5.3.2 Changes and trends in the landfast ice regimes

In MMS OCS STUDY 2005-068, compared the dates of the four key landfast ice events with similar events identified by Barry *et al.* (1979; *Hutchings and Rigor*, 2012) for regions of the coast corresponding to coastal zones 8 and 9 for the period 1973-77. Summarized data in this form do not exist to our knowledge for other sections of coast and so we can extend this comparison here. However, with 12 consecutive years of landfast data, we are now in a position to look for evidence of changes or trends in recent years. Figure 5.3.1 shows the annual mean occurrence for each of the four key landfast ice events over the period 1996-2008. Break-up and ice-free dates for 2008 are omitted as they are not considered reliable due to the availability of only a partial season of Radarsat SAR data.The data in Figure 5.3.1 do not indicate any ongoing widespread changes in the landfast ice regimes in either region. Furthermore, there is no significant correlation of occurrence dates of any events between two regions over the study period reinforcing the notion that landfast ice regimes in the the Chukchi and Beaufort seas are driven by different regional processes.

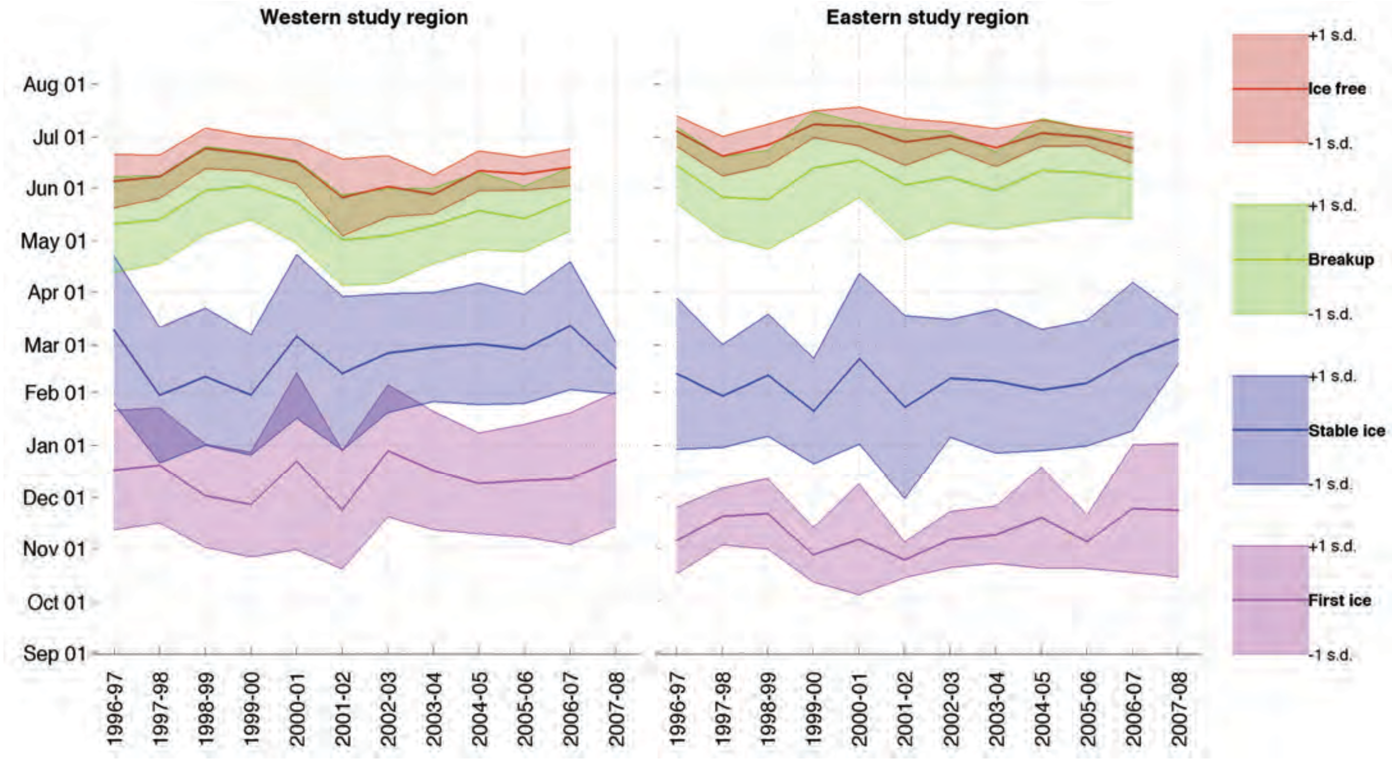

Figure 5.3.1: Timeseries of mean occurrence date for each key event in the landfast cycle over the period 1996-2008 calculated for the western and eastern landfast ice study regions

Part of the reason for the lack of any apparent trends in Figure 5.3.1 may be that they are masked by local variability. Figure 4.3.6 shows that there can be considerable differences in the timing of the annual cycle over relatively short sections of the coast, some of which can be related to the local coastal morphology in the form of lagoons, bays and headlands (Figure 4.3.7). Using the coastal morphology categorization shown in Figure 3.3.7, we calculated annual mean occurrence dates for each subregion, broken down by morphology type. These results are shown in Figure 5.3.2. Note that not all coastal morphology types are found in all zones. These results support the absence of any pronounced widespread changes shown in Figure 5.3.1, but there are trends significant at the 95% level in some regions. For example, away from headlands on the northern Chukotka and Seward peninsulas (zones 1 and 2), landfast ice has been stabilizing later by around 4 days per year. Similarly, outside of bays and lagoons, the coastline between Cape Lisburne and Wainwright (zone 7) has been becoming ice-free earlier by approximately 3 days per year. These trends are in the same directions as the longer-term changes found in MMS OCS STUDY 2005-068, which showed that landfast ice was in general forming later and breaking up earlier. However, we note that our data also indicate a slight negative trend in the data of landfast ice formation in lagoons in zone 10 (Kaktovik – Herschel Island) of approximately 1 day per year. Our data also indicate that open sections of coast in zone 5 (Cape Kruzenstern to Point Hope) have been experiencing an earlier advance of landfast ice to the 15 m isobath (3 days per year).

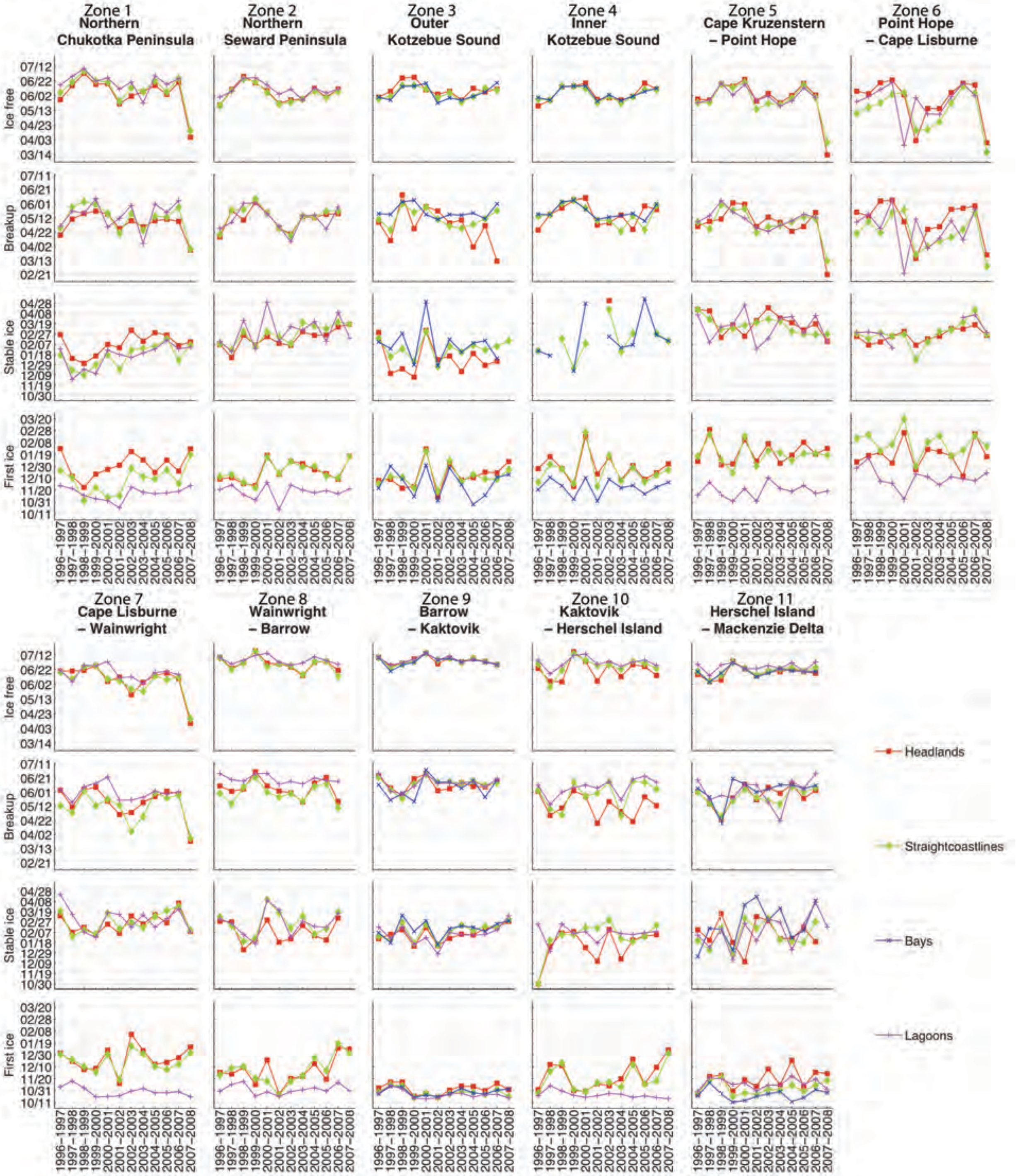

Figure 5.3.2: Mean occurrence dates for key events in the landfast ice annual cycle calculate separately according to coastal morphology for each coastal zone.

Given the changes observed between the 1970s and the period 1996-2004 that we reported on in MMS OCS STUDY 2005-068, the lack of a conistent trend in the timing of the annual is somewhat surprising. However, this does not necessarily mean the landfast ice of the Chukchi and Beaufort Seas is unresponsive to the larger scale changes occurring throughout the Arctic. As discussed in section 5.2.2, the composition, dynamics and lead patterns of sea ice in the Beaufort Sea exhibit significant changes since 2006, when a significant decline in multitear ice volume began. Figures 5.3.1 and 5.3.2 indicate that formation of landfast ice in these two seasons took place later than preceding years along most parts of the coast. In addtion, Figure 4.3.2 indcates that, particularly in the Beaufort Sea, landfast ice was less extensive than usual during these two seasons. This is illustrated more clearly in Figure 5.3.3, which shows the mean landfast ice width in the western and eastern study regions over the whole study period. The season 2006-07 is notable for having the lowest maximum extent in the Beaufort Sea (eastern region) during the period 1996-2008.

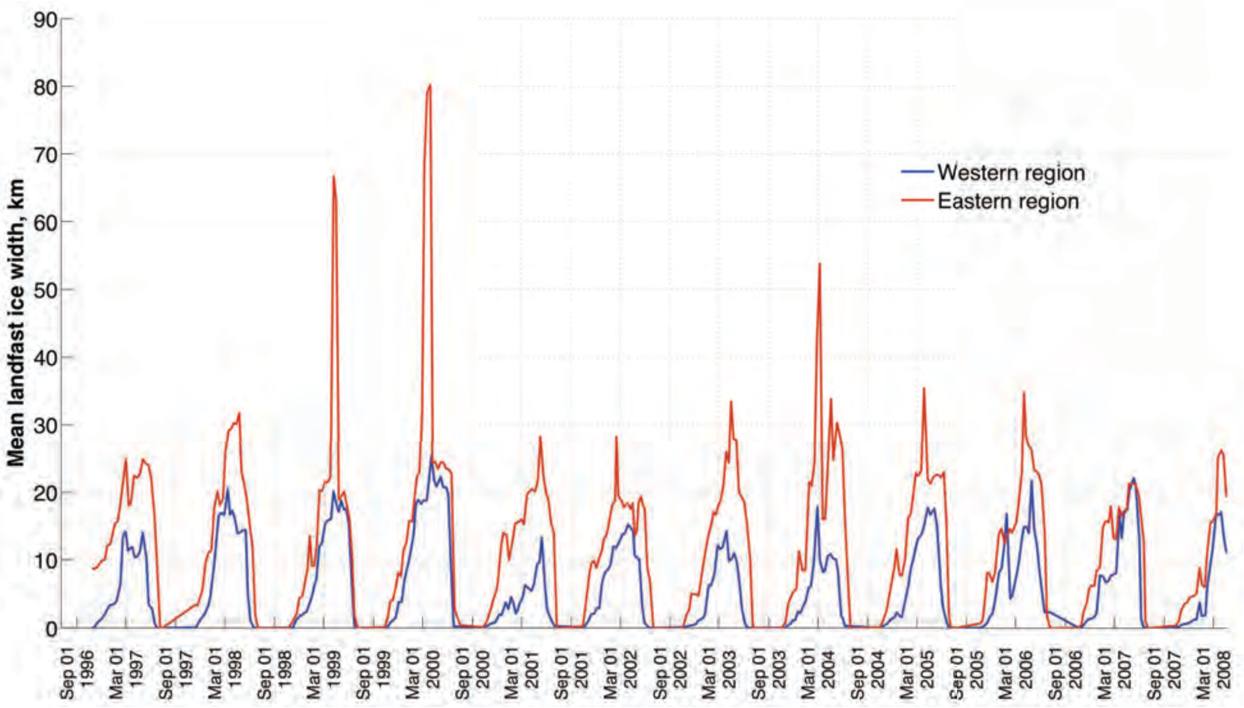

Figure 5.3.3: Mean landfast ice width in the western and eastern study regions over the period 1996-2008.

5.4 Discussion of results from InSAR-based landfast detection

5.4.1 Expanding L-band InSAR-based Landfast Ice analysis by Adding INSAR Phase Information

Besides using InSAR coherence for landfast ice detection as successfully demonstrated in Section 4.3, an analysis of the interferometric phase of landfast ice areas can provide additional insight into landfast ice stability and potential deformation processes. This information is of great value in the context of coastal ice use and ice operations (*Eicken et al.*, 2009) and is not accessible through other landfast ice mapping techniques with large areal coverage. In SAR interferograms of landfast ice regions, areas of uniform fringe pattern indicate landfast ice that has moved as a rigid body and the pattern and density of the fringes can be used to determine the nature and amount of any motion (e.g. translation, rotation or shear) (*Lang*, 2003). Discontinuities in the phase pattern can also be used to infer the location of cracks and individual ice floes comprising the landfast ice. As the InSAR phase is only sensitive to the line-of-sight component of the three-dimensional motion vector, it is often useful to augment the observed interferometric phase patterns with high resolution, sub-pixel accurate (real value and complex) cross-correlation techniques, which can quantify meter-scale motion in two dimensions.

An example of the amount of information that can be extracted from InSAR data is presented in Figure 5.4.1. An interferogram of landfast ice near Barrow, Alaska in Figure 5.4.1a shows isolated regions of high fringe density (marked by black ellipses) associated with significant deformation indicative of potential instability. Figure 5.4.1b shows the two-dimensional motion vectors measured from sub-pixel quality cross-correlation techniques. In coherent areas of interferograms, relative image shifts can be measured with accuracies of the order of 1/10 to 1/20th of a resolution cell, due to the wide-bandwidth nature of the speckle signature inherent to SAR images. The measurement accuracy is dependent on the patch size used in the analysis, the image resolution, and the interferometric coherence. A detailed description of the achievable accuracies can be found in (*Bamler and Eineder*, 2005). The colors in Figure 5.4.1b indicate the magnitude of the motion that occurred in the landfast ice over the time interval covered by the interferogram. Deformation of up to 10 m was detected in areas of highest fringe density. The black arrows in Figure 5.4.1b show the direction of motion extracted from the two-dimensional shift estimates for those regions that yielded spatially consistent motion vectors. The motion of the patch to the east is consistent with the landfast ice motion identified and illustrated in Figure 4.4.5b. A strong shear motion has been identified for the area to the west of Point Barrow (both from SAR imagery and the coastal radar at Barrow), which was identified as an area of hinging in Section 4.4.2.2.

To illustrate the value of such InSAR-derived information in assessing ice displacement and stability, and to further explore the nature of the linear feature of stable ice jutting out from the landfast ice towards the northeast (Figure 5.4.1b), we have analyzed concurrent ice thickness data. Airborne measurements of ice thickness were obtained by electromagnetic induction techniques, as detailed by Haas et al. (2009; 2010). Shown here (Figure 5.4.1b,c) are part of the thickness surveys covering sea ice that had been identified as grounded shear ridges (Figure 5.4.1d) based on information provided by local ice experts (*Brower*, Personal Communication, 2008). The thickness data also indicate that ridge thicknesses were sufficient to touch the seafloor and partially ground the ice, thereby stabilizing the landfast ice cover. However, during the deformation process with landfast ice interacting with the offshore ice pack, differential motion of semi-grounded ridges was sufficient to deform thinner ice (in some areas below 1 m thick, Figure 5.4.1c) south of the line of grounded ridges, explaining the fringe patterns and lack of coherence observed in this part of the interferogram (Figure 4.4.5b and Figure 5.4.1a). Hence, interpretation of features such as those shown in Figure 5.4.1a and b can provide important insight into the distribution and degree of grounding of pressure ridges and other landfast ice features important in assessing ice stability. Local ice experts also use the presence of ridge zones over shoals such as those shown in Figure 5.4.1d as an indication of ice stability for long stretches to the southwest of such features (*Brower*, Personal Communication, 2008; *Leavitt*, Personal Communication, 2009).

5.4.2 Spatial and Temporal Coverage of Arctic Coasts with L-band InSAR Data

In addition to demonstrating the technological feasibility of InSAR for landfast ice mapping, from an operational perspective, it needs to be ascertained that current and future L-band InSAR temporal and spatial coverage is sufficient for key applications. Figure 5.4.2 illustrates the *spatial* and *multi-temporal coverage* of ALOS PALSAR images for the Alaskan Arctic coast in winter of 2007/08 as a representative example. In Figure 5.4.2, only available ALOS PALSAR imagery suitable for interferometry is shown, while other acquisitions are ignored. Here, ALOS PALSAR is used as a proxy for all currently available spaceborne L-band SAR data. Frames colored in blue were covered twice between October 2007 and April 2008, yielding one 46-day interferogram. Areas in red were covered three times, producing two independent 46-day interferograms. Green and yellow areas were covered four and five times, respectively, potentially enabling an analysis of the entire landfast ice season. Figure 5.4.2 also shows that, at this geographic latitude, neighboring swaths show almost 40% overlap. For areas within these overlaps the number of coverages per season increases strongly, as the information from all overlapping swaths can be combined.

While the coverage shown in Figure 5.4.2 is typical for the ALOS PALSAR mission, the specific spatio-temporal sampling does vary from year to year. This is mainly due to the mode of operation of the ALOS mission. ALOS carries three different instruments, two optical sensors and one SAR sensor, which compete for system bandwidth and duty cycle. Additionally, the ALOS mission is divided into sub-cycles of 46-day duration. Within these cycles the satellite is operating in a constant mode, while the operational mode may change between cycles. The design of these modes is defined by weighing a large variety of user interests. The setup of consecutive modes of the PALSAR sensor does therefore not always provide data that are suitable for InSAR applications. In winter of 2008/09, for example, consecutive modes of PALSAR often varied in the used incidence angle and polarimetric mode, which is unsuitable for InSAR applications even if other sensor settings remained unchanged.

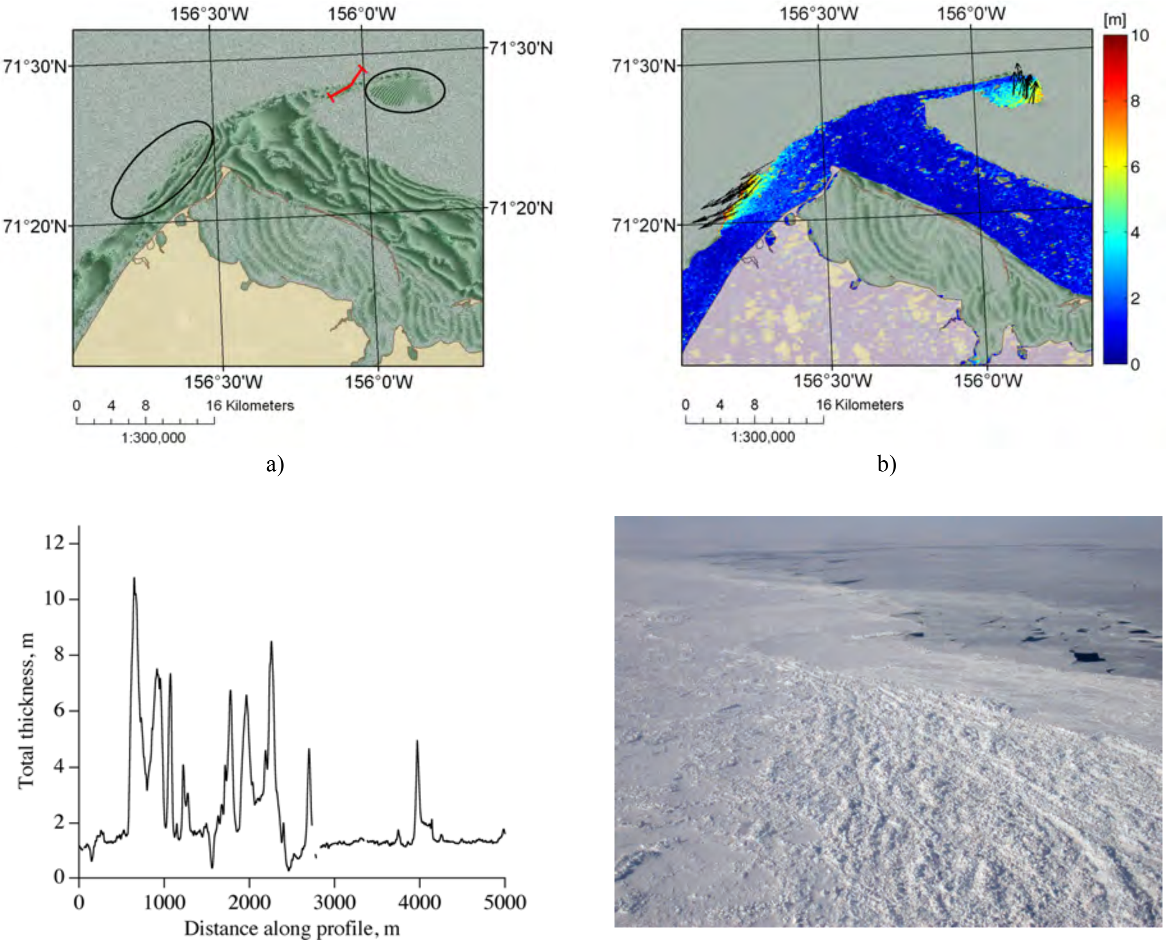

a)

b)

c)

d)

Figure 5.4.1: Examples of an analysis of fringe pattern (a) and two-dimensional ice surface displacements (b) observed in an interferogram over Barrow, Alaska. The combination of these measurements allows for a detailed study of ice stability and deformation. Figure 5.4.1c shows a profile of total ice and snow thickness obtained from airborne measurements along the red line shown in (a) on 15 April 2008. Figure 5.4.1d shows the shear ridges corresponding to the thick, deformed ice as seen from the aircraft during the thickness survey.

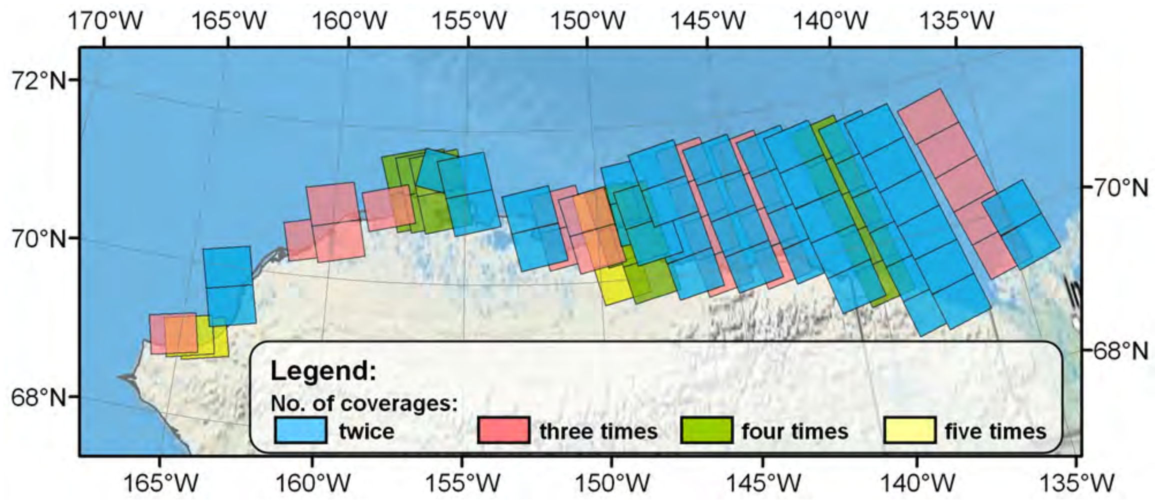

Figure 5.4.2: Multi-temporal coverage of the Alaskan and western Canadian Arctic coast with L-band interferograms stemming from the ALOS PALSAR mission for winter 2007/08 (October 2007 through April 2008).

Although not all regions of the Arctic are covered with sufficient frequency by currently available L-band SAR missions, the future of L-band SAR for landfast ice detection looks bright. This is mostly due to a series of low-frequency SAR sensors that are scheduled to be launched in the near future. Japan is preparing ALOS-2 which will carry a SAR sensor only and therefore reduce the amount of user and sensor conflicts. NASA is currently preparing for its L-band SAR mission DESDynI and is collaborating with the German Aerospace Center on preparations for TanDEM-L, a DESDynI analog. Besides these L-band missions, ESA will be launching its P-band SAR mission BIOMASS, which might show capabilities similar to ALOS PALSAR for landfast ice monitoring. All these future missions will also provide faster revisit times (8 days for DESDynI and TanDEM-L, 14 days for ALOS-2, and between 25 and 45 days for BIOMASS) that will improve interferometric coherence and increase the multi-temporal coverage of each landfast ice season. Thus it is likely that using the approach demonstrated here, an accurate, complete mapping of landfast ice distribution throughout the Arctic is possible, which is of value both in the context of the importance of landfast ice for Arctic ecosystems and people (*Eicken et al.*, 2009) and its role in ocean-atmosphere exchange.

6. CONCLUSIONS

6.1 Lead patterns

By expanding the prior work done under the MMS OCS STUDY 2005-068 project, this study was able to demonstrate a clear regional contrast in the distribution and seasonality of lead patterns in the Beaufort and Chukchi Seas. In the Beaufort Sea, aside from the Barrow Arch, most of the patterns identified were confined to a relatively narrow zone between the edge of the pack ice and the coast, and the forms and orientations of single or isolated clusters of leads within that zone were important. However, as noted in Section 4.2, the geometry of the Chukchi Sea boundaries relative to the prevailing wind directions, combined with the frequency with which storms cross the area keep the entire Chukchi Sea pack ice in a state of nearly continuous transition. While pack ice on any water body responds to changes in driving forces, the situation in the Chukchi Sea is such that regardless of the displacement direction, there is almost always open space for the pack ice to move into. As a result, deformation processes and large-scale movement impact the region as a whole, and the lead patterns that result tend to extend over large areas and can be characterized according to the displacement direction. These different deformation regimes and associated lead patterns have been summarized in Figure 5.2.3 for the Chukchi Sea.

Since large stretches of the pack ice are involved, it is often possible to identify an entire pattern from limited spatial observations. For example, the openings in the ice off the coast of Wrangel Island often indicate the displacement direction of the entire Chukchi Sea ice pack, and northwest facing leads arcing between the coast of Chukotka and Wrangel Island always appear as part of either a Chukotska Parallel or an Open East pattern (Figure 5.2.3). Finally, the opening of a coastal lead southeast of Point Hope can be an early indicator of the development of the West Coast Arc Lead pattern, possibly because that reach of coast is almost normal to the winds that are associated with the pattern.

Grounded ice masses, such as Katie's Floeberg on Hanna Shoal, which formed every year during the study period, play an important role as nucleation sites for leads under varying directions of ice movement. They also appear to act as stress concentrators such that large-scale lead systems such as those developed along the margin of the Beaufort Gyre or the lead parallel to the coast of Chukotka (Figure 5.2.3) tend to originate from these features. Due to the substantial deformation associated with such grounded ice masses, they may serve as source areas of deep-draft floebergs later in the season. While the growth of these features is reasonably well understood, the probability of bottom contact by deep-draft ice or ice ridges as an important prerequisite to their formation is less well described. Since these features are associated with persistent open water but at the same time massive grounding and presumably gouging of the seafloor, their ecological importance is far from clear.

As a result of the more dynamic ice conditions compared to the Beaufort Sea, Chukchi coastal polynyas and flaw leads are widespread and represent the most persistent lead pattern in the entire region. This includes lead systems forming off Wrangel Island, which are often linked to the same weather patterns responsible for open water off the Chukchi coast.

The most substantial finding concerns the major transformation of lead patterns and ice deformation and movement apparent in the Beaufort Sea beginning with the 2006 ice season. Thus, compared to previous years with very few leads outside of the Barrow Arch and the

Mackenzie flaw zone, the number density and extent of leads in this region appears to have increased substantially, mostly as a result of the changing composition of the Beaufort ice pack. Further work is required to assess whether these are reversible changes if the multiyear ice cover were to increase again in thickness and extent in this region. With more open water and a great influx of shortwave radiation, the changing ice regime is likely to have substantial, as of yet poorly understood, ecological impacts as well.

6.2 Landfast ice

Through detailed, consistent analysis of nearly 3,000 Radarsat images, we have mapped landfast ice growth and decay over the entire Chukchi and Beaufort coasts of Alaska for the period 1996-2008. In doing so, we have been able to make a comprehensive comparison between the landfast ice in the Chukchi and Beaufort Seas. This comparison shows that while landfast ice forms earlier and lasts longer in the Beaufort Sea than the Chukchi Sea, local variability in bathymetry and the configuration of the coastline have a greater influence on the timing of the annual cycle than such regional contrasts. In addition, we have found that the relationship between water depth and the location of the SLIE is not consistent between the Chukchi and Beaufort Seas. In MMS OCS STUDY 2005-068, we confirmed and quantified the relatively robust relationship between the stable location of the SLIE and isobaths near 20 m in the Beaufort Sea. In this study, we found that the SLIE in the Chukchi Sea does not exhibit a strong preferred water depth. We therefore conclude that isobaths are not suitable for approximating the location of the SLIE in the Chukchi Sea.

The acquisition of four additional seasons landfast ice data have allowed us to examine evidence of changes and trends in the landfast ice ice regimes of the Chukchi and Beaufort Seas in recent years. However, despite significant changes in the seasonality of landfast ice formation and break-up that we reported on in MMS OCS STUDY 2005-068, we found little evidence of ongoing widespread change (Figure 5.3.1). By refining our analysis to take account of local coastal variability (Figure 5.3.2), we found statistically significant trends toward later stabilization of ice in zones 1 and 2, and earlier ice-free conditions in zone 5. However, we also found opposing trends in two other coastal zones.

Unlike in MMS OCS STUDY 2005-068, which found little change in landfast ice extent since the 1970s, the results of this study suggest a possible reduction in landfast ice extent in response to the pronounced loss of multiyear ice in this sector of the Arctic, which began in 2006 (section 5.2.2 and Figure 5.3.3). Analysis of additional data covering the period after May 1 (when Radarsat data became a commercial product) would be required to confirm these findings, but they point toward unprecedented changes in the coastal ice regime of the Beaufort Sea.

6.3 InSAR mapping of landfast ice extent and deformation

Landfast sea ice along Alaska's coast remains interferometrically coherent in L-band SAR imagery over time intervals of at least 46 days. This makes it possible to distinguish landfast sea ice from drifting ice or open water based on interferometric coherence. We have developed an automated technique that agrees well with existing SAR-based techniques for delineating landfast ice, though some level of inspection is necessary to correctly interpret unlikely landfast ice configurations. While the presented approach was developed for Arctic environments, in principle L-band InSAR should be applicable anywhere landfast ice is found. However, there may be specific regional or seasonal processes (such as high tidal ranges) that may reduce its accuracy in some cases. Therefore, any comprehensive analysis of pan-Arctic landfast ice will require a multi sensor approach to achieve robust mapping results under a wide range of conditions.

Besides landfast ice mapping, L-band SAR interferometry also shows promise for investigating landfast ice motion on meter to sub-meter scales. By definition, landfast ice is stationary, but clearly there is an amount of lateral motion that can occur without rendering the ice non-landfast. In this study we highlighted one case where we were able to identify discrete zones of sub-pixel motion within the landfast ice. Although small, such motion can be significant for structures within or beneath the landfast ice. Furthermore the boundaries of such zones may be related to the presence of grounded, stabilizing features, which we were able to identify through airborne surveys concurrent with InSAR acquisition. Combined with such ground-based observations, L-band InSAR has the potential to expand our understanding of how landfast ice responds to dynamic forcing and the role that grounded ridges play in stabilizing it.

Although the spatio-temporal coverage of Arctic coasts with L-band InSAR data is currently limited, a larger fleet of upcoming low-frequency SAR systems with improved spatial coverage and temporal revisit cycle will render L-band SAR interferometry a promising tool for continuous observation of Arctic landfast ice areas.

7. REFERENCES CITED

Alam, A., and J. A. Curry 1998. Evolution of new ice and turbulent heat fluxes over freezing winter leads, *J. Geophys. Res.*, *103*(C8)15783-15802.

Arctic Council 2009. *Arctic Marine Shipping Assessment 2009 Report*, Arctic Council, 188 pp.

Bamler, R., and P. Hartl 1998. Synthetic aperture radar interferometry, *Inverse Problems*, *14*(4)R1-R54.

Bamler, R., and M. Eineder 2005. Accuracy of differential shift estimation by correlation and split-bandwidth interferometry for wideband and Delta-k SAR systems, *Ieee Geoscience and Remote Sensing Letters*, *2*(2), Doi 10.1109/Lgrs.2004.843203, 151-155.

Barnett, D. 1991. Sea ice distribution in the Soviet Arctic, edited by L. W. Brigham, pp. 47-62, Belhaven Press, London.

Barrett, S. A., and W. J. Stringer 1978a. Growth mechanisms of "Katie's Floeberg", *Arctic and Alpine Research*, *10*(4)p.775-783.

Barrett, S. A., and W. J. Stringer 1978b. Growth and decay of "Katie's Floeberg", *Alaska. Geophysical Institute. Report, UAG R-256*, Geophysical Institute, University of Alaska Fairbanks, Fairbanks, AK.

Barry, R. 1979. Study of climatic effects on fast ice extent and its seasonal decay along the Beaufort-Chukchi coasts, in *Environmental Assessment of the Alaskan Continental Shelf, vol.2 : Physical Science Studies, final report*, edited, pp. 272-375.

Barry, R. G., R. E. Moritz, and J. C. Rogers 1979. The fast ice regimes of the Beaufort and Chukchi Sea coasts, Alaska, *Cold Reg. Sci. Technol.*, *1*(2)129-152.

Bauer, J., and S. Martin 1983. A model of grease ice growth in small leads, *J. Geophys. Res.*, *88*(C5)2917-2925.

Belchansky, G. I., D. C. Douglas, I. V. Alpatsky, and N. G. Platonov 2004. Spatial and temporal multiyear sea ice distributions in the Arctic: A neural network analysis of SSM/I data, 1988–2001, *J. Geophys. Res.*, *109*C10017, doi:10010.11029/12004JC002388.

Brower, A. S. 2008. Personal Communication.

Bump, J. K., and J. R. Lovvorn 2004. Effects of lead structure in Bering Sea pack ice on the flight costs of wintering spectacled eiders, *J. Mar. Sys.*, *50*113-139.

Colony, R. 1979. Dynamics of near shore ice-Task 5, in *Environmental Assessment of the Alaskan Continental Shelf. Quarterly Reports of Principal Investigators, Oct-Dec 1978, v.2*, edited, pp. 273-276.

Comiso, J. C. 2002. A rapidly declining perennial sea ice cover in the Arctic, *Geophys. Res. Lett.*, *29*(20)1956, doi:1910.1029/2002GL015650.

CRRC 2009. Opening the Arctic Seas: Envisioning Disasters and Framing Solutions, Final Report, Coastal Response Research Center, Proceedings of Opening the Arctic Seas Workshop, University of New Hampshire, 18-20 March 2008.

Dammert, P. B. G., M. Lepparanta, and J. Askne 1998. SAR interferometry over Baltic Sea ice, *International Journal of Remote Sensing*, *19*(16)3019-3037.

Danielson, S., M. Johnson, S. Solomon, W. Perrie, and A. w. C. 1 km Gridded Bathymetric Dataset Based on Ship Soundings: A research tool for the waters of eastern Russia, 2008, Poster presentation at the 2008 Alaska Marine Science Symposium, Anchorage, Alaska. 2008. Alaska Region Bathymetric DEM, updated, Digital media, http://mather.sfos.uaf.edu/~seth/bathy/

Dickins, D., G. Hearon, K. Morris, K. Ambrosius, and W. Horowitz 2011. Mapping sea ice overflood using remote sensing: Alaskan Beaufort Sea, *Cold Reg. Sci. Technol.*, *65*(3), Doi 10.1016/J.Coldregions.2010.10.015, 275-285.

Divine, D. V., R. Korsnes, and A. P. Makshtas 2004. Temporal and spatial variation of shore-fast ice in the Kara Sea, *Cont. Shelf Res.*, *24*1717-1736.

Douglas, D. C. 2010. Arctic sea ice decline: Projected changes in timing and extent of sea ice in the Bering and Chukchi Seas, *U.S. Geological Survey Open-File Report 2010-176*, 32 pp.

Druckenmiller, M. L., H. Eicken, M. A. Johnson, D. J. Pringle, and C. C. Williams 2009. Toward an integrated coastal sea-ice observatory: System components and a case study at Barrow, Alaska, *Cold Regions Science and Technology*, *56*(2-3), DOI 10.1016/j.coldregions.2008.12.003, 61-72.

Eicken, H., A. L. Lovecraft, and M. L. Druckenmiller 2009. Sea-Ice System Services: A Framework to Help Identify and Meet Information Needs Relevant for Arctic Observing Networks, *Arctic*, *62*(2)119-136.

Eicken, H., L. Shapiro, A. Gaylord, A. Mahoney, and P. Cotter 2006. *Mapping and characterization of recurring spring leads and landfast ice in the Beaufort and Chukchi Seas*, Final Report, Minerals Management Service, OCS Study MMS 2005-068, Geophysical Institute, University of Alaska Fairbanks, Fairbanks, 180 pp.

Eicken, H., R. Gradinger, A. Graves, A. Mahoney, I. Rigor, and H. Melling 2005a. Sediment transport by sea ice in the Chukchi and Beaufort Seas: Increasing importance due to changing ice conditions?, *Deep-Sea Res. II*, *52*3281-3302.

Eicken, H., I. Dmitrenko, K. Tyshko, A. Darovskikh, W. Dierking, U. Blahak, J. Groves, and H. Kassens 2005b. Zonation of the Laptev Sea landfast ice cover and its importance in a frozen estuary, *Global Planet. Change*, *48*55-83.

Fett, R. W., R. E. Englebretson, and S. D. Burk 1997. Techniques for analyzing lead condition in visible, infrared and microwave satellite imagery, *Journal of Geophysical Research*, *102*(D12)13657-13671.

Gandhi, P. P., and S. A. Kassam 1988. Analysis of CFAR processors in homogeneous background, *IEEE Transactions on Aerospace and Electronic Systems*, *24*(4)427-445.

Gearheard, S., W. Matumeak, I. Angutikjuaq, J. Maslanik, H. P. Huntington, J. Leavitt, D. M. Kagak, G. Tigullaraq, and R. G. Barry 2006. "It's not that simple": A collaborative comparison of sea ice environments, their uses, observed changes, and adaptations in barrow, Alaska, USA, and Clyde River, Nunavut, Canada, *Ambio*, *35*(4)203-211.

George, J. C., H. P. Huntington, K. Brewster, H. Eicken, D. W. Norton, and R. Glenn 2004. Observations on Shorefast Ice Dynamics in Arctic Alaska and the Responses of the Iñupiat Hunting Community, *Arctic*, *57*(4)363-374.

Goldstein, R. M., and C. L. Werner 1998. Radar interferogram filtering for geophysical applications, *Geophysical Research Letters*, *25*(21)4035-4038.

Gordon, A. L., and J. C. Comiso 1988. Polynyas in the southern ocean, *Scientific American*, *256*90-97.

Grantz, A., and M. W. mullen 1992. Bathymetric map of the Chukchi and Beaufort seas and adjacent Arctic Ocean, 1 sheet, scale 1:1,000,000.

Haas, C., S. Hendricks, H. Eicken, and A. Herber 2010. Synoptic airborne thickness surveys reveal state of Arctic sea ice cover, *Geophysical Research Letters*, *37*, Artn L09501

Doi 10.1029/2010gl042652, -.

Haas, C., J. Lobach, S. Hendricks, L. Rabenstein, and A. Pfaffling 2009. Helicopter-borne measurements of sea ice thickness, using a small and lightweight, digital EM system, *Journal of Applied Geophysics*, *67*(3), DOI 10.1016/j.jappgeo.2008.05.005, 234-241.

Haralick, R. M., and L. G. Shapiro 1992. *Computer and Robot Vision*, Addison-Wesley Longman Publishing Co., Inc., 630 pp.

Hibler, W. D. I. 1986. Ice dynamics, edited by N. Untersteiner, pp. 577-640, Plenum Press, New York (NATO ASI B146).

Hoen, E. W., and H. A. Zebker 2000. Penetration depths inferred from interferometric volume decorrelation observed over the Greenland ice sheet, *Ieee Transactions on Geoscience and Remote Sensing*, *38*(6)2571-2583.

Huntington, H. 2000. Native observations capture impacts of sea ice changes, *Witness the Arctic*, *8*(1)1-2.

Hutchings, J. K., and W. D. Hibler 2008. Small-scale sea ice deformation in the Beaufort Sea seasonal ice zone, *Journal of Geophysical Research-Oceans*, *113*(C8), 10.1029/2006jc003971.

Hutchings, J. K., and I. G. Rigor 2012. Role of ice dynamics in anomalous ice conditions in the Beaufort Sea during 2006 and 2007, *Journal of Geophysical Research-Oceans*, *117*, Artn C00e04

Doi 10.1029/2011jc007182.

Jacobs, J. D., R. G. Barry, and R. L. Weaver 1975. Fast ice characteristics, with special reference to the eastern Canadian Arctic, *Polar Record*, *110*(17)521-536.

Kapsch, M.-L., H. Eicken, and M. Robards 2010. Sea Ice Distribution and Ice Use by Indigenous Walrus Hunters on St. Lawrence Island, Alaska, in *SIKU: Knowing Our Ice*, edited by I. Krupnik, C. Aporta, S. Gearheard, G. J. J. Laidler and L. K. Kielsen Holm, pp. 115-144, Springer Netherlands.

Kasper, J. L. 2010. Idealized modeling of circulation under landfast ice, 212 pp, University of Alaska Fairbanks, Fairbanks, Alaska.

Key, J. R., R. Stone, J. A. Maslanik, and E. Ellefsen 1993. The detectability of sea-ice leads in satellite data as a function of atmospheric conditions and measurement scale, *Annals of Glaciology*, *17*227-232.

Kottmeier, C., J. Olf, W. Frieden, and R. Roth 1992. Wind forcing and ice motion in the Weddell Sea region, *J. Geophys. Res.*, *97*20373-20383.

Kovacs, A. 1976. Grounded ice in the fast ice zone along the Beaufort Sea coast of Alaska, *CRREL Report*, *76-32*.

Kovacs, A., and M. Mellor 1974. Sea ice morphology and ice as a geologic agent in the southern Beaufort Sea, in *The coast and shelf of the Beaufort Sea*, edited by J. C. Reed and J. E. Sater, pp. 113-164, Arctic Instiituite of North America, Arlington, Va.

Krupnik, I. (Ed.) 2010. *SIKU: Knowing our ice: Documenting Inuit Sea-Ice Knowledge and Use* 523 pp., Springer, London.

Krupnik, I., and D. Jolly 2002. *The Earth is Faster Now: Indigenous Observations of Arctic Environmental Change*, Arctic Research Consortium of the United States, Fairbanks, Alaska.

Kwok, R. 1998. The RADARSAT Geophysical Processor System, edited by C. Tsatsoulis and R. Kwok, pp. 235-257, Springer Verlag, Berlin.

Kwok, R. 2006. Contrasts in sea ice deformation and production in the Arctic seasonal and perennial ice zones, *J. Geophys. Res.*, *111*(C11)1-14;doi:10.1029/2005JC003246.

Kwok, R., and G. F. Cunningham 1994. Use of time series SAR data to resolve ice type ambiguities in newly opened leads, Proceedings of IGARSS'94; International Geoscience and Remote Sensing Symposium. Surface and Atmospheric Remote Sensing: Technologies, Data Analysis and Intepretation, Institute of Electrical and Electronic Engineers, Pasadena, California, 1994.

Kwok, R., and G. F. Cunningham 2002. Seasonal ice area and volume production of the Arctic Ocean: November 1996 through April 1997, *J. Geophys. Res.*, *107*(C10)doi:10.1029/2000JC000469.

Laidre, K. L., I. Stirling, L. F. Lowry, O. Wiig, M. P. Heide-Jorgensen, and S. H. Ferguson 2008. Quantifying the sensitivity of arctic marine mammals to climate-induced habitat change, *Ecological Applications*, *18*(2)S97-S125.

Lang, O. 2003. Radar Remote Sensing in Western Antarctica with Special Emphasis on Differential Interferometry, Dissertation thesis, 127 pp, Julius-Maximilians-Universitaet Wuerzburg, Wuerzburg.

Lantuit, H., and W. H. Pollard 2008. Fifty years of coastal erosion and retrogressive thaw slump activity on Herschel Island, southern Beaufort Sea, Yukon Territory, Canada, *Geomorphology*, *95*(1-2)84-102.

Leavitt, J. 2009. Personal Communication.

Lindsay, R. W., and D. A. Rothrock 1994. Arctic sea ice albedo from AVHRR, *J. Climate*, *7*(11)1737-1749.

Lindsay, R. W., and D. A. Rothrock 1995. Arctic sea ice leads from advanced very high resolution radiometer images, *J. Geophys. Res.*, *100*(C3)4533-4544.

Liu, Y., J. R. Key, Z. Liu, X. Wang, and S. J. Vavrus 2012. A cloudier Arctic expected with diminishing sea ice, *Geophys. Res. Lett.*, *39*L05705, doi:05710.01029/02012GL051251

Lu, Z., C. Wicks, O. Kwoun, J. A. Power, and D. Dzurisin 2005. Surface deformation associated with the March 1996 earthquake swarm at Akutan Island, Alaska, revealed by C-band ERS and L-band JERS radar interferometry, *Canadian Journal of Remote Sensing*, *31*(1)7-20.

Lynch, A. H., E. N. Cassano, J. J. Cassano, and L. R. Lestak 2003. Case studies of high wind events in Barrow, Alaska: Climatological context and development processes, *Month. Weather Rev.*, *131*719-732.

Mahoney, A., H. Eicken, and L. Shapiro 2007a. How fast is landfast sea ice? A study of the attachment and detachment of nearshore ice at Barrow, Alaska, *Cold Regions Science and Technology*, *47*(3), 10.1016/j.coldregions.2006.09.005, 233-255.

Mahoney, A., H. Eicken, L. Shapiro, and A. Graves 2006. Defining and locating the seaward landfast ice edge in northern Alaska, Proceedings of 18th International Conference on Port and Ocean Engineering under Arctic Conditions (POAC '05), Potsdam, N.Y.

Mahoney, A., H. Eicken, A. G. Gaylord, and L. Shapiro 2007b. Alaska landfast sea ice: Links with bathymetry and atmospheric circulation, *Journal of Geophysical Research-Oceans*, *112*(C2), C02001

10.1029/2006jc003559.

Maslanik, J., J. Stroeve, C. Fowler, and W. Emery 2011. Distribution and trends in Arctic sea ice age through spring 2011, *Geophys. Res. Lett.*, *38*L13502, doi:13510.11029/12011GL047735.

Maslanik, J. A., C. Fowler, J. Stroeve, S. Drobot, J. Zwally, D. Yi, and W. Emery 2007. A younger, thinner Arctic ice cover: Increased potential for rapid, extensive sea-ice loss, *Geophysical Research Letters*, *34*(24), Doi 10.1029/2007gl032043, -.

Masterson, D. M. 2009. State of the art of ice bearing capacity and ice construction, *Cold Regions Science & Technology*, *58*(3), 10.1016/j.coldregions.2009.04.002, 99-112.

Maykut, G. A. 1986. The surface heat and mass balance, edited by N. Untersteiner, pp. 395-463, Martinus Nijhoff Publ., Dordrecht (NATO ASI B146).

Melnikov, I. A. 1997. *The Arctic sea ice ecosystem*, Gordon Breach Sci. Publ., Amsterdam.

Meyer, F., S. Hinz, A. Laika, D. Weihing, and R. Bamler 2006. Performance analysis of the TerraSAR-X Traffic monitoring concept, *Isprs Journal of Photogrammetry and Remote Sensing*, *61*(3-4), DOI 10.1016/j.isprsjprs.2006.08.002, 225-242.

Meyer, F. J. 2007. Topography and displacement of polar glaciers from multi-temporal SAR interferograms, *Polar Record*, *43*(227), Doi 10.1017/S0032247407006742, 331-343.

Miles, M. W., and R. G. Barry 1998. A 5-year satellite climatology of winter sea ice leads in the western Arctic, *Journal of Geophysical Research. C. Oceans*, *103*(C10)21723-21734.

Morris, K., S. S. Li, and M. Jeffries 1999. Meso- and microscale sea-ice motion in the East Siberian Sea as determined from ERS-1 SAR data, *Journal of Glaciology*, *45*(150)370-383.

Norton, D. W., and A. Graves Gaylord 2004. Drift velocities of ice floes in Alaska's northern Chukchi Sea flaw zone: Determinants of success by spring subsistence whalers in 2000 and 2001, *Arctic*, *57*(4)347-362.

Organization, W. M. 1985. *WMO sea-ice nomenclature, terminology, codes and illustrated glossary*, WMO/DMM/BMO 259-TP-145, Secretariat of the WMO, Geneva.

Pegau, W. S., and C. A. Paulson 2001. The albedo of Arctic leads in summer, *Ann. Glaciol.*, *33*221-224.

Perovich, D. K. 1990. Theoretical estimates of light reflection and transmission by spatially complex and temporally varying sea ice covers, *J. Geophys. Res.*, *95*9557-9567.

Perovich, D. K. 1998. Optical properties of sea ice, edited by M. Leppäranta, pp. 195-230, University of Helsinki, Helsinki.

Perovich, D. K. 2011. The Changing Arctic Sea Ice Cover, *Oceanography*, *24*(3)162-173.

Perovich, D. K., J. A. Richter-Menge, K. F. Jones, and B. Light 2008. Sunlight, water, and ice: Extreme Arctic sea ice melt during the summer of 2007, *Geophysical Research Letters*, *35*(11), Doi 10.1029/2008gl034007, -.

Polyakov, I. V., J. E. Walsh, and R. Kwok 2012. Recent Changes of Arctic Multiyear Sea Ice Coverage and the Likely Causes, *Bulletin of the American Meteorological Society*, *93*(2), Doi 10.1175/Bams-D-11-00070.1, 145-151.

Potter, R. E., J. T. Walden, and R. A. Haspel 1981. Design and construction of sea ice roads in the Alaskan Beaufort Sea, in *Offshore Technology Conference*, edited, pp. 135-140, Houston, Texas.

Pritchard, R. S. 1978. Dynamics of near shore ice, *OCSEAP Annual Reports of Principal Investigators for Year Ending March 1978: vol.XI, Hazards*39-49.

Pritchard, R. S. 1991. Sea Ice Mechanical Energy Balance: Nearshore Chukchi Sea 1982, *Ann. Glaciol.*, *15*63-72.

Pritchard, R. S., and D. J. Hanzlick 1987. Chukchi Sea Ice Motion 1981-82, *POAC 87*255-270.

Reimnitz, E. 2000. Interactions of river discharge with sea ice in proximity of Arctic Deltas: A review, *Polarforschung*, *70*123-134.

Reimnitz, E., and P. Barnes 1974. Sea ice as a geologic agent on the Beaufort Sea shelf of Alaska, in *The Coast and Shelf of the Beaufort Sea (proceedings of a Symposium on Beaufort Sea Coast and Shelf Research)*, edited by J. C. Reed and A. G. Slater, Arctic Institute of North America, Arlington, VA.

Rosen, P., S. Hensley, G. Peltzer, and M. Simons 2004. Updated repeat orbit interferometry package released, *Eos Trans. AGU*, *85*(5)47.

Rosen, P. A., S. Hensley, H. A. Zebker, F. H. Webb, and E. J. Fielding 1996. Surface deformation and coherence measurements of Kilauea volcano, Hawaii, from SIR-C radar interferometry, *Journal of Geophysical Research-Planets*, *101*(E10)23109-23125.

Rosenqvist, A., M. Shimada, N. Ito, and M. Watanabe 2007. ALOS PALSAR: A Pathfinder Mission for Global-Scale Monitoring of the Environment, *Ieee Transactions on Geoscience and Remote Sensing*, *45*(11)3307-3316.

Rothrock, D. A., and J. Zhang 2005. Arctic Ocean sea ice volume: What explains its recent depletion?, *J. Geophys. Res.*, *110*C01002, doi:01010.01029/02004JC002282.

Sandwell, D. T., D. Myer, R. Mellors, M. Shimada, B. Brooks, and J. Foster 2008. Accuracy and Resolution of ALOS Interferometry: Vector Deformation Maps of the Father's Day Intrusion at Kilauea, *Geoscience and Remote Sensing, IEEE Transactions on*, *46*(11)3524-3534.

Schmidt, C. 2011. Despite Data Gaps, US Moves Closer to Drilling in Arctic Ocean, *Science*, *333*(6044)812-813.

Service, C. H. 1968. Pilot of Arctic Canada, edited, Canadian Hydrographic Servive, Surveys and Mapping Branch, Department of Mines and Technical Surveys, Ottawa.

Seymour, M. S., and I. G. Cumming 1994. Maximum likelihood estimation for SAR interferometry, Proceedings of Geoscience and Remote Sensing Symposium, 1994. IGARSS '94. Surface and Atmospheric Remote Sensing: Technologies, Data Analysis and Interpretation., International, 8-12 Aug 1994.

Shapiro, L. 1975. A preliminary study of the formation of landfast ice at Barrow, Alaska. Winter 1973-74, *Geophysical Institute Report, UAG R-235*, 43 pp, Geophysical Institute, Fairbanks.

Shapiro, L., and J. Burns 1975. Satellite observations of ice movement in the Bering Strait region, in *Climate of the Arctic*, edited by S. Bowling and G. Weller, pp. 379-386, University of Alaska Press, Fairbanks.

Spreen, G., R. Kwok, and D. Menemenlis 2011. Trends in Arctic sea ice drift and role of wind forcing: 1992-2009, *Geophys. Res. Lett.*, *38*, Artn L19501

Doi 10.1029/2011gl048970.

Stirling, I. 1997. The importance of polynyas, ice edges, and leads to marine mammals and birds, *J. Mar. Sys.*, *10*9-27.

Stringer, W. J. 1974. Morphology of the Beaufort Sea shorefast ice, in *The Coast and Shelf of the Beaufort Sea*, edited by J. C. Reed and J. E. Sater, pp. 165-172, Arctic Institute of North America, Arlington, VA.

Stringer, W. J., S. A. Barrett, and L. K. Schreurs 1980. *Nearshore ice conditions and hazards in the Beaufort, Chukchi and Bering Seas*, Geophysical Institute, University of Alaska, Fairbanks, AK.

Stroeve, J., M. Serreze, M. Holland, J. Kay, J. Malanik, and A. Barrett 2012. The Arctic's rapidly shrinking sea ice cover: a research synthesis, *Climatic Change*, *110*(3), 10.1007/s10584-011-0101-1, 1005-1027.

Stroeve, J., M. Serreze, S. Drobot, S. Gearheard, M. M. Holland, J. Maslanik, W. Meier, and T. Scambos 2008. Arctic sea ice extent plummets in 2007, *Eos, Trans. Am. Geophys. Un.*, *89*(2)13-20.

Tin, T., and M. O. Jeffries 2003. Morphology of deformed first-year sea ice features in the Southern Ocean, *Cold Reg. Sci. Technol.*, *36*141-163.

Torgerson, L. J., and W. J. Stringer 1985. Observations of Double Arch Formation in the Bering Strait, *Geophys. Res. Lett.*, *12*(10)677-680.

Tschudi, M. A., J. A. Curry, and J. A. Maslanik 2002. Characterization of springtime leads in the Beaufort/Chukchi Seas from airborne and satellite observations during FIRE/SHEBA, *Journal of Geophysical Research*, *107*(C10)SHE9.1-SHE9.14.

Tucker, W. B. I., J. W. Weatherly, D. T. Eppler, D. Farmer, and D. L. Bentley 2001. Evidence for the rapid thinning of sea ice in the western Arctic Ocean at the end of the 1980s, *Geophys. Res. Lett.*, *28*(14)2851-2854.

U.S. Fish and Wildlife Service 2008. Endangered and Threatened Wildlife and Plants; Determination of Threatened Status for the Polar Bear (Ursus maritimus) Throughout Its Range; Final Rule, *Federal Register*, *73*(95)28211-28303.

Wang, M., and J. E. Overland 2009. A sea ice free summer Arctic within 30 years?, *Geophys. Res. Lett.*, *36*(7), 10.1029/2009gl037820, L07502.

Weeks, W. F., A. Kovacs, S. J. Mock, W. B. Tucker, W. D. Hibler, III, and A. J. Gow 1977. Studies of the movement of coastal sea ice near Prudhoe Bay, Alaska, U.S.A., *J. Glaciol.*, *19*(81)533-546.

Weingartner, T., K. Aagaard, R. Woodgate, S. Danielson, Y. Sasaki, and D. Cavalieri 2005. Circulation on the north central Chukchi Sea shelf, *Deep-Sea Research Part Ii-Topical Studies in Oceanography*, *52*(24-26), 10.1016/j.dsr2.2005.10.015, 3150-3174.

Woodgate, R. A., T. Weingartner, and R. Lindsay 2010. The 2007 Bering Strait oceanic heat flux and anomalous Arctic sea-ice retreat, *Geophys. Res. Lett.*, *37*(1), 10.1029/2009gl041621, L01602.

World Meteorological Organization 1970. *WMO sea-ice nomenclature, terminology, codes and illustrated glossary*, Secretariat of the WMO, Geneva.

Zebker, H. A., and J. Villasenor 1992. Decorrelation in interferometric radar echoes, *Ieee Transactions on Geoscience and Remote Sensing*, *30*(5)950-959.

Zubov, N. N. 1945. *Arctic ice*, Izd. Glavsevmorputi, Moscow.

Appendix 1 BIBLIGRAPHY OF LEADS AND LANDFAST ICE

This appendix lists articles concerning leads or landfast that have been published since MMS OCS STUDY 2005-068. For the complete list of references, please visit http://boemre.gina.alaska.edu/bibliography

Alkire, M. B., & Trefry, J. H. (2006). Transport of spring floodwater from rivers under ice to the Alaskan Beaufort Sea. Journal of Geophysical Research-Oceans. 111(C12).

Allen, A. A., & Nelson, W. G. (2005). Oil spill countermeasures in landfast sea ice. 2005 International Oil Spill Conference, IOSC 2005. Miami Beach, FL, United states.

Amoco Production Company, D. D. (1973). Landfast ice movement in the Prudhoe Bay - Harrison Bay area, winter 1974 to 1975. Alaska Oil and Gas Association, AOGA Project No.28 (Vol.1).

Banke, E., Lowings, M. G., Limited, M., & Dome Petroleum, L. (1982). Ice edge break-up in Lancaster Sound, Beaufort E.I.S. support document, Volume: no. BEISSD24. Calgary, Canada.

Blazey, B. (2005). Landfast Ice Breakouts on the Northern Alaskan Coast. 2005 Fall Meeting of the American Geophysical Union, San Francisco, CA.

Deal, C., Jin, M., & Wang, J. (2008). Modeling the Ice-Ocean Ecosystem in Landfast Ice on the Chukchi Shelf and within the Fluctuating Ice Margin of the Bering Sea. 2008 Ocean Sciences Meeting. Orlando, FL.

Divine, D. V., Korsnes, R., & Makshtas, A. P. (2004). Temporal and spatial variation of shore-fast ice in the Kara Sea. Continental Shelf Research, 24(15), 1717-1736.

Druckenmiller, M. L., Eicken, H., Johnson, M. A., Pringle, D. J., & Williams, C. C. (2009). Toward an integrated coastal sea-ice observatory: System components and a case study at Barrow, Alaska. Cold Regions Science and Technology, 56(2-3), 61-72.

Dumas, J., Carmack, E., & Melling, H. (2005). Climate change impacts on the Beaufort shelf landfast ice. Cold Regions Science and Technology, 42(1), 41-51.

Dumas, J. A., Flato, G. M., & Brown, R. D. (2006). Future projections of landfast ice thickness and duration in the Canadian Arctic. Journal of Climate, 19(20), 5175-5189.

Dumont, D., Gratton, Y., & Arbetter, T. E. (2010). Modeling Wind-Driven Circulation and Landfast Ice-Edge Processes during Polynya Events in Northern Baffin Bay. Journal of Physical Oceanography, 40(6), 1356-1372.

Ehn, J., Granskog, M. A., Kawamura, T., Lepparanta, M., Shirasawa, K., & Hokkaido University, J. (2004). Seasonal development of the properties and composition of landfast sea ice in the Gulf of Finland, the Baltic Sea. Journal Of Geophysical Research: Oceans.

Ehn, J. K., Granskog, M. A., Papakyriakou, T., Galley, R., Barber, D. G., Langhorne, P., et al. (2006). Surface albedo observations of Hudson Bay (Canada) landfast sea ice during the spring melt. Papers from the 2005 international symposium on Sea ice. United Kingdom.

Eicken, H., Mahoney, A. Gradinger, R. Gaylord, A. & Melling, H. (2005). Sediment transport by sea ice in the Chukchi and Beaufort Seas: Increasing importance due to changing ice conditions? Deep Sea Research Part II: Topical Studies in Oceanography, 52(24), 3281-3302.

Eicken, H., Shapiro, L. H., Gaylord, A. G., Cotter, P. W., Region., U. S. M. M. S. A. O., & Institute., U. o. A. F. G. (2006). Mapping and characterization of recurring spring leads and landfast ice in the Beaufort and Chukchi Seas. U.S. Dept. of the Interior, Minerals Management Service, Alaska Outer Continental Shelf Region.

Eicken, H., Blahak, U., Groves, J., Dmitrenko, I., Tyshko, K., Darovsikih, A., Dierking, W. & Kassens, H. (2005). Zonation of the Laptev Sea landfast ice cover and its importance in a frozen estuary. Global and Planetary Change, 48(1), 55-83.

Gagnon, A. S. & Gough, W.A. (2006). Future projections of landfast ice thickness and duration in the Canadian Arctic East-west asymmetry in long-term trends of landfast ice thickness in the Hudson Bay region, Canada. Journal of Climate, 19(20), 5175-5189.

Gagnon, A. S. & Gough, W. A. (2006). East-west asymmetry in long-term trends of landfast ice thickness in the Hudson Bay region, Canada. Climate Research, 32(3), 177-186.

George, J. C., Huntington, H. P., Brewster, K., Eicken, H., Norton, D. W., & Glenn, R. (2004). Observations on Shorefast Ice Dynamics in Arctic Alaska and the Responses of the Inupiat Hunting Community. Arctic, 57(4).

Gilchrist, H. G. & Robertson, G. J. (2000). Observations of marine birds and mammals wintering at polynyas and ice edges in the Belcher Islands, Nunavut, Canada. Arctic, 53(1), 61-68.

Graves, A. (2005). Examining landfast sea ice on Alaska's northern coast. Alaska Satellite Facility News and Notes, 2:02 (p.1)

Haas, C., Dierking, W., Busche, T. & Hoelemann, J. (2005). Envisat ASAR monitoring of polynya processes and sea ice production. In The Laptev Sea, Salzburg, Austria.

Hannah, C. G., Dupont, F. & Dunphy, M. (2009). Polynyas and Tidal Currents in the Canadian Arctic Archipelago. Arctic, 62(1), 13p.

Hwang, B. J., Langlols, A., Barber, D. G. & Papakyriakou, T. N. (2007). On detection of the thermophysical state of landfast first-year sea ice using in-situ microwave emission during spring melt. Remote Sensing of Environment, 111(2-3), 148-159.

Jeffries, M. O. & Sackinger, W. M. (1989). Airborne SAR characteristics of Arctic ice shelves and multiyear landfast sea ice, and the detection of massive ice calvings and ice islands. Digest - International Geoscience and Remote Sensing Symposium (IGARSS), 4, 2715-2718.

Jeffries, M. O., Sackinger, W. M., Shoemaker, H. D., Jeffries, M. O., Sackinger, W. M. & Shoemaker, H. D. (1988). Some physical properties of multiyear landfast sea ice, northern Ellesmere Island. Port & Ocean Engineering Under Arctic Conditions. Canada. United States.

Jin, M., Deal, C.J., Wang, J., Tanaka, N., Shin, K.H., Whitledge, T.E., Lee, S.H. & Gradinger, R.R. (2006). Controls of the landfast ice-ocean ecosystem offshore Barrow, Alaska. Annals of Glaciology, 44(1), 63-72.

Joint Tuk-Industry Task, F. (1982). Final report of the Joint Tuk-Industry Task Force to examine the effects of artificial islands on Beaufort Sea ice. Calgary, Canada.

Kasper, J., Weingartner, T. & Danielson, S. L. (2007). Modeling Circulation in the Landfast Ice Zone, 2007. Symposium on Marine Science. Anchorage, AK.

Kasper, J. L. & Weingartner, T. (2008). Modeling Circulation in the Landfast Ice Zone, 2008. Ocean Sciences Meeting. Orlando, CA.

Kawamura, T., Shirasawa, K. & Kobinata, K. (2001). Physical properties and isotopic characteristics of landfast sea ice around the North Water (NOW) Polynya region. Atmosphere-Ocean, 39(3), 173-182.

Konig Beatty, C. & Holland, D. M. (2010). Modeling Landfast Sea Ice by Adding Tensile Strength. Journal of Physical Oceanography, 40(1), 14p.

Konig, C. S. (2007). Arctic landfast sea ice. DAI, 68(01B), 94.

König, C. S. (2007). Arctic landfast sea ice. Unpublished Thesis, New York University.

Ledrew, B. R. (1976). The southestern Beaufort Sea (landfast ice zone) environmental De Finition.

Macdonald, R. W. & Carmack, E. C. (1991). The role of large-scale under-Ice topography in separating estuary and ocean on an Arctic shelf. Atmosphere-Ocean, 29(1), 37-53.

Mahoney, A. (2005). Examining landfast sea ice on Alaska's northern coast. ASF News and Notes. University of Alaska Fairbanks, Fairbanks, Alaska.

Mahoney, A. (2006). Alaska landfast sea ice dynamics. Unpublished Ph.D., University of Alaska Fairbanks, Alaska.

Mahoney, A., Eicken, H., Gaylord, A. G., Shapiro, L. & Nuna Technologies, U. S. (2007). Alaska landfast sea ice: links with bathymetry and atmospheric circulation. Journal of Geophysical Research, 02001-02001.

Mahoney, A., Eicken, H., Graves, A., Shapiro, L. & Cotter, P. (2004). Landfast sea ice extent and variability in the Alaskan Arctic derived from SAR imagery. International Geoscience and Remote Sensing Symposium (IGARSS). Anchorage, AK.

Mahoney, A., Eicken, H., Graves, A., Shapiro, L., Dempsey, J. P. & Nuna Technologies, U. S. (2005). Defining and locating the seaward landfast ice edge in

Northern Alaska. Proceedings of the Eighteenth international conference on Port and ocean engineering under Arctic conditions, 991-1000.

Mahoney, A., Eicken, H., Shapiro, L., Rachold, V., Brown, J., Solomon, S., Sollid, J.L., et. al. (2002). Alaskan landfast sea ice variability and episodic events. Arctic coastal dynamics; report of the 3rd international workshop, 60-63.

Mahoney, A., Eicken, H. & Shapiro, L. (2007). How fast is landfast sea ice? A study of the attachment and detachment of nearshore ice at Barrow, Alaska. Cold Regions Science and Technology, 47(3), 233-255.

Mahoney, A., Eicken, H., Shapiro, L. & Gaylord, A.G. (2007). Alaska landfast sea ice: Links with bathymetry and atmospheric circulation. Journal of Geophysical Research C: Oceans, 112(2).

Marko, J. R., Wright, B. D., Dempsey, J. P., Wright, B. & Associates, C. (2005). Satellite GPS measurements of landfast ice displacements in the Canadian Beaufort during the winter of 2003. Proceedings of the Eighteenth international conference on Port and ocean engineering under Arctic conditions, 725-734.

Morris, K. (1992). Annually recurring sea ice patterns in the nearshore region of the eastern Beaufort Sea as determined from satellite data (1974-1986). M.S. thesis, University of Alaska, Fairbanks.

Nikitin, V. A., Smirnov, V. N., Shushlebin, A. J. & Sheikin, I. B. (1995). Seismic activity of landfast ice. Proceedings of the International Offshore and Polar Engineering Conference, Hague, Netherlands.

Norton, D. W. & Gaylord, A. G. (2004). Drift Velocities of Ice Floes in Alaska's Northern Chukchi Sea Flaw Zone: Determinants of Success by Spring Subsistence Whalers in 2000 and 2001. Arctic, 57(4), 16p.

Ohshima, K. I. (2000). Effect of landfast sea ice on coastal currents driven by the wind. Journal of Geophysical Research-Oceans, 105(C7), 17133-17141.

Ohshima, K.I., Nihashi, S. & Tamura, T. (2005). Detection of coastal polynyas and ice production in the Antarctic and Okhotsk Seas from SSM/I. International Geoscience and Remote Sensing Symposium (IGARSS), Seoul, Korea.

Peterson, I., Smith, S. D., Prinsenberg, S. & Orton, R. H. (1991). Remote monitoring of thermal structure and growth of shore-fast ice off the Labrador coast. Cold Regions Science and Technology, 19(2), 123-130.

Prinsenberg, S. J., Fowler, G. A., van der Baaren, A. & Beanlands, B. (1997). Ice stress measurements from land-fast ice along Canada's Labrador Coast. Cold Regions Science and Technology, 25(1), 1-15.

Rowell, J., Metcalfe, L., Dempsey, J. P. & Labrador Inuit Association, C. (2005). Sea ice: obstacle vs. opportunity: reconciling two views of landfast sea ice. Proceedings of the Eighteenth international conference on Port and ocean engineering under Arctic conditions, 119-130.

Rowell, J., Metcalfe, L., Dempsey, J. P. & Labrador Inuit Association, C. (2005). Voisey's Bay Project: a challenge to Inuit use of the landfast sea ice. Proceedings of the Eighteenth international conference on Port and ocean engineering under Arctic conditions, 109-118.

Sayed, M. & Frederking, R. M. W. (1992). Landfast ice pressure measurements in the Beaufort Sea, San Francisco, CA, USA.

Shapiro, L. H., Harrison, W. D. & Bates, H. F. (1977). Mechanics of origin of pressure ridges, shear ridges and hummock fields in landfast ice (Vol. 15). Quarterly reports, Department of Commerce, Environmental Research lab, Boulder, CO.

Shirasawa, K., Lepparanta, M., Saloranta, T., Kawamura, T., Polomoshnov, A. & Surkov, G. (2005). The thickness of coastal fast ice in the Sea of Okhotsk. Cold Regions Science and Technology, 42(1), 25-40.

Smirnov, V. N., Shushlebin, A. I. & Sheikin, I. B. (1997). Interaction between landfast sea ice and a drilling platform. International Conference on Port and Ocean Engineering Under Arctic Conditions (POAC), Yokohama, Japan.

Spedding, L. G. & Hawkins, J. R. (1985). Comparison of the effects of natural meteorological conditions and artificial islands on regional ice conditions in the Beaufort Sea. Danish Hydraulic Institute (pp. 305-315). Narssarssuaq, Greenland.

Stevens, C., Moorman, B.J., Solomon, S.M. & Hugenholtz, C.H. (2009). Mapping subsurface conditions within the near-shore zone of an Arctic delta using ground penetrating radar. Cold Regions Science and Technology, 56(1), 30-38.

Verrall, R. I. & Todoeschuck, J. P. (1989). Rolls on Landfast Ice: Relation Between Thickness and Wavelength. United States.

Weingartner, T., Kasper, J., Danielson, S. L. & Okkonen, S. R. (2006). Circulation in the Landfast-Ice Zone of the Alaskan Beaufort Sea, 2006 Fall Meeting of the American Geophysical Union. San Francisco, CA.

Weingartner, T., Kasper, J., Danielson, S. L. & Okkonen, S. R. (2006). Modeling Circulation in the Landfast Ice Zone, 2006 Fall Meeting of the American Geophysical Union. San Francisco, CA.

Weingartner, T. J., Danielson, S. L. & Kasper, J. (2008). Circulation in the Landfast-Ice Zone of the Alaskan Beaufort Sea. 2008 Ocean Sciences Meeting. Orlando, FL.

Appendix 2 LITERATURE REVIEW OF POTENTIAL ICEBREAKER IMPACTS ON SEA ICE AS THEY RELATE TO THE BEAUFORT AND CHUKCHI SEAS

Interim task for CMI Agreement No.: AK-09-04 MMS09HQPA0004T
Mapping and Characterization of Recurring Spring Leads and Landfast Ice in the Chukchi and Beaufort Seas

Prepared for the
Bureau of Ocean Energy Management, Regulation, and Enforcement (BOEMRE) Alaska OCS Region
3801 Centerpoint Drive
Anchorage, Alaska 99503

A. Mahoney
Geophysical Institute, University of Alaska Fairbanks
Fairbanks, AK 99775 USA
Mahoney@gi.alaska.edu

A2.1 Table of Contents

A2.2 List of figures

A2.3 Introduction

This literature review aims to assess the current state of knowledge regarding the physical impact of icebreaking upon sea ice in terms of its mechanical strength and stability and its tendency to freeze or melt. These considerations appear to be absent from most environmental impact studies of icebreakers and icebreaking (e.g.: Swedish Polar Research Secretariat, 1993), which typically address the potential for spills and pollution or the disturbance of marine mammals by shipping noise. Part of the reason for the lack of work in this area is an apparently widely held view that there is no impact to study. This view is illustrated by a quotation in the abstract for the only document we were able to find that was specifically aimed at assessing the physical impacts of icebreaking on sea ice behavior (Hotzel and Noble, 1979). In the abstract, Hotzel and Noble quote an icebreaker captain as saying "one north-west gale is worth a whole fleet of icebreakers".

However, this review discusses a number of studies addressing the mechanical differences between broken and unbroken ice from the perspective of navigation or engineering as well as the human impacts of icebreaking in landfast ice. Although no work was found that specifically related to the Chukchi Sea, there have been a number of studies conducted in the Beaufort Sea. There was a significant amount of work done in the late 1970s and early 1980s related to hydrocarbon exploration and development, particular in Beaufort Sea and the Canadian Arctic Archipelago. Studies conducted elsewhere also contain information relevant for this review, which also cites more recent studies involving icebreaker activity in the Baltic Sea, the Central Arctic as well as Antarctica.

The most apparent effect of icebreaking is the channel of water and broken ice left behind an icebreaker, which can be thought of as an artificial lead. In this review we will first look at literature relevant to the effect on the ice in the immediate path of the icebreaker and then we will look at studies relevant to impacts on the surrounding ice. We will then discuss immediate and longer-term implications of these effects and identify relevant knowledge gaps.

A2.4 Impact upon sea ice in immediate path of icebreaker

Sea ice in the immediate path of an icebreaker is broken into pieces, which are typically rotated and at least partially submerged as they are deflected by the hull of the ship. Some of the broken ice is pushed underneath the intact ice either side, leaving a channel containing a mix of open water and ice, often called brash. Modern azimuth icebreakers, which have propellers that can be rotated to provide directional thrust, can push broken ice to the side of the channel with their wake, which is also capable of breaking ice. This can create a virtually ice-free channel wider than the hull of the icebreaker (Keinonen and Lohi, 2001). Immediately after the passage of an icebreaker, the channel left behind will be mechanically weaker than the surrounding ice and will have a lower albedo (reflectance) due to the presence of open water among the broken ice blocks. These effects will both be greater with less ice left in the channel. However, the longer-term impacts depend upon whether the icebreaking takes places in freezing or melting conditions and whether the broken ice is landfast or drifting.

In drifting pack ice, leads open and close naturally depending on local stresses within the ice cover (Fily and Rothrock, 1990). Transiting icebreakers will exploit any such leads thereby reducing the amount they need to break. Furthermore icebreaker channels created in pack ice will behave like leads. For example, Kanik *et al.* (1980) observed that the channel would generally remain open less than 12 minutes such that it was normally only 1-2 km long behind the icebreaker. Prinsenberg *et al.* (2009) also note that the channel can rapidly close behind an icebreaker in converging pack ice and provide a photograph (Figure 4 in their article) that illustrates this.

In landfast ice, by contrast, an icebreaker channel will remain open until it freezes over. If the channel is broken in summer, this may not happen unless the channel is cut in multiyear landfast ice, such as that in McMurdo Sound, Antarctica (Brunt et al., 2006). An ice-free channel will behave like a natural lead in the ice-cover, the freezing and solidification of which have been described by Wettlaufer et al. (2000). The refreezing rate of a rubble-filled icebreaker channel in landfast ice in wintertime was the subject of a number of studies during trials of the Canadian icebreaker *Kigoriak* in 1981-82. Cornett (1982) reported on track-crossing tests that were performed to assess the impact on icebreaker channels on Inuit travel routes. The tests found a channel filled with ice rubble would be crossable on foot or snowmobile in a matter of hours, though larger rubble fields such as at a mooring basin might take longer.

In the longer term, Cornett (1982) reports that traditional icebreaking ultimately results in thicker ice within the channel. By inverting blocks of ice so their cold upper surfaces are submerged in the water and their “warm” lower surfaces are exposed to the cold atmosphere, icebreaking enhances heat transfer from the ocean to the atmosphere and leads to an acceleration of ice growth. Repeated use of the channel further enhances this process. Hamza (1982) compared numerical models of accelerated ice growth in icebreaker channels in which each passage of a ship redistributed the rubble into a less compact configuration. Although this only partially represents the physics of the process, the models showed reasonable agreement with observations if a suitable porosity parameter was chosen.

A related study (Dome Petroleum, 1983) found that a channel in landfast ice in the Beaufort Sea became harder to travel through after it refroze between transits. Figure A2.1 shows how much slower successive transits in an icebreaker channel become over time. Tests were made for two channels in level ice. One channel was ice approximately 1.08 m thick and the other in ice around 1.3-1.5 m thick. The results show that immediately after the channel is made, a ship can travel 2-3 times faster in the channel that through the surrounding ice. After less than two weeks however, it becomes easier to break a new channel than to follow a previous one.

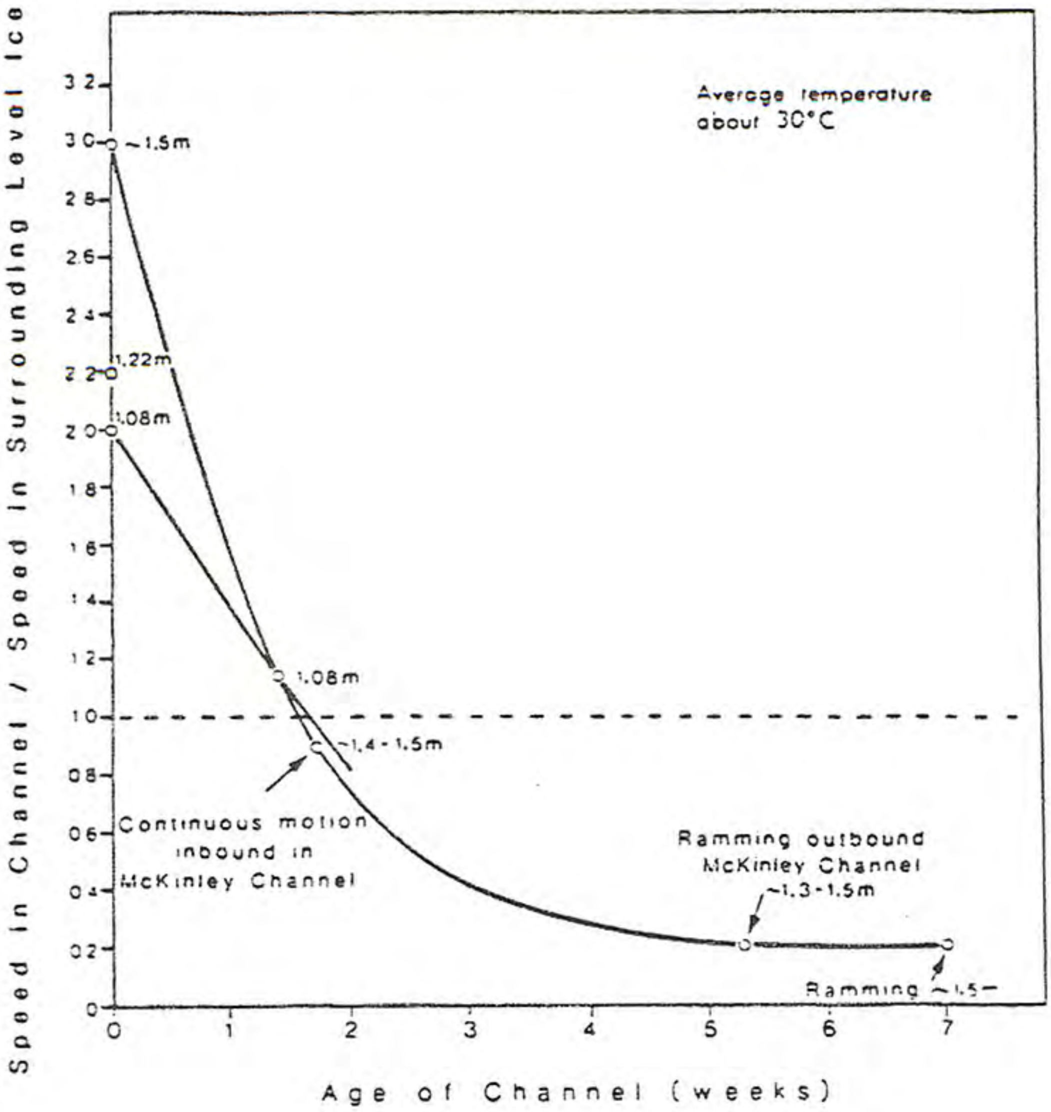

Figure A2.1: The effect upon vessel speed of repeated use and refreezing of an icebreaker channel. Taken from a report by Dome Petroleum (1983) (Figure 4.8, p36).

An alternative use of icebreakers is for ice management, where the intent is to reduce the ice load upon a vessel or structure. In this mode of operation, multiple icebreakers often work together to clear and break ice around a fixed or moored structure. Croasdale (2009) describes major milestones in the development of ice management methods and technology. Figure A2.2 shows three icebreakers operating in the drifting central polar pack to reduce ice loads on a drill ship during the Arctic Coring Expedition (ACEX) in 2004. The *Sovetskiy Soyuz* was performing primary ice management a few kilometers updrift from the *Vidar Viking*, which was acting as a drill ship for the expedition and was maintaining station. The *Oden* was working in between to break up ice into smaller pieces closer to the *Vidar Viking*.

Ice management operations such as those illustrated in Figure A2.2 break a large region of the sea ice up-drift of the protected vessel or structure into a brash of water and broken floes. Figures 3 and 4 show model results calibrated with data collected during the ACEX ice management operations. Figure A2.3 shows the effect of ice management in terms of a reduction in floe size. Two icebreakers are clearly more effective than one, but their effectiveness is reduced by higher ice concentration and thicker ice. Figure A2.4 illustrates the decrease in the strength of the ice cover as a result of ice management in terms of an effective thickness of ice intact ice. However, Wright (2001) notes that "overly managed ice" can lead to increased ice loads on structures due to refreezing.

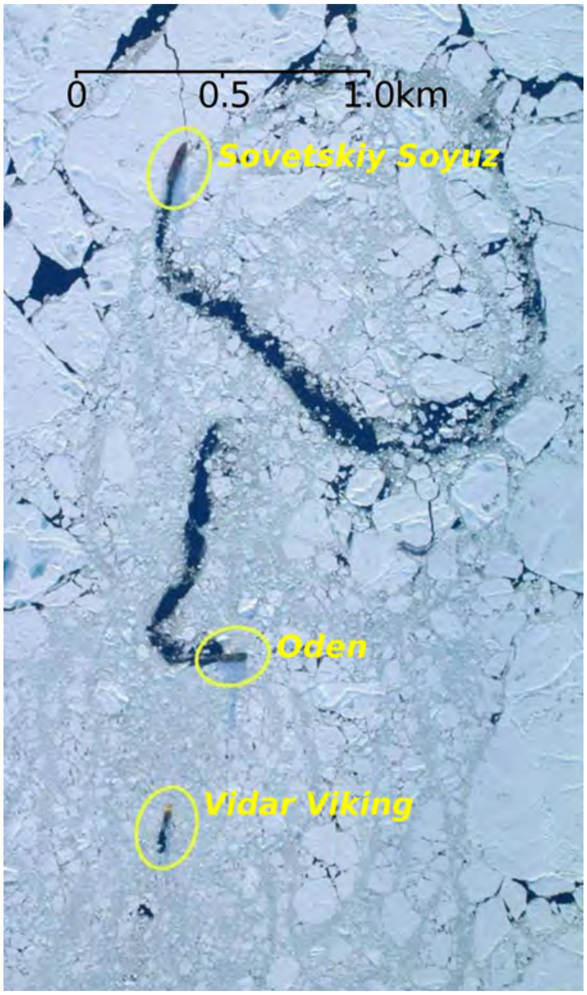

Figure A2.2: Ice management in drifting pack ice in support of ACEX. Taken from Moran (2006, Fig. 4, p11) with permission. Ice drift direction is top to bottom. The Sovetskiy Soyuz is breaking a large floe. The Oden is breaking the broken floe into smaller and smaller pieces. The Vidar Viking is holding position (photo taken by Per Frejvall).

In summertime, the ocean can be above it its freezing point and the icebreaker channel will not refreeze. In such conditions, icebreaking will not result in thicker stronger ice. Instead the broken ice will likely experience enhanced melting due to the decreased albedo and increased surface area exposed to the water [A. Keinonen, personal communication], which will both lead to greater absorption of solar radiation. However, this review found no literature documenting melt processes in icebreaker channels.

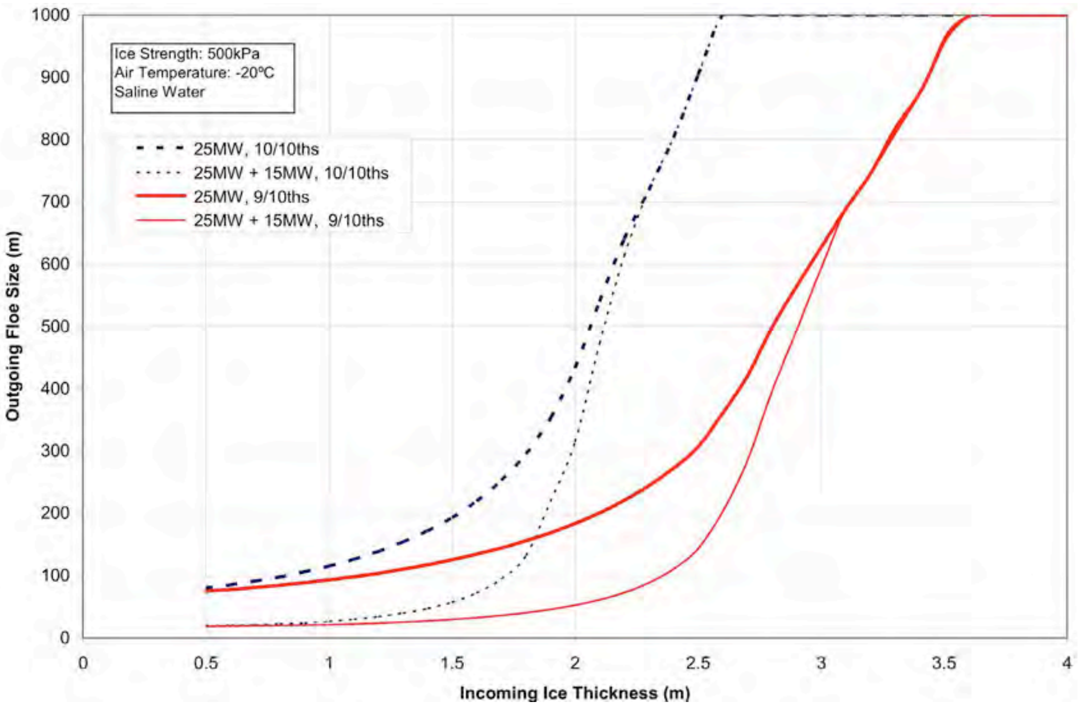

Figure A2.3: Floe size reduction by ice management operations using a single 25 MW icebreaker on its own and in conjunction with a 15 MW icebreaker. Ice drift speed 0.5 ms^{-1}. From Keinonen (2008, Fig 8, p11) with permission.

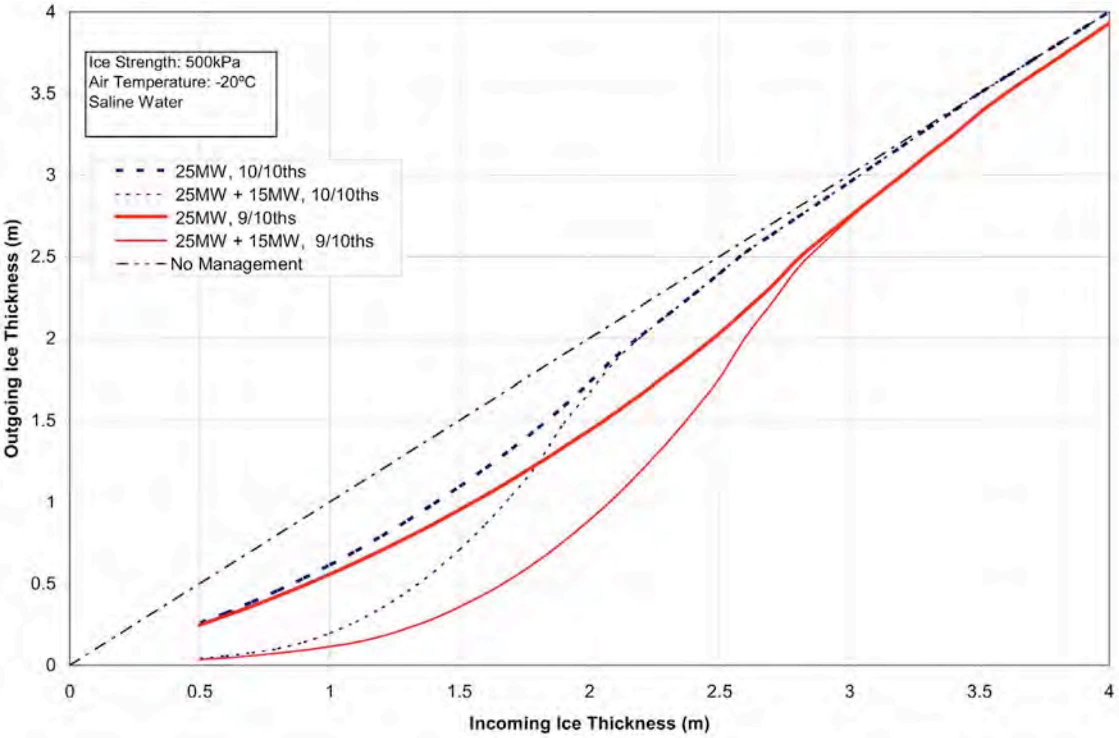

Figure A2.4: The effective reduction in ice thickness due to ice management operations using a single 25 MW icebreaker on its own and in conjunction with a 15 MW icebreaker. Ice drift speed 0.5 ms^{-1}. From Keinonen (2008, Fig 9, p11) with permission

A2.5 Impacts upon the surrounding ice

Icebreakers create very little direct disturbance to the sea ice outside of their immediate path. In drifting pack ice, the mechanical effect of a single icebreaker channel is unlikely to change the regional sea ice dynamics in any measurable way. It is conceivable that a large ice management operation could create detectable changes in the motion and behavior of the surrounding ice, but there is little if any literature on this subject. Based on the studies of the refreezing of a single channel (Cornett, 1982; Kanik et al., 1980), the reduction in ice strength would only be temporary and ultimately the ice would become thicker and stronger as a result of the management. If large-scale ice management were to have any broader impacts on the sea ice, then they would be most pronounced in the summertime when enhanced melting of the broken ice (through reduced albedo and increased surface area) could extend the effected area and prolong any impact.

Icebreaker channels are likely to have the greatest impact on surrounding sea ice when they are made in landfast ice, which could become destabilized. Hotzel and Noble (1979) addressed this concern in a report for Petro-Canada as part of the environmental impact assessment for the Arctic Pilot Project. Based on Landsat data from 1973-77, Hotzel and Noble (1979) present detailed patterns of break-up in Lancaster Sound and the typical climatic conditions that prevail. The authors then note that there was nothing unusual about the pattern of break-up in 1977 and 1979 when the CCGS *Louis St. Laurent* entered the landfast ice before break-up. They also point out that no unusual events were noted during the 1969-70 voyage of the SS Manhattan. Hotzel and Noble conclude that icebreakers will have no impact on landfast ice break-up or freeze-up and summarize by stating that icebreakers are controlled by the climatic environment and not the other way around. They also quote Captain Pelletier of the Quebec City Regional Office of Coast Guard as saying "one north-west gale had more effect than all the icebreakers in the fleet in breaking-up and moving out the ice".

In their report, Hotzel and Noble note that the *Louis St. Laurent* was not leaving an ice-free channel behind and winds were not favoring break-up at the time. Under other circumstances, it may be possible for multiple icebreaker channels to impact break-up of landfast sea ice. In their final section, Hotzel and Noble recommended that break-up and freeze-up conditions be closely monitored during the Arctic Pilot Project to allow for detailed analysis of ship effects. Since the project never went ahead, this work was never done. However, in McMurdo Sound, Antarctica, icebreakers have been used to cut wedges out of the landfast ice to widen the channel leading to McMurdo Station (A. Keinonen, personal communication). In at least 2008 and 2009 the landfast ice edge in McMurdo Sound was notched at the point where it intersected the icebreaker channel (Figure A2.5), but this appears to be the extent of any influence of icebreaking in McMurdo Sound upon the landfast ice. Dammert *et al.* (1998) examined landfast ice in the Baltic Sea using SAR interferometry. They observed approximately 1 m of motion in a patch of landfast ice "cut out" by two icebreaker channels over 2 km apart. Although the total displacement was small, it indicates the potential for icebreaker channels to destabilize landfast ice.

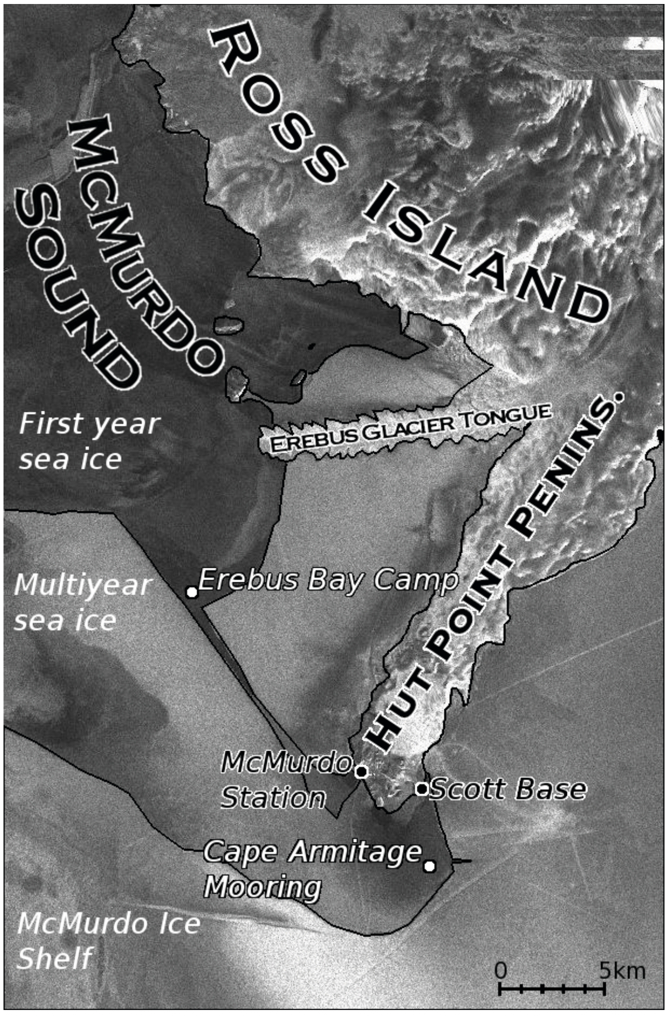

Figure A2.5: ENVISAT synthetic aperture radar image showing sea ice in McMurdo Sound on June 24, 2009, when the author was engaged in research at the location labeled Erebus Bay Camp. The edge of the multiyear landfast ice is clearly notched at the mouth of refrozen icebreaker channel, which can be clearly seen between the camp and McMurdo Station. Imagery courtesy of W. Rack, University of Canterbury, New Zealand.

A2.6 Implications of icebreaking effects on sea ice

The implications of the effects of icebreaking upon the sea ice depend upon whether the icebreaking takes place in pack ice or landfast and whether or not the ice will refreeze afterwards. During winter, icebreaking activity will ultimately lead to thicker ice through increased surface area and enhanced heat transfer from the ocean to the atmosphere. There is a reasonably established body of literature on the topic of refreezing in icebreaker channels (Cornett, 1982; Dome Petroleum, 1983; Hamza, 1982; Kanik et al., 1980). Icebreaker channels made during summer will likely lead to locally enhanced melt through decreased albedo and increased surface area. As a result, icebreaker channels are likely to be longer-lived in summertime, though the spatial density of natural leads is also greater (Eicken et al., 2006) and so the effect of a single channel would be less noticeable. However, we found no literature documenting the effects of summertime icebreaking.

The implications of icebreaking activity are likely to be greater in landfast ice than drifting pack ice. The immediate impact of icebreaking is the creation of a region of open water and broken ice. Drifting pack ice typically contains many such natural openings and an individual icebreaker channel is likely to be short-lived. In landfast ice, natural openings are rare away from the seaward edge and an icebreaker channels may therefore represent the only opening in a given region. The Arctic Marine Shipping Assessment (Arctic Council, 2009) notes that "*artificially opened water channels can be problematic for marine mammals and other species, which confuse them for polynyas and can get trapped too far from the ice edge as the channel eventually refreezes*". However, there are also documented cases of marine wildlife beneficially exploiting icebreaker channels. In McMurdo Sound, Antarctica, Andrews *et al.* (2008) report the use of icebreaker channels in the landfast ice by whales to reach otherwise inaccessible foraging ground. Similarly, Harkonen *et al.* (2008) describe the use of icebreaker channels in the Caspian and Baltic Seas to reach breeding areas.

Icebreaker channels in landfast ice have the potential to disrupt travel routes over the ice used by local hunters, but reports based on studies near Tuktoyaktuk (Cornett, 1982)] and Lancaster Sound (Kanik et al., 1980) suggest that either the channel will solidify within in a matter of hours or else the local hunters are more than resourceful enough to negotiate the obstacle. During the environmental assessment for the Arctic Pilot project, there was some concern that icebreaking might bring about delayed freeze-up or early break-up of landfast ice, but work by Hotzel and Noble (1979) concluded this concern was unfounded. However, Dammert et al. (1998) observed small-scale motion of a patch landfast ice that was destabilized by icebreaker activity.

A2.7 Summary

From a review of existing literature, it is apparent the consensus view is that icebreaker activity will only have negligible effects, if any, upon the sea ice. However, it should be noted that this view is based on only a few quantitative studies involving single channels made by transiting icebreakers. Vessels transiting between locations will seek a path of least resistance that requires the least amount of icebreaking, thereby inherently taking steps to minimize their impact. Vessels engaged in survey work or ice management operations will not be able to do this.

No articles were found documenting any impact or lack thereof from ice management operations, though experts in the industry consider it unlikely that even extensive ice management operations could have any regional effect (A. Keinonen, personal communication). However, an ice management operation such as ACEX potentially represents an opportunity to settle any uncertainty regarding the impact of icebreaking in pack ice. If no impact can be detected in the ice surrounding the operation, then there probably is no impact. This review was not able to find any work done during ACEX operations, but an analysis of satellite imagery over the drilling region might be able to determine whether or not the operation had any effect of the surrounding ice. Icebreaker channels can be easily identified in synthetic aperture radar imagery (see Figure 5 and Dammert et al., 1998; Johannessen, 2006) and a region of managed ice such as that shown in Figure A2.2 ought to be identifiable in MODIS imagery.

The implications of icebreaking are greatest landfast ice, where an icebreaker channel may represent the only large opening for many kilometers, which can affect the habits and distribution of marine mammals (Andrews et al., 2008; Harkonen et al., 2008). Studies of refreezing icebreaker channels in winter indicate their only lasting effect is thicker, stronger ice (Cornett, 1982; Dome Petroleum, 1983; Kanik et al., 1980). Hotzel and Noble (1979) considered the effect of icebreakers on landfast ice stability and concluded that icebreaking during 1977 and 1979 in Lancaster Sound did not lead to any unusual break-up patterns. However, Hotzel and Noble also note that two cases of landfast icebreaking they considered took place during weather conditions unfavorable for break-up. Overall, there appears to be a dearth of literature concerning icebreaking activity during summertime. In the absence of data to the contrary, it therefore is possible to contrive a set of circumstances in which extensive icebreaking activity combined with certain weather events to induce an early onset of break-up in a region. This matter could have been conclusively resolved had the Arctic Pilot Project proceeded and Hotzel and Noble's recommendations for monitoring of landfast ice been followed.

A2.8 References cited

Andrews, R.D., Pitman, R.L. and Ballance, L.T., 2008. Satellite tracking reveals distinct movement patterns for Type B and Type C killer whales in the southern Ross Sea, Antarctica. Polar Biology, 31(12): 1461-1468.

Arctic Council, 2009. Arctic Marine Shipping Assessment 2009 Report.

Brunt, K.M., Sergienko, O. and MacAyeal, D.R., 2006. Observations of unusual fast-ice conditions in the southwest Ross Sea, Antarctica: preliminary analysis of iceberg and storminess effects. Annals of Glaciology, 44: 183-187.

Cornett, S., 1982. Implications of ship's tracks for Inuit travel, ice thickness and ice growth acceleration in the Canadian Beaufort Sea, Dome Petroleum, Calgary.

Croasdale, K.R., Bruce, J.R. and Liferov, P., 2009. Sea ice loads due to managed ice, 20th International Conference on Port and Ocean Engineering under Arctic Conditions (POAC ' 09), Luleå, Sweden.

Dammert, P.B.G., Lepparanta, M. and Askne, J., 1998. SAR interferometry over Baltic Sea ice. International Journal of Remote Sensing, 19(16): 3019-3037.

Dome Petroleum, 1983. Full scale tests of the AML - X4 Canmar Kigoriak, 1979 - 1980, Final Report.

Eicken, H., Shapiro, L., Gaylord, A., Mahoney, A. and Cotter, P., 2006. Mapping and characterization of recurring spring leads and landfast ice in the Beaufort and Chukchi Seas. Final Report, Minerals Management Service, OCS Study MMS 2005-068, Geophysical Institute, University of Alaska Fairbanks, Fairbanks, 180 pp.

Fily, M. and Rothrock, D.A., 1990. Opening and Closing of Sea Ice Leads: Digital Measurements from Synthetic Aperature Radar. Journal of Geophysical Research, 95(C1): 789-796.

Hamza, H., 1982. Accelerated ice growth in ship tracks. Dome Petroleum, unnumbered report

Harkonen, T. et al., 2008. Pup Production and Breeding Distribution of the Caspian Seal (Phoca caspica) in Relation to Human Impacts. AMBIO: A Journal of the Human Environment, 37(5): 356-361.

Hotzel, S. and Noble, P., 1979. Study of influence of shipping on break-up and freeze-up in Lancaster Sound. Report 565C, Arctec Canada Limited.

Johannessen, O.M., 2006. Remote sensing of sea ice in the Northern Sea Route: studies and applications. Springer, 513 pp.

Kanik, B., Winsby, M. and Tanasichuk, R., 1980. Observations of marine mammal and sea bird interaction with icebreaking activities in the High Arctic, July 2-12, 1980, Hatfield Consultants Limited; Petro-Canada (sponsor).

Keinonen, A.J., 2008. Ice management for ice offshore operations, Offshore Technology Conference, Houston, Texas.

Keinonen, A.J. and Lohi, P., 2001. Azimuth icebreakers for ice offshore, 16th International Conference on Port and Ocean Engineering Under Arcitc Conditions, Ottawa, Ontario, Canada, pp. 887-890.

Moran, K., Backman, J. and Farrell, W., 2006. Deepwater drilling in the Arctic Ocean's permanent sea ice. In: J. Backman, K. Moran, D.B. McInroy, L.A. Mayer and the Expedition 302 scientists (Editors), Proceedings of the Integrated Ocean Drilling Porgram, Volume 302. Integrated Ocean Drilling Program Management International, Inc., Edinburgh.

Prinsenberg, S.J., Peterson, I. and Holladay, S., 2009. Formation of a 1.5km wide ice rubble field from a 60cm thick flaw lead in Eastern Canadian Beaufort Sea, 20th International Conference on Port and Ocean Engineering under Arctic Conditions, Luleå, Sweden.

Swedish Polar Research Secretariat, 1993. Environmental Impact Assessment - A study of the ice-breaker Oden in polar operations. Swedish Polar Research Secretariat.

Wettlaufer, J.S., Worster, M.G. and Huppert, H.E., 2000. Solidification of leads: Theory, experiment, and field observations. J. Geophys. Res., 105(C1): 1123-1134.

Wright, B., 2001. Ice loads on the Kulluk in managed ice conditions, 16th International Conference on Port and Ocean Engineering Under Arctic Conditions (POAC '01), Ottawa, Ontario, pp. 553-565.

A2.9 Appendix: Annotated bibliography

(Andrews et al., 2008)

This article present results from satellite-tracking of killer whales in Antarctica. Of relevance to this review, the authors state on page 1462, the authors state "*The whales have apparently learned to take advantage of foraging habitat made available when the icebreaker(s) opens up the channel, which allows whales to forage deeper into the fast ice than they could otherwise (Pitman and Ensor 2003).*"

(Arctic Council, 2009)

The Arctic Marine Shipping Assessment is a concise summary of the diverse scientific, economic, political and legal issues surrounding the future of shipping in the Arctic. The report does not specifically address the physical impacts of icebreaking on sea ice, but it does describe some of their social and ecological implications. On page 146, it states "*The opening of channels through the ice by icebreaking vessels can impact Arctic residents and alter animal behavior. Open water channels take time to freeze and this can disrupt the movements of animals and people over the ice. In many areas of the Arctic in winter, the only naturally occurring ice openings are polynyas caused by winds or ocean currents. Artificially opened water channels can be problematic for marine mammals and other species, which confuse them for polynyas and can get trapped too far from the ice edge as the channel eventually refreezes.*"

With specific regard to the Canadian Archipelago, the report states on page 149 "*In this region, icebreakers leave behind open water channels that may disrupt the movements of wildlife and people traveling on the ice. Icebreakers or other ships traveling through ice-covered waters where seals are whelping can impact nearby seals through flooding dens and wetting baby seals with their wakes*". On page 127, the report also states "*The community of Tuktoyaktuk is right in a harbor where a lot of fishing takes place. ... The east entrance is a place where a lot of people here that do their fishing set their nets right in the channel. Because the ships had made a ship track through the east entrance, they kept it open up right until November sometime, and the people couldn't set their nets there because of the ships going back and forth. That is one of the impacts of shipping on our harvest"*

(Brunt et al., 2006)

A study of the response of landfast ice in McMurdo Sound to the anomalous presence of massive tabular icebergs, which originated from the Ross Ice Shelf and partially blocked the Sound for a number of years. The authors note that the presence of the icebergs caused an unusually large extent of landfast ice to develop, which inhibited the work of US Coast Guard icebreakers that were trying to maintain a channel into McMurdo Station

(Cornett, 1982)

This article presents observed refreezing rates of an icebreaker channel over time and, which the authors compare with model results. The article described tests that were conducted to determine how soon after a passage by the icebreaker the channel was crossable on foot, by skidoo and with a loaded sled; basically a matter of hours. The key conclusions are that ice growth is accelerated in the tanker channel. More passages mean more ice growth, but multiple ships at once make little difference. Growth acceleration is greater for thicker ice, though the authors note that extra snow deposition on rough ice will retard ice growth.

(Croasdale et al., 2009)

This article summarizes operational ice management milestones over the years (*Kulluk* in Beaufort Sea 1982-92; *Molikpaq* off Sakhalin 1999- ; Lomonosov Ridge coring in 2004). The authors simplify managed ice into three categories: (1) thick ice features broken into large pieces; (2) all ice broken into small pieces - minimal pressured ice; (3) all ice broken into small pieces - pressured ice possible. The authors go on to derive some simple estimates of ice loads on structures for different thicknesses of rubbled ice in each of these, but no comparison with un-managed ice.

(Dammert et al., 1998)

This article presents and interferometric SAR analysis over sea ice in Baltic Sea. Nice illustrations of icebreaker tracks in ERS imagery. Figure 2 shows two icebreaker channels in SAR imagery. Figure 4 shows the channels in an interferometric coherence image. On page 3029, the authors state "*the two newly made icebreaker tracks show up very sharp*" (sic), though unfortunately they do not state how new the channels are. The two ice breaker channels in question cut out a patch of landfast ice, which can been seen to behave differently from the surrounding ice as a result. The 16km-long patch of remained ice landfast but uniform small-scale motion. On page 3035, the authors conclude "*icebreaker channels have an effect on ice mechanics in fast ice zones.*" Although the horizontal motion was only small (94cm), this could have potential impacts for structures embedded in or beneath the ice cover.

(Dome Petroleum, 1983)

During the early 1980s, Dome Petroleum sponsored a number of studies concerning the freezing of icebreaker channels. We did not receive a full copy of this report in time for inclusion in this review, but we included one figure (Figure 4.8, p36) that was kindly provided by A. Keinonen.

(Eicken et al., 2006)

This is a report prepared for the US Minerals Management Service that mapped and characterized leads and landfast ice within the Chukchi and Beaufort Seas. The study presents detailed maps of lead and landfast sea ice distributions, which show a strong transition in lead patterns that occurs in late spring. The authors also describe and quantify the annual cycle of landfast ice in this region.

(Fily and Rothrock, 1990)

A demonstration of a technique using consecutive colocated Radarsat SAR imagery to monitor changes in lead area over time. The authors note that even a relatively small area (100 km square) contains leads that are opening while others are closing.

(Hamza, 1982)

The author compares three numerical models to predict the acceleration of ice growth within icebreaker channels with repeated transits. One model is rejected after failing numerical tests and generating unreasonable ice thickness results. The other two models are simple parametric models that appear to consider only the porosity of the broken blocks that fill the icebreaker channel after transit. He finds good agreement with observational data, but However all three models appear to grow additional ice only through the loose piling of rubble in the icebreaker channel without regard for mechanical disruption of the temperature gradient with the ice blocks.

(Harkonen et al., 2008)

This study addresses the impact of human activity on pup production and breeding distribution of the Caspian Seal. Of relevance to this review, the authors state on page 360 "*Artificial leads are created by icebreakers. These were evidently used extensively in 2006 both as corridors and as pupping habitats, although they were little used in 2005. This raises the possibility that seals may have been using the icebreaker channel as an artificial access lead to good breeding ice, a finding supported by observations from the aerial survey. There is therefore a need to investigate how ice formation processes affect distribution and breeding densities of Caspian seals and under which conditions this may be influenced by icebreaker tracks. Grey seals (Halichoerus grypus) have been observed to breed in areas that are isolated from the main seal breeding habitat by very heavy ice in the northern Baltic (E. Helle pers. comm.). Because there is regular icebreaker traffic in the northern Baltic, it is believed that seals can use the channels for passing through ice that would otherwise limit their distribution. It is possible that Caspian seals may make similar use of such man-made channels, especially in years when ice conditions are severe. The potential benefits to breeding Caspian seals of exploiting the icebreaker channel habitat and also the potential costs due to disturbance from industrial shipping warrant separate study.*"

(Hotzel and Noble, 1979)

This is a report prepared for Petro-Canada specifically examining the effect of shipping on break-up and freeze-up. The study is concerned with Lancaster Sound, though without any icebreaking activity to observe in that area, the authors consider the effects of ship traffic in other areas such as the Gulf of St Lawrence, the St Lawrence River and the northern Baltic Sea.

(Johannessen, 2006)

A detailed textbook explaining various remote sensing techniques as applied to operational use and monitoring of the northern sea ice. Of relevance for this review, Figure 4.19 on page 198 shows icebreaker track in synthetic aperture radar imagery.

(Kanik et al., 1980)

This a report prepared for Petro-Canada of a study aimed at assessing the impact of icebreaking activities upon marine mammals and seabirds. However, the first of four objectives listed in Section 1 is “to observe and change in ice and ice lead characteristics caused by icebreaker passage”. They go on to specify that their focus is on changes to the landfast ice edge caused by icebreaker activity. The second and third objectives were to consider both the immediate impacts upon wildlife caused by the passage of the icebreaker and longer term effects caused by changes to the ice. Their fourth objective was to observe how the icebreaker’s track would affect Inuit travel routes.

Their observations of icebreaking are usefully categorized according pack ice and landfast ice. In pack ice, they state that icebreaker channel “generally remained open for less that .2hr or 1 to 2 km behind the ship”. They note that the landfast ice had mostly deteriorated by the time observations could be made and so part of the marine mammal/icebreaker interaction program was cancelled. However, they also note wave-induced break-up of landfast ice created more numerous fragments at the point where the icebreaker entered the landfast ice. However, they cite the Arctic Pilot Project (Supplementary Information Volume) as stating that there is no evidence for icebreaking leading to premature break-up of landfast ice.

(Keinonen and Lohi, 2001)

In this extended abstract, the authors provide a brief description of the advantages of icebreakers with azimuthal propulsion compared with traditional icebreakers

(Keinonen, 2008)

In this conference paper, the author compares the effectiveness of different ice management techniques in reducing floe size, effective ice thickness and ultimately the ice load on stationary vessels in drifting pack ice.

(Moran et al., 2006)

In this conference paper, the authors describe ice conditions during the Arctic Coring Expedition (ACEX) in 2004, in which a drill-ship (the *Vidar Viking*) successfully remained on station for up to 9 consecutive days in the Central Arctic pack ice. The Article contains an excellent figure (Figure 4) that illustrates the method of ice management and its effect on the ice around the drill ship.

(Prinsenberg et al., 2009)

The authors describe observations made from an icebreaker during a wind event that compressed an 18km wide flaw lead containing 60 cm thick sea ice into a 1.5 km wide rubble field with an average ice thickness of 8 m. The authors also describe being able to “see” the inhomogeneous stress field within the sea ice from the different rates at which the icebreaker channel closed behind the ship. Figure 4 is a clear photograph illustrating this.

(Swedish Polar Research Secretariat, 1993)

This is a summary of the environmental impact assessment prepared for the operation of the Swedish icebreaker *Oden* in polar waters. The table on page 11 categorizes the impacts considered. There is no mention of the physical impact upon the sea ice itself.

(Wettlaufer et al., 2000)

In this paper, the authors present theory and data from experiments and field observations of the freezing of ocean water in leads. The paper contains detailed information on the thermal evolution of the ice and the buoyancy of the brine expelled during growth. Of particular relevance to this review, Figures 3 and 4 show ice growth in the first few days for different temperatures.

(Wright, 2001)

A description of ice management around the Kulluk in the Beaufort Sea 1982-1992. In general, ice management reduces loads on moored structures though mechanically weakening the ice, but "over management" can increase loads due to refreezing of ice.

The Department of the Interior Mission

As the Nation’s principal conservation agency, the Department of the Interior has responsibility for most of our nationally owned public lands and natural resources. This includes fostering the sound use of our land and water resources, protecting our fish, wildlife and biological diversity; preserving the environmental and cultural values of our national parks and historical places; and providing for the enjoyment of life through outdoor recreation. The Department assesses our energy and mineral resources and works to ensure that their development is in the best interests of all our people by encouraging stewardship and citizen participation in their care. The Department also has a major responsibility for American Indian reservation communities and for people who live in island communities.

The Bureau of Ocean Energy Management

The Bureau of Ocean Energy Management (BOEM) works to manage the exploration and development of the nation's offshore resources in a way that appropriately balances economic development, energy independence, and environmental protection through oil and gas leases, renewable energy development and environmental reviews and studies.